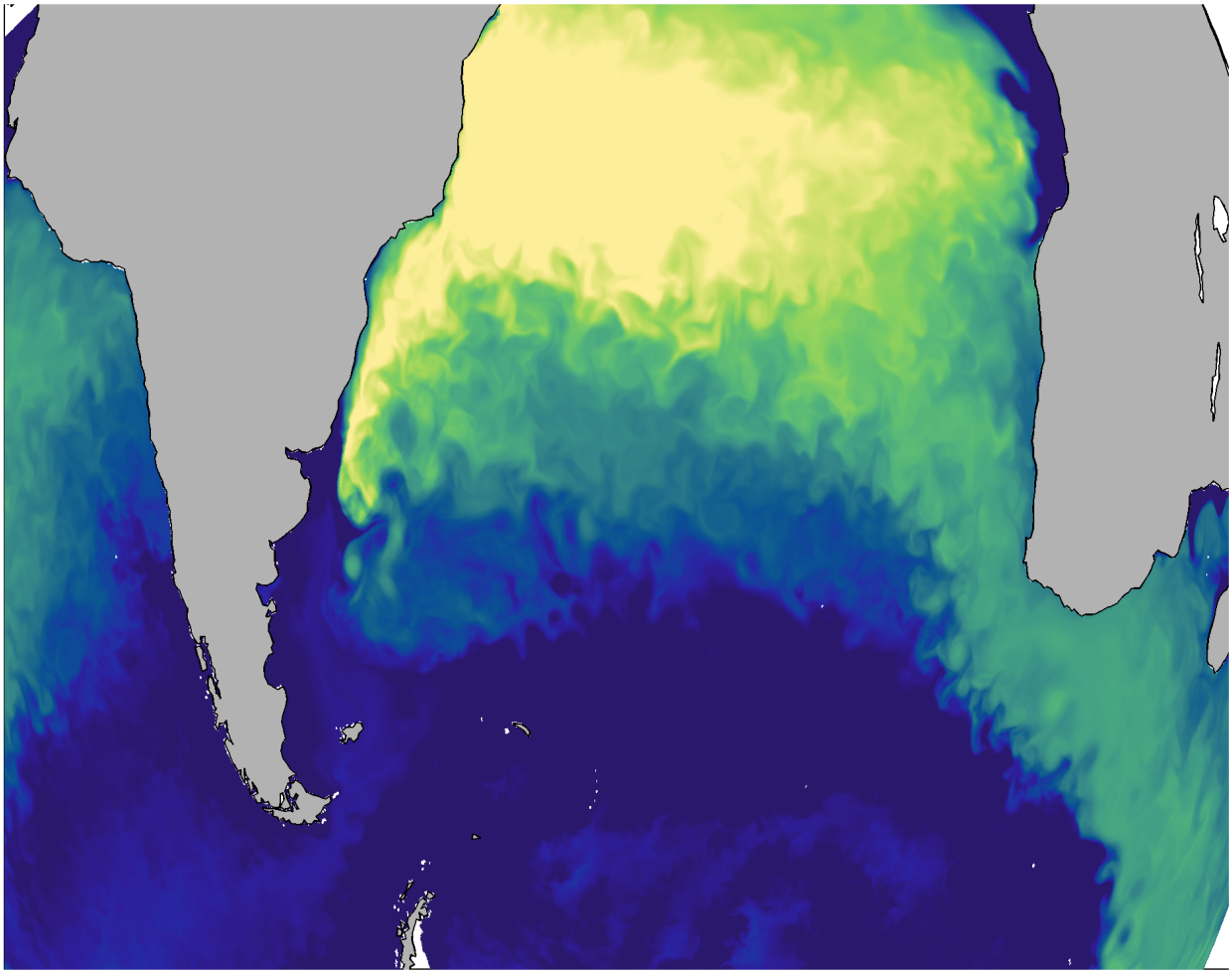

The Brazil-Malvinas Confluence: from local to global scales

Dorleta Orúe-Echevarría Iglesias

2019

UNIVERSITAT POLITÈCNICA DE CATALUNYA BARCELONATECH

The Brazil-Malvinas Confluence: from local to global scales

Dorleta Orúe-Echevarría Iglesias

The Brazil-Malvinas Confluence: from local to global scales

Dorleta Orúe-Echevarría Iglesias

Tesis doctoral presentada para obtener el título de Doctora por la Universidad Politécnica de Cataluña, Programa de Doctorado en Ciencias del Mar. Departamento de Ingeniería Civil y Ambiental.

La Doctoranda	El Director
Dorleta Orúe-Echevarría Iglesias	Josep Lluis Pelegrí

Barcelona, Noviembre de 2019

Gurasoei eta Estiri, familiari
eta, nola ez, Nestorri

Preface

This dissertation, entitled *The Brazil-Malvinas Confluence: from local to global scales*, is presented as a partial requirement to obtain the Doctoral degree from the Universitat Politècnica de Catalunya. This investigation is the compilation of 5 studies aimed at describing the circulation and mixing processes within the Brazil Malvinas Confluence. The research presented here has been conducted between 2014 and 2019 under the guidance of Dr. Josep Lluis Pelegrí Llopart, who is a Research Professor at the Intitut de Ciències del Mar – Consejo Superior de Investigaciones Científicas, supported through a FPU predoctoral grant (FPU13/02884). It has been developed in the framework of the projects TIC-MOC (Tipping Corners of the Meridional Overturning Circulation, reference CTM2011-28867, carried out between January 2012 and December 2015) and VA-DE-RETRO (Retroflexiones de frontera oeste: conexiones en transportes latitudinales y recirculación de giro en el océano Atlántico, reference CTM2014-56987-P, carried out between January 2015 and December 2018).

This doctoral dissertation is structured into a brief Introduction and the presentation of the main Datasets. The following five chapters constitute the core of the dissertation, each of them presented as a scientific article. Four of them (the two datasets and Chapters 3, 4) have already been published or are in the final steps of the publication process, while the other three (Chapters 1, 2 and 5) are still in preparation and should therefore be considered as preliminary drafts. The thesis concludes with the exposition of the main results of this work, as well as with comments on the potential future lines of research. Along this period of research two collaborative research stays were done, at University of Las Palmas de Gran Canaria under the guidance of Dr. Francisco Machín, and at the University of Southampton under the guidance of Prof. Alberto Naveira Garabato. The derived works are shown in Chapters 3 and 5, respectively. During this period the author of this thesis has attended a total of four conferences and two summer colloquia and has participated in three research cruises.

Contents

Summary

The Southwest Atlantic Ocean is a key component of the global climate system. It holds the Confluence of the Brazil and Malvinas Currents (BMC), one of the highest frontal systems of the world ocean. The BMC is the encounter point of subtropical origin warm and salty waters, transported southward within the Brazil Current, and subantarctic waters flowing equatorward along the Malvinas Current. The intense mixing and cross-frontal exchanges highly transform the water masses at this region, which will finally flow southward, eastward or will be subducted into the subtropical thermocline. This PhD dissertation aims at extending our knowledge on the circulation and dynamics in the BMC, placing these results in perspective from the small to the global scales.

The intense property contrast found in this region resemble the intense temperature gradients between low and high latitudes. We first analyse the changes in the heat content of the atmosphere and upper ocean compartments for the last 450 kyr and analyse the sensitivity of the system to changes in albedo, cloud cover and atmospheric and oceanic heat transports.

We then describe the hydrographic conditions found at the BMC during and early fall cruise (TIC-MOC cruise). These reveal the presence of brackish river water on top the frontal system. The salinity anomaly at the surface correlates with the presence of large ageostrophic velocities along the frontal jet. In addition, the rapid evolution of these waters impinges on the thermohaline variability in the proximity of the front. The comparison of surface overview during the cruise is well represented by the high-resolution reanalysis, although at depth it misses the thermohaline intrusions developed both sides the front. On the other hand, climatological data, as it shows the monthly fields, is not able to reproduce the numerous mesoscale features.

We also examine the circulation pattern in the upper 2000 m depth. We find a relatively weak MC near 41^{o}S, 56^{o}W followed by its cyclonic retroflection, an intense subtropical anticyclone replacing the BC-overshoot (BCO), a subantarctic inflow near 53^{o}W maintained both by an upstream earlier diversion of the MC and the cyclonic recirculation of the flow leaving the east along the confluence front. On the northern extreme of the Confluence we found the southward flow of BC, close to its mean value. The results in this chapter also suggest the existence of dianeutral mixing and cross-frontal exchanges resulting in water mass tranformations at the conflunce region.

Combining sea surface temperature images with novel high-resolution SeaSoar measurements (RETRO-BMC cruise), in chapter 4, we further assess the high-frequency temperature variability at at the BMC. We found spatio-temporal scales between 1.5 and 6 days and between 20 and

50 km with the shortest scales along the shelf-break BC and over the Confluence front and the largest ones along the MC and MRC. We conclude that Variability increases at the subsurface due to submesoscale thermohaline intrusions.

Finally, in chapter 5, we analyse the relative role of dianeutral mixing by small scale turbulence and isoneutal mixing induced by mesoscale eddy stirring in setting the temperature-salinity relationship in the Argentine basin. Using microstructure measurements along the Subtropical Front, we found that dieneutral mixing is enhanced in the upper 500 m of the water column, especially downstream the BCO, and at depth over the shelf-break and the eastern limit of the basin, at the mid-Atlantic ridge. Isoneutral diffusivity dominates below 500 m in the centre of the basin. Moreover, we determine the cross-frontal eddy-advective mass flux. These induce the subduction of about 3 Sv of mode and intermediate waters into the subtropical thermocline and the poleward transport of Upper Circumpolar Deep Water.

Resumen

El suroeste del Océano Atlántico es clave del sistema climático global. En esta región se encuentran las corrientes de Brasil y Malvinas, dando lugar a uno de los sistemas frontales más intensos del océano mundial, la Confluencia de Brasil-Malvinas (BMC). Esta región frontal es el punto de encuentro de aguas de origen subtropical, cálidas y saladas, que son transportadas hacia el sur en la corriente de Brasil y aguas de origen subantárctico que viajan hacia el ecuador a lo largo de la corriente de Malvinas. La intensa mezcla y los intercambios frontales cruzados transforman en gran medida las masas de agua que aquí se encuentran y que finalmente fluirán hacia el sur, hacia el este o que serán subducidas hacia la termoclina subtropical. Esta tesis tiene como objetivo principal ampliar nuestro conocimiento sobre la circulación y dinámica en la BMC, colocando estos resultados en perspectiva, desde la pequeña escala a la escala global.

El intenso contraste de propiedades de las aguas que se encuentran en esta región se asemeja a los intensos gradientes de temperatura que encontramos entre las altas y bajas latitudes. En un primer trabajo, analizamos los cambios en el contenido de calor de la atmósfera y el océano superior durante los últimos 450 millones de años.

A continuación, describimos las condiciones hidrográficas encontradas en la BMC a principios de otoño de 2015 a partir de los datos recogidos en una campaña oceanográfica (TIC-MOC) y su comparación con datos de reanálisis y climatológicos. Estos revelan la presencia de aguas salobres del Río de la Plata en los primeros metros del sistema frontal. La anomalía de salinidad presenta una correlación positiva con las intensas velocidades ageostróficas a lo largo del jet frontal. La comparación de la visión general de las condiciones superficiales durante la campaña está bien representada por el reanálisis de alta resolución, aunque en profundidad su exactitud es menor debido a la presencia de intrusiones termohalinas desarrolladas a ambos lados del frente, no reproducidas por el modelo. Los datos climatológicos, sin embargo, al representar las condiciones medias del mes, no muestran las numerosas estructuras de mesoescala encontradas en la región.

Asimismo, examinamos el patrón de circulación en los primeros 2000 metros de la columna de agua. Al sur del frente encontramos un transporte débil de la MC aproximadamente a 41^{o}S, 56^{o}W, seguido de su retroflexión ciclónica, un anticiclón subtropical intenso que reemplaza la retroflexión de la corriente de Brasil, un flujo de aguas subantárcticas a 53^{o}W alimentado por un desvío aguas arriba de la MC y la recirculación ciclónica del flujo que sale al este a lo largo del frente de Confluencia. En en extremo norte, encontramos el transporte hacia el sur, dentro de los valores medios, de la corriente de Brasil. Los resultados en este capítulo sugieren también la existencia de mezcla dianeutra e intercambios frontales en la BMC.

Evaluamos la variabilidad de alta frecuencia de la temperatura en esta región combinando imágenes de temperatura superficial del mar con nueva mediciones de alta resolución recogidas con un SeaSoar (campaña RETRO-BMC). Encontramos escalas espacio-temporales características de entre 1.5 y 6 días y entre 20 y 50 km. Las escalas más cortas se encuentran la lo largo de la corriente de Brasil en su proximidad a la plataforma continental y sobre el frente de Confluencia, mientas que las mayores escalas corresponden a la MC y su retroflexión. La variabilidad aumenta en profundidad debido a la presencia de las intrusiones termohalinas submesoescalares.

Finalmente, analizamos el papel relativo de la mezcla dianeutra debida a turbulencia de pequeña escala y de la mezcla isoneutra inducida por remolinos de mesoescala en establecer la relación temperatura-salinidad en la cuenca argentina utilizando para ello mediciones de microestructura. La mezcla dianeutra es máxima en los primeros 500 m de la columna de agua, especialmente aguas abajo de la BCO, y en profundidad sobre el borde de la plataforma continental y el límite oriental de la cuenca sobre la Dorsal Mesoatlántica. La difusividad isoneutral domina en profundiad (>500 m) en el centro de la cuenca. Además, determinamos el flujo de masa meridional debido a la advección inducida por los remolimos mesoscalares.

Acronyms list

AABW	Antarctic Bottom Water
AAIW	Antarctic Intermediate Water
ACC	Antarctic Circumpolar Current
ADT	Absolute Dynamic Topography
AMOC	Atlantic Meridional Overturning Circulation
BC	Brazil Current
BCF	Brazil Current Front
BCO	Brazil Current Overshoot
BMC	Brazil Malvinas Confluence
CTD	Conductivity-Temperature-Depth
LADCP	Lowered Acoustic Doppler Current Profiler
LCDW	Lower Circumpolar Deep Water
MAR	Mid-Atlantic Ridge
MC	Malvinas Current
MOC	Meridional Overturning Circulation
MRC	Malvinas Return Current
NADW	North Atlantic Deep Water
OSTIA	Operational Sea Surface Temperature and Ice Analysis
PPW	Plata Plume Water
PV	Potential vorticity
RdlP	Rio de la Plata and Patos-Mirim Lagoon system
SAC	South Atlantic Current
SACW	South Atlantic Central Water
SAF	Subantarctic Front
SAMW	Subantarctic Mode Water
SASW	Subantarctic Shelft Water
SeaSoar	Winged and towed undulating sensor platform
STMW	Subtropical Mode Water
STF	Subtropical Front
STSF	Subtropical Shelf Front
STSW	Subtropical Shelf Water
TW	Tropical Water
UCDW	Upper Circumpolar Deep Water
VADCP	Vessel-mounted Acoustic Doppler Current Profiler

Part I ‖ Introduction

General Introduction

The ocean modulates the Earth's heat distribution

The thermodynamic state of the Earth system depends on different physical parameters, such as the incoming solar energy, the greenhouse effect and atmospheric and oceanic circulation, as well as on the strong internal climate feedback mechanisms such as snow/ice albedo, water vapour and cloud feedbacks. Biogeochemical factors are also potentially important in controlling the Earth's thermodynamic state, although they act in a more subtle way, indirectly through the regulation of carbon dioxide (CO_2) and other greenhouse gases.

Incoming solar radiation is the primary source of energy and the main driver of the Earth climate system. Tropical latitudes, due to their particular astronomical and atmospheric conditions, receive more short-wave radiation in comparison to higher latitudes. On the other hand, outgoing long-wave radiation does not vary much with latitude, resulting in a heat-gain at latitudes less than 35^o while at higher latitudes there is a deficit (Bryden and Imawaki, 2001). This difference settles a meridional heat transport from the equator towards the poles, aimed at addressing this imbalance.

The atmospheric and oceanic circulation contribute near - equally to the meridional heat flux, although atmospheric transports dominate at high latitudes and oceanic transports do so in tropical regions (Wunsch, 2005; Czaja and Marshall, 2006). Both compartments also differ in the predominant transport mechanisms: in the atmosphere the poleward heat flux is mainly achieved through the release and transport of dry static and latent energy (Trenberth and Stepaniek, 2003) while in the ocean this occurs through large-scale (wind-driven and thermohaline) circulation and mesoscale eddies (Wunsch, 1999; Jayne and Marotzke, 2002; Ferrari and Ferreira, 2011). In particular, the Meridional Overturning Circulation (MOC) [Fig. 1] is responsible of a large fraction of the poleward heat transport, becoming a key element in the global energy balance (Talley, 2003).

Changes in any of the transport and feedback mechanisms can result in changes in the thermodynamic state of the Earth. These fluctuations occur at multiple time scales, from interannual and interdecadal periods such as El Niño-Southern Oscillation or North Atlantic Oscillation to centuries and even glacial-interglacial periods. Most of these climate phenomena are related to changes in the way the ocean stores and transports heat. Lower-frequency variability changes, that is from centennial to glacial periods, are linked to changes in the deep ocean circulation and stratification (Ferrari et al., 2014) responding to the reorganization and variations in the intensity of the MOC (Broecker et al., 1997; 2003). Furthermore, the MOC interacts with the carbon reservoir of the deep ocean and therefore conditions the atmospheric CO_2 concentration (Sigman et al., 2010; Watson et al., 2015), amplifying or diminishing the greenhouse effect.

Time-independent box-type models, time-dependent heuristic models and deterministic box-type models have been used to identify and parameterize the factors controlling the way the Earth changes between different thermodynamic states (Sarmiento and Toogweiller, 1984; Siegenthaler and Wenk, 1984; Paillar, 1998; Paillard and Parrenin, 2004; Garcia-Olivares and Herrero, 2012; 2013; Pelegrí et al., 2013). Despite their relative simplicity, these models are able to satisfactorily reproduce the glacial-interglacial periods as well as the maximum and minimum CO_2 concentration or $\delta^{18}O$ (used as a proxy of temperature). However, less is known about the mechanisms controlling the effect of different feedback mechanisms at these temporal scales. In **Chapter 1**, we develop a simple time-dependent coupled ocean-atmosphere model aimed at analysing the changes in the heat content of the atmosphere and upper-ocean during the last four glacial-interglacial periods. In addition, we assess the effect of changes in the MOC, the atmospheric and upper-ocean circulation and the different feedback mechanisms such as cloud coverage and ice-albedo.

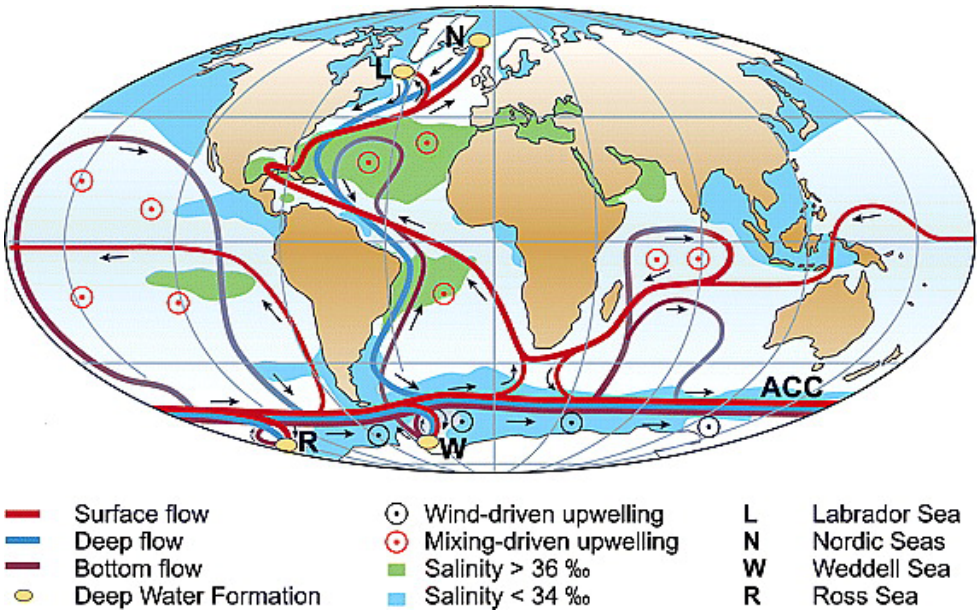

Fig. 1: Schematic of the global MOC. The red curves in the Atlantic indicate the northward flow of water in the upper layers (MOC upper limb). The blue and purple curves denote the deep and bottom water circulation (MOC lower limb). The filled orange circles in the Nordic and Labrador Seas indicate regions where near-surface water cools, releasing heat to the atmosphere, and becomes denser, causing the water to sink to deeper layers of the Atlantic (deep water formation). At the southern end of the Atlantic, the AMOC connects with the Antarctic Circumpolar Current (ACC). Deep waters formed in the Southern Ocean spread at levels deeper than those used by waters from the North Atlantic. The circles with interior dots indicate regions where water upwells from deeper layers to the upper ocean. Black arrows indicate the direction of the circulation. Reproduced from Kuhlbrodt et al. (2007) after Rhamstorf (2002).

The Atlantic meridional overturning circulation

According to paleoclimate records, changes in the Atlantic branch of the global MOC, the Atlantic MOC (AMOC), have been related to abrupt climate changes (Peterson et al., 2000; Ganopolski and Rahmstorf, 2001; Stott et al., 2002). The worldwide implications of the AMOC circulation arise from the overall northward heat transport in this basin, from the Southern to the Northern hemisphere across the equator (Trenberth and Caron, 2011; Ganachaud and Wunsch, 2003), in contraposition to the poleward circulations, asymmetric about the Equator, in the Pacific and Indian oceans.

The AMOC schematic circulation consists of two primary overturning cells forced by polar water mass formation: (1) an upper cell formed by the southward flow of cold North Atlantic Deep Water (NADW) at 1500-4500 m depth and the compensating northward flow in the upper 1000 m of relatively warm and salty waters and (2) a deep cell in which Antarctic Bottom Water (AABW), formed around Antarctica, flows northward at about 4500 m and gradually rises into the lower part of the southward flowing NADW (Talley et al., 2013) [Fig. 1].

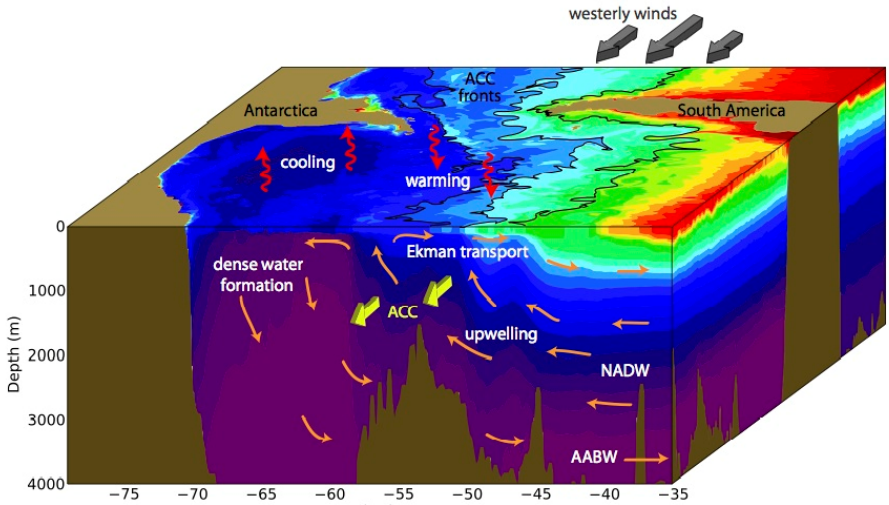

Fig. 2: A schematic view of the dynamics in the Southern Ocean with water density colored from red for surface light waters to purple for the densest deep waters. The westerly winds drive northward Ekman transports at the ocean's surface. The latitudinal variation in the westerlies creates a divergence in the Ekman transport, which causes water to upwell along the sloping density layers from the deep ocean to the surface. Both eddies and the strong eastward Antarctic circumpolar current over topographic ridges also influence the upwelling. Upon reaching the upper ocean, the upwelled waters split into two pathways: Water that reaches the surface close to Antarctica's sea ice is cooled, sinks along the continental shelf, and is transformed into dense bottom water; water that surfaces north of the sea-ice edge is warmed and flows northward with the Ekman layer. Reproduced from Morrison et al. (2015).

In order to sustain the AMOC, it is necessary that the dense deep waters return to the sea surface (Wunsch and Ferrari, 2004; Visbeck, 2007). Two possible mechanisms have been proposed for this upwelling: turbulent mixing in the deep ocean and northward wind-driven Ekman transports in the Southern Ocean. The first mechanism, turbulent mixing in the ocean interior,

is driven by the energy cascading from mesoscale to submesoscale internal waves and small-scale motions. It diffuses heat downward across surfaces of equal density (diapycnal mixing) and contributes to the lightening and hence upwelling of cold and dense waters (Munk and Wunsch, 1998; Nikurashin and Vallis, 2011), forming the returning path of the lower cell of the MOC. The second mechanism, upwelling of deep waters, happens primarily along the outcropping isopycnal surfaces in the Southern Ocean, which are driven by the strong westerly winds blowing around Antarctica (Toggwailer and Samuels, 1995; Marshall and Speer, 2012) [Fig. 2]. The zonal wind stress induces downwelling equatorward of the maximum zonal wind stress of mode and intermediate waters, which will end up reaching the North Atlantic, and poleward upwelling supplied by southward geostrophic flow at depth. The deep flow along the steep isopycnals is baroclinically unstable and forms mesoscale eddies, which enhance a vertical cell across the ACC, which in the upper layers opposes the wind-induced transport and enhances upwelling down to some 2000 m (Marshall and Radko, 2003; Marshall and Speer, 2012). Therefore, the water mass transformations associated with the AMOC is the complex outcome of the interaction between surface currents, deep currents and eddy-driven circulation (Buckley and Marshall, 2016).

The South Atlantic circulation

Thermocline and intermediate waters subducted at the southern extreme of the South Atlantic Subtropical gyre, along the Subtropical Front, contribute greatly to the returning path of the AMOC (Campos et al., 1999). Part of these waters are originated in the South Atlantic Ocean (Stramma and England, 1999) but most of them come from the Pacific Ocean through the Drake Passage, known as the cold route (Rintoul, 1991), and the Indian Ocean via the Agulhas leakage, referred to as the warm route (Gordon, 1986). All these water masses experience important modifications along their journey in the South Atlantic basin due to air-sea interactions, small scale diapycnal mixing (Bianchi et al., 1993; 2002; Sloyan and Rintoul, 2002), eddy-induced isopycnal mixing, subduction and advection processes (Garzoli and Matano, 2011). This variety of processes makes the circulation of this basin a fundamental component of the AMOC.

The South Atlantic subtropical gyre circulation is driven by both wind and large-scale thermohaline imbalances. The upper 500 m of the subtropical South Atlantic are dominated by the wind-driven anticyclonic subtropical gyre (Peterson and Stramma, 1991; Stramma and England, 1999), consisting of the South Equatorial Current (SEC), Brazil Current (BC), South Atlantic Current (SAC) and Benguela Current [Fig. 3]. The circulation of intermediate waters (500-1200 m) is also coupled to this gyre (Reid, 1989; Rintoul, 1991; Gordon et al., 1992).

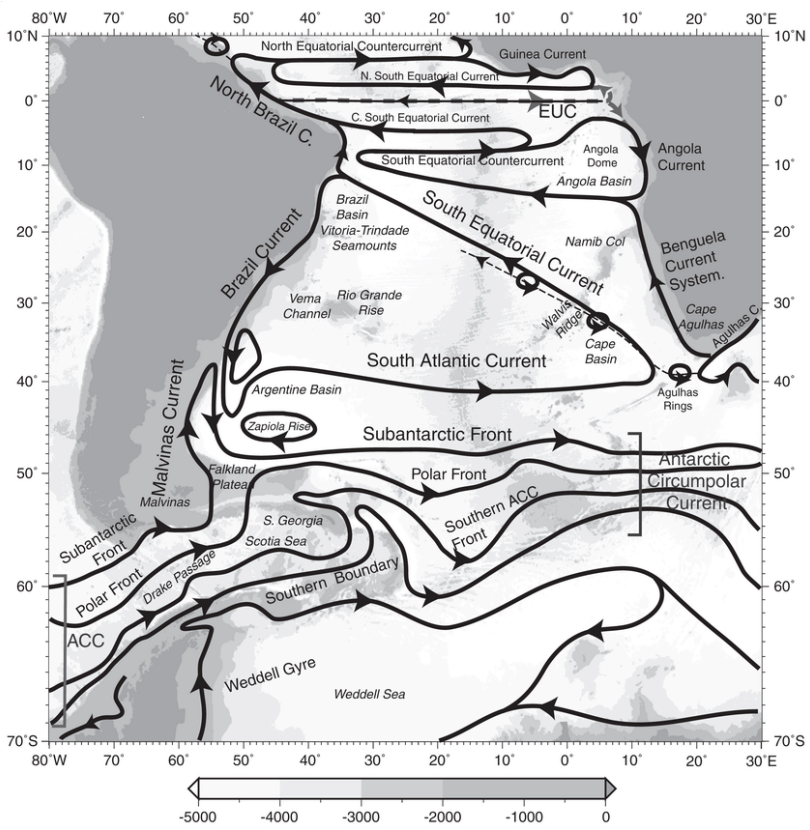

Fig. 3: Schematic representation of the surface circulation in the South Atlantic Ocean. The main ocean currents are depicted in black, with the arrows indicating their direction. The depth of the water column is grey-shaded, in meters. Reproduced from Talley et al. (2011).

The southern limit of the South Atlantic Subtropical gyre is formed by the SAC, flowing quasi-zonally eastward from 50^{o}W towards the African continent. Near South Africa, a branch continues into the Indian Ocean while the other turns north into the Benguela Current and finally into the SEC. The SEC transports subtropical waters from the Benguela Current region westward, towards Brazil, representing the northern limit of the subtropical gyre. Once this current reaches the South America continental slope, near 15^{o}S, it bifurcates to the north as the North Brazil Current and to the south as the BC. At intermediate depths this bifurcation occurs further south, near 27^{o}S, feeding the southern flow of the Intermediate Western Boundary Current (Boebel et al., 1999; Legeais et al., 2013).

The poleward western boundary circulation of the subtropical gyre is governed by the BC, which carries warm and salty waters at central and intermediate levels and NADW in the Deep Western Boundary Current (Reid et al., 1977). The BC encounters the Malvinas Current (MC) near 38^{o}S, in a region known as the Brazil Malvinas Confluence (BMC) (Gordon and Greengrove, 1986), where it separates from the boundary and continues south drawing a tight loop known as the Brazil Current Overshoot (BCO) (Saraceno et al., 2004). The BCO retroflects northward at around 45^{o}S-55^{o}W, splitting into one branch that turns northward as the BC offshore recirculation (Stramma and England, 1999; Valla et al., 2018) and another one that

continues eastward as the SAC, closing the subtropical gyre. The Subtropical Front (STF), as the southern extreme of the Subtropical gyre, separates warmer and saltier subtropical water masses to the north from cold, fresh and highly oxygenated subantarctic water masses to the south.

South of the STF, the circulation is governed by the eastward flowing ACC. Its zonal flow is organized in three frontal systems, which correspond to water mass boundaries as well as deep-reaching eastward flowing jets, the Subantarctic Front (SAF), Polar Front (PF) and Southern ACC Front (Orsi et al., 1995) [Fig. 3].

In the southwestern basin, the MC transports equatorward subantarctic water as part of the cold path source for the upper limb of the AMOC. Originated as an offshoot of the Antarctic Circumpolar Current (ACC), it enters the Argentine Basin east of the Malvinas Islands (Lumpkin and Johnson, 2013) and then flows northward along the path of the SAF following the 1000-2000 m isobaths (Piola et al., 2013) up to 38^{o}S where it encounters the BC. After the confluence, it sharply turns south as the Malvinas Return Current (MRC) (Piola et al., 2013) before finally flowing east at about 45^{o}S (Peterson and Whitworth, 1989).

The Brazil-Malvinas Confluence

The BMC is a key site in the AMOC, with important implications on the global climate system (Campos et al., 1999). Its characteristics and variability depend on several dynamic processes. Firstly, the convergence of the STF and SAF at this site, and thus the encounter of subtropical and subantartic waters, favours the exchange of properties across the front and controls the distribution of heat and salt over the basin (Jullion et al., 2010). Secondly, the intense mixing and water mass transformation processes occurring in the BMC (Sloyan and Rintoul, 2001) to a large extent condition the water mass structure of the South Atlantic Ocean (Garzoli and Matano, 2011). Finally, it is the locus of the ventilation of the subtropical gyre, as some of these young and oxygen-rich formed waters and Antarctic origin surface waters are subducted under the surface subtropical waters and extend northward (Karstensen and Quadfasel, 2002; Donners et al., 2005). Therefore, understanding processes and dynamics at this region would contribute to improve our knowledge of the role of the South Atlantic as a major component of the global climate.

The high variability of the BMC (Garzoli, 1993; Lumpkin and Garzoli, 2011) and the reduced number of in-situ measurements hinders the description of its regional circulation. The complexity of the water mass structure, characterized by the convergence of multiple water masses of very different origin and hence properties (Maamaatuaihutapu et al., 1992, 1994) [Fig. 4],

challenges an accurate description of this region. Due to the scarcity of in-situ velocity measurements, the hydrographic observations have been used to identify the different water masses and the spatial distribution of properties has led to propose different spreading pathways [Fig. 5] (Stramma and England, 1999; Wienders et al., 2000; Valla et al., 2018).

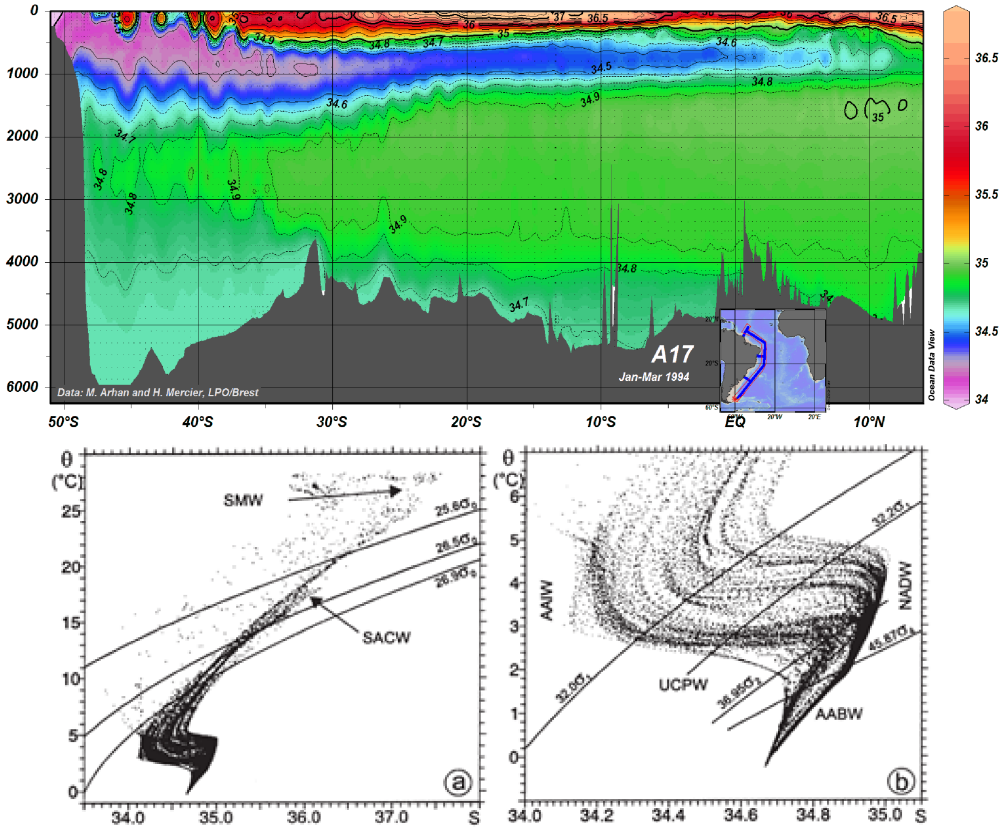

Fig. 4: (Top) Vertical section of salinity across the WOCE A17 section. Retrieved from the eWOCE gallery (Schlitzer, 2000). (Bottom) θ-S diagram for the A17 section showing the main water masses in the western South Atlantic: SMW (Salinity Maximum Water), SACW (South Atlantic Central Water), AAIW (Antarctic Intermediate Water), UCPW (Upper Circumpolar Water), NADW (North Atlantic Deep Water) and AABW (Antarctic Bottom Water). The panel on the right shows a zoom to the intermediate and deep waters. Reproduced from Mémery et al. (2000).

The upper 200 m of the BC water column are characterized by the salty and warm Tropical Water (TW). This water mass is modified Salinity Maximum Water, which is formed in the subtropics where evaporation exceeds precipitation (Mémery et al., 2000). Thus, it is the saltiest (>36) and warmest (>20^{o}C) water mass found in the Argentine Basin. After mixing at the BMC, a fresher and colder TW splits into two branches, one flowing eastward within the SAC and the other recirculating northward as the BC offshore recirculation.

Below TW, between 200 and 600 m (shallower in the core of the BC) we find South Atlantic Central Water (SACW). It is characterized in the potential temperate-salinity (θ-S) diagram by a near-straight line between (5-6^{o}C, 34.6) and (18-20^{o}C, 36.0) (Stamma and England, 1999) [Fig.

5]. This water mass comprises two mode waters: Subtropical Mode Water (STMW) and Subantarctic Mode Water (SAMW). STMWs are found in every western boundary current system (Hanawa and Talley, 2001). Three different types of STMW have been identified in the South Atlantic (Provost et al., 1999), covering a range of temperatures between 12^{o}C and 18^{o}C. In particular, two of them are formed mainly in the BCO as the result of air-sea exchanges and thermodynamic processes at the BMC (Provost et al., 1999; Sato and Polito, 2014). The STMW shows a circulation pattern analogue to TW. On the other hand, the SAMW water characterizes the first meters of the MC, being much colder ($\theta \cong$ 5-8^{o}C) and fresher (S $\cong$ 34.1) than STMW. This water mass is formed north of the SAF by winter convection (McCartney, 1977, 1982) and flows northward within the MC. At the BMC front, it subducts into the subtropical thermocline and continues northward (Piola and Gordon, 1989).

Intermediate levels of the BMC are occupied by Antarctic Intermediate Water (AAIW), which is characterized by salinity minimum values (S <34.3) and maximum dissolved oxygen content. It is formed through the subduction of Antarctic Surface water in the northern Drake Passage and the MC loop (Talley, 1996). At the BMC, these relatively new AAIW mixes intensely with warmer, saltier and less oxygenated older AAIW, which flows poleward south of 27^{o}S under the BC (Valla et al., 2018; Orúe-Echevarría et al., 2019). After the confluence, the AAIW splits into three branches: one that flows northward under the offshore BC recirculation, another that continues southward with the MRC, and a final fraction flows eastward within the SAC (Valla et al., 2018).

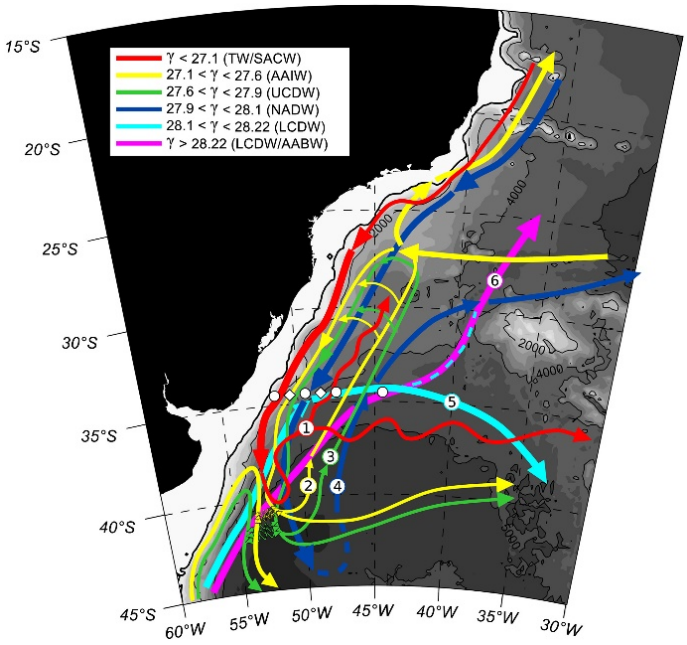

Fig. 5: Schematic pathways of the water masses in the northwest Argentine Basin, colour-coded according to the different water masses defined by neutral density ranges (in kg m^{-3}): TW/SACW (red), AAIW (yellow), UCDW (green), NADW (blue), LCDW (cyan), AABW (magenta). The zigzag yellow and green arrows indicate property exchanges in the BMC region, and the dashed paths indicate sporadic or unconfirmed pathways. Reproduced from Valla et al. (2018).

Below AAIW and down to about 2000 m depth, we find Upper Circumpolar Deep Water (UCDW). It is a large body of relatively fresh (S >34.3) and oxygen-poor (<4.2 ml l^{-1}) water, characterized by a maximum broad silicate concentration (Stramma and England, 1999). It is formed from the mixing of upwelled NADW with waters circulating within the ACC (Reid et al., 1977). It presents the same circulation patters as AAIW, that is, a more pristine (less oxygenated and colder) UCDW entering the Argentine basin mixes with the older recirculated UCDW flowing under the BC core. After the BMC, the UCDW splits in two branches, one that flows beneath the BC offshore recirculation into the subtropical Atlantic and another that moves into the subantarctic zone with the MRC.

Below UCDW, we find NADW flowing along the deep western boundary current. It is identified by its relatively high potential temperature ($\theta \cong 3^{o}C$) and salinity ($S \cong 34.9$) values. South of the BMC, there is a recirculation cell and a diluted variety of NADW turns northward. Deepest water masses correspond to Lower Circumpolar Deep Water (LCDW) and AABW. Both cross northward the Argentine Basin, from the Drake Passage until the deep MC waters (Georgi, 1981; Reid, 1989).

A useful technique to aid these descriptions is inverse modelling. The inverse method is based on the principle of conservation of properties in any closed box, such as a region delimited by the coast and certain hydrographic lines (Wunsch, 1996). These methods have been applied to the Argentine basin and the BMC region in order to estimate mass and property transports (Maamaatuaihutapu et al., 1998; Sloyan and Rintoul, 2001; Jullion et al., 2010). However, these studies have used low-resolution or non-synoptic hydrographic data. Therefore, some small-scale local pathways, but with regional or even global implications, could be missed. In this study we use a recently gathered hydrographic and velocity dataset (**Dataset on TIC-MOC cruise** and **Chapter 2**), together with satellite data in order to analyse the circulation and main water - mass modifications in the BMC at two different spatial scales (**Chapter 3**). Our results reveal the prominent role of mesoscale structures in the circulation and exchanges between the subtropical and subantarctic region and point at the important modifications that water masses experience in the region.

On top the regional BMC circulation pattern, there is a rich mesoscale eddy and filament field (Legeckis and Gordon, 1982; Olson et al., 1988; Pilo et al., 2015; Mason et al., 2017). The anticyclonic/cyclonic eddies confine subtropical/subantartic waters, which contrast with the properties of surrounding waters. These mesoscalar features distort the large-scale STF and SAF, giving rise to less pronounced fronts along these features. Further, the large-scale fronts and the mesoscalar features experience displacements that cause variability that ranges from months to weeks (Legeckis and Gordon, 1982; Pilo et al., 2015). At the submesoscale, the features experience faster changes, which suggests the existence of much shorter (of the order of days

and tens of kilometres) temporal and spatial scales. The sharp surface property contrasts have allowed to determine the variability of this region from satellite imagery, although most of the studies have focused on the semi-annual or interannual variability (Legeckis and Gordon, 1982; Olson et al., 1988; Goni and Wainer, 2001; Goni et al., 2011). However, little is known about the high-frequency surface and subsurface correlation scales. In **Chapter 4**, based on novel data from two high-resolution near-synoptic three-dimensional surveys in the frontal region (**Dataset on RETRO-BMC cruise**) and high-resolution SST imagery, we assess the surface temporal, cross-front vertical and both surface and subsurface spatial correlation scales of the temperature field at the BMC.

Mixing in the Southwest Atlantic

The large-scale ocean patterns rely significantly upon the mesoscale and submesoscale processes, which are responsible for the turbulent diffusion and redistribution of heat and salt, among other properties. In the absence of diffusive processes, advection would bring about sharp physical and biogeochemical property contrasts. The submesoscale diffusion (with typical scales of several kilometres and days) is responsible for smoothing out these contrasts, in such a way that the advective currents themselves also weaken out. The combination of external forcing, advection and diffusion leads to what we view as the mean state of the ocean.

Diffusion occurs both along and cross isopycnals – isopycnal and diapycnal – in directions close to the horizontal and vertical. The small-scale turbulent processes associated with the submesoscale motions occur at horizontal lengths shorter than O (10 km) and O (100 m), typically one order of magnitude less than the mesoscalar eddies. Rather than being globally uniform, these processes are intensified in certain specific areas, often related to topographic obstacles and variations in external forcing (Wunsch and Ferrari, 2004).

Diapycnal mixing caused by small-scale turbulence varies with depth and location (Whalen et al. 2012; Mackinnon et al., 2013). In the upper 1000 m of the water column, dissipation is enhanced by the downward propagation and breaking of near-inertial waves generated by winds acting on the surface mixed layer (D'Asaro, 1985; Waterman et al., 2013). At depth, elevated dissipation values are found above rough topography, such as abrupt isolated ridges, related to the generation and dissipation of internal lee waves or to strong near-bottom flows (Polzin et al., 1997; Ledwell et al., 2000; Nikurashin and Ferrari, 2011; Naveira Garabato et al., 2014; Waterhouse et al., 2014) [Fig. 6].

Eddies play a primary role in the distribution of tracers such as heat, nutrients, dissolved gases and other biogeochemical properties in the world ocean. This mechanism is indeed necessary to transfer the net input of heat at low latitudes towards the high latitudes, where it is eventually

lost to the atmosphere (Johnson and Bryden, 1989). Eddies affect tracers' distributions through three mechanisms: (1) eddy-diffusive transport or isopycnal stirring, which results from eddies stirring tracers due to their rotation primarily along interior neutral surfaces (Redi, 1982; Naveira Garabato et al., 2011) [Figs. 6], (2) eddy-advective transport or 'bolus velocity', as these features extract potential energy from the mean flow and induce a flattening of isoneutral surfaces by volume fluxes (Gent and McWilliams, 1990; Bates et al., 2014), and (3) eddy trapping and advection, where water properties are quasi-isolated and laterally transported to ocean areas with other physico-chemical properties (Flierl, 1981; Chelton et al., 2011).

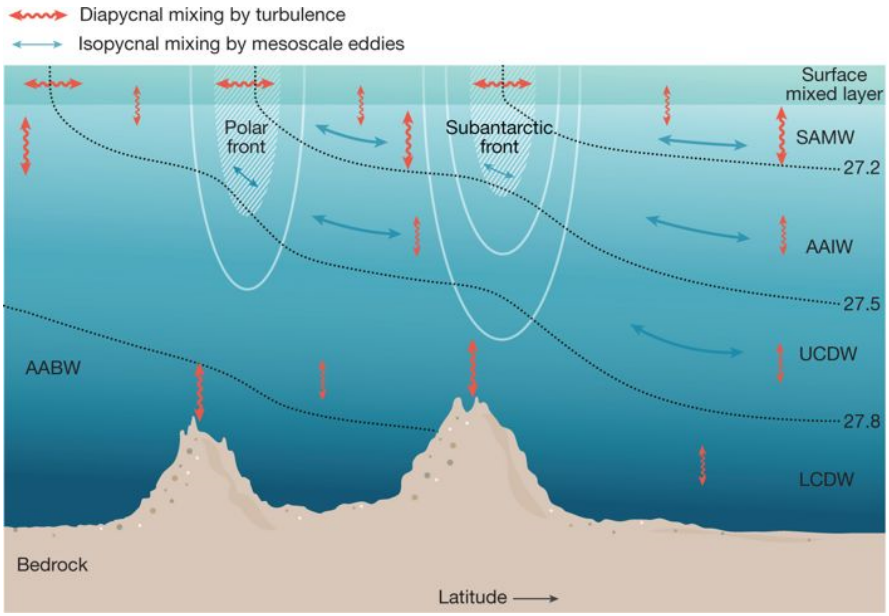

Fig. 6: Scheme of the spatial variability of mixing processes in the Southern Ocean. Isopycnal mixing (double headed blue arrows) is inhibited in the upper part of the ACC jets, where the mean flow is strong relative to the eddies. Diapycnal mixing (squiggly red arrows) is enhanced near the sea surface and near bottom rough topography. The dotted lines indicate contours of neutral density and the principal water masses are indicated. Reproduced from Rintoul et al. (2018).

Isopycnal mixing by mesoscale eddies is enhanced in regions of high eddy kinetic energy, such as western boundary currents and along the ACC (e.g. Cole et al., 2015; Roach et al., 2018). This mixing process is especially relevant in the transport of properties across the zonal jets of the ACC which act as barriers to the poleward transport of properties (Abernathey et al., 2010; Naveira Garabato et al., 2011). These transports are suppressed by one to two orders of magnitude in the core of the jets (Naveira Garabato et al., 2011, 2016), due to the much larger velocity of the ACC as compared with the eddy's phase speed (Ferrari and Nikurashin, 2010), and it is intensified at depth, where the flow's speed is reduced [Fig. 6].

At the Southern Ocean, the poleward eddy heat flux is enhanced in several hotspot regions [Table 1], where the fronts meander around major topographic obstacles or interact with western boundary currents, such as Drake Passage, Kerguelen Plateau or the BMC (Foppert et al., 2017).

The BMC has indeed a large contribution to the Southern Ocean heat budget, accounting for the 47 % of the total heat flux across the STF and 11 % of the heat crossing the southern boundary of the ACC [Table 1]. However, most of the studies have focused on the eddy diffusion across the Drake Passage (Ferrari et al., 2014; Dufour et al., 2015; Watts et al., 2016). In this thesis we use in-situ data along the STF in the Argentine basin to estimate both diapycnal and isopycnal diffusivities at the BMC in order to characterize mixing rates (**Chapter 5**).

Table 1: The last column shows the along circumpolar integrated streamline time-mean and depth-integrated meridional eddy heat flux across five major ACC fronts, as defined using sea surface height contours ($\overline{SSH_{sat}}$) criteria (N-Edge: northern edge of the Subantarctic front; SAF: Subantarctic Front; PF: Polar Front; SACCF: Subantarctic Circumpolar Current Front; S-Edge: southern edge of the SACCF). The other columns show the fraction (%) of the transport associated with hot spots of eddy activity (ARC: Agulhas Return Current; BMC: Brazil Malvinas Confluence; SWIR: Southwest Indian Ridge; KP: Kerguelen Plateau; SEIR: Southeast Indian Ridge; MR: Maquarie Ridge; PAR: Pacific Antarctic Ridge; DP: Drake Passage). Reproduced from Foppert et al. (2017).

Label	$\overline{SSH_{sat}}$ (m)	ARC	BMC	SWIR	KP	SEIR	MR	PAR	DP	Total (PW)
N-Edge	0.3	42	47			5		1		-1.06
SAF	-0.1	14	27	1	6	16	14	4	12	-0.33
PF	-0.4	1	13	15	6	15	12	6	23	-0.24
SACCF	-0.8		7	22	21	15	3	6	15	-0.08
S-Edge	-1.0		11	26	21	7	3	9	7	-0.02

Furthermore, mesoscale eddies can play an important role in the ventilation of the subtropical thermocline at oceanic frontal systems (Marshall, 1997; Qu et al., 2002). At the upper ocean the eddy lateral advection across large density gradients at frontal structures leads to the subduction of mode waters. This is achieved by the thickness flux in the northward direction down the mean thickness gradient, and across the mean flow (Nishikawa et al., 2010). We use the isoneutral diffusivity determined in **Chapter 5** together with potential vorticity changes along the basin to determine the eddy-induced meridional overturning streamfunction across the STF (**Chapter 5**).

Aims and Outline of the Thesis

The main objective of this doctoral dissertation is to broaden our knowledge of the circulation and dynamics in the Brazil Malvinas Confluence, placing these results in perspective from the small to the global scales.

In order to achieve this objective, we divide this dissertation in two dataset chapters and five chapters covering the main results. These chapters are structured as scientific papers, which can result in some reiteration but allows reading them as independent pieces of research. Finally, we end with a conclusions chapter where we summarize the principal conclusions.

Dataset on the TIC-MOC cruise onboard R/V Hespérides, March 2015, Brazil-Malvinas Confluence

The TIC-MOC cruise was designed to characterize the mesoscale and regional dynamics of the BMC. It was carried on board the R/V Hespérides, between 8 and 22 March 2015, with departure from Ushuaia and arrival to Salvador de Bahía. In this chapter we describe the experimental design, instrument types, field methodology, data processing and sensor calibration. This dataset is used in **Chapter 2** and **Chapter 3**.

Dataset on the RETRO-BMC cruise onboard R/V Hespérides, April 2017, Brazil-Malvinas Confluence

In this chapter we present the dataset gathered during the RETRO-BMC cruise, which was aimed at analysing the structures and variability of the BMC at different spatial scales. The cruise was carried on board the R/V Hespérides, between 8 and 17 April 2017, with departure from Ushuaia and arrival to Santos. We describe the cruise design, the hydrographic data acquisition and processing methodology. This dataset is used in **Chapter 4**.

Chapter 1: Idealized box models as effective tools to understand the glacial-interglacial response of the ocean-atmosphere systems

The Earth climate system has shifted between glacial and interglacial periods during the last 3 Myr, alternating between different temperature and atmospheric-CO_2 states. These variations arise from modifications in key global processes, such as CO_2 atmospheric concentration, incoming solar radiation, meridional overturning circulation and albedo, and the consequent variations in the numerous energetic feedback mechanisms that condition the climate state. In this chapter we present a simple idealized box model to analyse the effect that changes in these processes have on the heat content in the atmosphere and upper ocean during the last 450 kyr.

Chapter 2: A 3D view of the Brazil-Malvinas Confluence

In this chapter we present a description of the BMC as deduced from the hydrographic dataset gathered during the TIC-MOC cruise and compare this description with both the mean climatological situation and numerical model data. This includes the description of the thermohaline

and chemical characteristics along a perimeter enclosing the entire BMC as well as in several sections across and along the BMC front. Besides, we analyse the water exchange between the platforms and deep waters during the first three months of 2015, as well as the relationship between surface ageostrophic velocity and the presence of brackish waters.

Chapter 3: Inverse modelling the Brazil-Malvinas Confluence region

In this chapter we assess the circulation pattern of the BMC using hydrographic and satellite data. To this end, we determine the baroclinic and barotropic water mass transports using box-inverse models at two different spatial scales: frontal area and confluence region. The frontal area focuses on the flow at the frontal system itself while the confluence region is used to identify the impinging BC and MC, as well as the MRC and BCO. In addition, we identify the most important water mass modifications in the region.

Chapter 4: Temperature spatio-temporal correlation scales in the Brazil-Malvinas Confluence from high-resolution in-situ and remote sensing data

The BMC is a highly variable region, with numerous mesoscale structures and intense thermohaline modifications occurring within a few hours and kilometres. In this chapter we characterize the temporal and spatial, both horizontal and vertical, high-frequency autocorrelation function and correlation scales of the temperature field. To this end, high-resolution SST images are combined with novel near-synoptic high-resolution hydrographic data gathered during the RETRO-BMC cruise.

Chapter 5: Mixing in the Brazil-Malvinas Confluence

The Argentine basin is of special relevance in the AMOC, as it holds intense water mass transformations, exchange of properties between subtropical and subantarctic waters and contributes to the ventilation of the subtropical gyre through the northward transport of Subantarctic Mode Water and Antarctic Intermediate Water. Based on in-situ microstructure data and climatological data, we explore how the mean potential temperature-salinity relationship is established in the Argentine basin and investigate what is the contribution of eddy-induced overturning across the Subtropical Front. In particular, we focus on the relative role of both dianeutral stirring via small-scale turbulence and is isoneutral stirring induced by mesoscale eddies.

Part II ‖ Datasets

Dataset on the TIC-MOC cruise onboard R/V Hespérides, March 2015, Brazil-Malvinas Confluence

Orúe-Echevarría, D., Pelegrí, J. L., Alonso-González, I. J., Benítez-Barrios, V. M., De La Fuente, P., Emelianov, M., Gasser, M., Herrero, C., Isern-Fontanet, J., Peña-Izquierdo, J., Ramírez-Garrido, S., Rosell-Fieschi, M., Salvador, J., Saraceno, M., Valla, D., and Vidal, M.

Data in Brief (2019), 22, 185-194.

Abstract

This oceanographic dataset was gathered during the TIC-MOC cruise, which was designed to characterize the dynamics of the Brazil-Malvinas Confluence. The cruise was carried on board the R/V Hespérides, with departure from Ushuaia and arrival to Salvador de Bahía. A total of 66 conductivity-temperature-depth (CTD) stations were completed between 8 and 22 March 2015, offshore from the continental platform and within 45^{o}S-35^{o}S and 61^{o}W-50^{o}W. At each station, water samples were collected, which were used to calibrate the CTD salinity-oxygen sensors and to determine inorganic nutrient concentrations, and the horizontal current was measured. Along its track, the vessel recorded surface temperature and salinity, as well as the horizontal flow down to about 700 m. Lastly, eight position-transmitting drifters were launched and two profiling floats were deployed and later recovered.

Data

This dataset presents the different measurements collected during an oceanographic cruise, with a careful description of the experimental design, instrument types, field methodology, data processing and sensor calibration. All data files are available at Mendeley Data (see the readme.txt file at https://data.mendeley.com/datasets/hk8t43z3t3/2 for a description of the actual contents of each data file).

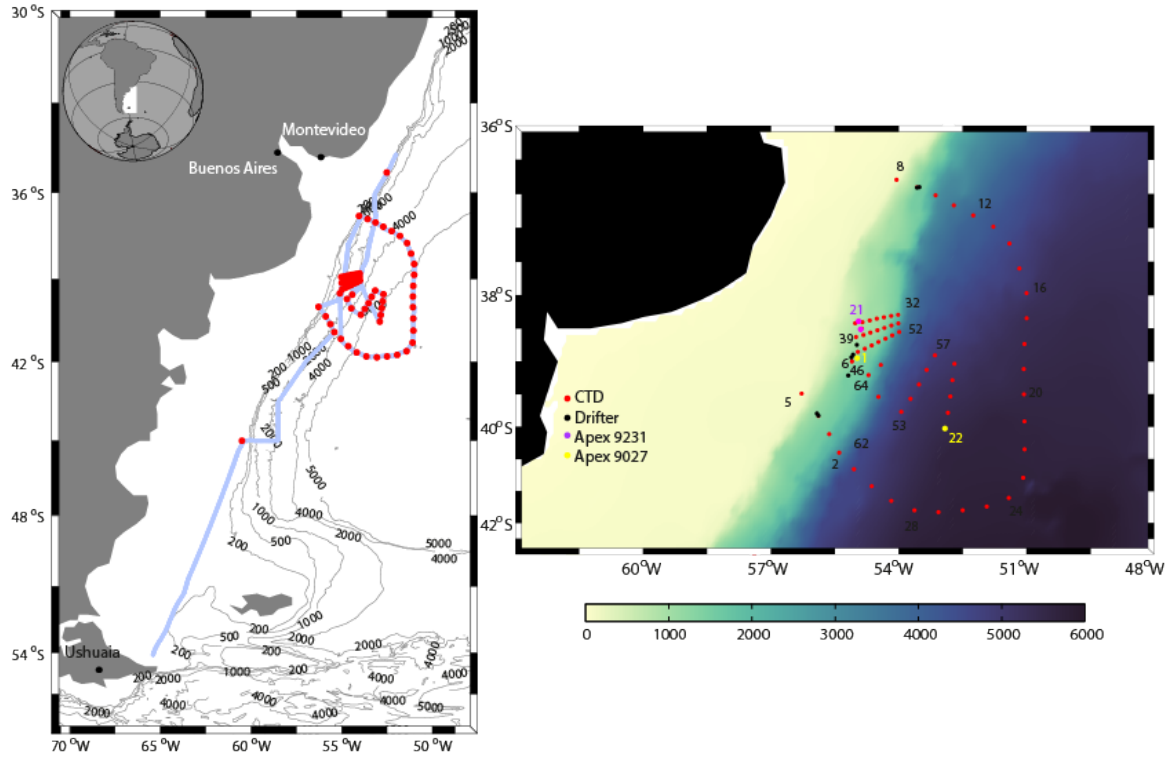

Fig. 7: (Left) Vessel track during the TIC-MOC cruise (blue line) and location of the CTD stations (red dots). Black lines represent the 200, 500, 1000, 2000, 4000 and 5000 m isobaths. (Right) Map showing the location of all CTD stations (red dots), the position where the drifters were deployed (black dots), and the release and recovery locations for Apex profilers 9231 (magenta points) and 9027 (yellow points), on top the bathymetry (smoothed GEBCO 2008; color-coded in meters).

One type of data corresponds to the hydrographic stations [Fig. 7], a total of 66 stations including conductivity-temperature-depth (CTD) data, inorganic nutrient concentrations and water velocity obtained with a lowered acoustic Doppler current profiler (LADCP). In addition, it comprises flow velocity recorded along the ship track (with a vessel-mounted ADCP, VADCP) and near-surface temperature and salinity (with a thermosalinograph). The dataset also includes 42 vertical profiles completed by two profiling floats, holding salinity, conductivity and pressure sensors (one of them having additional oxygen and fluorescence sensors) and the trajectories of eight near-surface drifters.

Experimental design, materials and methods

The TIC-MOC (Tipping Corners in the Meridional Overturning Circulation) cruise was carried onboard the R/V Hespérides (Spain), with departure from Ushuaia (Argentina) on 5 March 2015 and arrival to Salvador de Bahía (Brazil) on 30 March 2015 [Fig. 7]. The study area was offshore from the continental platform, within 45°S-35°S and 61°W-50°W. Of the 66 completed hydrographic stations, 14 reached down to the seafloor, 24 stations down to 2000 m and 28 stations down to 400-500 m.

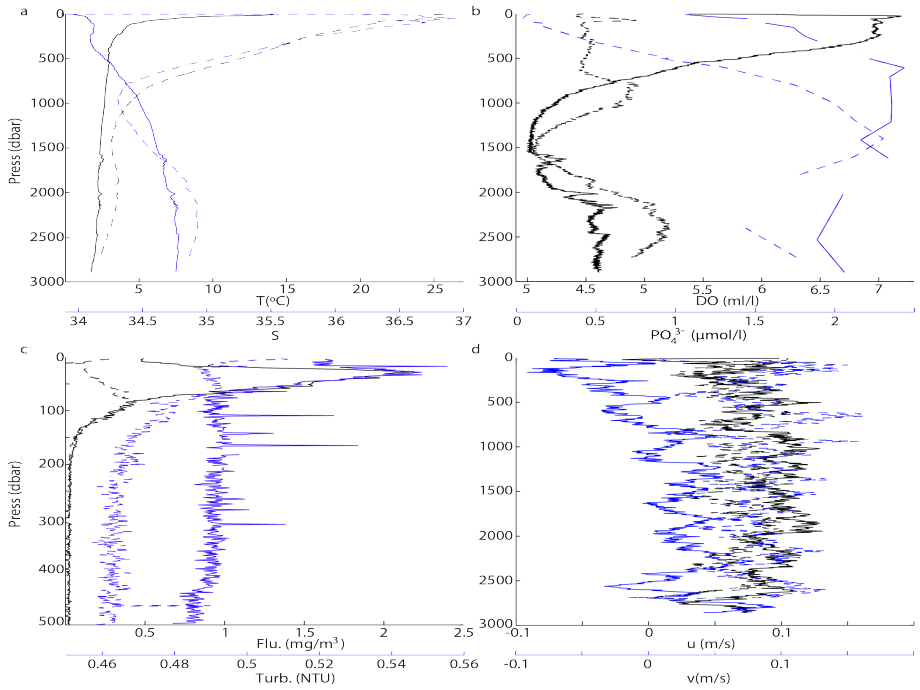

Fig. 8: Vertical profiles for stations 2 (continuous line) and 10 (dotted line), respectively characterizing the subantarctic and subtropical waters, of (a) potential temperature (T in °C) and salinity (S), (b) dissolved oxygen concentration (DO in ml l^{-1}) and phosphate concentration (PO_4^{-3} in μmol l^{-1}), (c) fluorescence (Flu in mg m^{-3}) and turbidity (Turb in NTU) and (d) zonal (u in m s^{-1}) and meridional (v in m s^{-1}) velocity components. The black and blue lines correspond to the black and blue axes, respectively.

CTD and thermosalinograph data

At each hydrographic station [Fig. 7], CTD data were obtained with a SeaBird 911 Plus multiparametric probe with redundant temperature and conductivity sensors and a SBE-43 dissolved oxygen sensor, Wetlabs AFL-NTU-RTD fluorescence and turbidity sensors and Biospherical QSP-2300 PAR (Photosynthetically Active Radiation) sensor. The CTD data were vertically averaged at 1 dbar pressure intervals after processing. The probe was mounted on a 12-l 24-Niskin-bottles rosette and water samples were collected at standard depths in all stations, which were later used for several biogeochemical analyses (only inorganic nutrients are presented in this study).

For each hydrographic station there are two sorts of files with CTD data: (1) the variables gathered in a near-continuous mode during the entire cast, with about three samplings per second, which are presented as 1-dbar averaged values, with separate files for the descending and ascending portions of the cast (hereafter CTD cast) [Fig. 8]; (2) the variables gathered at the depth where the Niskin bottle was closed during the rosette ascension (hereafter bottle data).

A SBE 21 SeaCAT thermosalinograph recorded temperature and salinity data in a continuous mode (one value every five seconds) from the vessel's underway system, approximately located at a depth of 5 m [Fig. 9]. These data include the vessel's position, obtained through two differential global positioning systems.

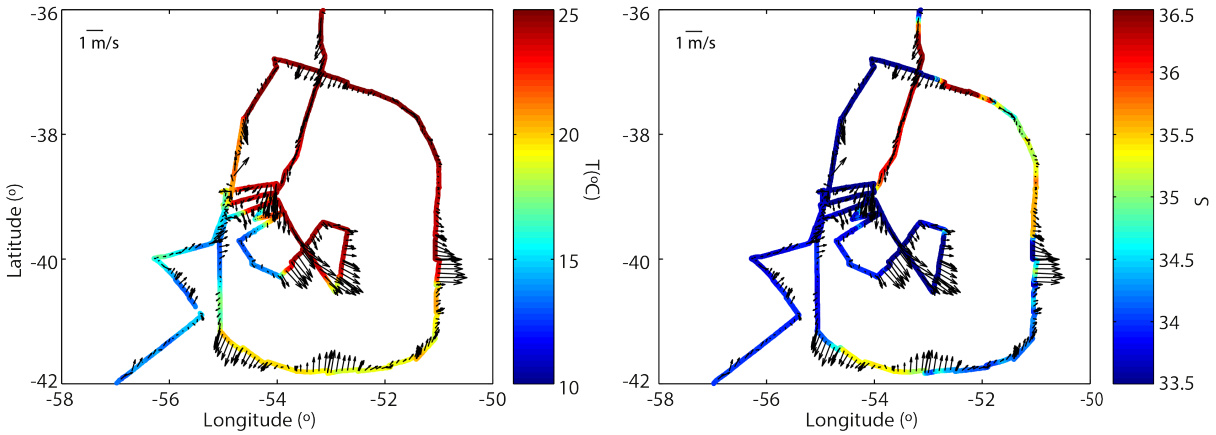

Fig. 9: (a) Temperature (in ºC) and (b) salinity as measured by the thermosalinograph (color-coded) along the ship's trajectory; the plot includes (a) the mean velocity in the top 700 m and (b) and the velocity at 20 m as obtained with the VADCP (vectors).

LADCP and VADCP data analysis

Velocity data was recorded on each cast with the LADCP fixed to the rosette. It consisted of a dual-head setup (down-looking master, up-looking slave) four-beam RDI Workhorse Monitor with a working frequency of 300 kHz, set to obtain velocities in 4-m bins. Two configurations were initially prepared: one for casts reaching the sea bottom, which used staggered pings in order to avoid previous-ping interference, and another for profiles not reaching the sea bottom. During CTD profile 9 a major malfunction occurred, which caused that only the down-looking four-beam head worked properly on the next casts. A careful processing and data quality control confirmed that velocity profiles posterior to the instrument malfunction suffered no significant increase in observed error. LADCP data were processed with the Matlab LDEO IX toolbox (Visbeck et al., 2002), which uses CTD, vessel's navigation and bottom-tracking data.

The VADCP consists of an Ocean Surveyor Broadband/Narrowband 75 kHz Teledyne RDI equipment. The instrument was set to provide one velocity profile or ensemble every 5 min,

between about 24 m and 800 m at 8-m bins. Raw data were quality controlled, corrected and edited with the Common Oceanographic Data Access System (CODAS) (Firing, 1995). The Single-Ping processing scenario proposed by the CODAS software was used to process the VADCP data acquired with the RDI velocity processing software (VMDAS). The calibration of the instrument was checked and heading-corrected according to the bottom-tracking and water-tracking results.

Salinity

The CTD was equipped with duplicate conductivity sensors in order to detect any possible drift. In addition, a total of 65 water samples collected from the Niskin bottles were analysed onboard using a Guildine Autosal 8400B salinometer (installed in a constant temperature room) with the objective of calibrating the CTD conductivity sensors. These water samples were gathered at stations scattered throughout the entire cruise, typically at depths where the vertical property gradients were low. Water samples were analysed by lots, about 24 h after collection, after having equilibrated to laboratory temperature. Previous to each batch of samples, the instrument was calibrated using a standard seawater sample (SSS) from the International Association for the Physical Sciences of the Oceans. At the end of each batch, again a SSS was analysed to verify the instrument's stability.

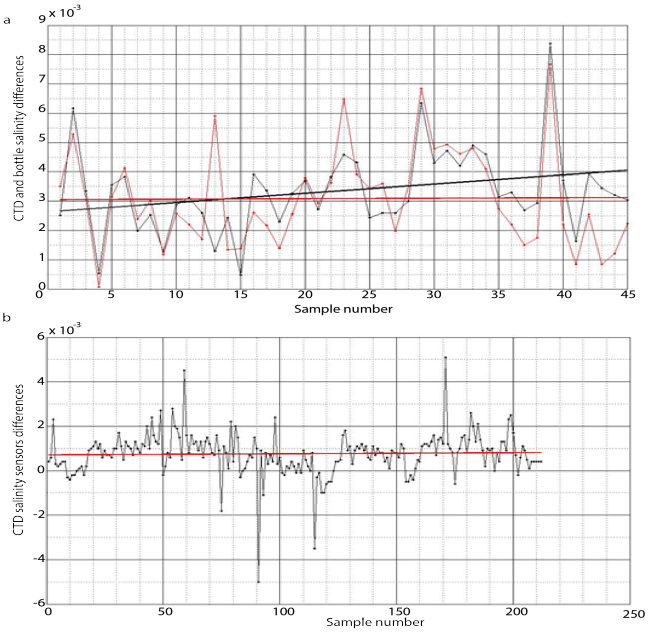

Fig. 10: (a) Differences between the CTD salinity data (thin lines) and the salinometer measurements, and linear adjustments for these differences after discarding outliers (thick lines). The black and red lines correspond to the primary and secondary sensors, respectively. (b) Difference between the CTD primary and secondary salinity sensors in bottles closed deeper than 1000 m. The red line shows the linear adjustment.

The comparison between the salinity measured with the salinometer and the salinity derived from the CTD shows a mean offset of 0.003 and a shift of 0.0014 for the primary CTD conductivity sensor and a mean offset of 0.003 and a variation of 7×10^{-5} for the secondary sensor, with the shift corresponding to the 15-day entire cruise period [Fig. 10a]. Further, a comparison of

the primary and secondary CTD conductivity sensors for all bottles closing at depths higher than 1000 m shows an offset of 7.1 x 10^{-4} which is less than the differences with the salinometer [Fig. 10b]. Therefore, we may conclude that the measurements from both CTD conductivity sensors were stable throughout the cruise, with no significant offsets. Since the secondary sensor shows slightly more stable measurements, with an offset close to the salinometer detection limit, we recommend using the data provided by this sensor.

Oxygen sensor calibration

In order to calibrate the CTD oxygen sensor (Sea-Bird, 2012), 183 water samples from the Niskin bottles were used to determine the dissolved oxygen concentration via the Winkler-titration method (Winkler, 1888). The comparison shows good agreement between the CTD and Winkler method oxygen measurements [Fig. 11]. The correction factor for the CTD oxygen is 1.0746, with no specific temporal or spatial significant dependences. After using the correction factor, the difference between CTD and Winkler oxygen concentrations is 0.002 $\pm$ 0.051 ml l^{-1} This factor has been applied to the enclosed datasets.

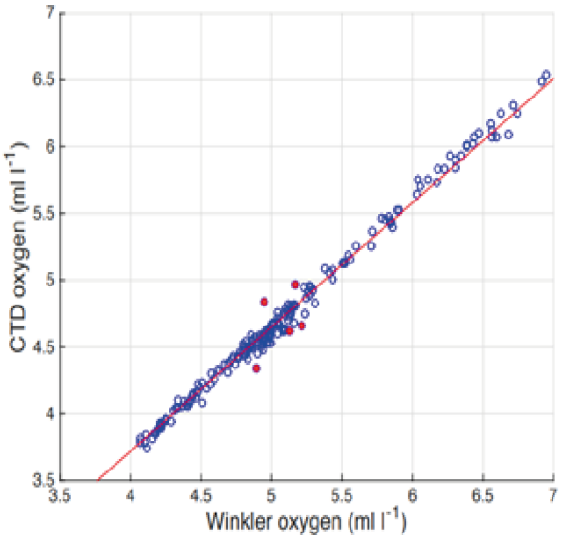

Fig. 11: Linear regression between the Winkler and CTD oxygen concentrations for the samples used to compute the correction factor. The red dots indicate outliers eliminated for the calibration.

Drifters

Eight subsurface drifting buoys (drifters) were launched during the cruise [Figs. 7 and 12, Tab. 2]. These drifters have a spherical surface buoy, containing the batteries and the electronics of the system, and a 15-m holey sock dragged at 100-200 m depth (García-Ladona et al., 2016). The electronics consists of a global positioning system and a satellite data transmitter (Global Star in four buoys and Iridium in the other four); positions were acquired every 30 min in all drifters. The data presented corresponds to the period between the launching and the 26 March 2015.

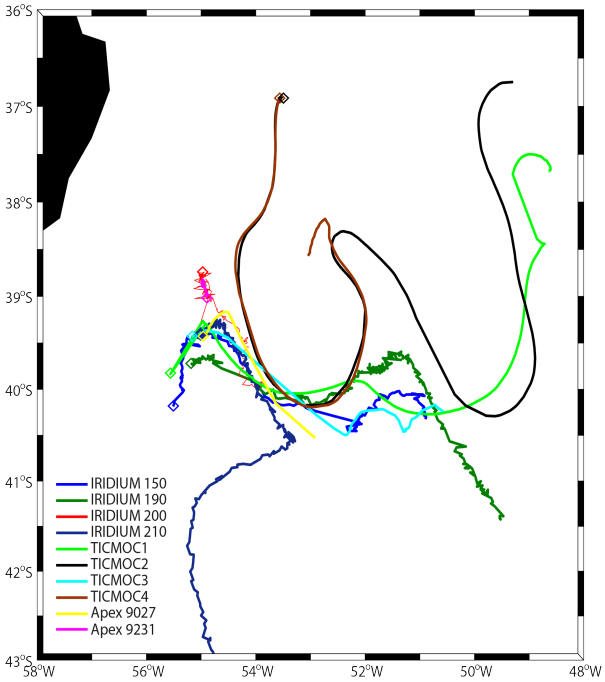

Fig. 12: Trajectories of the surface drifters and profiling floats between their launching and 26 March 2015, with the deployment point indicated by a diamond.

Table 2: Deployment times and positions for the near-surface drifters

Name	Date (yyyy/mm/dd)	Time (GMT)	Latitude S	Longitude W	Transmitter	Drogue (m)
TICMOC 1	2015/03/11	08:20:00	39°14.85′	54°58.90′	Global Star	100
TICMOC 2	2015/03/12	08:24:00	36°53.93′	53°31.11′	Global Star	100
TICMOC 3	2015/03/10	16:50:00	40°19.80′	55°52.80′	Global Star	200
TICMOC 4	2015/03/12	08:08:00	36°54.39′	53°34.23′	Global Star	200
IRIDIUM150	2015/03/10	17:31:00	40°18.45′	55°53.18′	IRIDIUM	100
IRIDIUM190	2015/03/11	03:50:00	39°44.75′	55°12.35′	IRIDIUM	100
IRIDIUM200	2015/03/11	06:34:00	39°29.50′	55°05.50′	IRIDIUM	100
IRIDIUM210	2015/03/11	11:21:00	39°00.29′	54°52.25′	IRIDIUM	100

Vertical profiling floats

Two Argo-type Apex profilers (Teledyne Webb Research) were deployed and recovered during the cruise [Fig. 7 and 12, Tab. 3]. Both floats were equipped with SBE41CP CTD sensors (float 9027 also had fluorescence and oxygen sensors) and Iridium transmitters with bidirectional communication. These transmitters allowed modifying the programmed cycle while the drifter was in the water, changing the profiling and parking depths and the time the float remained at the parking depth and at the sea surface. In all cases (except for float 9027 between profiles 20 and 21) we asked the profiles to not remain at the parking depth and to stay at the sea-surface only until it successfully connected with the satellite.

Float 9027 was deployed on 11 March and recovered on 19 March, completing a total of 22 profiles. The maximum pressure was about 500 dbar for the first 12 profiles and around 750

dbar for the remaining 10 profiles. The first 13 profiles sampled in continuous mode (one measurement approximately every 2 dbar) and since profile 14 the vertical resolution was set to 10 dbar. After profile 17, the communication with the float was lost, emerging two days later after having performed three profiles, two of them (18 and 19) not positioned. This was caused by the presence of significantly fresh Rio de la Plata waters in the uppermost 10-20 m of the water column (e.g. at 04:04:56 UTM on 16 March, with the buoyancy bladder fully extended, drifter 9027 was at 11.5 dbar; having no capacity to gain further buoyancy, it descended again to the parking depth). Between profiles 20 and 21 the float remained at the sea surface while providing 33 surface positions.

Table 3: Deployment and recovery times and positions for the profiling floats

	Start			End		
Float	Date (yyyy/mm/dd)	Latitude S	Longitude W	Date (yyyy/mm/dd)	Latitude S	Longitude W
9027	2015/03/11	39º30.01′	55º06.00′	2015/03/19	40º31.50′	52º57.78′
9231	2015/03/11	39º00.29′	54º52.25′	2015/03/17	38º53.52′	54º56.52′

Float 9231 was deployed on 11 March and recovered on 17 March after doing 20 profiles. The first 9 profiles reached down until around 300 dbar and from profile 10 to 20 the maximum pressure was about 800 dbar. During the first 14 casts, continuous-mode sampling was set for the upper 200 dbar and 10-dbar sampling further deep; for the last 6 profiles continuous-mode sampling was set for the entire profile.

Inorganic nutrients

At each station, 50-ml water samples were obtained from the Niskin bottles and later used to determine inorganic nutrient concentrations (nitrate, nitrite, silicate and phosphate). These water samples correspond to the standard water depths plus a selected number of depths, which changed depending on the maximum sampling depth and the observation of particular features during the descending CTD cast. Samples were immediately frozen at -20^{o}C and analysed within three months at the Institute of Marine Sciences in Barcelona using an AA3 HR Seal Analytical instrument. The nutrients analyses allowed determining the concentrations of nitrate, nitrite, phosphate and silicate (Grasshoff, 1983). Data detection limits and accuracies are included in Table 4 (EPA, 2003).

Table 4: Lowest range (μM), coefficient of variation and detection limit (μM) in the lowest range of the inorganic nutrient analysis method

	Lowest range	Coefficient of variation (10 replicates at 50 %)	Detection limit in lowest range (MDL)
Nitrate + Nitrite	0 to 2.9	0.21 %	0.0100
Nitrite	0 to 0.3	0.20 %	0.0015
Silicate	0 to 8.0	0.50 %	0.0160
Phosphate	0 to 6.5	0.20 %	0.0200

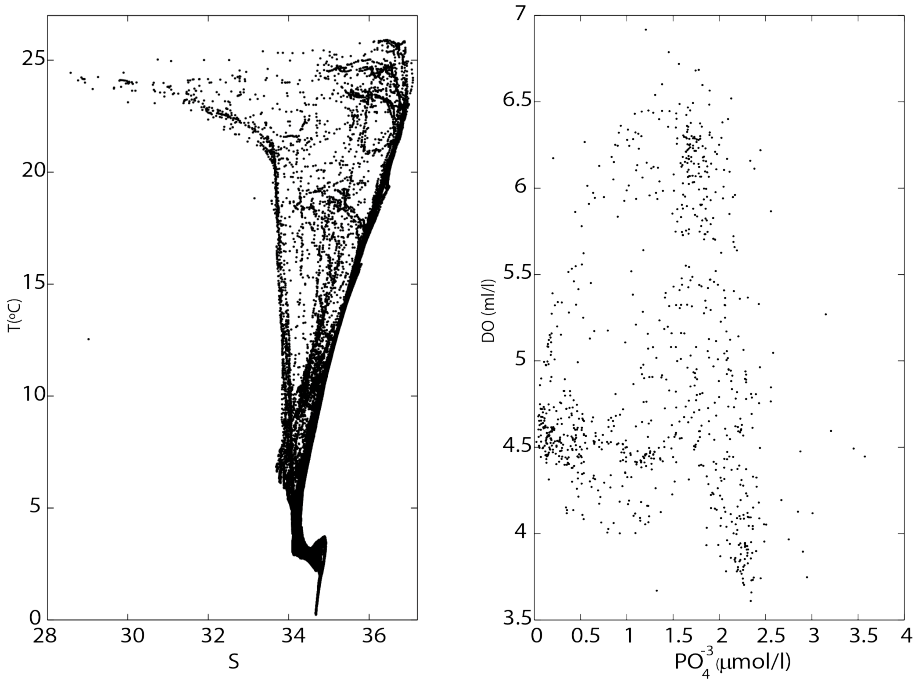

Fig. 13: (Left) Potential temperature - salinity (T-S) and (right) dissolved oxygen - phosphate concentration (DO-PO_4^{-3}) diagrams.

Acknowledgments

We are very grateful to the crew, technicians and scientists in the R/V Hespérides for their work during the TIC-MOC cruise. We thank Maravillas Abad for the nutrient analysis. This research has been supported by the Spanish Government, through projects TIC-MOC (CTM2011-28867) and VA-DE-RETRO (CTM2014-56987-P) and through the funding of PhD scholarships for D.O.E. (FPU2013-02884), S.R.G. (BES-2012-055970) and C.H. (CSIC JAE-Predoc program).

Dataset on the RETRO-BMC cruise onboard R/V Hespérides, April 2017, Brazil-Malvinas Confluence

Orúe-Echevarría, D., Pelegrí, J.L., Castellanos, P., Guallar, C., Marotta, H., Marrasé, C., Martín, J., Masdeu, M.,Paniagua, G.F., Peña-Izquierdo, J., Puigdefábregas, J., Rodríguez-Fonseca, B., Roget, E., Rosell-Fieschi, M., Salat, J., Salvador, J., Vallès-Casanova, I., Vidal, M., and Viúdez, A.

[In preparation]

Abstract

This dataset, gathered during the RETRO-BMC cruise, reports multiple-scale measurements at the Confluence of the Brazil and Malvinas Currents. The cruise was carried out between 8 and 28 April 2017 onboard R/V Hespérides, departing from Ushuaia and arriving to Santos. Along its track, the vessel recorded near-surface temperature and salinity, as well as the horizontal flow from 20 m down to about 800 m. A total of 33 hydrographic stations were completed in a region between 41.5^{o}S-35.9^{o}S and 58^{o}W-52^{o}W. At each station, a multiparametric probe and velocity sensors were deployed inside the frame of a rosette used to collect water samples at selected depths; these samples were later used for several water analyses, including inorganic nutrient concentrations. Microstructure measurements were carried out in 11 of these hydrographic stations. In addition, two high-resolution three-dimensional surveys were conducted with an instrumented undulating vehicle between 40.6^{o}S-39.0^{o}S and 55.6^{o}W-53.8^{o}W. Lastly, eight high-frequency vertical profilers were deployed in the region and five position-transmitting drifters (dragged at a nominal depth of 100 m) were launched.

Data

This dataset describes the observations gathered during an oceanographic cruise (RETRO-BMC) in an intense frontal region, the Confluence of the Brazil and Malvinas Currents, which is characterized by the coexistence of substantial variability at many different temporal and spatial scales. The instruments configuration and deployment and the cruise planning were done such as to allow an unprecedented multi-scale analysis of this frontal system: from regional and mesoscale, assessed through continuous along-track sampling and hydrographic stations, to horizontal submesoscale and vertical fine-structure, evaluated with the help of an undulating vehicle, to the microscale structures, studied with a free-falling microstructure profiler.

The continuous along-track measurements include near-surface salinity and temperature, as well as the velocity fields at depths from 20 to 800 m. There were a total of 33 hydrographic stations, each consisting of a vertical profile with a multi-parametric probe, a velocity sensor, and a 24-bottle carrousel to collect water samples at discrete vertical positions. In 11 of these stations, microstructure measurements were also carried out. In addition, the dataset includes two high-resolution surveys, through a towed instrumented undulating vehicle (SeaSoar), between about 5 and 360 m depth. Further, it comprises data from eight high-frequency vertically-profiling instruments, six of them released as part of the international Argo program (http://www.argo.net) and reaching down to 2000 m and the other two sampling at an even higher frequency and reaching down to typically 500 m. Finally, it contains positioning data from five near-surface drifting buoys (dragged at a nominal depth of 100 m) for the time of the cruise. Data files are available at https://digital.csic.es/handle/10261/188363.

Experimental design, materials and methods

The RETRO-BMC survey observations were collected onboard R/V Hespérides in April 2017, departing from Ushuaia (Argentina) on 8 April and ending in Santos (Brazil) on 28 April, on the framework of the VA-DE-RETRO project. The study area was the Brazil-Malvinas Confluence (BMC), at the time of the cruise comprising the region offshore the South American continental platform within 41.5^{o}S-35.9^{o}S and 58^{o}W-52^{o}W [Fig. 14].

Prior to the cruise, the frontal system was positioned thanks to daily sea surface temperature (SST) and sea surface height (SSH) images together with one-week forecasts of temperature, salinity and horizontal velocity down to 1000 m, as provided by the MERCATOR Ocean PSY4V3R1 operational model (1/12^{o} resolution) (http://marine.copernicus.eu). The BMC region was sampled between 13 and 24 April 2017.

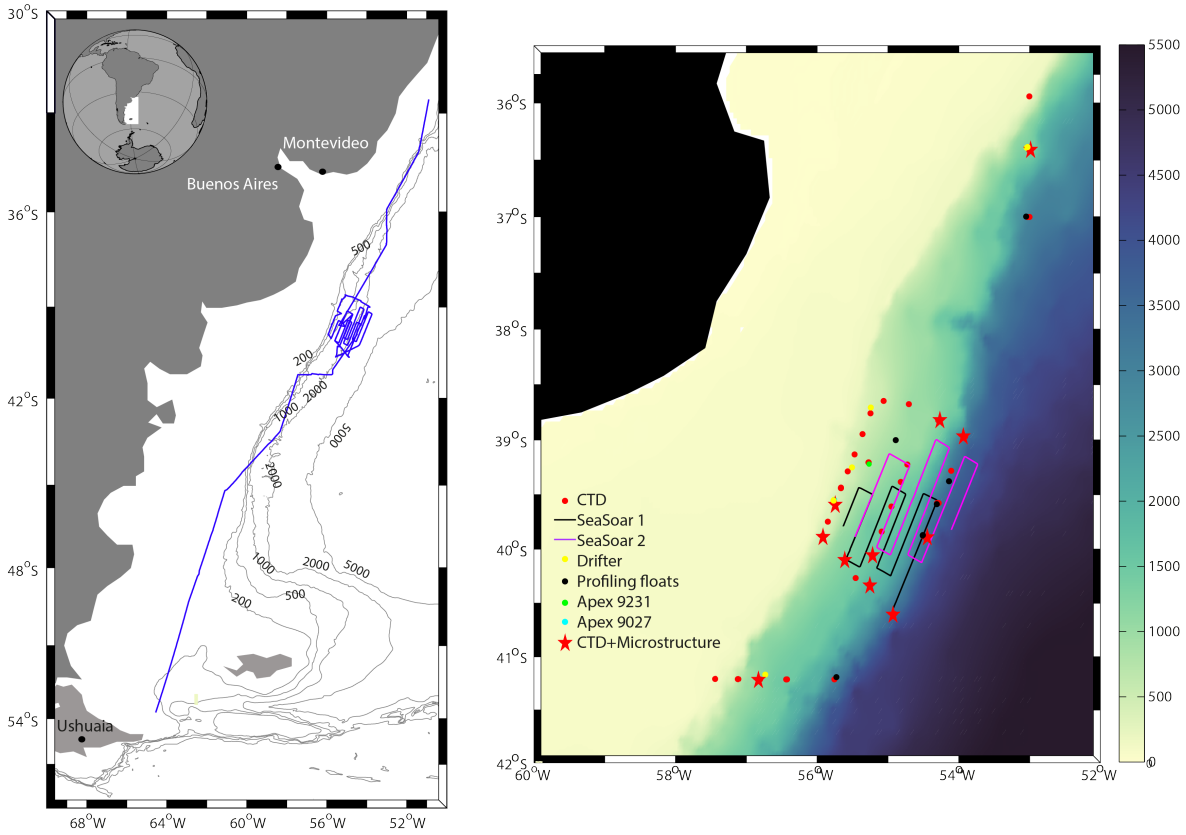

Fig. 14: (Left) Track of the vessel during RETRO-BMC (blue line) with the 200, 500, 1000, 2000 and 5000 m isobaths (grey contours). (Right) Position of the CTD stations (red dots), SeaSoar1 and SeaSoar2 transects (black and magenta respectively) and the launching position of the high-frequency profiling floats (black dots), profiles of Apex 9231 (green dots) and Apex 9027 (cyan dots) profilers and sub-surface drifters (yellow dots) on top the bathymetry (smoothed GEBCO, 2008, color coded in meters).

CTD and continuous measurements

A total of 33 hydrographic stations were done. In 26 out of the 33 hydrographic stations, the water depths were less than 2000 m and the CTD cast reached down to the seafloor. In the other 7 stations the sampling reached down to 2000-3500 m.

One core instrument in the hydrographic stations was a SeaBird 911 Plus multi-parametric probe with a pressure gauge and redundant temperature and conductivity sensors. The probe had attached dissolved oxygen (SBE-43), fluorescence and turbidity sensors (Wetlabs AFL-NTU-RTD). The vertical profile obtained with this probe is commonly known as a CTD cast, standing for the conductivity-temperature-depth measurements.

The probe was mounted on the lower portion of a 12-liters 24-Niskin-bottles rosette, which descended and ascended at typical speeds of about 1 m s^{-1}. The probe sampled at a rate of 24 measures per second, which was vertically averaged at 1 dbar pressure intervals using the Sea-Bird Electronics Data Processing software. There are both downcast and upcast profiles but, as is standard for CTD casts, we recommend using the downcast simply because of the

location of the sensors, which allows sampling the water column before the rosette generates any significant turbulence.

The rosette collected water samples in all stations. The water samples were taken during the upcast, at standard depths plus possibly several other levels of potential interest, identified during the downcast. The water samples were used for several biogeochemical analyses, including the determination of inorganic nutrient concentrations.

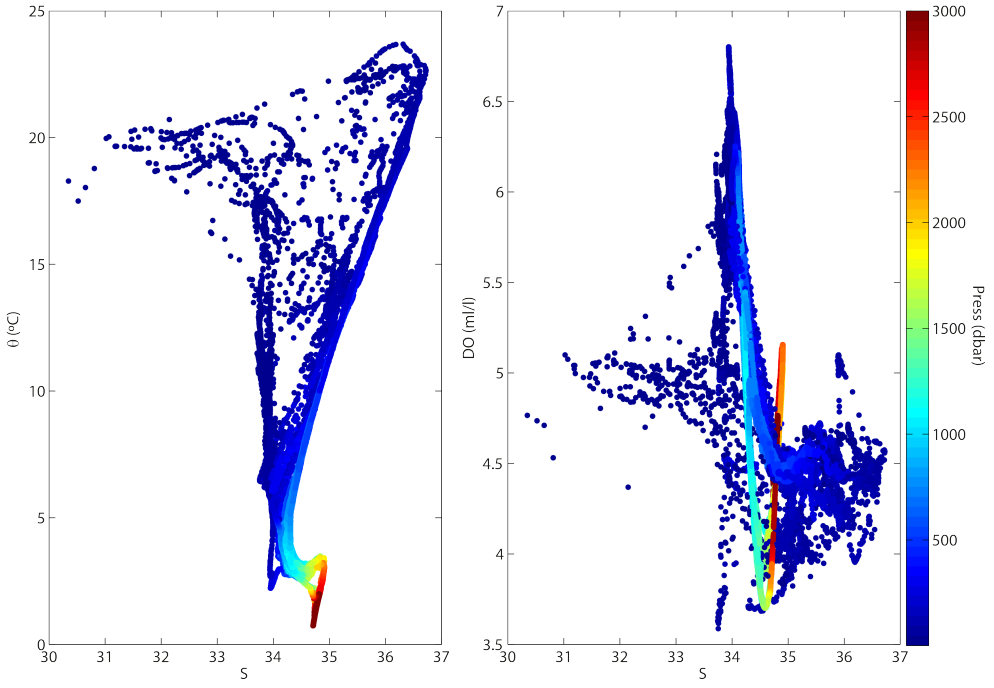

Fig. 15: (Left) θ-S and (right) DO-S diagrams, color-coded with pressure (dbar).

All property vertical profiles were first visually checked to detect possible instrument anomalies. During the first two stations there was a clear drift in the primary conductivity sensor (noticeable by comparing the two sensors as well as the downcast-upcast profiles). After the adjustment of the probe connector, the problem was solved in the successive stations. Anomalies were also checked through property-property diagrams, such as the standard potential temperature-salinity (θ-S) diagrams [Fig. 15]. In the θ-S diagrams the entire data set is clearly located in a domain that lies between the contrasting subtropical and subantarctic water types (Fig. 15, left). When using other properties, such as dissolved oxygen (DO), the separation between the two water masses may take very different forms (Fig. 15, right).

Additionally, during the entire track of the vessel in the BMC (1600 nm), a SBE 21 SeaCAT thermosalinograph recorded temperature and salinity data in a continuous mode (4 Hz). The vessel's underway system is approximately located at a depth of 5 m [Fig. 16]. The equipment was finally set to register 1 data every 6 seconds. The data was displayed visually and hel-

ped identify when the vessel was crossing the frontal system, characterized by temperature gradients as sharp as 0.2 ^{o}C km^{-1}.

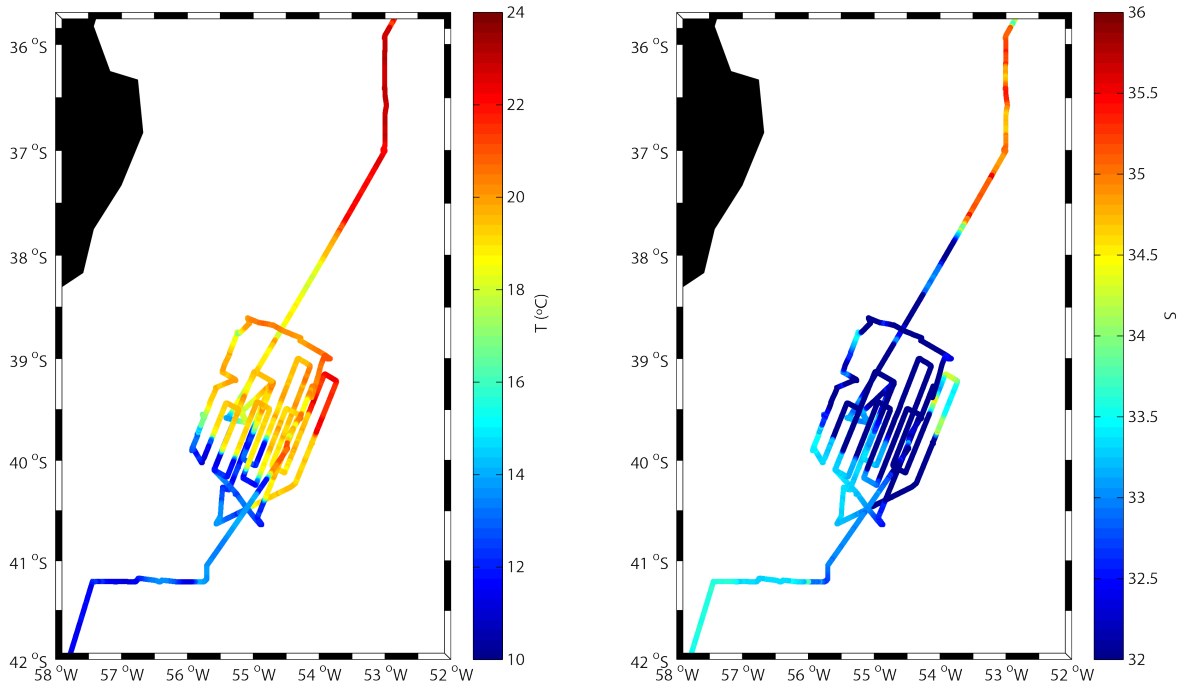

Fig. 16: (Left) Temperature (^{o}C) and (right) salinity along the cruise track as measured by the vessel's thermosalinograph.

LADCP and VADCP data analysis

The velocity fields were sampled with two different types of acoustic Doppler current profilers (ADCP). The first one was a lowered-ADCP (LADCP), mounted on the rosette frame, which allowed gathering profiles of horizontal velocity on each cast [Fig. 17]. It consisted of a dual-head set-up (down-looking master, up-looking slave) four-beam RDI Workhorse Monitor with a working frequency of 300 kHz, set to obtain velocities in 4-m bins. Two configurations were used: one for casts reaching the sea bottom, which used staggered pings in order to avoid previous-ping interference, and another for profiles not reaching the sea bottom. In those stations down to the seafloor, an altimeter on the lowered package allowed sampling until about 10 m above the sea bottom. The LADCP data were processed with the Matlab LDEO IX toolbox (Visbeck, 2002), which uses CTD, vessel's navigation and bottom-tracking data.

The second velocity sensor is the vessel-mounted ADCP (VADCP), which allowed gathering velocity data in a continuous mode along the vessel's track. It consists of an Ocean Surveyor Broadband/Narrowband 75 kHz Teledyne RD Instrument mounted on the hull of the vessel. The instrument was set to provide one velocity-profile ensemble every 5 min between about 24 m and 800 m at 8-m bins [Fig. 17]. Raw data were quality controlled, corrected and edited with

the Common Oceanographic Data Access System (CODAS) (Firing et al., 1995). The calibration of the instrument was checked and heading-corrected according to the bottom-tracking and water-tracking calibration results.

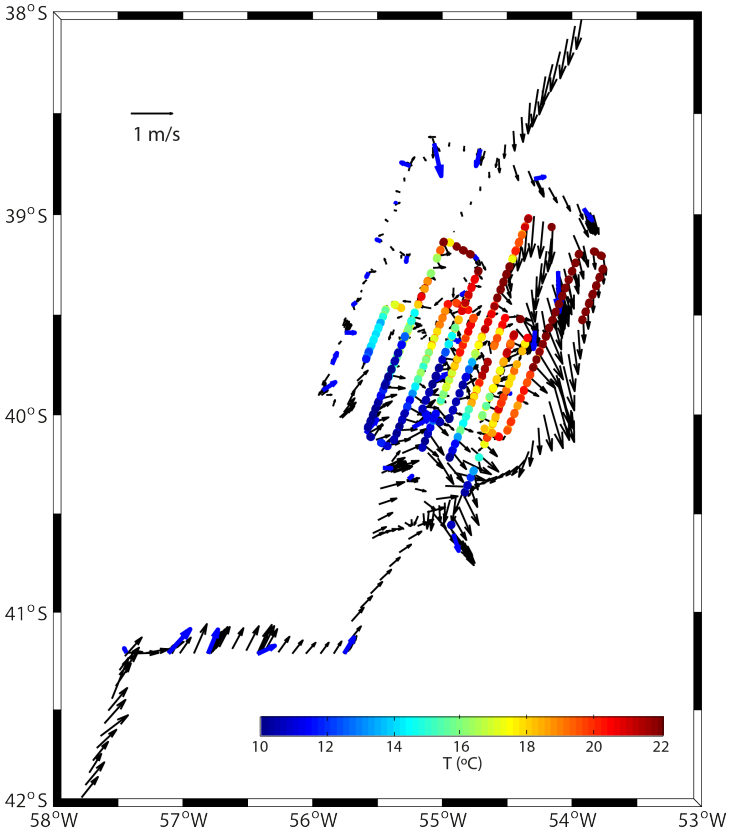

Fig. 17: Mean velocity in the upper 800 m of the water column, as obtained with the VADCP (black vectors), and velocity at 4 m at each hydrographic station, as obtained with the LADCP (blue vectors). The temperature at 22-28 m, as measured during the SeaSoar surveys, is also shown (color-coded).

SeaSoar data

Two high-resolution frontal surveys were completed on 17-19 and 19-21 April, respectively, with a Chelsea Group Technologies towed undulating vehicle (SeaSoar) [Figs. 14 and 17]. The objective of this repeated high-resolution sampling was to assess the spatial and temporal variability and thermohaline intrusions of the Brazil Malvinas Confluence front. With this goal, each survey was designed onboard, continuously changing the location and length of the meridional transects according to in-situ continuous measurements provided by the thermosalinograph, VADCP and the SeaSoar itself. Grossly, each survey consisted of six cross-frontal near-parallel transects, each about 100 km-long. The first survey (SeaSoar1) was completed within 46 h, covering 620 km, while the second one (SeaSoar2) started 40 h after and sampled 751 km during 52 h.

The SeaSoar was equipped with a Sea-Bird 9 Plus CTD, with pressure, redundant temperature and conductivity sensors, and additional fluorescence and dissolved oxygen sensors. This equipment recorded data, while pulled by the vessel at a sustained speed of 8.5 knots, optimally

undulating in a sawtooth pattern between 5 and 360 m depth, with a horizontal spacing between apogees of 4 km. This range was generally completed except when changing the vessel's heading, where the vertical span was reduced and the upper and lower meters were lost. The distance between cross-frontal tracks in each of the surveys is 10 nm, with both survey-tracks interlaced in such a way that the spacing between tracks was 5 nm.

High-frequency profiling floats

During the cruise, six NKE Instrumentation ARVOR-I profilers from the Euro-Argo program (https://www.euro-argo.eu/) were launched, all them with parking depth at 1000 m [Fig. 14 and 18b]. Two of them were set up following the Argo standards, i.e. completing a temperature and salinity profile between the surface and 2000 depth every 10 days. The other four, launched at the frontal system, had a high-frequency cycling, completing one profile per day for 20 days, thereafter recovering the standard configuration cycle. These are identified by the platform numbers 3901891 to 3901896 of the World Meteorological Organization.

Table 5: Deployment and recovery times and positions for the APEXi profiling floats

	Start			End		
Float	Time and day	Latitude S	Longitude W	Time and day	Latitude S	Longitude W
9027	2017/04/16 19:16:54	39º 33.60′	55º 44.70′	2017/04/23 12:34:11	39º 31.74′	52º 57.78′
9231	2017/04/16 11:12:19	39º 14.76′	55º 17.58′	2017/04/23 09:00:40	39º 31.08′	55º 11.46′

Moreover, two APEXi profilers (Teledyne Webb Research) were also deployed [Fig. 14 and 18b, Table 5]. Their configuration, that is cycle-time and parking depth, was controlled from the vessel in real time thanks to their Iridium transmitters with bidirectional communication. During the 8 days they remained in the water, these two profilers completed a total of 53 profiles, in most of them between approximately the surface and 500 m. Each of them was equipped with CTD SBE41CP sensors. Further, float 9027 had additional fluorescence and dissolved oxygen sensors.

Drifting buoys

Five subsurface drifting buoys were launched [Figs. 14 and 18a, Table 6]. These drifters consist of a spherical surface buoy, containing the batteries and the electronics of the system, and a 15-m long and 1-m diameter holey sock dragged at a nominal depth of 100 m (García-Ladona et al., 2016). Each buoy was equipped with a global positioning system and a receiver/transmitter from Global Star satellites. Positions were acquired every hour.

Table 6: Deployment times and positions for the near-surface drifters

Name	Day (yyyy/mm/dd)	Time (GMT)	Latitude S	Longitude W
Vaderetro1	2017/04/24	20:37:33	36°24.85′	53°00.38′
Vaderetro2	2017/04/16	12:30:01	39°17.14′	55°33.75′
Vaderetro3	2017/04/16	02:14:11	38°44.44′	55°14.58′
Vaderetro4	2075/04/13	20:17:06	41°10.06′	56°43.87′
Vaderetro5	2017/04/16	17:51:35	39°32.82′	55°45.68′

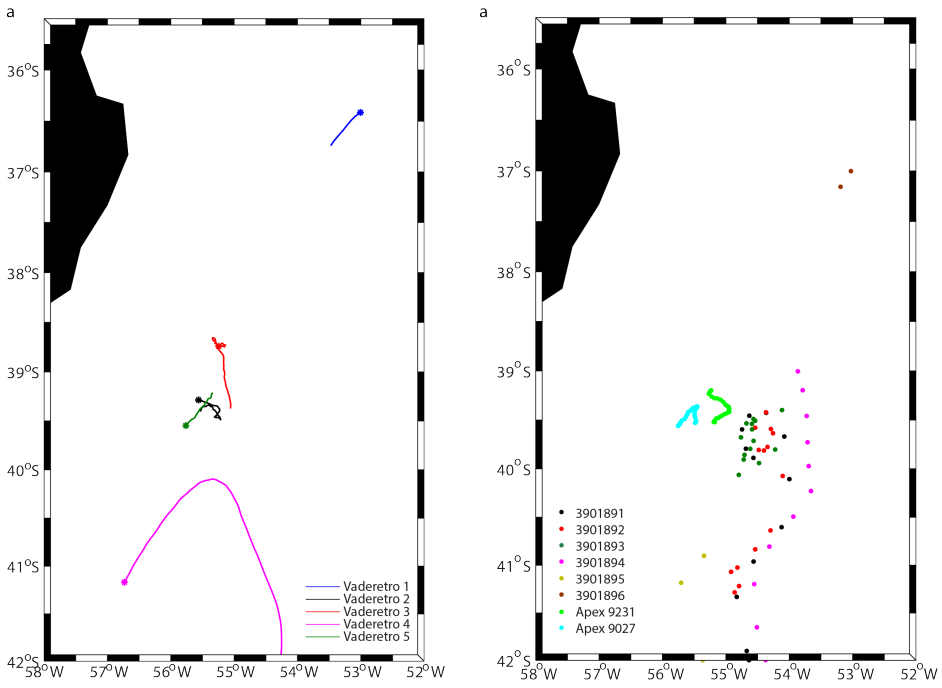

Fig. 18: (a) Trajectories of the surface drifters between their launching and 26 April 2017, with the deployment point indicated by a diamond. (b) Location of the profiles by the high-frequency ARVOR-I floats and the Apex 9231 and Apex 9027 floats.

Microstructure profiles

Microstructure profiles were gathered with a free-falling vertical microstructure profiler MSS90L (Sea Sun Technology) carrying two small scale shear probes and precision CTD sensors, all them calibrated by the manufacturing company before the cruise. A total of 41 profiles were collected in 11 CTD stations. A minimum of two (except in station CTD010 with only one because of an operational difficulty) and up to 7 microstructure profiles were collected at each single station, extending from the surface to between 160 m and 400 m (Fig.14, Table 7). The instrument provides in situ temperature (T), salinity (S) and kinetic dissipation rate (ϵ) as a function of pressure [Fig. 19].

Table 7: Microstructure profiles and maximum depth at each station

CTD station	Microstructure profiles	Maximum depth (m)
CTD003	MSS001-MSS007	300
CTD006	MSS008-MSS014	160
CTD009	MSS015-MSS018	280
CTD010	MSS019	195
CTD019	MSS020-MSS024	270
CTD021	MSS025-MSS027	300
CTD022	MSS028-MSS030	360
CTD023	MSS031-MSS032	320
CTD024	MSS033-MSS034	333
CTD026	MSS035-MSS039	400
CTD032	MSS040-MSS041	380

The data quality of the small-scale shear was tested by comparing their spectral representation (experimental spectra) with the theoretical Panchev-Kesich model (Greg, 1999). A best-fit ϵ was inferred by adjusting the Batchelor temperature spectra (maximum likelihood spectral method; Ruddick et al., 2000) to the 1D transversal Panchev-Kesich shear spectra (Roget et al., 2006; 2007) in the 6-20 cpm range. By comparing the ratio of the experimental spectra and the Panchev-Kesich theoretical spectra, we verified that the statistical variability of the fit follows a chi-squared distribution with 6 degrees of freedom, χ^2_6 , which was then used to obtain the likelihood function (Ruddick et al., 2000) (Fig. 7).

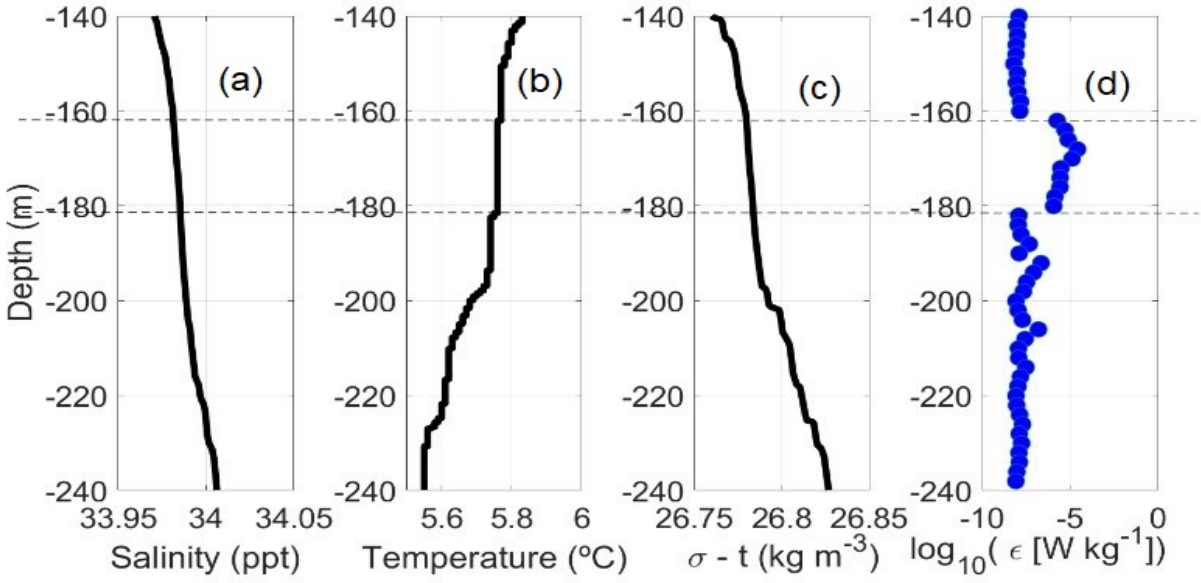

Fig. 19: (a-c) Example of the salinity, temperature and density profiles between 140 m and 240 m depth in a microstructure station and in panel (d) the corresponding profile of the dissipation rates obtained for segments of 2 m.

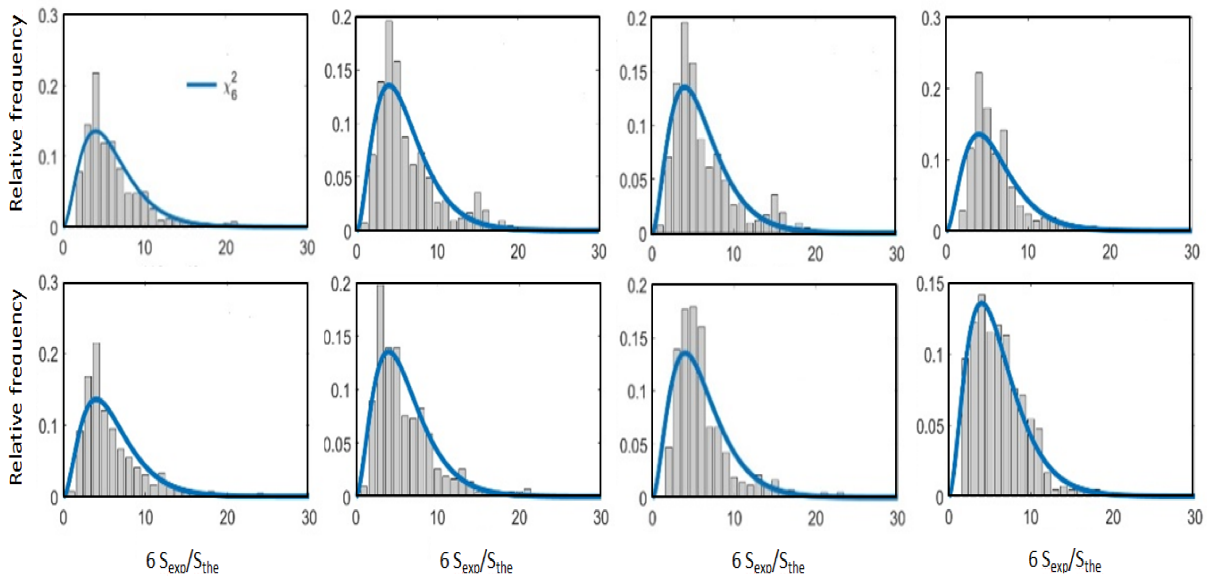

Fig. 20: Example of histograms of the ratio of the spectra derived from the recorded small-scale shear data (S_{exp}) and computed with the Panchev-Kesich model (S_{the}), and the theoretical χ^2_6 probability distribution functions (blue line), for the eight first 30-m segments in one single profile.

Inorganic nutrients

At each station, 50-ml water samples were obtained from the Niskin bottles. These water samples were obtained at the standard water depths plus a selected number of depths, which changed depending on the maximum sampling depth and the observation of particular features during the descending CTD cast; two replicate samples were obtained at each of these depths.

Samples were immediately frozen at -20^{o}C and analysed within three months at the Institute of Marine Sciences in Barcelona using an AA3 HR Seal Analytical instrument. These analyses included the determination of inorganic-nutrient, specifically the concentrations of nitrate, nitrite, phosphate and silicate (Grasshoff, 1983). Data detection limits and accuracies are included in Table 8 (EPA, 2003).

Table 8: Lowest range (μM), coefficient of variation and detection limit (μM) in the lowest range of the inorganic nutrient analysis method

	Lowest range	Coefficient of variation (10 replicates at 50 %)	Detection limit in lowest range (MDL)
Nitrate + Nitrite	0 to 2.9	0.21 %	0.0100
Nitrite	0 to 0.3	0.20 %	0.0015
Silicate	0 to 8.0	0.50 %	0.0160
Phosphate	0 to 6.5	0.20 %	0.0200

Acknowledgments

We are very grateful to the crew, technicians and scientists in the R/V Hespérides for their work during RETRO-BMC cruise. We thank Fernando García, Mariana Miracca and Rafael Santana for their support during the cruise and Maravillas Abad for the nutrient analysis. This research has been supported by the Spanish government (Ministerio de Economía and Competitividad through project VA-DE-RETRO, CTM2014-56987-P, and Ministerio de Ciencia, Innovación y Universidades through project SAGA, RTI2018-100844-BC33) and through the funding of PhD scholarships for D.O.E. (FPU2013-02884) and I.V.C. (BES- 2015-071314).

Part III ‖ Results

Chapter 1

Idealized box models as effective tools to understand the glacial-interglacial response of the ocean-atmosphere systems

Orúe-Echevarría, D., Pelegrí, J. L., and García-Olivares, A.
[In preparation]

Abstract

We have developed a simple time-dependent five-box box model that incorporates all the principal physical components of the Earth's climatic system. It has two active atmospheric and two active upper-ocean compartments and one passive deep-ocean compartment. The model allows simulating the time series of the temperature for all four active compartments as well as the heat fluxes between them. For the simulation, it requires the time series of solar radiation and the values of all intrinsic parameters that control the reflection and transmission of all heat fluxes. For this purpose, we set the greenhouse back-radiation as an empirical relation that depends on the time history of atmospheric carbon dioxide, and allow the surface albedo in the high-latitude compartments to depend on the upper-ocean temperature. We use the model to simulate the climate of the Earth during the last four glacial-interglacial cycles. The preliminary results are very encouraging, providing temperature time series that reproduce reasonably well the observed low- and high-latitude patterns, and that yield heat fluxes and patterns in fair agreement with proxies. Our results suggest that the major elements in the Earth's internal climatic system are the horizontal exchange between the adjacent atmospheric and oceanic low- and high-latitude regions, and the dependence of the high-latitude albedo on temperature. In particular, the introduction of the albedo feedback mechanism brings about the relevance of the 100 kyr band in the temperature energy spectra. This study, when completed, will provide a useful tool for governmental officers and climate scientists, which shall allow them to assess not only general trends but also to investigate specific features. One such feature, of particular interest for this thesis, is the heat transfer between the two adjacent ocean boxes, which parallels the contrasting subantarctic and subtropical regions on both sides of the Brazil-Malvinas Confluence.

1.1 Introduction

The climate on the Earth system is essentially the result of three elements: (1) the radiation coming from the Sun, (2) the circulation in the ocean and atmosphere, and (3) the radiative characteristics of the atmosphere and land-sea surface. Numerous processes and feedback mechanisms determine the role of these processes on the radiative budget of the Earth [Fig. 1.1] and therefore on its temperature. All starts with the amount of radiation arriving from the Sun and the way this is distributed in latitude through time. And continues with the way the energy surplus at low latitudes is transferred to high latitudes through winds and ocean currents. But equally important are the internal processes within the atmosphere, which determine how much of the Sun's radiation is reflected by the atmosphere and the land-sea surface and also how much of the Earth's radiation can effectively reach the outer space. It is the non-linear combination of these three factors that causes the thermodynamic variables to oscillate within a relatively narrow range of values, constituting what we know as climate.

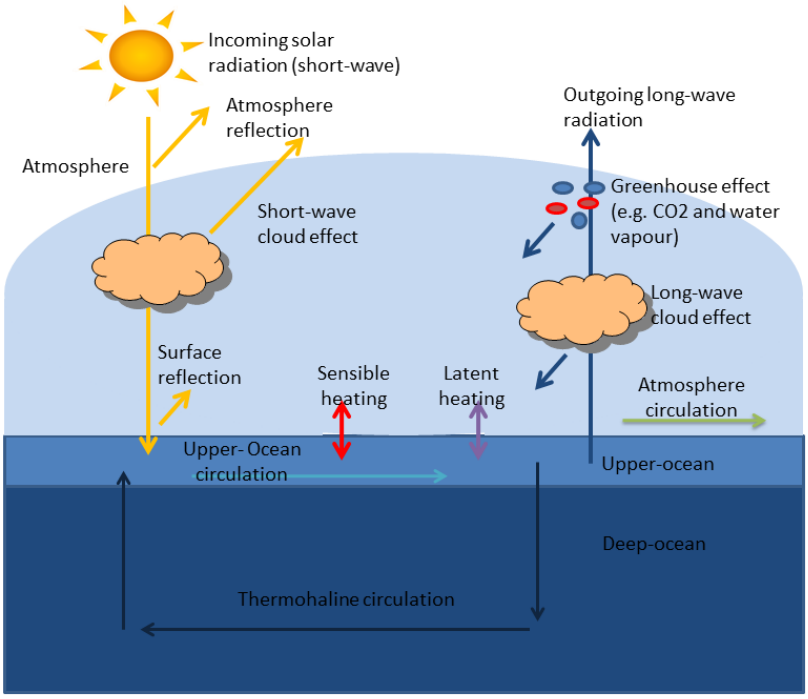

Fig. 1. 1: Schematics with the principal fluxes in the Earth's heat balance.

The Earth has alternated between glacial and interglacial states during the last 3 Myr (Imbrie et al. 1993; Paillard 2001). The temperature changes between the peak glacial and interglacial periods are considerable, nearly 7^{o}C between the last glacial maximum and the preindustrial period (Hansen et al., 2004). Different processes have been suggested as responsible for these climate transitions, being the most important: (1) the latitudinal distribution of the solar radia-

tion, (2) the reflection of this incoming radiation (planetary albedo), (3) the concentration of greenhouse gases (GHG), and (4) the intensity of the global overturning circulation (GOC).

The amount of energy arriving to the entire Earth over one full year has remained nearly unchanged during the last several mission years but its latitudinal distribution has substantially changed, majorly because of the Milankovitch cycles: eccentricity, obliquity and precession (e.g. Paillard, 2001). These differences in latitudinal distribution have brought about relatively large insolation changes at high latitudes, which may have been largely increased and have had planetary impacts because of different feedbacks.

One such feedback is the amount of ice at high latitudes: a cooling brings about an increase in ice coverage that in turn increases the albedo and leads to less radiation being absorbed by the system (e.g. Gildor and Tziperman 2003). Another feedback is the amount of GHGs, particularly CO_2, with low/high concentrations during glacial/interglacial periods (e.g. Petit et al. 1999; Siegenthaler et al. 2005). These CO_2 changes may be caused by variations in biological and chemical processes (biological and carbonate pumps) but also through fluctuations in the amount of CO_2-rich deep waters recirculating through the upper oceans, i.e. through the intensification or weakening of the GOC (the physical pump). Additionally, changes in the GOC would drive differences in the amount of heat transported to high latitudes (e.g. Kageyama et al. 2013); actually, different MOC equilibrium configurations have been related to different equilibrium states of the climate (Broecker et al. 1985; Manabe and Stouffer, 1988; Rahmstorf 2001).

Numerical modelling of the temperature distribution during glacial/interglacial periods evolved from the early radiative models (Budyko, 1969; Sellers, 1969; Held and Suarez, 1974) to intermediate- and high-complexity numerical models. Numerical modelling of the Earth system, aimed at reproducing the Earth's climate, evolved from the initial low-complexity atmosphere-ocean models (Manabe and Bryan, 1969; Manabe et al., 1975; Bryan et al., 1975) into the intermediate- and high-complexity models, progressively increasing the temporal and spatial resolution and incorporating more and more processes (e.g. Bush and Philander, 1999; Ganopolski and Rahmstorf, 2000; Holloway et al. 2016), including the carbon cycle (e.g. Cox et al., 2000); see Flato et al. (2013) for a review.

Box models appeared somewhat later than numerical models, with the pioneering works of Sarmiento and Toggweiler (1984) and Siegenthaler and Wenk (1984), and became more sophisticated with the incorporation of more processes and numerous compartments (e.g. Birchfield, 1989; Paillard et al., 1993; Toggweiler, 1999; Peacock et al., 2006; Skinner, 2009). These box models, however, focused on reproducing the energy and carbon balance during one single period, typically the last glacial maximum or the recent preindustrial interglacial, rather than on the time evolution of climate.

In contrast with numerical models, box models have been rarely used to reproduce the full glacial-interglacial cycle (see Pelegrí et al., 2013, for a review). Their low computational cost and the possibility of turning on/off some of the boxes and internal processes, without the model's collapse, turns them into a very convenient tool to explore the temporal evolution of the system for glacial-interglacial periods. Hence, we propose a simple time-dependent coupled ocean-atmosphere model to analyze changes in the heat content of the atmosphere and the upper-ocean for the last 4.5 kyr, exploring the sensitivity of the atmosphere-ocean system to changes in albedo, cloud cover, thermohaline circulation and atmospheric and oceanic heat transports. The model is still undergoing careful testing but we have decided to include some of the preliminary results as a chapter of this thesis; we foresee that further work shall eventually lead to a manuscript that will be submitted to a scientific journal.

The presentation of the ongoing work is structured as follows. Firstly, we present a five-box model that includes two atmospheric and two upper-ocean compartments plus an immutable deep-ocean compartment. We carefully discuss the parameterization of the different terms – atmospheric radiative, atmospheric and oceanic convective, and ocean-atmosphere heat exchange terms – and define a set of output parameters that will be used to characterize the behaviour of the climate system. We next show some initial results, including the time series of the temperatures in the different compartments, a description of the climatic changes as depicted by the output parameters, and the analysis of the energy spectra. Finally, we conclude with some preliminary conclusions.

1.2 The five-box model

1.2.1 Model equations

Box models are a simple yet effective tool for studying the evolution of the temperature in the Earth system. These models are composed of several well-mixed compartments, externally forced by the Sun's radiation and interconnected through time-dependent energy equations.

The simplest option would probably be a three-box model, composed by single atmospheric, upper-ocean and deep-ocean compartments (Annex 1.1, Supporting Information); we ignore the land and cryosphere compartments, assuming that the amount of energy they store is negligible as compared with the atmospheric and ocean compartments. All three boxes are interconnected through the upper-ocean. The atmosphere and upper ocean are allowed to evolve in time, driven by the external forcing and the internal connections, but the deep ocean is considered to remain immutable through time. However, such a model would cause that warm surface waters go back to the deep ocean, hence ignoring the possibility of this heat being released to the atmosphere. Further, as the deep ocean is not an infinitely large compartment, the heat incorporated to the deep ocean would warm it on time scales of the order of 1-10 kyr.

Nevertheless, since the simplicity of the model is illustrative of some of the responses and interactions between the compartments, some results from this model are presented in Annex 1.2 (Supporting Information).

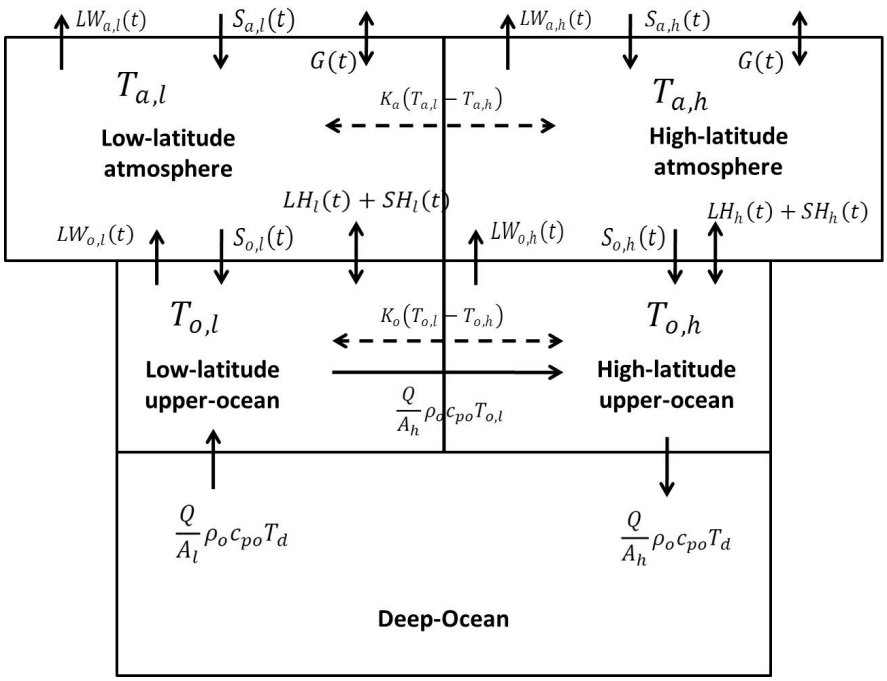

Fig. 1. 2: Compartments and heat fluxes in the five-box model.

The above limitations are removed with a five-box model: two boxes for the atmosphere plus three boxes for the ocean: one box for the deep ocean, one box for the low-latitude upper-ocean and one box for the high-latitude upper-ocean. The model schematics is shown in Figure 1.2 and the dimensions and major characteristics of the compartments are presented in Table 1.1; as for the three-box model, we ignore the land and cryosphere compartments. The cold deep- ocean waters, after their return to the surface, will capture atmospheric heat in the low-latitude. These waters will follow to the high-latitude compartment where they will release heat to the atmosphere before returning, as cold waters, to the deep-ocean. The deep ocean is again considered to remain steady through time. The model also includes heat exchange between the two atmospheric compartments and between the two upper-ocean ones, simulating both diffusive and advective near-horizontal fluxes.

The five-box conceptual model is represented as a system of four heat equations, one for each of the active compartments: the low-latitude atmosphere and ocean and the high-latitude atmosphere and ocean; the time dependent variables are the temperatures T of these four compartments. The heat in the low- and high-latitude atmospheric compartments is exchangeable through horizontal fluxes; similarly, in the low- and high-latitude oceanic compartments, heat is transferred directly through horizontal fluxes but energy is also converted as water recircu-

lates through the deep ocean. For simplicity, we consider each compartment to have constant depth and further assume that the areas of the upper- and deep-ocean are the same; finally, we let the entire upper-ocean to be in contact with the atmosphere but allow that some fraction of the atmosphere lies over land.

Table 1. 1: Dimensions and properties of the atmosphere and ocean in the five-box model

Property	Deep-ocean	High-latitude atmosphere	High-latitude upper-ocean	Low-latitude atmosphere	Low-latitude upper-ocean
Horizontal area, A (m^2)	1.65 x 10^{14}	2.5 x 10^{14}	1.65 x 10^{14}	2.5 x 10^{14}	1.65 x 10^{14}
Depth, h (m)	3500	8000	1400	8000	1400
Salinity, S (kg m^{-3})	34.9		35.5		36.0
Specific heat, C_p (J kg^{-1} K^{-1})	4000	1000	4000	1000	4000

We build the equations as the rate of change of heat per unit area that results from the several heat fluxes (heat transports per unit area) into and out of each compartment. The heat per unit volume is expressed as $\rho\, c_p T$, where ρ is the density and c_p the specific heat, so that the heat contained in a compartment of volume V is $\rho\, c_p T\, V$; writing the volume as the mean area times the mean depth, $V = A\, h$, it turns out that the heat per unit area is $\rho\, c_p T\, h$ and the temporal rate of change is $d\left(\rho\, c_p T\, h\right)/dt$.

The latitudinal heat fluxes are caused by flows at different scales that exchange waters with different properties. This junction of horizontal motions, from small to global scales (basin-scales for the ocean), is commonly divided into diffusive and advective motions carrying waters from different latitudes. However, in our simple model, the temperature of each basin is uniform so all motions carry the same water temperature and the heat exchange is simply proportional to the total volume transferred between the adjacent compartments. Therefore, we add up all water exchanges in one single horizontal exchange transport E (with units of volume per time) such that the heat transport is $\rho\, c_p\, T\, E$, and the heat transport per unit area is $\rho\, c_p\, T\, E/A$. When exchanging fluid between two adjacent compartments, the net heat transfer per unit (horizontal) area is $\rho_h\, c_{p,h}\, T_h\, E/A_h\; - \rho_l\, c_{p,l}\, T_l\, E/A_l \equiv K_h T_h - K_l T_l$, where the l and h subindexes stand for the low- and high-latitude compartments, respectively; for the particular case that both compartments have equal sizes, and since the changes in density and specific heat are much less than the variations in temperature, this can be approximated by $K\left(T_h - T_l\right)$, with one single mixing coefficient $K = \rho\, c_p\, Q/A$.

In the ocean, asides the near-horizontal exchange between adjacent compartments, we must consider advection associated with the formation of deep waters at high latitudes and their recirculation through the deep-ocean compartment, i.e. the global overturning circulation. The

intensity of this global overturning transport can be expressed in terms of the deep-ocean volume and a characteristic residence time-scale, $Q_0 = V_d/\tau_0$. The overturning volume transport is constant through all oceanic compartments but the water, after being incorporated to each chamber, changes its properties. Hence, the associated heat transport per unit area would be $\rho\, c_p\, T\, Q_0/A = \rho\, c_p\, T\, V_d/(\tau_0 A)$, where the temperature and properties correspond to the departing compartment; there is one single exception, however, as we assume that deep water formation at high latitudes will only occur in winter, we consider that the water departing the high-latitude upper-ocean into de deep ocean will carry the same water temperature as the deep ocean.

Finally, we have the non-advective fluxes, again expressed as energy flux per unit of surface area. These are the solar and greenhouse radiation terms, S and G, and the atmosphere-ocean heat exchange terms due to net long-wave radiation, and latent and sensible heat transfer, LW, LH and SH. The expressions used to specify the average fluxes (per unit area) for these different terms are discussed in next section.

The resulting equations are the following:

$$\rho_{a,l} c_{pa,l} h_{a,l} \frac{dT_{a,l}}{dt} = S_{a,l}(t) - LW_{a,l}(t) + G(t) - f_l S_{o,l}(t) + f_l\,(LH_l(t) + SH_l(t)) - K_{a,l} T_{a,l} + K_{a,h} T_{a,h} \quad (1.1)$$

$$\rho_{o,l} c_{po,l} h_{o,l} \frac{dT_{o,l}}{dt} = \frac{Q}{A_l}\left(\rho_{o,d} c_{po,d} T_d - \rho_{o,l} c_{po,l} T_{o,l}\right) + S_{o,l}(t) - LW_{o,l}(t) - LH_l - SH_l - K_{o,l} T_{o,l} + K_{o,h} T_{o,h} \quad (1.2)$$

$$\rho_{a,h} c_{pa} h_{a,h} \frac{dT_{a,h}}{dt} = S_{a,h}(t) - LW_{a,h}(t) + G(t) - f_h S_{o,h}(t) + f_h\,(LH_h(t) + SH_h(t)) + K_{a,l} T_{a,l} - K_{a,h} T_{a,h} \quad (1.3)$$

$$\rho_{o,h} c_{po} h_{o,h} \frac{dT_{o,h}}{dt} = \frac{Q}{A_h}\left(\rho_{o,l} c_{po,l} T_{o,l} - \rho_{o,d} c_{po,d} T_d\right) + S_{o,h}(t) - LW_{o,h}(t) - LH_h - SH_h + K_{o,l} T_{o,l} - K_{o,h} T_{o,h} \quad (1.4)$$

where sub-indexes o and a stand respectively for the oceanic and atmospheric compartments, sub-indexes l and h stand respectively for the low and high latitude compartments, and subindex d stands for the deep-ocean compartment; in particular, $T_{a,l}$, $T_{o,l}$, $T_{a,h}$, $T_{o,h}$ are the unknowns and T_d is taken as constant.

All other quantities are parameters that need to be specified: $\rho, C_{p,} h$, are the density, specific heat and thickness of each reservoir; f_l and f_h are the land fractions in each of the atmospheric compartments, indicating how the fluxes from the ocean into the atmosphere have to be distributed over the entire atmospheric compartment; V and A are the volume and area of each oceanic compartment; τ_0 is the characteristic glacial MOC recirculation time; K_a and K_o are the heat-transfer coefficients between the low- and high-latitude atmospheric and oceanic compartments, respectively.

The above analysis shows that the equations depend on the size of each box, as determined by the thickness of each compartment and the critical latitude θ_c separating the low- and high-

latitude compartments. The critical latitude affects both the advective fluxes, through the relative sizes of the adjacent compartments, and the radiative and sensible-latent heat fluxes, because of the different fractions of the ocean compartments in contact with the atmospheric compartments. One possibility is to choose this latitude to be 30^{o}, which corresponds to the actual latitude where the atmosphere-ocean heat exchange changes sign. This allows having one single mixing coefficient, K, and sets the approximation $f_l = f_h = f$. In this work we will present the results for this case, although the software has been adapted to allow changes in this critical latitude. Further, assuming that the thickness of the low- and high-latitude compartments is the same and neglecting the changes in density and specific heat as compared with the changes in temperature, the equations become:

$$\rho_a c_{pa} h_a \frac{dT_{a,l}}{dt} = S_{a,l}(t) - LW_{a,l}(t) + G(t) - fS_{o,l}(t) + f\left(LH_l(t) + SH_l(t)\right) - K_a\left(T_{a,l} - T_{a,h}\right) \tag{1.1'}$$

$$\rho_o c_{po} h_o \frac{dT_{o,l}}{dt} = \frac{Q\rho_o c_{po}}{A}\left(T_d - T_{o,l}\right) + S_{o,l}(t) - LW_{o,l}(t) - LH_l - SH_l - K_o\left(T_{o,l} - T_{o,h}\right) \tag{1.2'}$$

$$\rho_a c_{pa} h_a \frac{dT_{a,h}}{dt} = S_{a,h}(t) - LW_{a,h}(t) + G(t) - fS_{o,h}(t) + f\left(LH_h(t) + SH_h(t)\right) + K_a\left(T_{a,l} - T_{a,h}\right) \tag{1.3'}$$

$$\rho_o c_{po} h_o \frac{dT_{o,h}}{dt} = \frac{Q\rho_o c_{po}}{A}\left(T_{o,l} - T_d\right) + S_{o,h}(t) - LW_{o,h}(t) - LH_h - SH_h + K_o\left(T_{o,l} - T_{o,h}\right) \tag{1.4'}$$

1.2.2 Radiative and ocean-atmosphere heat exchange terms

In this section we propose expressions for the different radiative and atmosphere-ocean heat exchange terms discussed above. Consider first the short-wave solar radiative term. A time series for this value arriving at the outer atmosphere, $S\left(t\right)$, is available as a function of time and latitude (Berger, 1978; Berger and Loutre, 1991). We can integrate this function over time, e.g. to obtain monthly- or annual-mean values, and over space, to have the average insolation value for each compartment. Once having the average value, it can be divided by the surface area of the compartment in order to have the arriving solar radiation per unit area; the premise behind this spatial averaging is that each compartment mixes on time scales much shorter than our scales of interest (glacial-interglacial).

A fraction α_a of the incoming Sun's radiation is reflected by the atmosphere, associated with the presence of clouds and aerosols. The amount of radiation ultimately reaching the upper-ocean, $S_o\left(t\right)$, is further influenced by the sea-surface albedo α_o (with the lowest values for water and the highest ones for fresh snow) and the cloud cover n_c (Gill, 1982).

$$S_a(t) = S(t)\left(1 - \alpha_a\right) \tag{1.5}$$

$$S_o(t) = S(t)\left(1 - \alpha_a\right)\left(1 - \alpha_o\right)\left(1 - 0{,}7n_c^2\right) \tag{1.6}$$

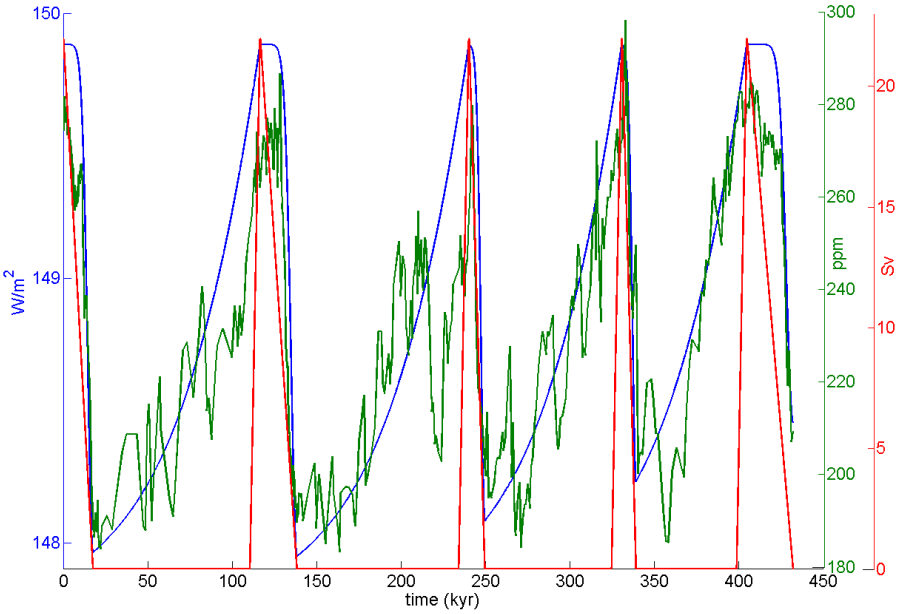

Fig. 1. 3: Greenhouse gas forcing (blue line) as inferred using the CO_2 model data (Pelegrí et al., 2013) (blue line) adjusted to the Vostok's CO2 time series (Petit et al., 1999) (green line). The corresponding MOC water mass transport is also shown (red line) (Pelegrí et al., 2013).

Next consider the long-wave radiative terms. The outgoing long-wave radiation emitted from the atmosphere is proportional to its temperature – emitted as if it was a blackbody – according to Stefan's law,

$$LW_a(t) = \sigma T_a^4 \tag{1.7}$$

where σ is the Stefan-Boltzmann constant. Part of this outgoing flux is retained by GHGs in the atmosphere and is radiated back to the sea surface. The amount of this is is calculated with the help of an empirical relation between the concentration of carbon dioxide in the atmosphere $C\,(t)$ and the radiative forcing relative to all greenhouse gases, referenced to the preindustrial value of G_0=144.2 W m^{-2} (Ramaswamy, 2001; Hogg, 2008; Roca and Pelegrí, 2019)

$$G(t) = G_0 + A \log\left(\frac{C(t)}{C_0}\right) \tag{1.8}$$

where A= 20.5 W m^{-2} and C_0=280 ppm. For the carbon dioxide time series, we use the simulation values for the last 450 kyr by Pelegrí et al. (2013). The resulting time series for the greenhouse radiation is shown in Figure 1.3.

The expression for the long-wave radiation emitted from the sea surface differs from equation (1.7) because of several correction factors: departures from blackbody behaviour (0.985); radiation emitted back to the surface because of water vapour in the atmosphere; and cloud effects. The proposed expression is (Gill, 1982):

$$LW_o(t) = 0{,}985\sigma T_o^4 \left[0{,}39 - 0{,}05\,(e_A)^{1/2}\right]\left(1 - 0{,}6 * n_c^2\right) \tag{1.9}$$

where e_A is the vapour pressure of water at a standard height and n_c the cloud cover fraction.

We express the water vapour pressure in terms of the relative humidity in decimal form (r) and temperature of the atmosphere (T_a) (Haney 1971).

$$e_a = r10^{\left(9{,}4051 - \frac{2353}{T_a}\right)} \tag{1.10}$$

Finally, we use a very simple approximation for the latent and sensible heat fluxes. There are different empirical expressions for both quantities but commonly the sensible heat is set to be proportional to the product of wind speed times the temperature difference between air and water while the latent heat is set to depend on the wind speed times the difference in specific humidity at the sea surface and at some standard level (Gill, 1982); since specific humidity changes with temperature, the latent heat can also be thought to be proportional to the ocean-atmosphere temperature difference. Hence, we let the sum of both to depend on the temperature difference between the atmospheric and upper-ocean compartments,

$$HE(t) = SH(t) + LH(t) = B\,(T_o + T_a) \tag{1.11}$$

where B is a convective heat transfer coefficient. Hoffert et al. (1980) used a similar approximation and found that, for typical surface wind speed over the ocean, B may range between 9 and 90 W m^{-2} K^{-1}.

1.2.3 Model parameters

There are eight parameters that need to be specified, four for the low-latitude box and four for the high-latitude compartment – atmospheric albedo (α_a), surface albedo (α_o), relative humidity (r) and cloud cover (n_c) – plus the horizontal heat-transfer coefficients for the atmosphere and ocean (K_a, K_o).

We consider atmospheric albedo to be constant in time, but differentiate between 0.29 in the low-latitude box and 0.45 in the high-latitude compartment (Loeb et al., 2009; Donohoe and Battisti, 2011). In contrast, we let the surface albedo to change both in time and among the compartments; this is particularly important because of the dependence of this parameter on ice and snow coverage (Donohoe and Battisti, 2011) and its potential large influence on climate (Romanova et al., 2006). We do so by setting a relationship between temperature and albedo: for temperatures above 0^{o}C the surface albedo is equal to a modern reference value, 0.15 (Donohoe and Battistini, 2011), while for lower temperatures we establish an inverse linear relationship, increasing surface albedo as temperature falls:

$$\alpha_o = \begin{cases} 0{,}15 & T_o > 0 \\ 12074 - 0{,}05T_o & T_o < 0 \end{cases} \tag{1.12}$$

The saturation vapour pressure depends on the temperature and the relative humidity. We take this humidity as constant and equal to nowadays mean value over oceans, 0.8 (e.g. London, 1957; Peixoto and Oort, 1996). According to general circulation models that estimate small mo-

difications on relative humidity over oceanic regions during the Last Glacial Maximum (LGM) (Bush and Philander, 1999), we maintain this value constant.

Clouds have a double effect: they trap part of the long-wave radiation emitted from the surface (long-wave effect) but also reflect the solar radiation (short-wave effect) (Schneider, 1972; Wetherald and Manabe, 1980; Ramanathan et al., 1989). The long-wave effect is larger in mid- and high-latitudes while the short-wave effect predominates in the tropics. Global mean cloud-cover lies between 60 and 70 % (Warren et al., 1988; Rossow and Schiffer, 1999). We set the cloud at low-latitude value to be 0.65 and let it increase to 0.75 in the extratropical oceans, where cloud cover is largest (Warren et al., 1988; Rossow and Schiffer, 1999; Ross and Dueñas 2004).

The convective heat-transfer coefficient, B, accounts for all factors (wind speed, humidity, height and atmospheric stability) that determine the latent and sensible heat fluxes (e.g. Gill, 1982). Different estimates of the global annual mean energy budget show that latent heat (8810 W m^{-2}) is several times larger than sensible heat (247 W m^{-2}) (e.g. Kiehl and Trenberth, 1997; Stephens et al., 2012). Latent heat is high in tropical regions ($\cong$ 120 W m^{-2}) and decreases towards mid- and high-latitudes ($\cong$ 40 W m^{-2}), while sensible heat shows an inverse pattern (10 to 30 W m^{-2}) (OAFLUX Project, 2008). We set B to 50 and 20 W m^{-2} K^{-1} in the low- and high-latitude compartments, respectively.

The deep and upper-ocean are connected through the GOC. The current rate $Q_0 = V_d \tau_0$ is a function of the deep-ocean volume and a characteristic residence time-scale. However, this rate may have changed in the past; in particular, during glacial periods the deep-ocean was probably smaller and the rate of exchange between the upper and lower boxes was much less than nowadays. We follow Pelegrí et al. (2013), who adjusted the carbon-dioxide time series by locking the deep ocean during glacial periods and letting the GOC increase linearly between zero during the glacial maximum up to nowadays maximum transport rate (22 Sv, 1 Sv $\equiv 10^6$ m^3 s^{-1}) during the following interglacial peak. We have introduced a modification in the model, allowing the GOC to decrease linearly at the end of the interglacial, down to zero in a period of 500 years [Fig. 1.3].

One of the challenges of the model is to set the atmospheric and ocean heat-transfer coefficients between low and high latitudes boxes, K_a and K_o, respectively. We follow a practical approach that consists in choosing values that provide transports of the order of current observations. Poleward of 30^o latitude, the atmosphere is responsible of around 90 % of the total meridional heat transport, reaching its maximum near 35^oN, near the edge of the atmospheric boxes. In contrast, the ocean dominates the heat transport between 0^o and 17^oN (Trenberth and Caron, 2001), i.e. within the low-latitude box. Hence, for the atmosphere we set K_a= 1.35 W m^{-2} K^{-1}, which will account for meridional mass transports of the order of the observations, some 200 Sv (1 Sv $\equiv 10^9$ kg s^{-1}) (Czaja and Marshall, 2006), while for the ocean we set K_o= 1.0 W m^{-2} K^{-1} , leading to mass transports of the order of 40 Sv (Czaja and Marshall, 2006).

For the numerical solution we use a leapfrog time integration scheme, with equal time steps for both the atmospheric and oceanic compartments. These time steps are either one year when using the annual-mean values or one month when using the monthly values. In this work we will restrict our discussion to the results obtained using the annual-mean insolation averaged over each compartment.

1.2.4 Study cases and output variables

Table 1.3 summarizes the characteristics of all cases explored with the five-box (5B) model. A total of six cases (5B-1 through 5B-6) have been considered. In case 5B-1 we set the same albedo, cloud cover, relative humidity, and heat-transfer coefficients for the low- and high-latitude boxes, and let no horizontal exchange between the low and high latitudes. We progressively explore the effect of changing the parameters: in case 5B-2 we differentiate between the low- and high-latitude atmospheric albedos and in case 5B-3 we discriminate between the low- and high-latitude cloud cover. We then modify case 5B-3 by first distinguishing between the low- and high-latitude heat-transfer coefficients (case 5B-4) and then incorporating the horizontal exchanges in both the ocean and atmosphere (case 5B-5). Finally, we modify this last case by letting the high-latitude albedo to depend on temperature. In all cases we allow the GOC to develop during the interglacial but lock the circuit during the glacial periods, following Pelegrí et al. (2013).

Table 1. 2: Parameters for the low/high latitude boxes in each of the five-box (5B) model cases.

Case	B ($Wm^{-2}K^{-1}$)	α_a	α_o	n_c	r	K_a ($Wm^{-2}K^{-1}$)	K_o ($Wm^{-2}K^{-1}$)
5B-1	30/30	0.3/0.3	0.15/0.15	0.65/0.65	0.8/0.8	0	0
5B-2	30/30	0.28/0.45	0.15/0.15	0.65/0.65	0.8/0.8	0	0
5B-3	30/30	0.28/0.45	0.15/0.15	0.65/0.75	0.8/0.8	0	0
5B-4	50/20	0.28/0.45	0.15/0.15	0.65/0.75	0.8/0.8	0	0
5B-5	50/20	0.28/0.45	0.15/0.15	0.65/0.75	0.8/0.8	1.3	0.35
5B-6	50/20	0.28/0.45	0.15/ $\alpha_o(t)$	0.65/0.75	0.8/0.8	0	0

The references used to set these values are: Kiehl and Trenberth (1997), Stephens et al. (2012), OAFLUX Project (2008) for B; Loeb et al. (2009), Donohoe and Battisti (2011) for ; Warren et al. (1988), Rossow and Schiffer (1999), Ross and Dueñas (2014) for n_c; Warren et al. (1988), Rossow and Schiffer (1999), Ross and Dueñas (2014), London (1957), Peixoto and Oort (1996), Bush and Philander (1999) for r; Czaja and Marshall (2006) for K.

We explore the different cases in three different ways: exploring the character of the time series of temperature, horizontal heat fluxes (both the heat-transfer and GOC fluxes), and shortwave and longwave radiative and ocean-atmosphere heat-exchange fluxes; calculating the energy spectra for these temperature time series; and considering the mean ($\pm$ standard deviation) values of several complementary variables during glacial and interglacial conditions. These additional variables are the glacial and interglacial peak temperatures and the glacial-interglacial temperature differences, as well as the radiative fluxes (incoming, outgoing and net), the ocean-

atmosphere heat-exchange flux, and the low-to-high latitude atmospheric and oceanic heat fluxes at the time of the peak temperatures [Fig. 1.4].

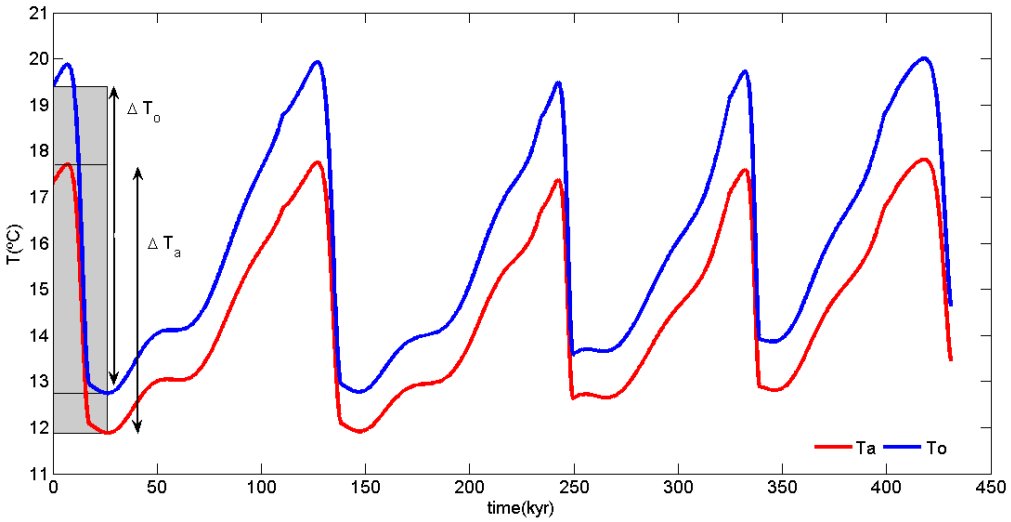

Fig. 1. 4: The glacial-interglacial temperature change is calculated as the difference between the temperature during one glacial maximum and the following interglacial, both for the atmosphere (ΔT_a) and the upper-ocean (ΔT_o) compartments.

1.3 Results

As indicated in the Prologue of this thesis, this chapter reports work in progress. For this reason, here we solely present some preliminary results, leaving more complete calculations and a careful discussion of the results to future works.

1.3.1 Time series

In Figures 1.5 to 1.8 we show the time series of the temperature and fluxes for cases 5B-4, 5B-5 and 5B-6, while the main output parameters for all cases are presented in Tables 1.3 and 1.4. A brief narrative of some of these results follows.

Table 1. 3: Glacial-interglacial temperature differences, with negative values indicating cooling during the glacial period

Case	$\Delta T_{o,h}$	$\Delta T_{o,l}$	$\Delta T_{a,h}$	$\Delta T_{a,l}$
5B-1	-1.9±0.5	0.9±0.3	-1.7±0.4	0.7±0.2
5B-2	-2.1±0.4	1.1±0.3	-1.9±0.4	0.8±0.3
5B-3	-2.1±0.4	1.1±0.3	-1.9±0.4	0.8±0.3
5B-4	-2.1±0.4	0.9±0.3	-1.8±0.4	0.7±0.3
5B-5	-1.0±0.2	-0.1±0.1	-0.9±0.2	-0.1±0.1
5B-6	-4.0±0.3	-0.9±0.2	-3.0±0.2	-0.9±0.2

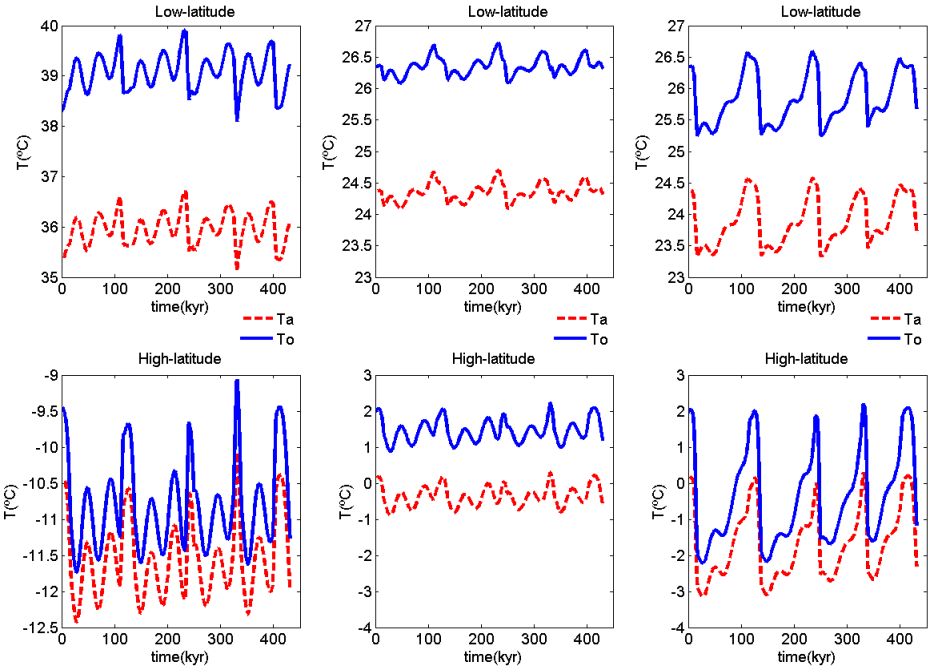

Fig. 1. 5: Atmospheric (red) and upper-ocean (blue) temperatures in low (dashed lines) and high latitudes (continue line) for cases 5B-4 (top), 5B-5 (middle) and 5B-6 (bottom).

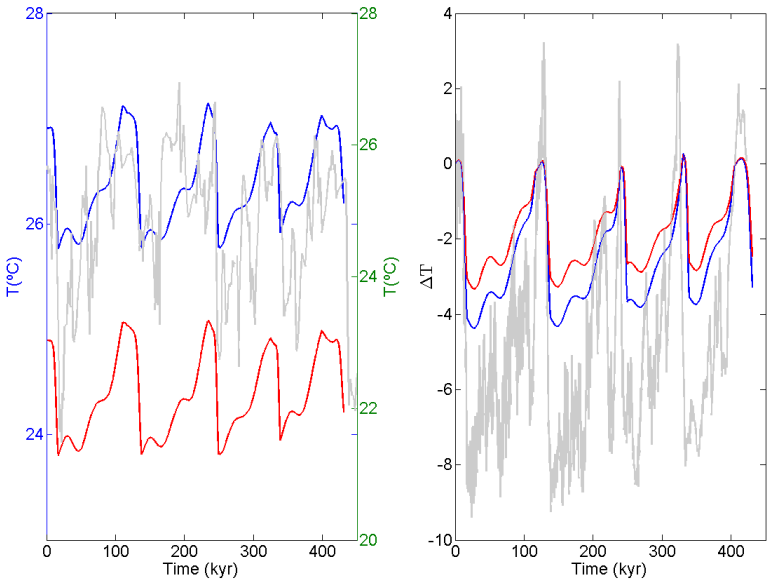

Fig. 1. 6: Upper-ocean (blue) and atmosphere (red) temperatures for case 5B-6. (Left) Comparison of the low-latitude model outputs with Harbert et al. (2010) proxy data (grey) for tropical sea surface temperature. (Right) Comparison of the high-latitude model output – here expressed as the temperature difference with respect to time 0 – with the temperature anomaly estimated by Petit et al. (1999) from the Vostok ice core data.

Table 1. 4: Mean glacial/interglacial values for the temperature (°C), long-wave radiation (LW), latent and sensible heat fluxes (HE) as well as the flux between both atmospheric compartments (At) and upper-ocean ones (Oc). All fluxes are in W m^{-2}, with positive values indicate flux towards high-latitudes.

Case	$T_{o,h}$	$T_{o,l}$	$T_{a,h}$	$T_{a,l}$	$LW_{o,h}$	$LW_{o,l}$	HE_h	HE_l	Oc	At
5B-1	1.2±0.1 / 3.1±0.4	38.0±0.1 / 37.1±0.2	-0.0±0.1 / 1.7±0.4	33.3±0.1 / 32.6±0.2	65.9±0.0 / 66.0±0.0	24.9±0.2 / 26.9±0.8	36.6±0.2 / 43.1±0.8	143.0±0.2 / 135.4±1.2	0 /0	0/0
5B-2	-8.5±0.1 / -6.4±0.3	41.3±0.1 / 40.2±0.3	-9.2±0.1 / -7.3±0.3	36.1±0.1 / 35.2±0.2	56.2±0.0 / 56.9±0.1	14.8±0.2 / 17.8±1.0	21.2±0.1 / 27.9±0.5	157.8±0.2 / 148.5±1.3	0 /0	0/0
5B-3	-9.4±0.1 / -7.3±0.3	41.3±0.1 / 40.2±0.3	-9.9±0.1 / -8.1±0.3	36.1±0.1 / 35.2±0.2	56.2±0.0 / 56.9±0.1	14.8±0.2 / 17.8±1.0	16.9±0.1 / 23.5±0.4	157.8±0.2 / 148.5±1.3	0 /0	0/0
5B-4	-9.1±0.1 / -7.0±0.3	39.3±0.1 / 38.4±0.2	-10.0±0.1 / -8.2±0.3	36.1±0.1 / 35.4±0.2	56.4±0.0 / 57.2±0.1	14.2±0.2 / 16.9±1.0	16.7±0.1 / 22.8±0.4	158.4±0.2 / 149.9±1.3	0 /0	0/0
5B-5	2.7±0.1 / 3.7±0.2	26.9±0.0 / 26.9±0.1	0.8±0.1 / 1.7±0.1	24.8±0.0 / 24.9±0.1	59.0±0.0 / 59.1±0.0	46.0±0.1 / 45.7±0.2	38.2±0.1 / 40.9±0.3	102.5±0.1 / 100.7±0.3	24.1±0.1 / 23.2±0.3	31.3±0.1 / 31.3±0.4
5B-6	-0.3±0.3 / 3.7±0.2	26.0±0.0 / 26.9±0.3	-1.4±0.2 / 1.7±0.2	24.0±0.1 / 24.9±0.1	58.3±0.1 / 59.1±0.0	47.4±0.2 / 45.7±0.2	21.1±1.5 / 40.8±0.3	98.8±0.4 / 100.7±0.3	26.3±0.2 / 23.2±0.3	34.3±0.2 / 31.3±0.4

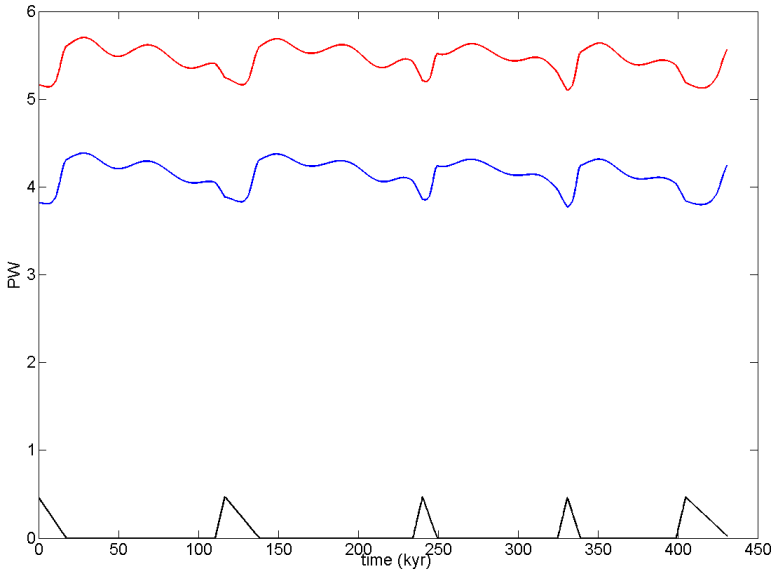

Fig. 1. 7: Integrated latitudinal heat transports for case 5B-6. Horizontal transports in the atmosphere (red) and the upper-ocean (blue), and transport associated with the GOC (black).

The model is able to reproduce the temperature gradient between both compartments, forced by the different solar radiation reaching each of them. In all cases we can appreciate the GOC's influence at the end of the glacial period [Fig. 1.5]; however, when MOC is the only direct mechanism connecting the low and high latitudes, the modelled temperatures are much warmer/colder than expected for interglacial/glacial periods (cases 5B-1 through 5B-4). As we include the horizontal fluxes we find that the high (low) latitude box warms up (cools) some 10^{o}C (case 5B-5). Additionally, the high-latitude compartment always warms during the interglacial but the effect on the low-latitude box differs: in the absence of horizontal fluxes, the low latitudes cool down; as we incorporate the horizontal transport, the low-latitude cooling disappears (case 5B-5); and when letting the albedo depend on temperature, we find that the low-latitude box warms while the GOC remains active (case 5B-6).

The effect of the albedo feedback mechanism is striking: the low latitudes show interglacial periods substantially warmer than the glacial ones and the polar cooling during the glacial periods is remarkable. Without this mechanism, the glacial-interglacial temperature anomaly in the high-latitude upper-ocean would range between 1 and 2^{o}C [Table 1.3], which is much less than observed. If we consider the albedo feedback, the low-latitude anomalies in both the ocean and atmosphere are about 1^{o}C and the high-latitude anomaly increases to some 4^{o}C in the upper-ocean and 3^{o}C in the atmosphere.

The glacial-interglacial temperature differences for case 5B-6 lead to oceanic/atmospheric estimates that are higher/lower than inferred by Annan and Hargreaves (2013). This is probably the consequence that HE decreases at high latitudes during glacial periods [Table 1.3] but it is

worth noting that we have not considered the possibility of atmospheric and upper-ocean compartments being isolated by the ice sheet. This would intensify the atmosphere high-latitude cooling and would reduce the high-latitude upper-ocean warming, leading to a better agreement with observations. Further, this would reduce the horizontal heat exchange between low and high latitudes, leading to a better agreement with observations (Annan and Hargreaves, 2013; Ballantyne et al. 2005).

A comparison of the low-latitude predictions (case 5B-6) with the tropical sea surface temperature (SST) (Herbert et al., 2010) shows that we cannot reproduce the temperature anomaly and the high variability during glacial periods. However, the model does reproduce the patterns at the end of the glacial and during the interglacial.

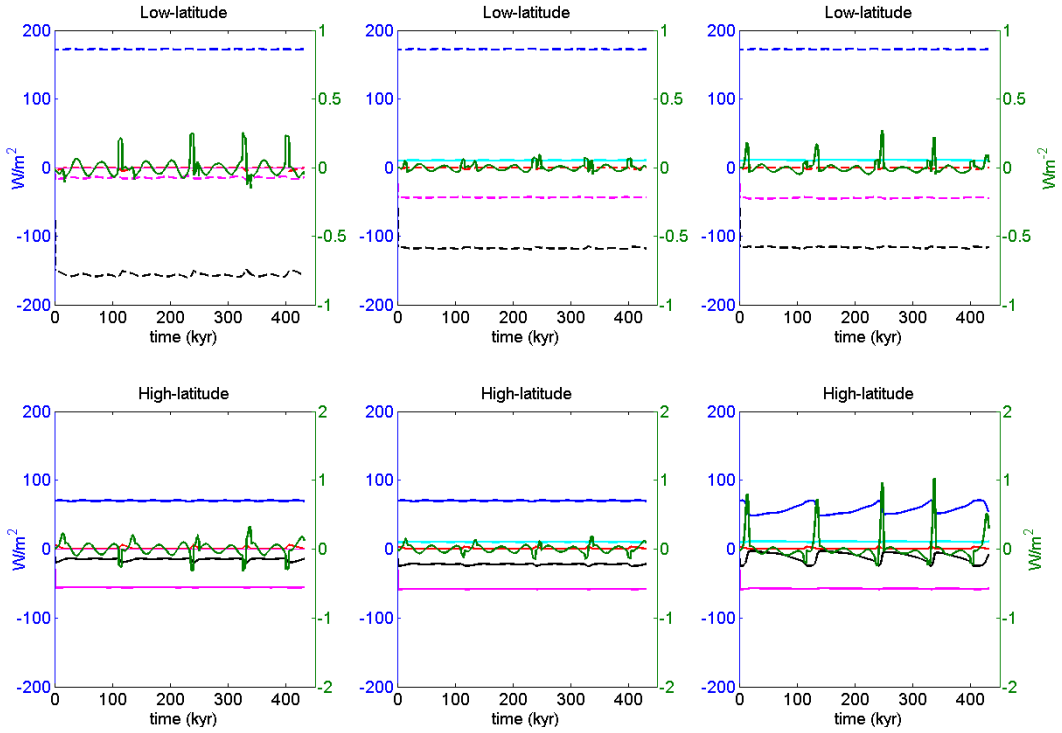

Fig. 1. 8: Fluxes in the upper-ocean compartment for cases 5B-4 (top), 5B-5 (middle) and 5B-6 (bottom): short-wave insolation (blue), long-wave back radiation (magenta), latent and sensible heat fluxes (black), GOC flux from the deep ocean (red), horizontal flux between upper-ocean compartments (cian) and the net energy in the upper-ocean compartment (green, right hand axis), for the low- (dashed lines) and high-latitudes (continue line) boxes.

Considering now the fluxes in each upper-ocean box [Table 1.4 and Figure 1.8], we observe that the infrared long-wave radiation emitted from the surface is larger in the high-latitude box than in the low one. This is counterintuitive, as warmer bodies are expected to have larger emissions. This can be explained by the water vapour/infrared radiation feedback, according to which above a certain temperature threshold this flux is smaller (Alexeev and Lindberg 2004). The sum of sensible and latent heat in the high/low latitude compartment is higher/lower during interglacial periods, with a mean value of 40/100 W m^{-2}, which are less than present values

(OAFLUX Project 2008).

The total oceanic heat diffusion to high latitudes varies between 4.5 PW during interglacial periods and 4 PW during glacial [Fig. 1.7]. Deep recirculation contributes with around 0.5 PW and the upper-ocean circulation with around 4 PW. The upper-ocean circulation is intensified during glacial, what corresponds to the suggestion of a shallower and stronger tropical circulation during the LGM (Ballarota el al. 2014). The influence of the atmospheric flux is higher, reaching 5.2 PW, which is close to current annual peak estimates 5.0 ± 0.14 PW (Trenberth and Caron 2001), although these maximum occurs at latitudes of 43^{o} instead of 30^{o}. As a result of the increase of the latitudinal temperature gradient, the atmospheric heat transport increases during glacial periods, as has been suggested by proxy data (Bush and Philander, 1999).

Finally, we may consider the resulting heat balance for each box, which is the temporal rate of change of energy contained in that compartment [Fig. 1.8]. At the beginning of the interglacial, the low-latitude compartment losses energy as a consequence of the activation of deep water recirculation; however, this loss only lasts for 1 kyr, afterwards gaining energy, as the latent and sensible heat fluxes to the atmosphere decrease, recovering a near-equilibrium in about 6 kyr. When the GOC stops, the heat flux from low to high-latitudes stops and the low-latitude compartment gains energy since, recovering again the glacial equilibrium in about 7 kyr. In the high-latitude compartment, the maximum energy gain is achieved when the MOC is active, recovering equilibrium in about 10 kyr. At the end of the interglacial, as the heat flux from low-latitudes in the ocean stops, the high-latitude compartment losses energy, stabilizing in 6 kyr. During glacial periods, both oceanic compartments have a net energy balance that oscillates around cero, with changes reflecting the variations in solar radiation. Similarly, the net flux in each of the atmospheric compartments displays a pattern similar to the underlying upper-ocean box, with a somewhat reduced range of variation.

1.3.2 Spectra

Glacial-interglacial periods during the last 800 kyr have been associated to astronomical changes in the latitudinal and temporal distribution of the solar energy received by the Earth (Berger, 1978; Hays, 1976; Imbrie et al., 1984). These variations in solar insolation, known as Milankovitch cycles, are due to changes in obliquity, precession and eccentricity with a frequency of about 41, 23 and 100 kyr, respectively. Surprisingly, while most of the changes are related to obliquity, the analysis of proxy data reveals that the dominant frequency is in the 100 kyr band (Hays et al. 1976).

We calculate the spectra of the upper-ocean temperature time series for cases 5B-5 and 5B-6. For case 5B-5, we observe that both the low- and high-latitude compartments have the main energy peaks at 39 and 108 kyrs, with the highest peak at the shorter period, particularly in

the low-latitude box; the 23-kyr period is weakly present in both compartments. For case 5B-6, when considering the albedo temperature feedback, the 39-kyr peak practically disappears and the 108 kyr one is greatly enhanced, in agreement with the analysis of proxy data.

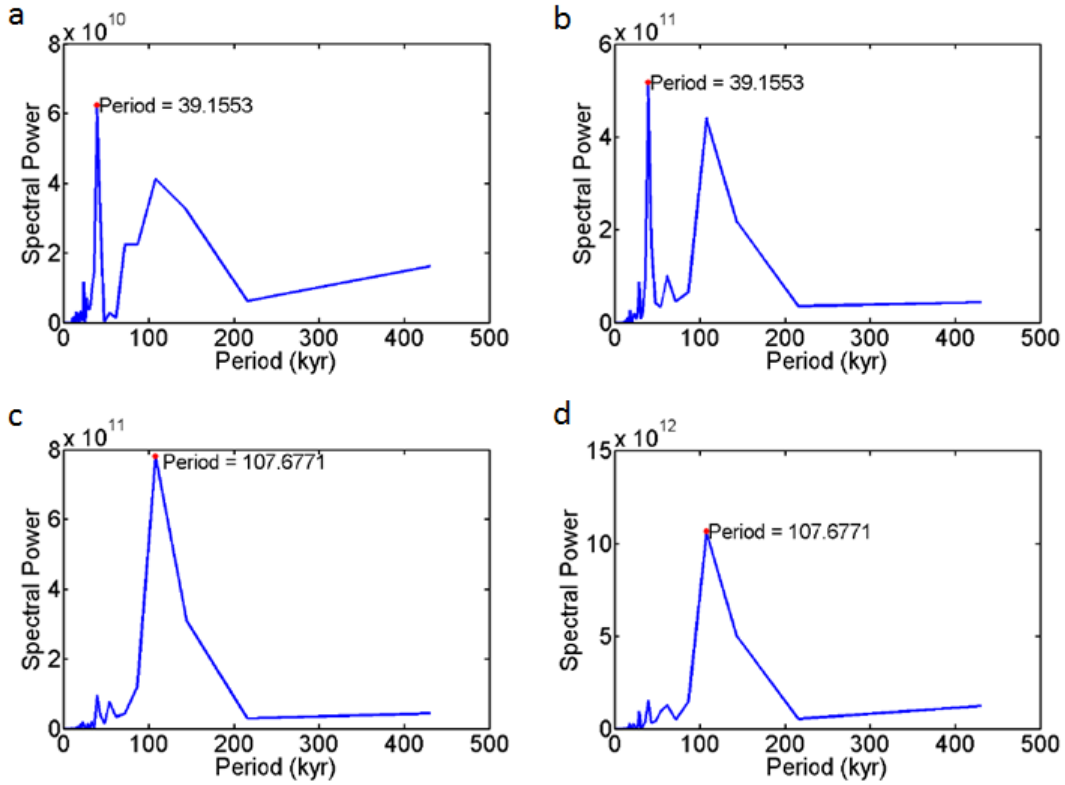

Fig. 1. 9: Spectral power for the temperature time series in the upper ocean: case 5B-5 at (a) low and (b) high latitudes, and case 5B-6 at (c) low and (d) high-latitudes.

1.4 Conclusions

We have developed a simple five-box model with two atmospheric and two upper-ocean boxes, plus a deep-ocean compartment. The model has all major physical factors controlling the Earth's climate: the short-wave solar radiation, the long-wave radiation from the Earth and its atmosphere, the latitudinal heat fluxes within the oceanic and atmospheric compartments, and global overturning circulation between the deep-ocean and upper-ocean compartments. The greenhouse effect is incorporated in a deterministic way from the time history of the concentration of carbon dioxide in the atmosphere.

Because of its simplicity, the model can be used to provide a rapid assessment of the importance of the different climatic elements and the impact of feedback mechanisms on the Earth's energy balance during glacial-interglacial cycles. It allows assessing the sensitivity of the temperature and the diverse heat fluxes to all internal parameters: those that control the ingoing and emitted radiations (atmospheric and surface albedos, cloud coverage, vapour content, greenhouse

gases) and those that regulate the latitudinal heat fluxes (horizontal exchange coefficients and the intensity of the global overturning circulation).

We have produced some preliminary results that confirm the model's potential. We realize that in order to produce feasible results we have to incorporate all elements. In this manner, for the interglacial conditions, we obtain radiative, atmosphere-ocean exchange, and latitudinal heat fluxes that are not far away from current values; however, the temperatures in the high-latitude compartment are higher/lower in the ocean/atmosphere than the present ones for interglacial periods. The reconstructed time series display realistic patterns, although the glacial maximum values are slightly less than predicted by more complex climatic models and proxy data. This likely reflects the lack of those effects associated with changes in ice coverage, atmospheric dust or the biosphere's albedo.

Our results suggest that changes in the annual mean solar radiation and the greenhouse gases have small direct contributions to the global heat balance, not being able to produce the glacial-interglacial climatic transitions. The glacial collapse of the global overturning circulation contributes to reduce the poleward heat transport during glacial; however, the intensification in the meridional temperature gradient during these periods strengthens the atmospheric fluxes, diminishes the temperature difference between compartments. The main parameter controlling the cooling in high latitudes during glacial periods is indeed the change in surface albedo due to the presence of ice. This is in agreement with other studies that have pointed at the terrestrial and sea-surface albedo as the most significant factor leading to the amplification of climate change (Holland and Bitz, 2003; Romanova et al., 2006). Interestingly, the spectral analysis of the model time series shows major energy peaks both in the 41 kyr and especially the 100 kyr bands. This suggests that the model has the skill of reproducing the non-linear mechanisms that lead to the amplification of the solar insolation.

All these encouraging results motivate us to complete this study with the objective of producing a tool that can be useful for the assessment of potential future climatic scenarios, both for scientists and governmental officers. This is work in progress. Undoubtedly, we expect that while completing this study there will be other aspects of interest that will be revealed.

Supporting Information

Annex 1.1: Formulation of the three-box model

We consider the time-dependent energy-conservation equations for a three-box model consisting of two active compartments (one for the atmosphere and for the upper-ocean) and on passive compartment (for the deep ocean). Each box is well mixed and the three boxes are

interconnected through the upper-ocean compartment. The governing equations are:

$$\rho_a c_{pa} h_a \frac{dT_a}{dt} = S_a(t) - LW_a(t) + G(t) - f\left(S_o(t) - LH_o(t)\right) + f\left(LH(t) - SH(t)\right) \quad \text{(S1.1)}$$

$$\rho_o c_{po} h_o \frac{dT_o}{dt} = \frac{Q}{A}\left(\rho_d c_{p,d} T_{d0} - \rho_o c_{po} T_o\right) + S_o(t) - LW_o(t) - LH(t) - SH(t) \quad \text{(S1.2)}$$

where the subindexes a and o correspond to the atmospheric and upper-ocean compartments, respectively. All variables are defined as in the description of the five-box model (section 1.2.1), with the single exception that there is no distinction between the low- and high-latitude compartments.

For the three-box model we set constant atmospheric and oceanic albedos of 0.3 and 0.15, respectively. We also set constant cloud cover, being either 0 or 0.65. Finally, we set the heat-exchange coefficient B = 30 W m^{-2} K^{-1}, in order to have ocean-atmosphere exchange fluxes close to present values. Finally, we set the intensity of the GOC to either be zero, a constant value or to change between maximum interglacial and zero glacial values, $Q(t)$, as discussed in the main text. The set of parameters are shown in Table S1.2.

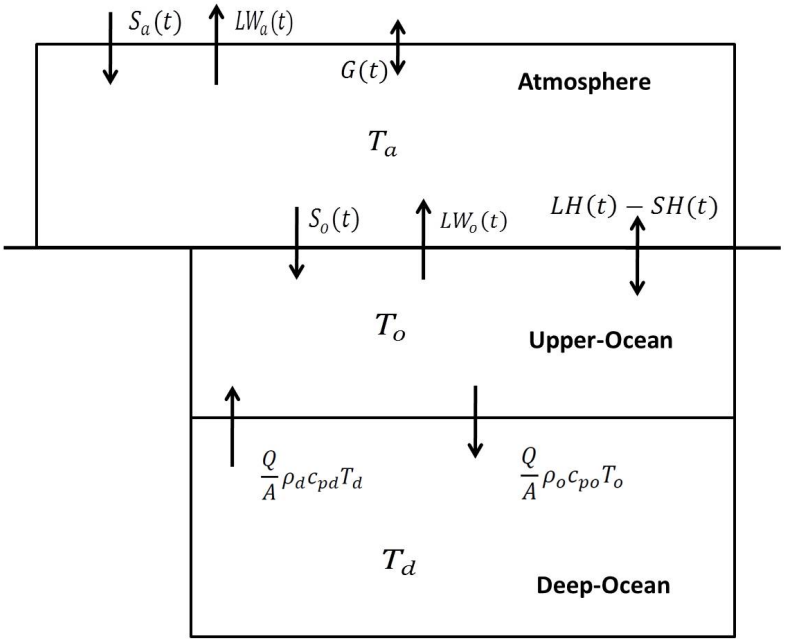

Fig. S.1. 1: Compartments and heat fluxes in the three-box model.

Table S.1. 1: Properties of the atmosphere and the upper-ocean in the three-box model

Property	Deep ocean	Upper ocean (i=o)	Atmosphere (i=a)
Horizontal area, A (m^2)	1.65 x 10^{14}	3.3 x 10^{14}	5.1 x 10^{14}
Depth, h_i (m)	3500	1400	8000
Salinity, S (kg m^{-3})	34.9	35.7	
Specific heat, C_{pi} (J kg^{-1} K^{-1})	4000	4000	1000

Annex 1.2: Results from the three-box model

Table S1.2 summarizes all cases explored with the three-box model and some selected results are shown in Figures S1.2 and S1.3. A total of seven cases (3B-1 through 3B-7) have been considered. In the first four cases (3B-1 through 3B-4) we analyse the effects of water vapour and cloud cover on the radiative terms. In cases 3B-5 through 3B-7 we include latent+sensible heat exchange between the ocean and atmosphere and explore the effect of collapsing (case 3B-6) and maintaining a constant rate (case 3B-7) of deep-water formation.

When we do not consider water vapour and cloud cover (case 3B-1), the model shows the surface air temperature to be slightly colder and the upper-ocean warmer in the glacial than during the interglacial. If we consider the long-wave retention by water vapour (case 3B-2) the upper-ocean warms to 60^{o}C and the atmosphere remains below 10^{o}C, due to the long-wave radiation scattered back to the surface [Fig. S1.2].

Table S.1. 2: Parameters used for each of the three-box (3B) model cases.

Case	B (Wm^{-2}K^{-1})	Q	α_a	α_o	n_c	r
3B-1	0	$Q(t)$	0.3	0.15	0	0
3B-2	0	$Q(t)$	0.3	0.15	0.65	0
3B-3	0	$Q(t)$	0.3	0.15	0	0.8
3B-4	0	$Q(t)$	0.3	0.15	0.65	0.8
3B-5	30	$Q(t)$	0.3	0.15	0.65	0.8
3B-6	30	0	0.3	0.15	0.65	0.8
3B-7	30	60	0.3	0.15	0.65	0.8

Regarding the fluxes, in the uncoupled cases (3B-1 to 3B-4) the net long-wave radiation at the surface is around 170 W m^{-2}, largely exceeding the modern annual mean, 53$\pm$13 W m^{-2} (e.g. Stephens et al. 2012). When both compartments are coupled, the long wave radiation reduces to realistic values, 58 W m^{-2}. The latent+sensible heat fluxes varies between 63 W m^{-2} during the interglacial and 66 W m^{-2} at glacial, both less than current values (120 W m^{-2}); the model cannot reproduce this flux even when increasing the heat transfer coefficient. During the interglacial maximum, the total flux from the deep ocean is around 1.5 PW (1 PW = 10^{15} W), in the order of current rates (Ganachaud and Wunsch 2003; Johns et al. 2011), which leads in the upper-ocean to a loss of around 4 W m^{-2} and a cooling of 0.8^{o}C [Fig. S1.3].

In the case of the coupled model (3B-5), the upper-ocean releases this heat excess to the atmosphere in the form of latent and sensible heat, warming the atmosphere up to 17^{o}C while the upper-ocean cools down to 20^{o}C, these values still larger than current mean ones. In this case, both boxes show the same pattern as the solar forcing. This is interrupted during the interglacial when the MOC is active, as it brings cold waters to the upper-ocean and thus cools

both compartments around 0.5^{o}C [Fig. S1.2]. Although the atmosphere is not directly affected by MOC, as the ocean is colder during interglacial, latent and sensible heat fluxes are reduced, with the consequent decrease in the temperature of the atmosphere. This leads to a cooler upper-ocean during interglacial, what is counterintuitive; we expect higher temperatures during interglacial periods. In contrast, when we do not consider changes in MOC, either constant or null (cases 3B-6 and 3B-7), the glacial is colder than the interglacial, although this decrease is lower than reports that have estimated anomalies to be around 4^{o}C for the LGM (Annan and Hargreaves, 2013).

The atmosphere is near equilibrium during the entire period being the net energy almost cero (2 x 10^{-4} W m^{-2}). During glacial, the net energy in the upper-ocean follows the pattern of the solar radiation. The main changes occur during interglacial, when the MOC is active, with the flux of water towards the deep ocean leading to an energy loss in the upper compartment. Once the MOC slows down, this upper compartment gains energy because the flux to the deep ocean stops; after the MOC collapse, the system recovers equilibrium in about 2 kyr.

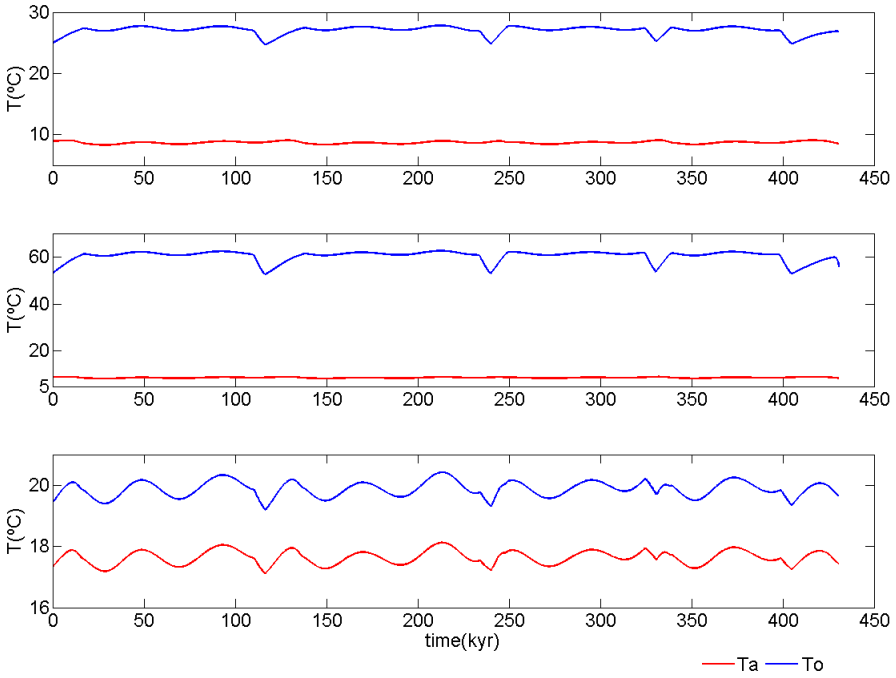

Fig. S.1. 2: Temperature of atmosphere (red) and upper-ocean (blue) for cases 3B-1 (top), 3B-4 (middle) and 3B-5 (bottom).

Table S.1. 3: Main results from the three-box model. The temperature anomaly corresponds to the difference between glacial and interglacial temperature, with negative values indicating cooling during the glacial period. Temperature, long-wave radiation (LW) and latent and sensible heat fluxes (HE) in the upper-ocean for nowadays (interglacial) and during the LGM; positive values indicate fluxes out the compartment.

			Glacial				Interglacial			
Case	ΔT_o	ΔT_a	T_o	T_a	LW_o	HE	T_o	T_a	LW_o	HE
3-B1	2.0±0.3	-0.5±0.1	27.0±0.1	8.4±0.1	176.8±0.1	0	25.0±0.2	8.9±0.1	172.0±0.6	0
3-B2	2.3±0.3	-0.5±0.1	22.7±0.1	8.4±0.1	124.5±0.1	0	20.4±0.2	8.9±0.1	120.7±0.4	0
3-B3	5.7±0.6	-0.5±0.1	65.5±0.2	8.4±0.1	176.8±0.1	0	59.8±0.5	8.9±0.1	163.4±0.6	0
3-B4	7.3±0.6	-0.5±0.1	60.6±0.2	8.4±0.1	124.5±0.1	0	53.3±0.6	8.9±0.1	112.7±0.5	0
3-B5	0.1±0.2	0.0±0.2	19.5±0.1	17.3±0.1	57.9±0.1	66.6±0.2	19.4±0.2	17.3±0.2	57.8±0.2	63.0±0.6
3-B6	-0.7±0.2	-0.6±0.2	19.5±0.1	17.3±0.1	57.9±0.1	66.6±0.2	20.2±0.2	17.3±0.2	57.2±0.2	67.9±0.6
3-B7	0.6±0.2	-0.6±0.2	18.7±0.1	16.7±0.1	58.5±0.1	61.8±0.2	19.4±0.2	17.3±0.2	57.8±0.4	62.9±0.5

Different MOC modes have been proposed for different climate situations. The 'Interglacial Mode', corresponding to the current one, the 'Glacial Mode' with a weaker circulation rate and a southward shift of deep water formation location, and 'MOC collapse' caused by an intense discharge of freshwater in the North Atlantic that leads to the stop of MOC for a certain period (Rahmstorf 2006). In our model, based on Pelegrí et al. (2013), we have proposed MOC to be active during interglacial periods and collapse during glacial.

In order to evaluate the influence of this flux in our model we consider three scenarios: case 3B-5, with a linearly increasing MOC during interglacial from zero to the current water formation rate (22 Sv) which stops during the glacial period; case 3B-6 without MOC (3B-6); and case 3B-7 with a constant MOC (22 Sv) at all times. The interglacial MOC conduces to the upper ocean cooling 0.7^{o}C (Fig. S1.4). If we consider a constant recirculation rate the upper ocean would be 0.8^{o}C colder during the entire period.

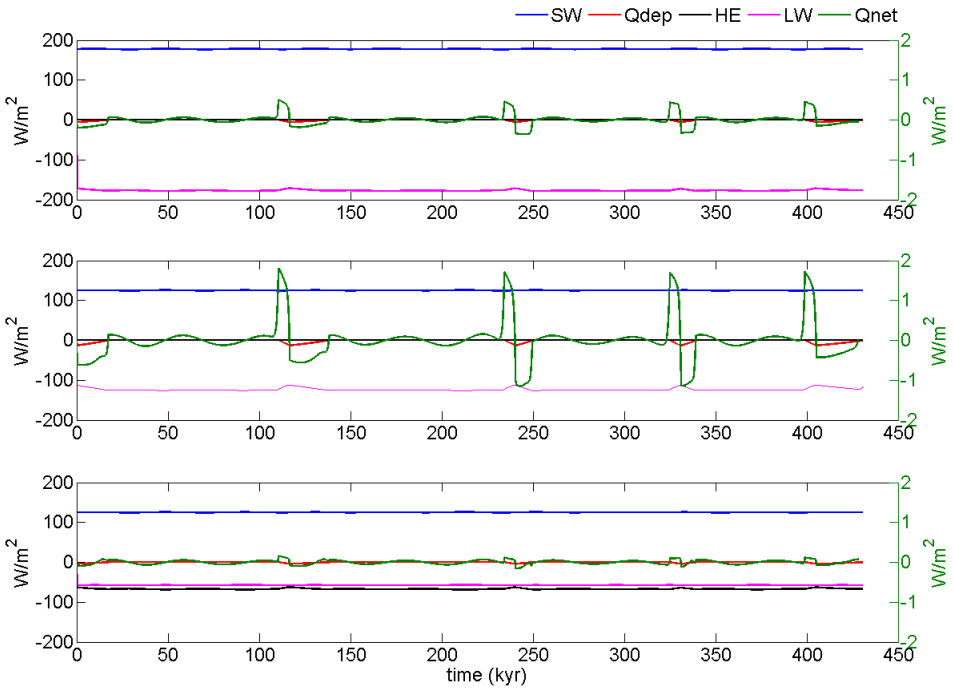

Fig. S.1. 3: Fluxes in the upper-ocean compartment: short-wave radiation (blue), long-wave radiation (magenta), latent and sensible heat fluxes (black), the flux from the deep ocean (red) and the net energy flux (green, right hand axis) for cases 3B-1 (top), 3B-4 (middle) and 3B-5 (bottom).

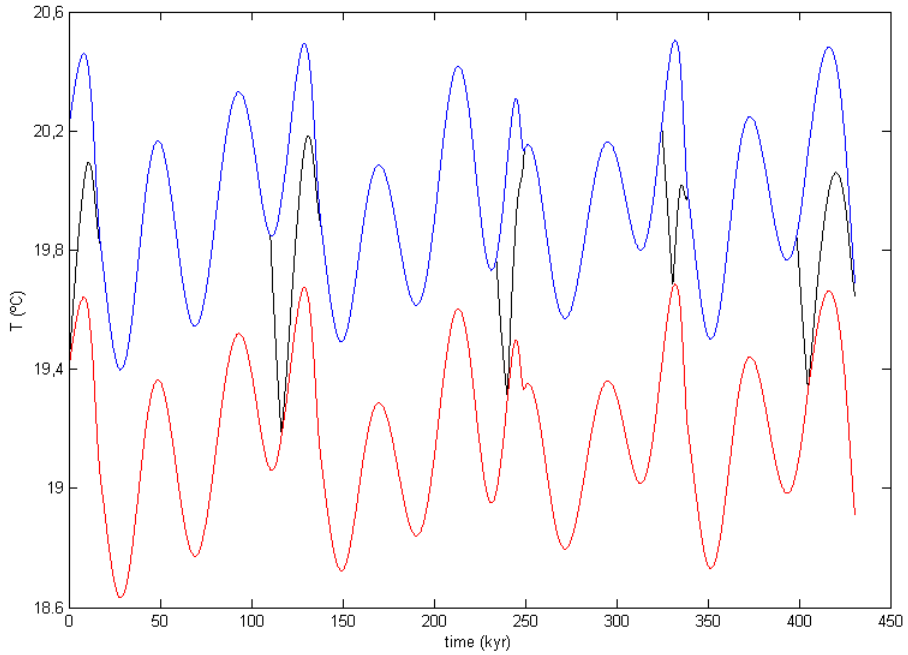

Fig. S.1. 4: Effects of different MOC configurations in the three-box model: case 3B-5 (interglacial MOC, black line), case 3B-6 (no MOC, blue line) and case 3B-7 (permanent MOC, red line).

Chapter 2

A 3D view of the Brazil-Malvinas Confluence

Orúe-Echevarría, D., Pelegrí, J. L., Alonso-González, I. J., Benítez-Barrios, V. M., De La Fuente, P., Emelianov, M., García-Olivares, A., Gasser, M., Herrero, C., Isern-Fontanet, J., Masdeu, M., Peña-Izquierdo, J., Piola, A.R., Ramírez-Garrido, S., Rosell-Fieschi, M., Salvador, J., Saraceno, M., Valla, D., Vallès-Casanova, I., and Vidal, M.

[In preparation]

Abstract

The encountering of the subtropical Brazil Current (BC) and the subantarctic Malvinas Current (MC) constitutes the Brazil-Malvinas Confluence, an important site for the modification and generation of intermediate waters that conform the returning limb of the Atlantic Meridional Overturning Circulation system. Here, we provide a comprehensive description of the BMC with the help of physical and biogeochemical data – hydrographic stations, profiling floats and Lagrangian instruments – gathered in March 2015. We use these data in order to characterize the impinging and outflowing currents and describe the cross- and along-frontal structure. In addition, we compare the in-situ measurements with both climatological data and the Mercator Ocean eddy-resolving reanalysis. The hydrographic sections illustrate the contrasting properties between the two boundary currents: warm, salty, nutrient- and oxygen-poor oligotrophic subtropical waters encountering the cold, fresh, oxygen- and nutrient-rich subantarctic waters. The frontal system is also characterized by the presence of thermohaline intrusions, with the frontal gradients and along-front velocities sharpening as the colliding currents get entrained into the frontal system. We also observe brackish waters spreading on top the frontal jet as a result of advection favoured by north-easterly winds, which are positively correlated with the surface ageostrophic speeds. The sight provided by the cruise data illustrates the high regional and mesoscale variability as compared with climatological conditions, and further evidence the submesoscale subsurface complexity that remains yet to be captured by operational models.

2.1 Introduction

The continental shelf and slope circulation of the southwest Atlantic Ocean has significant implications in the biogeochemistry and water mass structure of the entire Atlantic basin. This significance arises from exchanges between subantarctic and subtropical waters and between shelf and deep-ocean waters, which lead to high primary production and intense water mass transformations (Acha et al., 2004; Jullion et al., 2010; Valla et al., 2015; Combes and Matano, 2018; Orúe-Echevarría et al., 2019b).

The regional circulation is controlled, both over the shelf and in the open ocean, by the opposing flow and consequent encounter of cold, fresh, nutrient-rich subantarctic waters flowing equatorward and the poleward warm, salty, nutrient-poor subtropical waters (Palma et al., 2008; Matano et al., 2010). At the open ocean these flows correspond to the Malvinas Current (MC) and Brazil Current (BC), respectively. Both boundary currents flow close to the shelf break until their collision point around 38^{o}S, giving rise to an intense thermohaline front known as the Brazil Malvinas Confluence (BMC) (Gordon and Greengrove, 1986). Once these currents meet, both veer offshore, with the MC turning south in a cyclonic loop, then referred to as the Malvinas Return Current (MRC; Piola et al., 2013) whereas the BC continues southward east to the MRC and finally retroflects northeastward at about 45^{o}S (Brazil Current Overshoot, BCO; Saraceno et al., 2004). Following this retroflection, the BCO splits into two branches: one continues northward offshore the BMC (BC offshore recirculation; Valla et al., 2018) while the other flows eastward forming the South Atlantic Current (SAC) (Stramma and Peterson, 1990) [Fig. 2.1a].

The MC and BC follow the path of two frontal structures, the Subantarctic Front (SAF) and the Brazil Current Front (BCF), respectively, which converge in one single front at the BMC (BMCF) (Saraceno et al., 2004). The SAF corresponds to the northern branch of the Antarctic Circumpolar Current (ACC) system, separating subtropical and subantarctic origin waters (Orsi et al., 1995) while the BCF defines the southern limit of the BC (Roden, 1986). The BMCF extends over the shelf-break at about 36^{o}S separating over the platform subtropical and subantarctic origin waters, over the shelf being referred as the Subtropical Shelf Front (STSF) (Piola et al., 2000).

The encounter of the different water masses at the BMCF generates a complex vertical thermohaline front (Provost et al., 1996), depicted by the interleaving of different water masses (Bianchi et al., 1993). Furthermore, the retroflection of each of the currents results in the creation of structures of multiple scales, such as eddies and filaments (Legeckis and Gordon, 1982; Garcia et al., 2004; Barré et al., 2006; Lentini et al., 2006). The interleaving and mesoscale structures enhance epipycnal and diapycnal mixing between the water masses that converge at the BMC (Bianchi et al., 1993; 2002; Gaube et al., 2014; Mason et al., 2017; Orúe-Echevarría et al., 2019b).

The BMC is also a preferential site for the exchange of properties across the shelf. The off-shelf detrainment of platform waters, primarily Subantarctic Shelf Water (SASW), is enhanced during spring/summer southeast of the Rio de La Plata mouth (Strub et al., 2015). The prevailing north-easterly winds during these seasons produce a southward displacement of the Rio de La Plata and Patos-Mirim Lagoon waters (hereinafter referred as RdlP), which coincide with a southern position of the BMC over the shelf-break (Olson et al., 1988; Wainer et al., 2000; Goni and Wainer, 2000). Both southward migrations, together with the influence of local winds and boundary currents over the shelf, favour the seasonal advection of platform and river waters towards the deep ocean, contributing to the off-shelf export of freshwater and organic matter, among other properties (Combes and Matano, 2014a; Matano et al., 2014; Combes and Matano, 2018; Franco et al., 2018).

The interest over this region dates back to the 1980's, when the R/V Atlantis II cruise 107-3 (Gordon, 1981) and Marathon cruises 7-8-9 (Gordon, 1989) were carried out (October- November 1984). About six years later, another intense study was completed, with three surveys done from November 1988 to February 1990 by the Confluence Program (Confluence Principal Investigators, 1990). These field data were used to characterize the spring (Gordon, 1989) and summer (Provost et al., 1996) conditions, including the heat and salt fluxes (Bianchi et al., 1993; 2002), current velocity and transports (Gordon and Greengrove, 1986; Peterson, 1992; Garzoli, 1993; Maamaatuaiahutaou et al., 1998; Vivier and Provost, 1999b) and water masses (Maamaatuaiahutaou et al., 1992; 1994).

Motivated by the high productivity along the shelf-break upwelling (Acha et al., 2004; Dogliotti et al., 2014) and its relevance in the biogeochemical cycle of carbon (Bianchi et al., 2009; Kahl et al., 2017), most recent studies have done cross-shelf measurements (e.g. Piola et al., 2000; 2005; 2010; Möller et al., 2008; Valla and Piola, 2015; Carranza et al., 2017) and fewer studies have addressed the open-ocean circulation. In the early 1990's and 2000's, and recently between 2013 and 2017, moorings have been installed in the northern and southern margins of the BMC in order to study the variability of the BC (34.5^{o}S) (Meinen et al., 2012; 2013; 2017; 2018; Valla et al., 2018) and MC (41^{o}S) (Vivier and Provost, 1999a; Spadone and Provost, 2009; Ferrari et al., 2017; Artana et al., 2018a; Paniagua et al., 2018). Other studies have dealt with the surface dynamics at the confluence based on satellite data (e.g. Saraceno et al., 2004; 2005; Barré et al., 2006; Lumpkin and Garzoli, 2011; Saraceno and Provost, 2012; Strub et al., 2015) or on either regional or general circulation models (e.g. Matano et al., 1993; Palma et al., 2004; Fetter and Matano, 2008; Combes and Matano, 2014a,b; Matano et al., 2014).

Pursuing the cruises in the 1980's and 1990's, the TIC-MOC cruise was a renewed effort to produce a high-resolution quasi-synoptic survey of the BMC, capable of providing a new picture of the physical and biogeochemical frontal structure and dynamics. Here, we present the

physical and chemical conditions found during the cruise and compare it with climatological and reanalysis data. In section 2.2 we describe the field, reanalysis and climatological datasets. In section 2.3 we use the remote sensing and cruise data to describe the surface and three-dimensional (3D) structure of the frontal system. In section 2.4 we start comparing the cruise observations with the reanalysis data, and place both views under the climatological perspective, and continue by exploring the sources of surface and subsurface variability at the BMC. Finally, we close with the main conclusions in section 2.5.

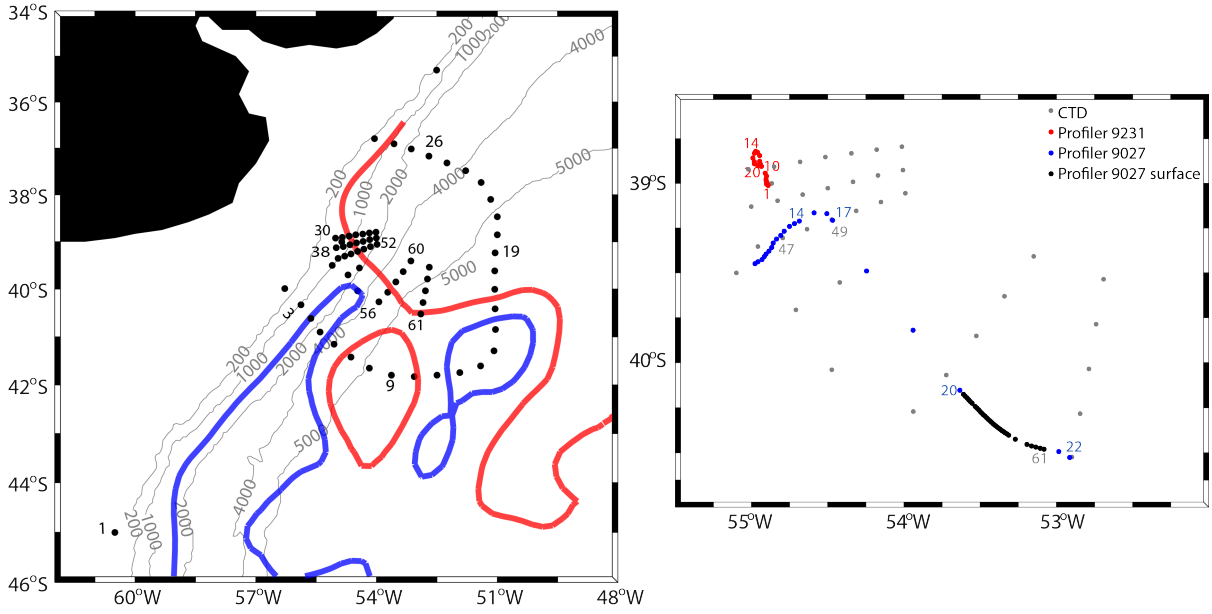

Fig. 2. 1: (Left) CTD stations during TIC-MOC cruise. Red (blue) lines represent the BCF (SAF) paths as defined by the 0.3 m (-0.05 m) ADT contours (Ferrari et al., 2017). The position of the main currents is indicated: Brazil Current (BC), BCO (Brazil Current Overshoot), Malvinas Current (MC), MRC (Malvinas Return Current). SW-AC/SE-C show the position of the main anticyclonic/cyclonic eddies sampled during the cruise. The black dots represent the stations over the outer perimeter while the blue dots indicate the cross-frontal sections. Roman/Arabic numbers indicate the section/station number. Grey lines represent the 200, 500, 1000, 2000, 4000 and 5000 m isobaths (GEBCO 2008 bathymetry). (Right) Cross-frontal sections (grey dots), positions of the profiles realized by float 9231 (red dots) and 9027 (blue dots), and surface positions provided by float 9027 between profiles 20 and 21 (black dots).

2.2 Data

2.2.1 Field measurements

Hydrographic data were gathered during the oceanographic TIC-MOC cruise onboard R/V Hespérides, between March 8 and 22, 2015. Figure 2.1a shows the location of the hydrographic stations and their position relative to the main frontal systems. Throughout this study, we will distinguish three study regions for our analysis: (1) the outer section, formed by 28 stations in a nearly circular perimeter delimiting the confluence; (2) the western near field, formed by the westernmost cross-frontal sections (sections I-III); and (3) the far field, which includes the two

eastern cross-frontal interior sections (sections IV-VI) plus seven stations along the meridional section of the outer perimeter (51^{o}W). In the outer perimeter, the stations are spaced about 45 km and sampling reaches down to a depth of 2000 m in the open ocean or to the sea floor over the upper slope. Each of the interior cross-frontal sections has a length of approximately 100 km, with stations spaced about 15 km and sampling down to the sea floor over the slope or 400/500 m depth in the near/far field sections. Below we include a brief description of the cruise and methodology for the data acquisition and processing. Further information can be found in Orúe-Echevarría et al. (2019a) and the data are available at Pelegrí et al. (2018).

At each of the 66 hydrographic stations, a conductivity-temperature-depth (CTD) cast was performed with a CTD SBE 911+ instrument, with redundant salinity and temperature sensors and additionally equipped with a SBE 43 oxygen sensor. Raw data, after processed, were vertically averaged into 1 dbar. At each station, water samples were collected at standard depths to determine nitrate (NO_3^-), phosphate (PO_4^{-3}) and silicate (Si) concentrations.

Throughout the cruise, continuous vertical profiles of horizontal current from 20 m to around 700 m, in 8-m depth bins, were obtained with the vessel's acoustic Doppler current profiler (VADCP). Raw data were quality controlled, corrected and edited with the Common Oceanographic Data Access System (CODAS, Firing et al., 1995). Besides, the thermosalinograph provided continuous near-surface temperature and salinity data from the vessel's underway system.

With the objective of getting a better detail of the BMC front, two profiling floats (identified as 9027 and 9031) were deployed [Fig. 2.1b]. Both Apex-type floats were equipped with a SBE 41CP CTD, enabling this to monitor water mass properties along their journey. Float 9027 completed 22 profiles in 9 days while Float 9231 did 20 profiles in 7 days. The journey of float 9027 was peculiar and deserves a brief mention. After profile 17 the communication with the float was lost for two days, performing two additional (non-positioned) profiles and recovering the position data for the 20th profile. We estimate the location of those two profiles from the positions of profiles 17 and 20 and the time spent between them. Between profiles 20 and 21 the float drifted at the sea surface, providing 33 additional positions.

Finally, subsurface drifters and profiling floats of the Argo program were launched during the cruise. A total of eight near-surface drifting buoys were launched in order to track near surface waters in the frontal area (six dragged at 100 m and two dragged at 200 m); drifting positions were acquired with a frequency of 30 minutes. A total of six Argo floats were also launched in the region during the cruise. During one month, four of these units (hereafter identified as TICMOC-1 through TICMOC-4) had a 5-day cycle and their parking depth at 400 m.

2.2.2 Remote sensing data

A description of the sea-surface conditions in the entire region is obtained with sea surface temperature (SST) and altimetry satellite products. Satellite altimetry data corresponds to the delayed time DUACS altimeter gridded product (Pujol et al., 2016) provided by Copernicus Marine and Environment Monitoring Service (CMEMS, http://marine.copernicus.eu/) (daily $1/4^{o}$ Mercator grid, multi-satellite, delayed time product), which includes absolute dynamic topography (ADT) and surface geostrophic velocity. SST correspond to $1/4^{o}$ gridded AMSR-2 7-day average images (Advanced Microwave Scanning Radiometer, http://www.remss.com/).

2.2.3 Reanalysis and climatological data

A climatological view is available from the World Ocean Atlas 2013 v.2 (WOA13), which provides monthly-mean fields of temperature and salinity at 69 vertical level (0-5600 m) for the global ocean at $1/4^{o}$ resolution on a Mercator grid (https://www.nodc.noaa.gov/OC5/woa13/) (Locarnini et al., 2013; Zweng et al., 2013).

High-resolution operational CMEMS model PSY4QV2R2 predictions for ADT and SST – as well as for temperature, salinity and velocity at 0, 92, 453 and 1062 m – were received onboard the vessel. These data were fundamental for the cruise design, particularly in the preliminary location of the frontal system. Artana et al. (2018b) compare this forecasting model with in-situ measurements and conclude that it correctly reproduces the large-scale circulation at the BMC. Instead of model predictions, here we use the GLORYS12V1 reanalysis product (hereafter reanalysis), largely based on the CMEMS forecasting system. This is a reanalysis between 1993 and 2018 on a $1/12^{o}$ grid and 50 standard vertical levels, from the sea surface down to 5500 m. It uses the NEMO3.1 numerical model forced at the surface with the European Centre for Medium-Range Weather Forecasts (ECMWF) ERA-Interim reanalysis, continuously assimilating in-situ temperature and salinity profiles, SST from the $1/4^{o}$ resolution Advanced Very High Resolution Radiometer (AVHRR) and along-track altimetry data. This reanalysis has recently been used to analyze the MC at the BMC (Artana et al., 2019).

Finally, we use the daily-mean Cross-Calibrated Multi-Platform (CCMP, https://podaac.jpl.nasa.gov/dataset/) winds (25 x 25 km resolution) (Atlas et al., 2011) from the 1st January to the end of March 2015. This wind dataset has shown to have a good correspondence with in-situ measurements at the BMC, being able to capture the high variability of this region (Carranza et al., 2017).

2.3 Results

2.3.1 Surface fronts

SST and SSS images [Fig. 2.2] allow the identification of the MC's signature as colder, fresher and lighter waters flowing northward along the Patagonian shelf-break until reaching the BCMF located at about 39.5^{o}S. At this point, it encounters higher ADT, SST and SSS values that characterize the subtropical waters to the north of the BCF. The differences between both sides of the BCF front are around 10^{o}C, 0.8 m and 1.5 practical salinity units, respectively. The satellite and reanalysis images in Figure 2.2 show data for 17th March 2015, when the sampling of the interior cross-frontal sections began (the reanalysis SST/SSS evolution before and during the entire cruise is available in Figs. S2.1 and S2.2, Supplementary materials); Artana et al. (2018b; 2019) have already confirmed the fairly good performance of the model for this region.

The model's mesoscale fields are very similar to the satellite SST and ADT ones, as expected from its assimilation of these datasets. However, there are some significant differences. First, the high horizontal resolution of the reanalysis shows submesoscale structures, such as various vortex and filaments southeast the BMC, which are not visible in the satellite and altimetry data. Second, while the position of the BCF derived from satellite and reanalysis data is almost the same, the location of the reanalysis ADT-derived SAF is about 75 km further south than the one derived from altimetry data. Additionally, the satellite SST shows slightly colder waters than the reanalysis in the northern part of the interior cross-frontal sections, with a more intense temperature gradient at the front.

On the other hand, WOA13 data shows a much smoother field than either the satellite or the reanalysis, displaying only each of the main currents and the front, whose position differs from the other datasets. The SSS fields from the reanalysis and WOA13 also present large differences, with the BC and MC core waters being fresher in the reanalysis. In the reanalysis image, we can identify the offshore RdlP freshwater on top the frontal jet. The northern edge of the interior cross-frontal sections is within this plume, which allows us to characterize its dimensions [sections 2.4.1 and 2.4.2]. On the contrary, WOA13 does not represent this feature. The near-surface salinity measured along the cruise-track [Fig. 2.2h] is consistent with the reanalysis SSS image.

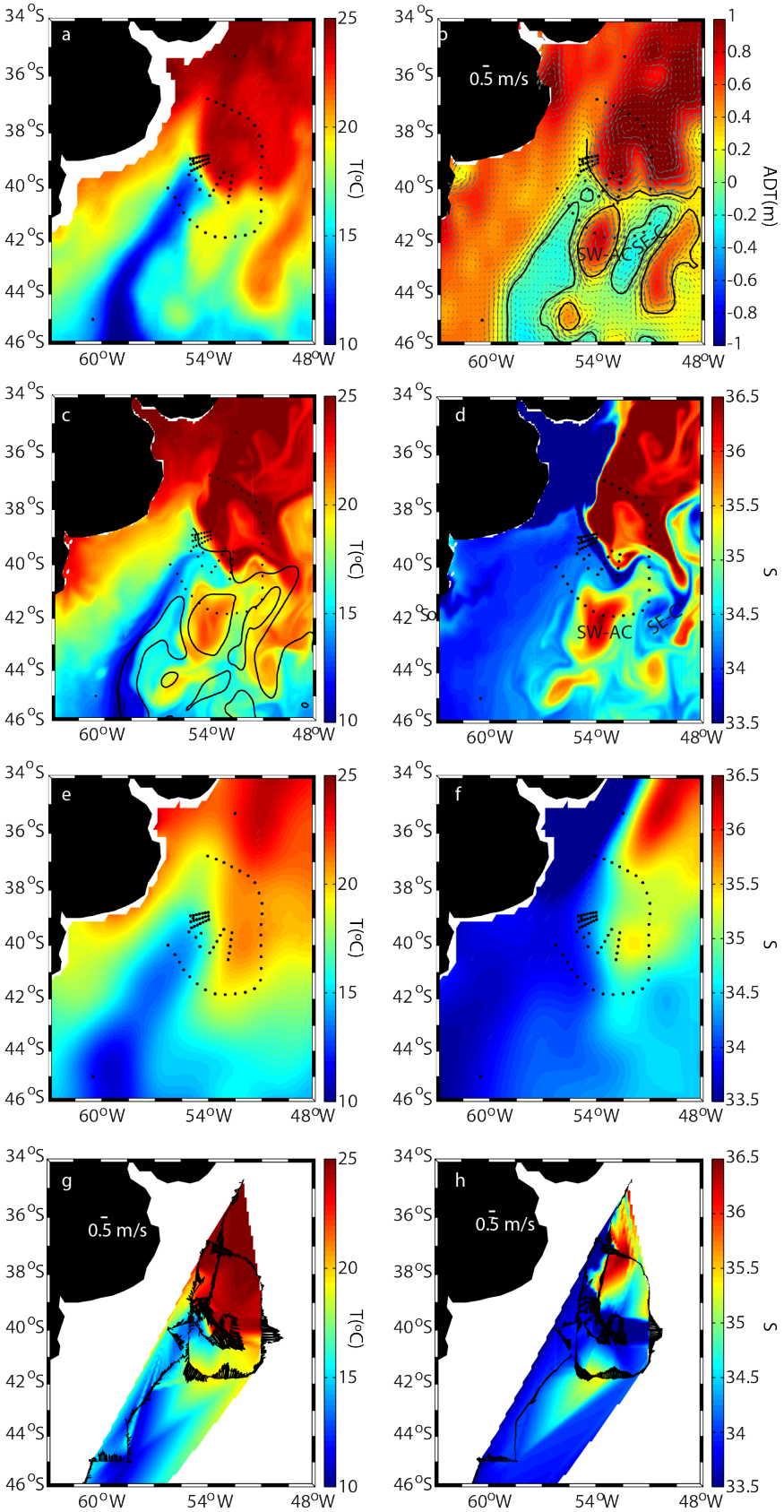

Fig. 2. 2: (a) Satellite SST (°C) and (b) ADT and geostrophic velocity on 17th March 2015. (c) SST and (d) SSS from reanalysis data on 17th March 2015. (d) SST and (f) SSS March-mean fields from WOA13. (g) SST and (h) SSS from the TIC-MOC thermosalinograph data; the vectors show the VADCP velocity (g) at 20 m and (h) averaged in the upper 700 m. The black dots represent the position of the CTD casts during TIC-MOC, and the black contours in (b,c) show the position of the SAF and BCF (ADT contours for -0.05 m and 0.3 m, respectively).

From Figure 2.2 we get the general view of the confluence area for March 2015. The regional circulation patterns and mesoscale features are clearly identifiable in all datasets. Both the reanalysis and satellite fields show the complex surface dynamics of the BMC. The northern half of the outer section is within the warm and saline waters of the BC. In the southern sector, the four western stations are characterized by surface cold and fresh waters of the MC. East from the MC, there is a warm and salty anticyclonic ring (SW-AC) followed by subantarctic waters revolving around a cyclonic eddy (SE-C) that contributes to the frontal jet. The SAF reaches approximately 40^{o}S before retroflecting southward following the MRC. The surface geostrophic and in-situ velocity fields identify the BC and MC as well as the frontal jet flowing eastward as a result of the collision [Fig. 2.2b,g,h].

2.3.2 Frontal system

We present cross-frontal sections of salinity (S) and potential temperature (θ) [Fig. 2.3], dissolved oxygen (DO) and silicate (Si) [Fig. 2.4], nitrate (NO_3^-) and phosphate (PO_4^{-3}) [Fig. 2.5] and horizontal water velocity [Fig. 2.6] for the outer, near-field and far-field sections. Each section is referenced at the southern extreme.

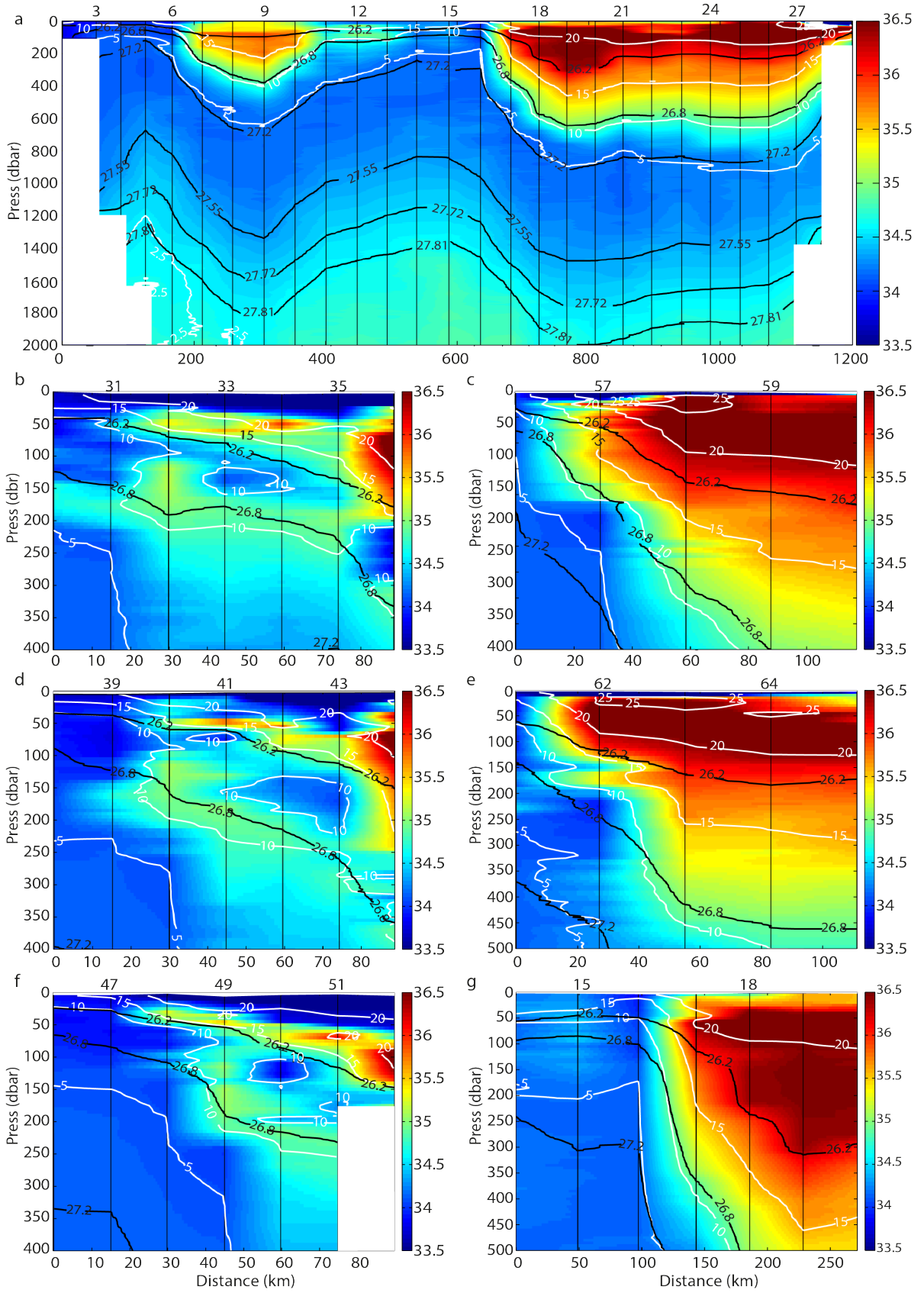

Fig. 2. 3: Vertical sections of S for (a) the outer section, (b, d, f) the near-field cross-frontal sections, and (c, e, g) the far-field sections. The white lines represent isothermals (ºC), black lines indicate isoneutrals (kg m^{-3}) and the black dots show the measurement points. The numbers on top indicate the stations, with their position as shown in Figure 2.1.

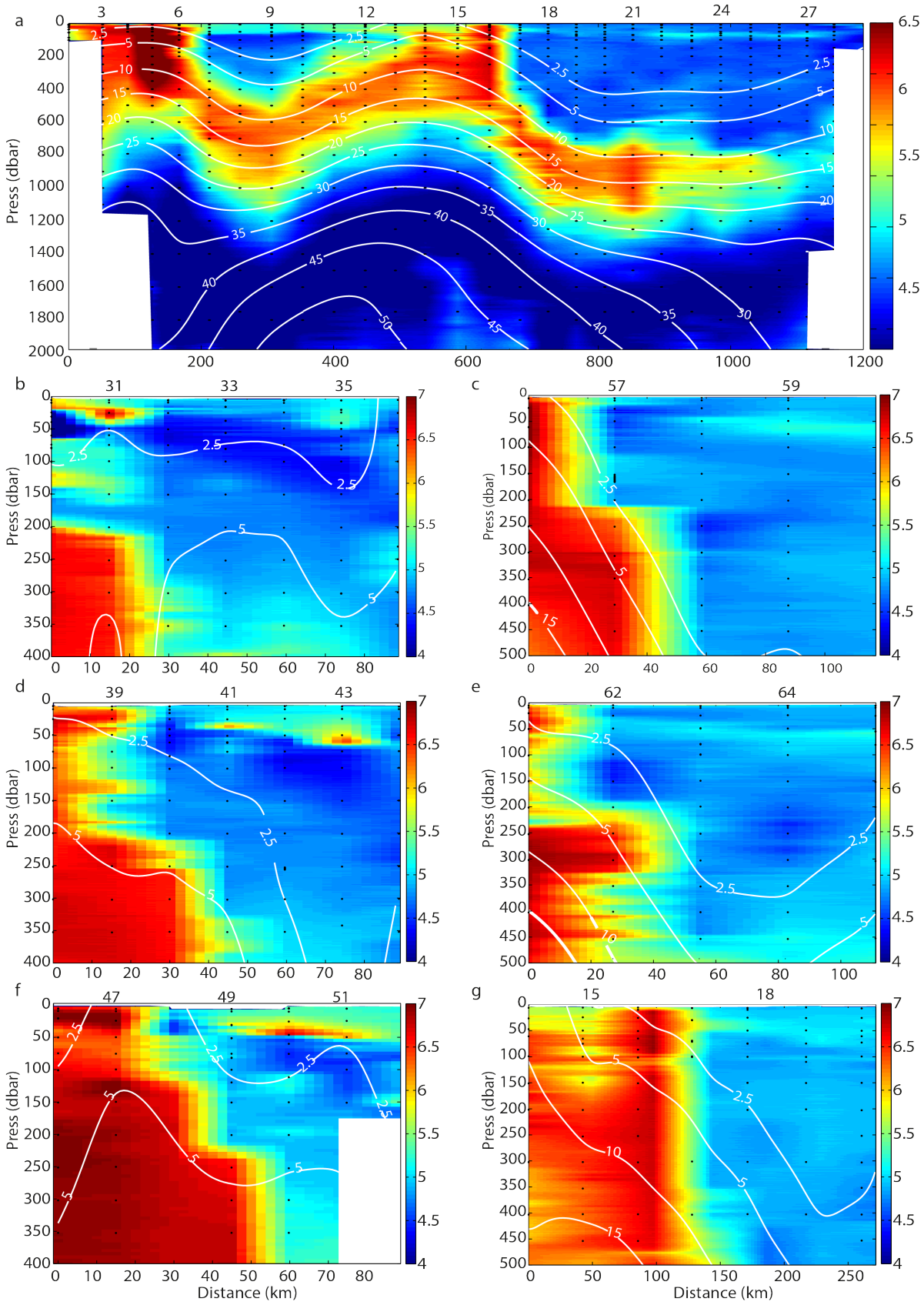

Fig. 2. 4: Vertical sections of DO (ml l^{-1}) for (a) the outer section, (b, d, f) the near-field cross-frontal sections, and (c, e, g) the far-field sections. The white lines represent Si concentration (μmol l^{-1}) and the black dots show the measurement points. The numbers on top indicate the stations, with their position as shown in Figure 2.1.

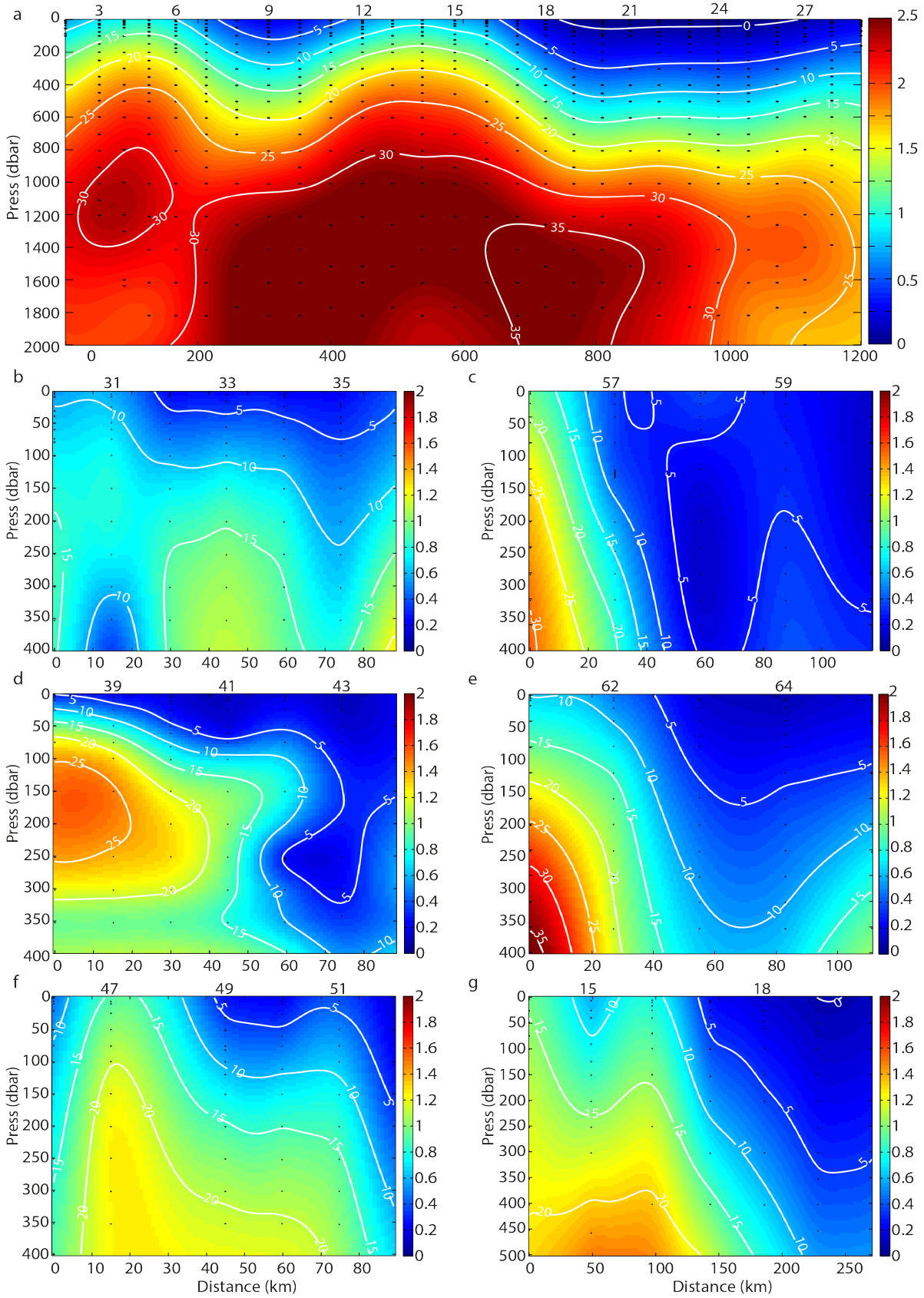

Fig. 2. 5: Vertical sections of PO_4^{-3} (μmol l^{-1}) for (a) the outer section, (b, d, f) the near-field cross-frontal sections, and (c, e, g) the far-field sections. The white lines represent NO_3^- concentration (μmol l^{-1}) and the black dots show the measurement points. The numbers on top indicate the stations, with their position as shown in Figure 2.1.

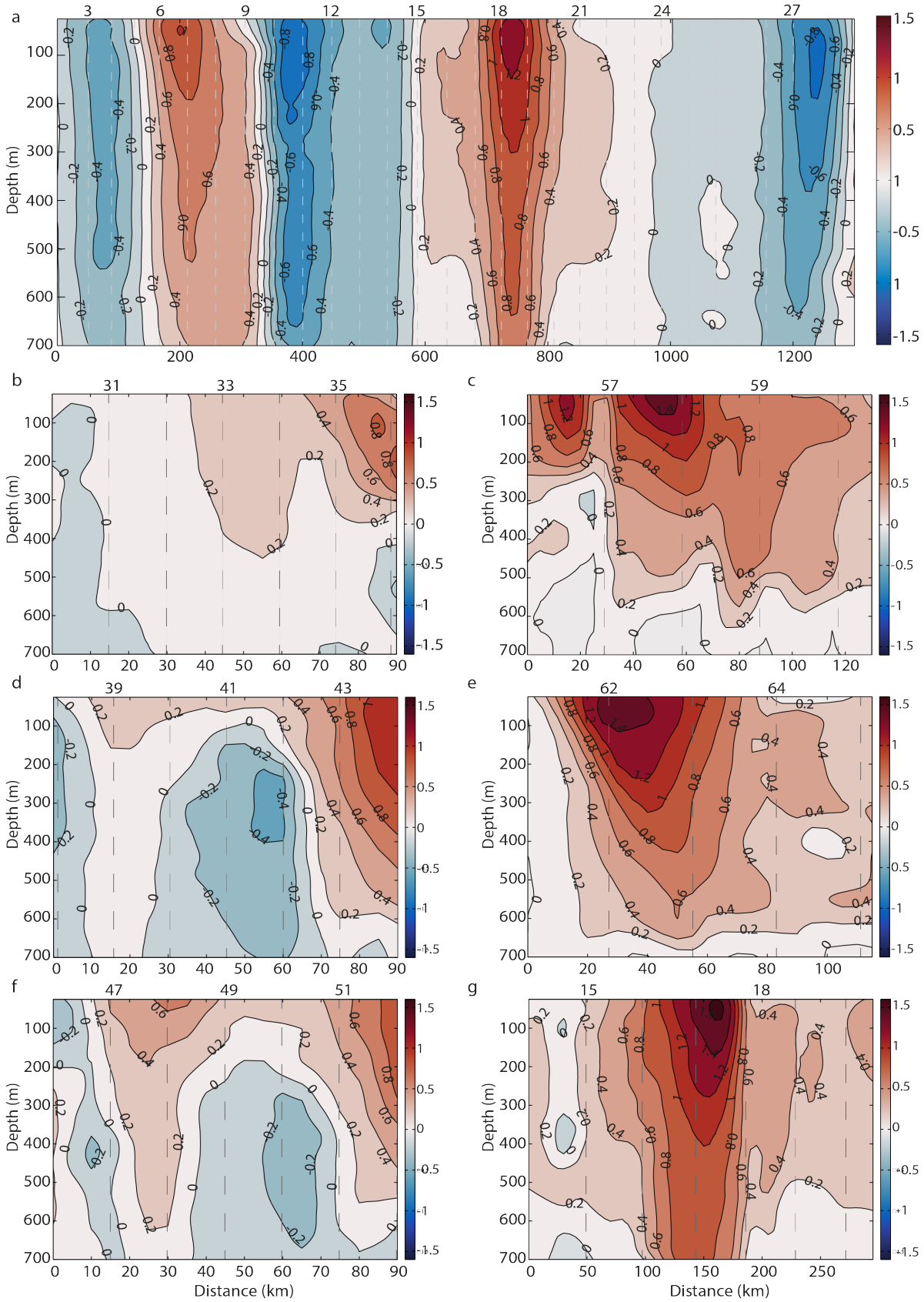

Fig. 2. 6: Vertical sections of absolute speed normal to the section (m s^{-1}) from 25 m down to 700 m as measured by the VADCP: (a) outer section, (b, d, f) near-field cross-frontal sections, and (c, e, g) far-field sections. In the outer section, negative/positive values indicate flow into/out of the BMC area. In the cross-frontal sections, negative/positive values indicate eastward/westward flow.

2.3.2.1 Outer section

The outer perimeter of the BMC displays substantial contrasts in almost all properties in the upper 800 m. These contrasts are evident both in the BMCF and between each eddy core and its surrounding waters. The SW-AC has a radius of around 200 km and extends down to 400 m; its core has θ/S values of 17^{o}C/35.8 at 100 m, which are about 10^{o}C/1.2 colder/fresher than the neighbouring waters. The SE-C presents the same water mass structure as the MC, though slightly saltier and warmer as a result of mixing at the BMC and the incorporation of warmer waters recirculating around the BCO (Orúe-Echevarría et al., 2019b). In the meridional section along 51^{o}W, we can identify the BMCF at approximately 40^{o}S-51^{o}W (stations 16-17) extending from the sea surface down to 500 m depth, where θ/S changes from 5^{o}C/34.2 to 17^{o}C/36.1 in 50 km. Below 800 m, both temperature and salinity differences are reduced.

We use θ-S diagrams [Fig. 2.7] together with the vertical property sections to identify the presence of the different water masses [Table 2.1], using as reference the definitions in Maamaatuaiahutapu et al. (1992) and Álvarez et al. (2014). In the westernmost stations of the outer section, the upper part of the water column is occupied by very low salinity Plata Plume Water (PPW, S<32.5 of river origin) (Piola et al., 2008), SASW flowing along the Patagonian shelf (fresher and warmer than MC waters: <21^{o}C, S<34; Piola et al., 2000), and Subtropical Shelf Water (STSW) formed north of the SASW as a mixture of river and BC waters (θ>18.5^{o}C, S<36; Piola et al., 2000; Möller et al., 2008). North of BMCF, in the upper 90 m we find the warmest (θ>20^{o}C) and saltiest (S>36.5) Tropical Water (TW). This is formed at tropical latitudes and transported southward with the BC, being poorly oxygenated (DO $\sim$ 4.5 ml l^{-1}) and depleted in nutrients (Worthington, 1976); this water mass was not found south of the BMCF.

Table 2. 1: Average potential temperature (θ), salinity (S), dissolved oxygen (DO), and silicate (Si), nitrate (NO_3^-) and phosphate (PO_4^{-3}) concentrations in each water mass layer as defined by neutral density ranges (γ^n).

Water mass	γ^n (kg m^{-3})	θ(ºC)	S	DO (ml l^{-1})	Si (μmol l^{-1})	NO_3^- (μmol l^{-1})	PO_4^{-3} (μmol l^{-1})
TW	<26.2	24	36.7	4.5	1.0	2.2	0.2
STMW	26.2-26.8	13.0	35.1	4.6	3.4	16.5	1.0
SAMW	26.8-27.2	6.7	34.4	5.4	8.5	27.8	1.6
AAIW	27.2-27.55	3.8	34.2	5.4	21.8	35.4	2.0
UCW	27.55-27.92	2.9	34.6	4.0	50.0	38.8	2.2

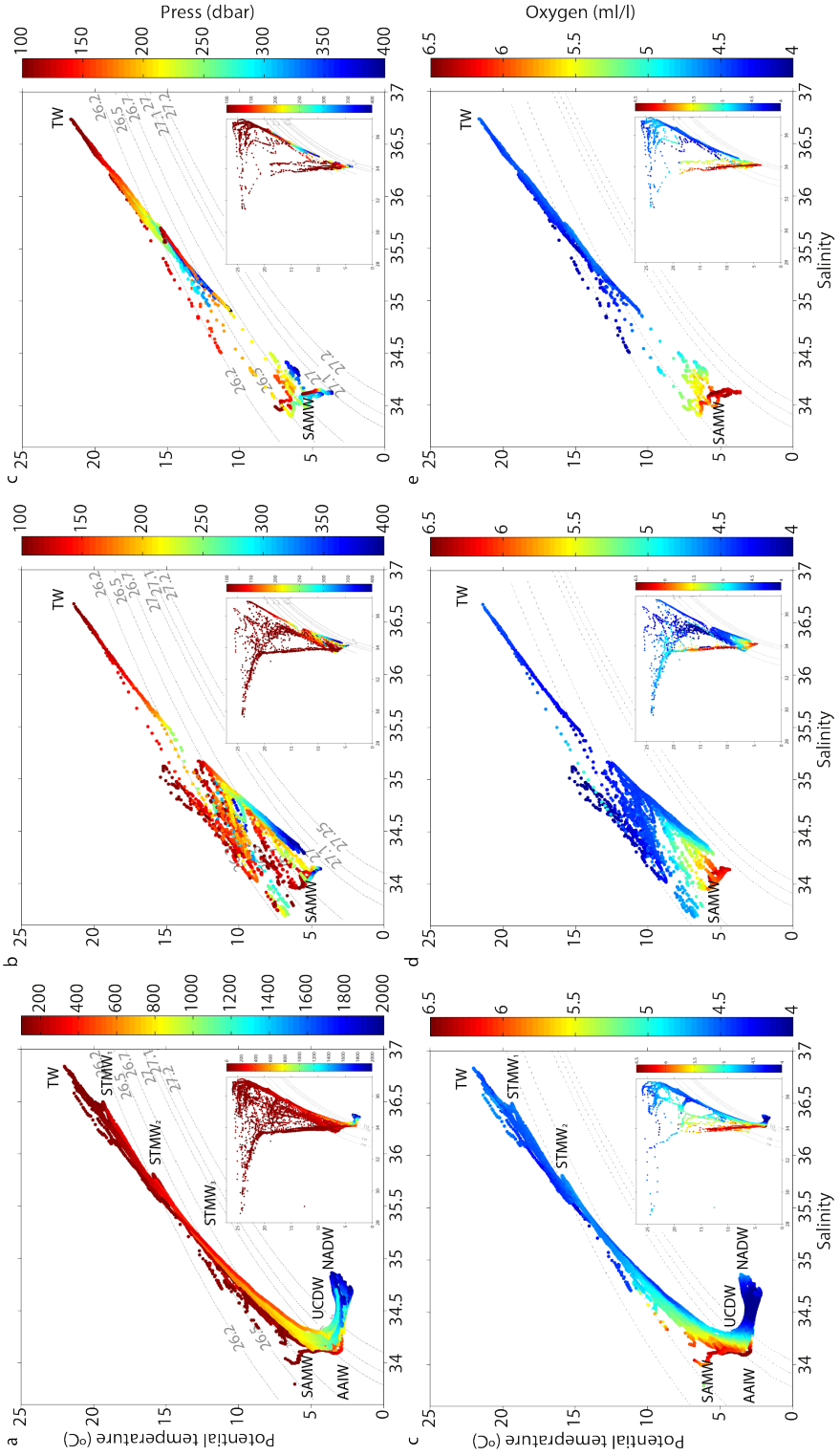

Fig. 2. 7: Potential temperature-salinity (θ-S) diagram for (a, c) the outer section, (b, d) the near-field sections and (c, e) the far-field sections, excluding the upper 100 m. Small diagrams in each figure include data from the surface. Colours represents the (a, b, c) pressure and (c, d, e) DO (ml l^{-1}) content of each point. Grey colours indicate constant potential density. The water masses are: Tropical Water (TW), Subtropical Mode Water Type I ($STMW_1$), Subtropical Mode Water Type II ($STMW_2$), Subantarctic Mode Water (SAMW), Antarctic Intermediate Water (AAIW), Upper Circumpolar Deep Water (UCDW) and North Atlantic Deep Water (NADW).

Central waters are occupied by South Atlantic Central Water (SACW), which is characterized by a straight line joining 5^{o}C-34.15 and 19^{o}C-36.2. It includes two mode waters, Subtropical Mode Water (STMW) and Subantarctic Mode Water (SAMW). On the northern border of the BCF we find STMW ($\theta \cong$ 12-18^{o}C, S $\cong$ 35.2-36.2) below the TW and to a depth of 500 m; this water mass is not present south of the BCF, except for the SW-AC core. The STMW is formed along the Subtropical Front of the South Atlantic Ocean and at the BCF during austral winter and early spring (Provost et al., 1999). The θ-S diagram shows two inflection points at around 19^{o}C-36.5 and 15-8^{o}C-35.8, each corresponding to a different STMW type [Fig. 2.7]. Considering the three STMWs defined by Provost et al. (1999) for the South Atlantic, the first point corresponds to $STMW_1$ ($\theta \cong$ 16-18^{o}C, S $\cong$ 36.2-36.9), which extends from below the TW down to approximately 250 m, while at deeper layers we find $STMW_2$ ($\theta \cong$ 14-16^{o}C, S $\cong$ 35.5-35.9). South of the BCF and below the warm summer mixed-layer, waters are dominated by the coldest variety of mode water, the SAMW ($\theta \cong$ 5-8^{o}C, S $\cong$ 34.16; Piola and Gordon, 1989). Due to its winter-convection origin in a nutrient-rich region, along the subantarctic zone of the northern Drake Passage (McCartney, 1977, 1982; Palter et al., 2010), these waters are relatively cold and fresh and have high DO, PO_4^{-3} and Si concentrations (>6.2 ml l^{-1}, >1.8 μmol l^{-1} and >6 μmol l^{-1}, respectively). North of the BCF, SAMW is found at deeper levels (500-800 m), where it is saltier (S $\cong$ 34.4); stations east of the BC core, and especially those along the meridional section at 51^{o}W, present higher DO values (>5.5 ml l^{-1}) in the SAMW layer than in the BC core (DO $\cong$ 4.6 ml l^{-1}). These changes are the consequence of intense mixing at the BMCF (Valla et al., 2018; Orúe-Echevarría et al., 2019b).

Intermediate waters are characterized by salinity-minimum Antarctic Intermediate Water (AAIW; S $\cong$ 34.12, $\theta \cong$ 3.1^{o}C). The core of this water mass deepens from 200 m in the southern sector to around 1000 m in the northern flank of the BMCF. It originates from the subduction of SAMW along the northward flow of the MC (McCartney, 1982; Piola and Gordon, 1989; Talley, 1996; You, 2002), so it presents a DO maximum (>6.0 ml l^{-1}) in the inner MC. The AAIW is highly modified in the BMC (Sloyan and Rintoul, 2000; Valla et al., 2018; Orúe-Echevarría et al., 2019), contributing to the freshening and oxygenation of the northern part of the front. Once the AAIW leaves the BMC, one part recirculates northward (Valla et al., 2018) and another continues east with the SAC, mixing in the eastern South Atlantic basin with AAIW from the Indian ocean, incorporated through the Agulhas Current Retroflection. After crossing the subtropical gyre, some of these waters return south with the BC (Garzoli and Gordon, 1996; Schmid and Garzoli, 2009; Schmid et al., 2000; Rodrigues et al., 2010). Thus, saltier (S $\cong$ 34.3) and lower DO ($\cong$ 4.9 ml l^{-1}) waters near 900 m between stations 27 and 29 (core of the BC) correspond to this older AAIW.

Below the AAIW, we find Upper Circumpolar Deep Water (UCDW), extending in most of the stations down to 2000 m. It is saltier (S >34.3) and slightly colder (θ <2.9^{o}C) than AAIW, charac-

terized by very low DO (<4.2 ml l^{-1}) and enhanced nutrient concentrations, especially by high Si values (>50 μmol l^{-1}). The low DO and high nutrient concentrations respond to the old age of this water mass, having travelled from the South Pacific across the Drake Passage and north with the MC (Peterson and Whitworth, 1980; Tsuchiya et al., 1994). UCDW is slightly fresher and oxygenated in the core of the BC than in the MC, because of diapycnal mixing with AAIW and NADW along the South Atlantic basin (Valla et al., 2018). In the deepest stations over the MC (Station 4) and in the SE-C (stations 11 to 15), we find North Atlantic Deep Water below 1800 m (NADW, $\theta \cong 3^{o}$C, S $\cong$ 34.9, DO $\cong$ 4.6 ml l^{-1}).

South of the BMCF the velocity record shows the barotropic nature of both the MC and the associated SE-C (Goni et al., 1996; Vivier and Provost, 1999a; Piola et al., 2013), with fairly constant velocities in the upper 600 m [Figure 2.6a, where blue/red colours indicate flow into/out of the confluence domain]. In the SW-AC, the velocity in the top 200 m exceeds 0.8 m s^{-1}, remaining over 0.6 m s^{-1} down to 600 m. The frontal jet presents the most intense flow, above 1 m s^{-1} in the first 300 m and staying higher than 0.8 m s^{-1} down to 600 m. North of the BMCF and east of the BC, the current is very weak, not exceeding 0.2 m s^{-1}. The BC extends its main core down to 600 m (Piola and Matano, 2001), with the highest velocities ($\cong$ 0.8 m s^{-1}) between 70 and 200 m and decreasing its intensity with depth, evidencing the baroclinic nature of this current (Matano et al., 2010).

2.3.2.2 Near field

The cruise measurements in the near-field cross-frontal sections [Fig. 2.3b,d,f] show SST values that agree fairly well with the reanalysis and satellite images [Fig. 2.2a,c], which locate the southern three stations of each section south of the BMCF. However, when considering the three-dimensional structure of the BMCF, we appreciate that the sub-surface front it not completely crossed by these sections. Using the definitions that the front is located at the intersection of the 10^{o}C isotherm and the 200 m level (Garzoli and Bianchi, 1987) or the crossing of the 26.96 kg m^{-3} isopycnal at 380 m (Artana et al., 2018b), the subsurface front appears to be located further north.

The most notorious features of the near field sections are the thermohaline intrusions. These are most evident in the salinity field of sections I and II [Fig. 2.3b, d] where high θ/S subtropical origin waters intrude into fresher subantarctic waters. These structures are around 10-50 m thick and 10-20 km wide and intrude some 50 km into the subantarctic side of the front.

The low salinity PPW layer extends down to only 20-30 m. Below the PPW, we find TW and STSW north of the BMCF (down to 200-250 m) and SASW and SAMW south of the BMCF (down to 400 m). The southern stations, with waters of subantarctic origin, are characterized by relatively high DO and nutrient concentrations (DO >5 ml l^{-1}, NO_3^- >26 μmol l^{-1}, PO_4^{-3}

>1.6 μmol l^{-1}). On the contrary, the northern stations are occupied by oligotrophic and poorly oxygenated subtropical waters (DO <4.4 ml l^{-1}, NO_3^- <222 μmol l^{-1}, PO_4^{-3} <1.2 μmol l^{-1}).

Surface velocities increase northward, towards the position of the maximum temperature gradients, where the highest velocities are found [Fig. 2.2]. Thus, velocities in the northern stations are higher than in the south, 1.2 and 0.2 m s^{-1}, respectively. The southern stations show westward velocities from the surface down to 400 m (west/east velocities in blue/red in Fig. 2.6b, d, f). This westward component can be identified in the altimetry derived geostrophic surface velocity [Fig. 2.2b] representing an extension of the MC towards the shelf.

2.3.2.3 Far field

The satellite and reanalysis SST show some significant differences over the far-field sections [Fig. 2.2a, c]. In the satellite image, the sections appear on the warm side of the BMCF while, in the reanalysis image, they cross the front. The cruise sections confirm that most stations belong to the subtropical side but also show that the subantarctic sector is sampled in the southern two stations of sections IV and V, being separated by a more vertical and a sharper front than in the near field [Fig. 2.3c, e].

Comparing with the near field sections, the property gradients are more intense (0.18 psu and 0.25 ^oC km^{-1} respectively at 100 m depth) and there are no intrusions. These sections evidence that the 200-m subsurface front is in a more northern position than the surface one. The subsurface front is characterized by an abrupt temperature change, around 10^oC in 30 km. The PPW is still present in the top meters, although it is shallower than in the near field sections (about 5-15 m in section IV and less than 10 m in section V). Depending on the chosen threshold, we can estimate the horizontal width of the jet to be 20-40 km. The freshwater plume is thus becoming thinner and narrower as it separates from the source, and once it reaches 51^{o}W [Fig. 2.3g] it only appears in the upper few meters of the station just north of the BCF.

The stations south of the BCF are occupied by SAMW down to 400 m while north of the BCF, under the PPW, we find salty-warm TW in the top 200 m and STMW below. As occurs in the near field sections, there is an abrupt change in oxygen and nutrient concentrations from the southern (DO >5.5 ml l^{-1}, NO_3^- >30 μmol l^{-1}, PO_4^{-3} >1.5 μmol l^{-1}) to the northern ends (DO <5 ml l^{-1}, NO_3^- <15 μmol l^{-1}, PO_4^{-3} <1 μmol l^{-1}). There is a slight modification of the water masses along the frontal jet, with the major transformation in the SAMW layer, about 0.1 psu saltier in the far field as compared with the near field.

The velocity in the far field is eastward from the surface down to 700 m and increases towards the north, reaching a maximum over the front where the surface velocities exceed 1.6 m s^{-1} [Fig. 2.6c, e, g], higher than in the near field (1 m s^{-1} maximum at the frontal jet). These high

speeds are similar to those experienced by RAFOS floats in the frontal jet (Vigan et al., 2000) and by the drifters launched during the TIC-MOC cruise [section 2.3.3]. At depth, velocities are also higher than in the near field, remaining over 0.6 m s^{-1} in the first 600 m of the BMCF.

2.3.3 Along-front description

The drifting buoys and profiling floats deployed on both sides the BMCF converged into the frontal jet and eventually ran eastward along it, providing an approximate Lagrangian description of the frontal system [Fig. 2.8a]. All units launched at the northern flank of the BMC travelled southward with the BC and ran over the northern border of the BMCF, while those deployed in the southern margin remained mostly south, with only one instance temporarily crossing the front to the north [Fig. 2.8a].

The subsurface buoys travelled along the frontal jet with mean speeds slightly over 0.7 m s^{-1}, exceeding 1.6 m s^{-1} at certain intervals and with peak values of 2.0 m s^{-1}. The BMCF is not stationary, fluctuating and undulating during the duration of the cruise, with the drifters and floats changing their trajectory accordingly. Several drifters were trapped by different mesoscale features, which drove them out of the frontal jet [Fig. 2.8b].

The two Apex profiling floats present very different trajectories [Figs. 2.1b and 2.8a]. Float 9027 was deployed in the southern edge of the BMCF, reached the frontal position in three days and moved along the front afterwards. The overall velocity of float 9027, taking into account both the surface and subsurface drift, was around 0.2 m s^{-1}. However, if we only consider the drifting between profiles 20 and 21, when the float remained at the surface, we get a sustained velocity of around 1.5 m s^{-1}. On the other hand, float 9231, which was deployed in the northern side of the BMCF, moved first westward to later loop anticlockwise to end up near its initial position. Float 9231 travelled at low speeds, most of the time less than 0.1 m s^{-1}, reaching maximum values of 0.3 m s^{-1}.

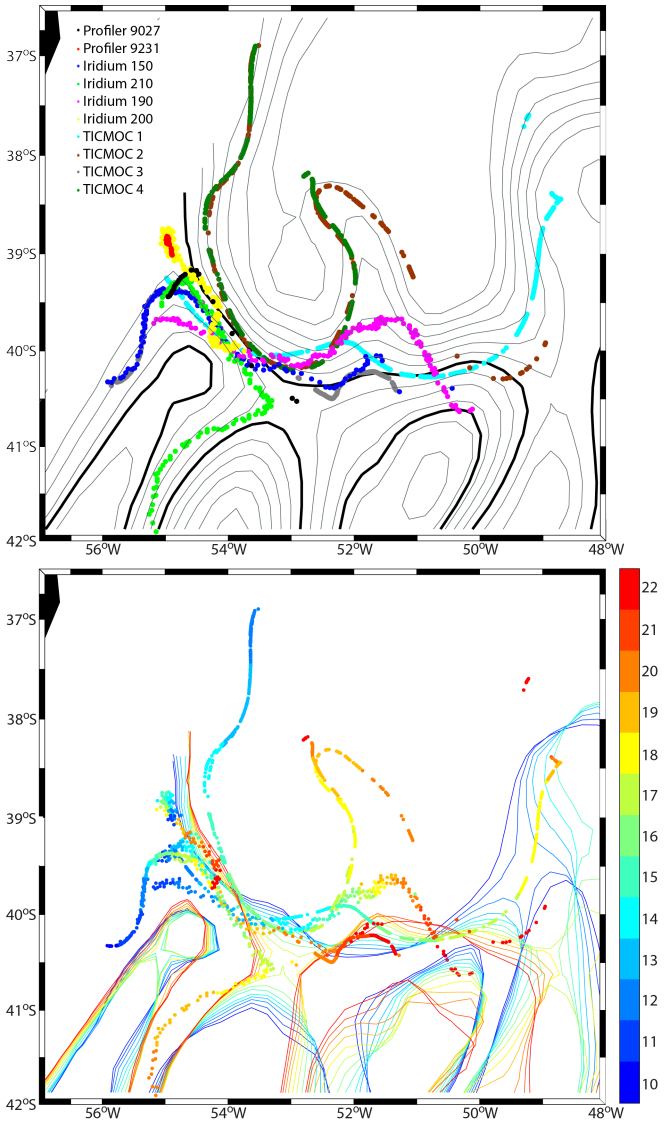

Fig. 2. 8: (a)Trajectories of subsurface drifters and profiling floats over mean ADT contours (from -0.2 to 0.9 m every 0.1 m; grey contours) between the 10th and 22nd March 2015, and position of the SAF and BCF (black contours). (b) Floats positions (dots) and SAF and BCF locations (northern and southern thin lines, corresponding to ADT=-0.05 and 0.3 m, respectively), color-coded by the day of March.

The first 14 profiles of float 9027 covered an area between the SAF and BMCF, in the inner part of the MC, where water properties are homogeneous and there are no subtropical water intrusions [Fig. 2.9]. Between profiles 15 and 17, the float crossed the BMCF and stayed very close or even over the frontal jet, in a band where both MC and BC waters coexist, hence explaining the warm and salty intrusions between 80 and 200 m. Most of the structure is confined to the upper 400 m. For example, in profile 17 there is a salty intrusion at 65 m depth extending horizontally until profile 18, or two intrusions of STMW below 150 m centred in station 19 and stretching 50 km until profile 20. The salty and warm intrusions affecting down to 700 m in profile 20 are remarkable. The water column in profiles 21 and 22 is slightly warmer and saltier than in the previous casts, as the float occupied positions in the border of the SW-AC. During

the along-frontal journey (profiles 15 to 20), the upper 10-20 m are characterized by very low salinity PPW waters, in agreement with the vertical extension of the plume observed in the CTD cross-frontal sections.

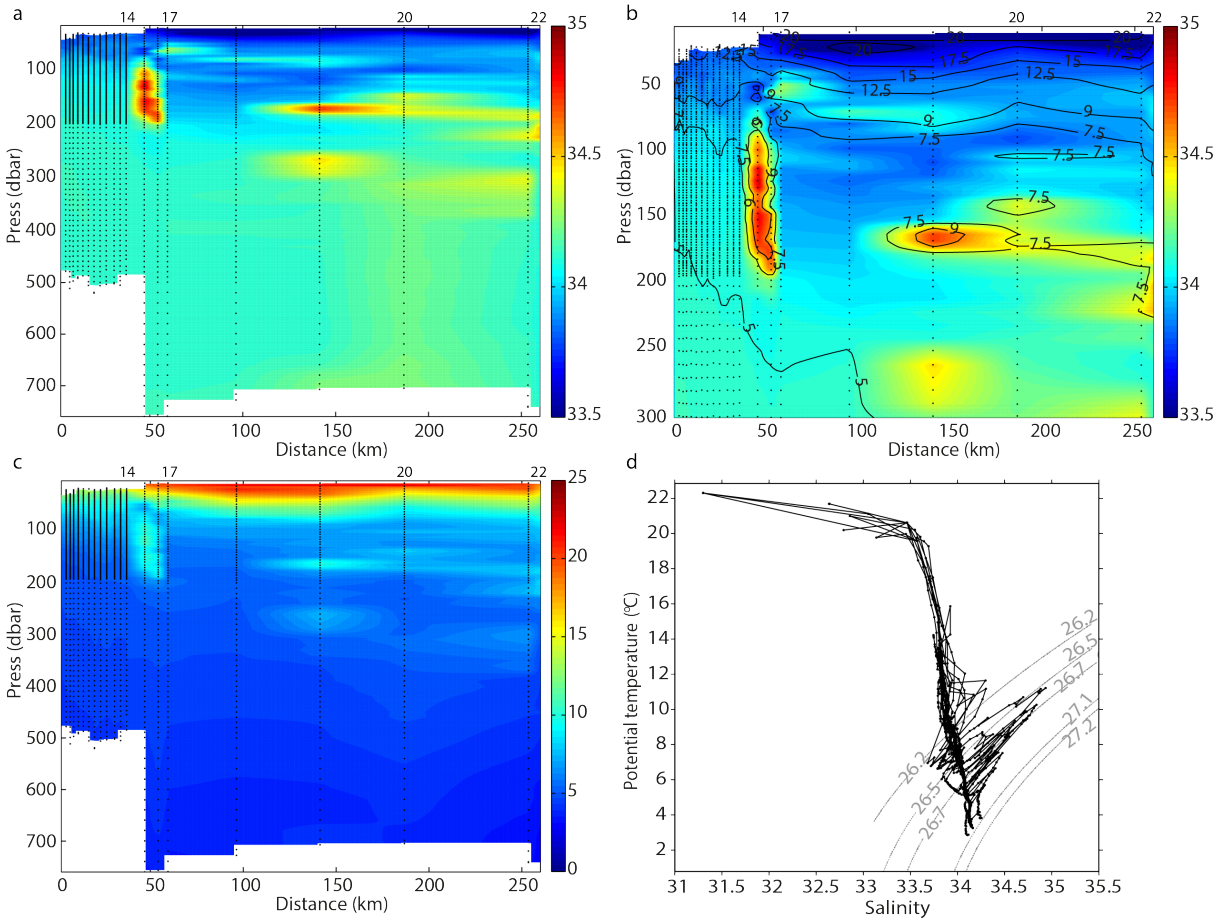

Fig. 2. 9: Vertical distributions of (a, b) S and (c) θ along the path of float 9027, for the upper (a, c) 740 m and (b) 300 m; the contours in panel b represent isotherms. (d) θ-S diagram for the trajectory of float 9027.

On the other hand, float 9231 was deployed in the northern margin of the inner MC just south of the BCF and close to the shelf break, in some sort of stagnation point in the western margin of the frontal system [Figs. 2.1b and 2.8a]. As a consequence, this profile ran a short distance, providing a high-resolution perspective of the area before the collision. The θ structure is very similar to profile 9027 but the S differences are larger [Fig. 2.10]. The upper 40 m present very low salinity SASW followed by a 250-m thick layer of SACW where colder and fresher waters intrude. Below the subsuperface salinity maximum (30-70 m), we find (profiles 1-6 and 8-13) STMW intrusions, with vertical (horizontal) extension of 80 m (8 km). After profile 13, the surface layer of SASW deepens to 60 m. Profile 13 revisited the area between profiles 9 and 10 approximately 4.5 days later. In this second visit, the structure below 300 m remains fairly unchanged but the surface has changed drastically; in particular, the SASW layer is 50 m thick while days before it was only 20 m. Contrary to expectations, considering the proximity to

the shelf, the θ-S diagram does not show the presence of PPW [Fig. 2.10d], though there is a significant presence of SASW. This probably responds to the southern position of the sampling area with respect to the BMCF, far from the main locus of PPW offshore detrainment (Franco et al., 2018).

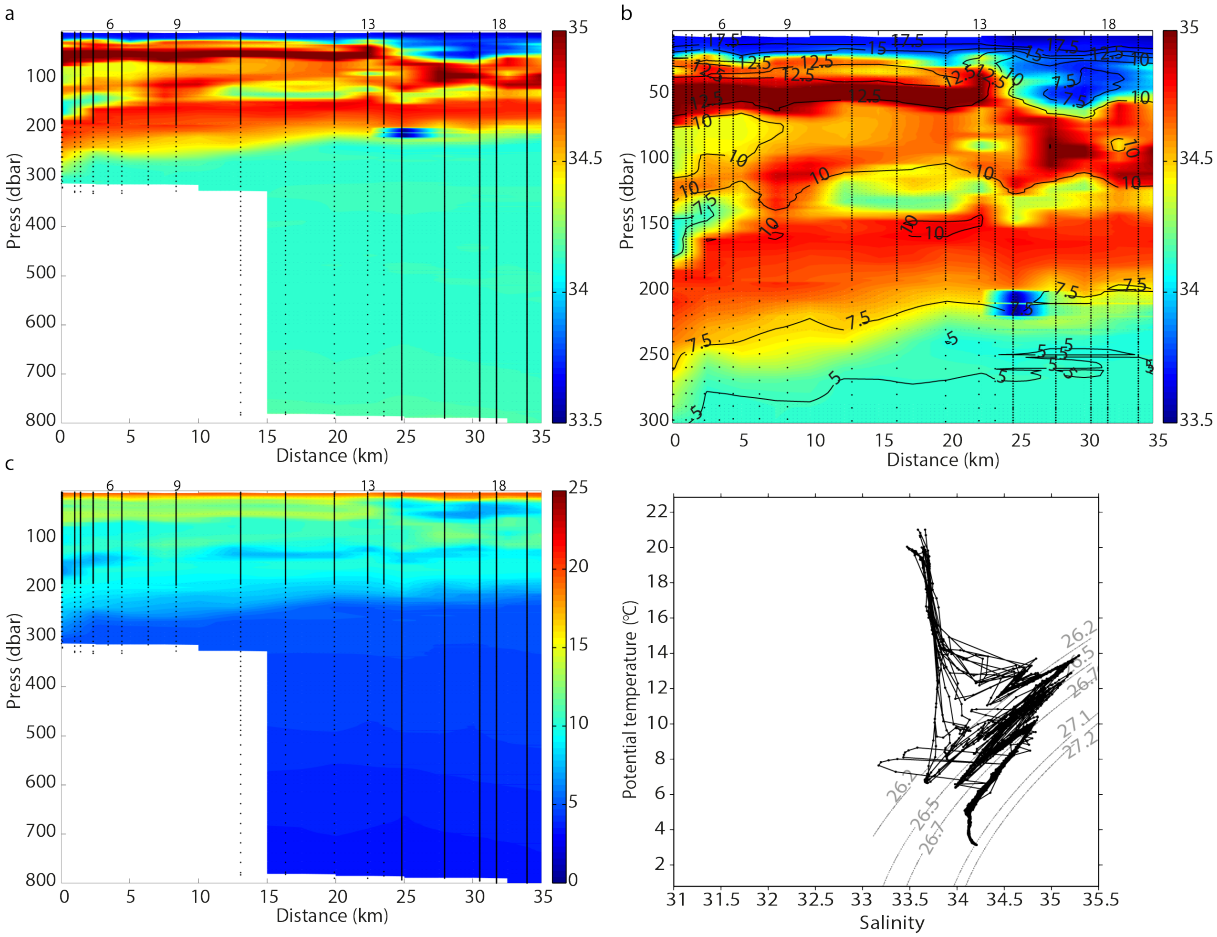

Fig. 2. 10: Vertical distributions of (a, b) S and (c) θ along the path of float 9231, for the upper (a, c) 740 m and (b) 300 m; the contours in panel b represent isotherms. (d) θ-S diagram for the trajectory of float 9231.

2.4 Discussion

2.4.1 Comparison with satellite, reanalysis and climatological data

The satellite, reanalysis and in-situ measurements show good agreement in the surface fields. The comparison between observations and the reanalysis is particularly good, certainly because of the assimilation of in-situ and satellite data. The high-resolution reanalysis data is able to reproduce the PPW on top the frontal jet and matches well the hydrographic SST at each station.

The GLORYS12V1 and WOA13 datasets also provide data at 50 and 69 vertical levels, res-

pectively, which can be compared with the TIC-MOC stations. For this purpose, we consider sections II and VI, with spatial resolutions of 10 and 45 km, respectively [Fig. 2.11], and retrieve the corresponding reanalysis outputs (for the same day of the sampling, 18th March for section II and 14th March for section VI). The major differences are found in section II, where the reanalysis cannot reproduce the thermohaline intrusions shown by CTD data [Figs. 2.12a,c,e]. GLORYS12V1 reproduces well the frontal structure and location, and even the presence of PPW in the surface, but fails at replicating the submesoscale features (despite its horizontal resolution is higher than the CTD data). Regarding section VI, the comparison shows a similar vertical structure in the observations and reanalysis, a simple consequence of the lack of intrusions in this outer section [Figs. 2.11b,d]. In the case of the climatology, the differences with the observations are very large in both sections; clearly, the monthly fields are unable of reproducing the BMC variability.

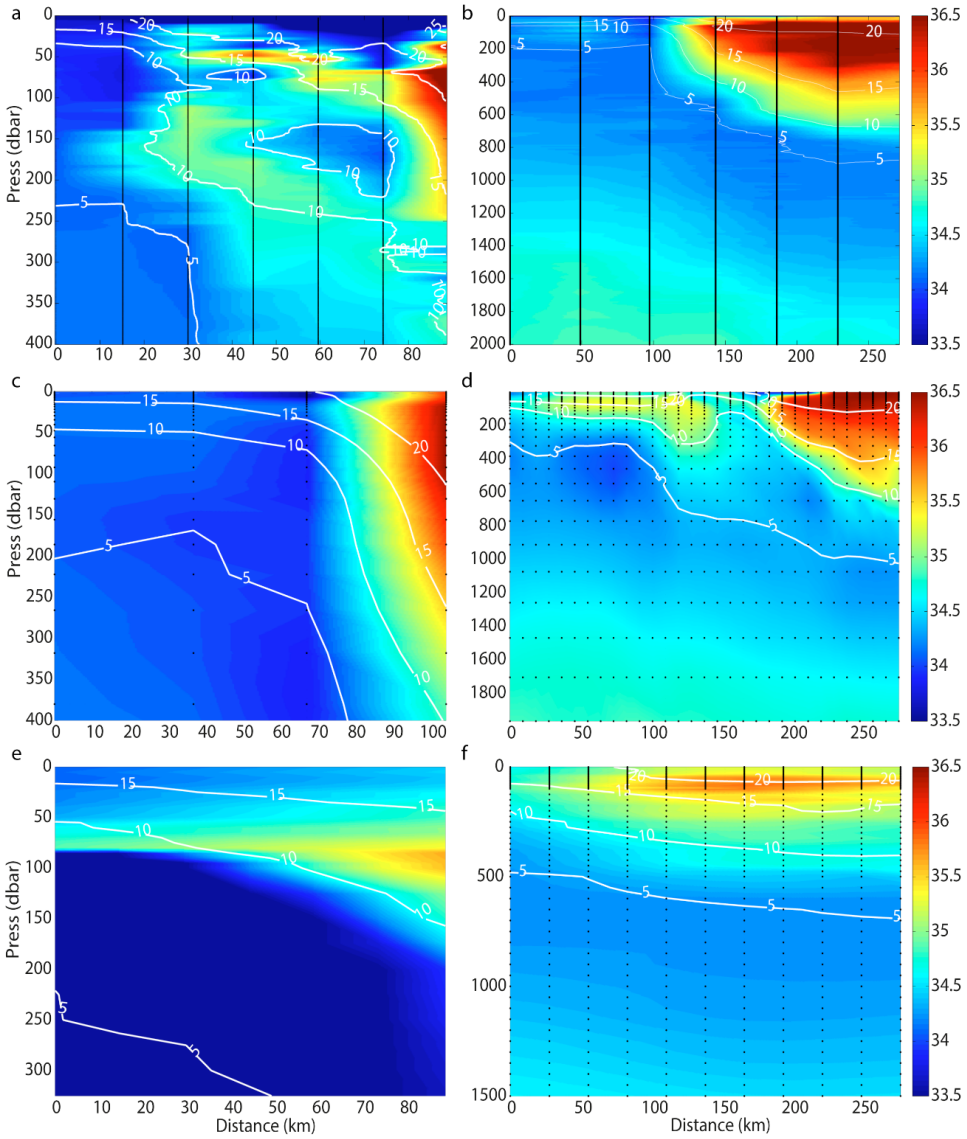

Fig. 2. 11: S (color-coded) and θ (white contours) vertical sections for (a, c, e) section II and (b, d, f) section VI from (a, b) the CTD casts, (c, d) the MERCATOR reanalysis and (e, f) the WOA13 climatology.

Based on these results, we can conclude that the reanalysis simulates correctly the surface structure of the BMC region and its main dynamics such as the BMCF/BCF location and the presence of the PPW plume on top the frontal jet. However, it cannot reproduce the subsurface submesoscale structures, clearly present at the frontal system in the form of thermohaline intrusions. This suggests that GLORYS12V1 dataset is useful in studies concerning surface properties and their variability but is a limited tool to identify and analyse subsurface submesoscale or mixing processes.

2.4.2 Presence of shelf water

Franco et al. (2018) identified the BMC region as the main detrainment point of SASW into the deep ocean, at a rate of about 1 Sv (1 Sv = 10^6 m^3 s^{-1}) for early fall. The position of this off-shelf export is influenced by the location of the BMCF while the local wind regime controls the magnitude of the transport (Combes and Matano, 2018). This explains the large amount of SASW found by Apex-9231, at a position close to both the shelf break and the confluence point. Besides shelf waters, during the TIC-MOC cruise we found river origin waters (PPW, S<32.5) as far as 100-300 km from the river mouth [Fig. 2.12b]. CTD cross-frontal sections show how the RdlP plume becomes thinner as it travels to the east, primarily along the subtropical side of the front. We obtain a similar picture from the GLORYS12V1 monthly-mean (March 2015) data: selecting positions along the track of the plume, we observe a 15-20 m thick PPW/SASW layer extending from the shelf-break to around 400 km [Fig. 2.12].

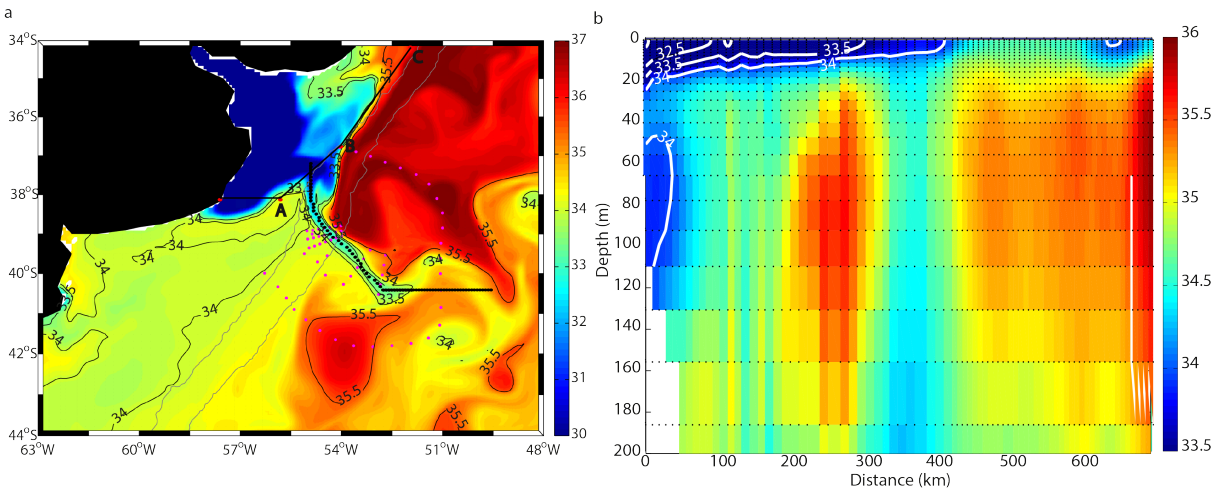

Fig. 2. 12: (a) Mean SSS field for March 2015, as deduced for the reanalysis. The black contours represent the 33.5, 34 and 35.5 isohalines while the grey lines indicate the 200 and 500 m isobaths. Magenta dots are TIC-MOC stations, red dots indicate the points used for the cross-shelf volume balance [Fig. 2.13] and black dots display the locations along the RdlP plume shown in panel b. (b) Salinity vertical section of the first 200 m along the RdlP plume, following the stations shown in panel a.

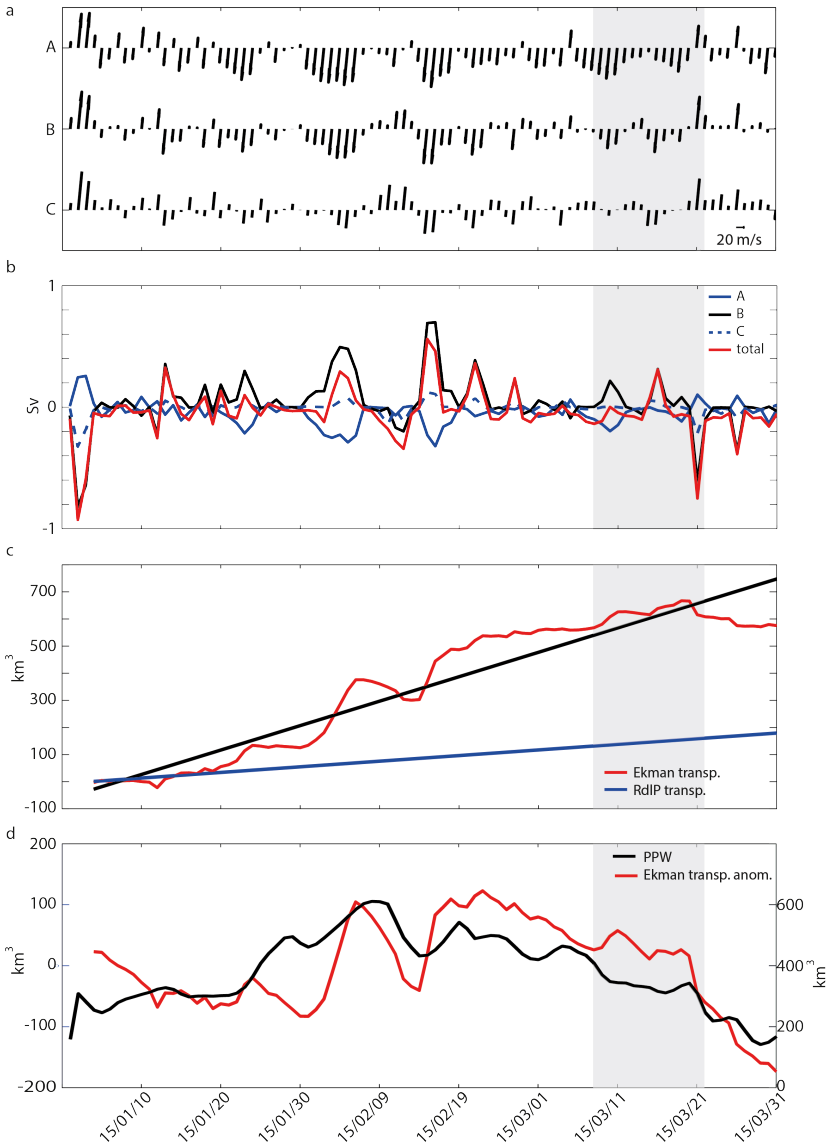

Fig. 2. 13: (a) Daily surface wind vectors from January to March 2015 at points A, B and C in Figure 2.12a. (b) Ekman layer transport at the southern (dashed blue), eastern (black line) and northern (blue line) sections delimited by the coastline and points A, B and C, and the total shelf balance (red line); negative/positive values indicate transports into/out of the shelf area in Figure 2.12a. (c) Off-shelf Ekman transport (red line) and its lineal fit (black line) accumulated starting on January 4 2015, and the accumulated river discharge for this same period (blue line) (km^3). (d) Anomaly of the accumulated Ekman transport determined as the difference between the accumulates off-shelf transport and the lineal fit in panel c (red line) together with the off-shelf volume of PPW in the BMC as determined from GLORYS12V1 data (black line, right axis). The shaded region highlights the cruise period.

Previous studies have suggested that the presence of PPW in the BMC region is mainly controlled by the along-slope wind regime, with shelf-water being exported during periods of north-easterly winds (Combes and Matano, 2014a; Guerrero et al., 2014; Matano et al., 2014). Following Matano et al. (2014), we have analysed the wind regime at three points bounding the RdlP outflow [Fig. 2.13a]. With these winds and considering a mean river discharge of 0.024 Sv, we have calculated the surface (Ekman plus river) export from the shelf between 34^{o}S and 38^{o}S [Fig. 2.13b] for the first three months of 2015. Further, from the reanalysis data, we have

calculated the amount of PPW over the BMC (defined as waters with S<32.5; Piola et al., 2008).

During March 2015 the north-easterly winds prevailed, in agreement with the seasonal wind-patterns (Piola et al., 2008), hence favouring the offshore detrainment of surface shelf waters at a rate that reached almost 0.6 Sv during the peak winds [Fig. 2.13b]. In order to calculate the relation of the off-shelf transport of brackish waters and the amount of PPW over the BMC we follow a simple procedure [Figs. 2.13c,d]. First, we calculate the accumulated off-shelf Ekman transport; we start this summation on January 4 simply because this day is the start of a week of relatively calm winds, which allows assuming that it is a reasonably good time to reset the offshore system; second, we fit a lineal curve to this accumulated offshore transport; third, we calculate the accumulated anomaly as the difference between the actual accumulated transport and the lineal fit; and finally, this accumulated anomaly is compared with the volume of PPW over the BMC.

The premise behind these calculations is that the discharge of the RdlP, because of its extremely large basin (over 3 million squared kilometres), changes at relatively slow (seasonal) frequencies (García and Vargas, 1996). Hence, the river discharge reaches the shelf at a nearly constant rate but it is intermittently exported into the BMC region through the wind pulses. Further, we may assume that the amount of fresh water over the BMC region has some characteristic residence time, which results from the Confluence dynamics. Hence, we may imagine that the rate of removal of surface waters from the BMC region will be approximately constant, which will cause that for each value of RdlP discharge there is a characteristic PPW volume (i.e. if the river water was transported into the BMC at a constant rate then the PPW over the Confluence would tend to this value). The result is that the amount of PPW in the BMC will increase or decrease essentially as a consequence of the intermittent wind-induced export of shelf waters, as confirmed by a correlation value of 0.54 between both time series [Fig. 2.13d].

The above calculations also show that the accumulated river discharge (182 km^3 in 88 days; Fig. 2.13c) is about 4 times less than the amount of surface waters exported from the shelf. This can be interpreted as if the brackish water exported out of the shelf will have one/four parts of fresh/salty waters or, assuming that the environment water has a salinity of 35 psu, a salinity of about 28 psu. Obviously, this water is further diluted with the salty surface offshore waters over the BMC leading to the definition of S<32.5 for PPW. This is confirmed by the fact that the offshore wind pulses account for exports of the order of 100 km^3, which is much less than the average volume of PPW in the region (382.4 km^3).

All these analysis evidence an important cross-shelf exchange of properties along the BMC, such as freshwater, chlorophyll, nutrients and organic matter, which would contribute to the freshening of deep waters and could sustain the elevated primary production of the region (Brandini et al., 2000; Garcia et al., 2004; Romero et al., 2006; Carranza et al., 2017).

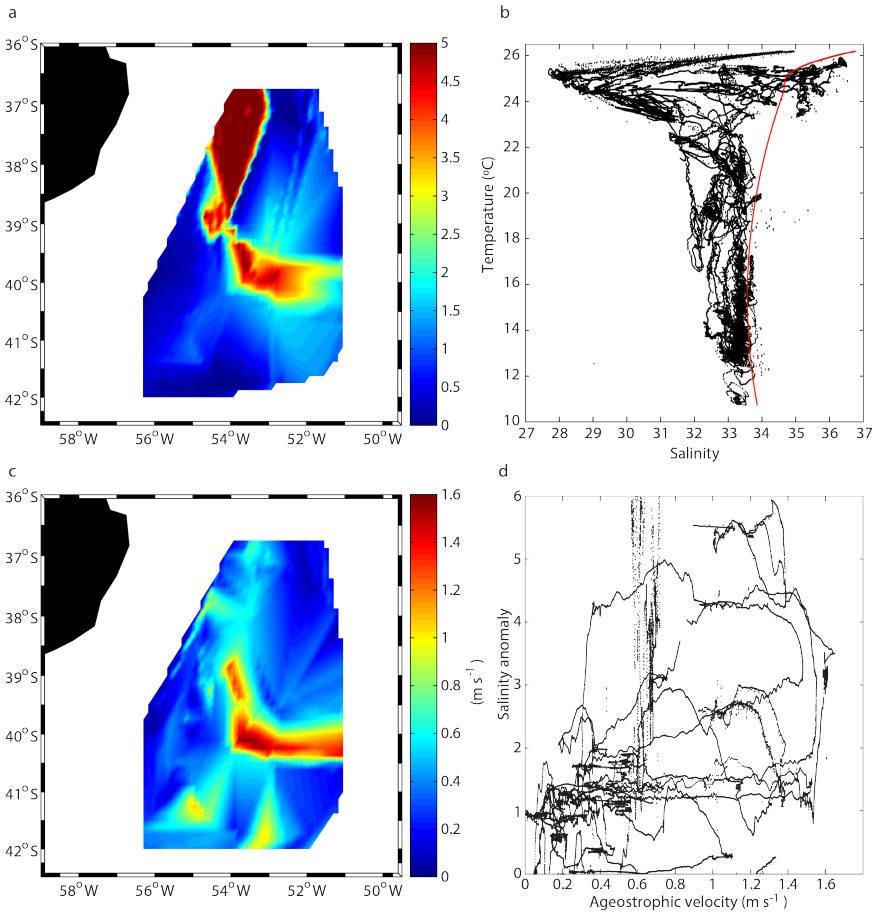

Fig. 2. 14: (a) Surface (negative) salinity anomaly (psu) as determined from the thermosalinograph data. (b) θ – S diagram for the thermosalinograph and surface CTD data (black dots), including the PPW-free best-fit curve (red line). (c) Ageostrophic surface speed field (m s^{-1}). (d) Salinity anomaly – ageostrophic speed relationship.

Finally, we explore the correlation between brackish waters, as reflected by the negative salinity anomaly, and the ageostrophic speeds along the frontal jet [Fig. 2.14]. We expect that the brackish-water filaments will be relatively small and highly intermittent, hence hardly in geostrophic balance. For this purpose, we define the (negative) salinity anomaly variable as the absolute value of the difference between the measured salinity and the value it should have according to its temperature in the absence of PPW waters over the confluence area; the PPW-free values correspond to the best-fit curve to the θ–S diagram formed with thermosalinograph and surface CTD data, after excluding salinity values less than 33.6 [Fig. 2.14b]. Further, the ageostrophic velocity along the ship track is determined as the imbalance between the in-situ VADCP velocity at 20 m depth, which it the first VADCP bin, and the altimetry-inferred surface geostrophic velocity [Fig. 2.14c]. The largest ageostrophic speeds (>1 m s^{-1}) are found along the BCF path, where salinity anomalies are also high [Fig. 2.14a].

From the salinity anomaly – ageostrophic speed diagram, it is possible to infer a positive correlation between both variables [Fig. 2.14 d]. For this calculation we exclude the data points over the BC, where the surface velocity is well reproduced by the altimetry data and the salinity

anomalies are high because of the proximity of the main site of SASW detrainment (Franco et al., 2015). It is worth point that some of the scattering in this last diagram may partly relate to the low spatio-temporal resolution of altimetry, 15 days and 40 km according to Pujol et al. (2016).

2.4.3 BMC variability

Up to now we have mainly presented a static picture of the BMC for March 2015. However, this is an extraordinarily variable region, mostly related to the high-frequency migrations of the BCF, as evidenced by its displacements and meandering during the time of the cruise [Fig. 2.8]. Next, by combining the CTD and APEX-9027 profiles, we explore the temporal variability of the thermohaline properties of the upper ocean (down to about 400-500 m) in approximately one same location at time lapses less than 5 days; in all cases, the separation between both casts is less than 2 km [Table 2.2, Fig. 2.15]. We consider two locations belonging to the near field (CTD49-Apex17 and CTD47-Apex10 pairs) and one location in the outer field (CTD81-Apex 22 pair).

Table 2. 2: Pair of CTD-Apex profiles used to analyse the temporal variability at the frontal area

	Station	Latitude	Longitude	Day	Distance (km)
CTD	49	-54.474	-39.203	2015/03/18	20.7
Apex	17	-54.468	-39.207	2015/03/15	
CTD	47	-54.795	-39.306	2015/03/18	21.9
Apex	10	-54.808	-39.292	2015/03/13	
CTD	61	-52.897	-40.523	2015/03/19	21.4
Apex	22	-52.913	-40.525	2015/03/19	

The largest thermohaline changes are found between CTD49 and Apex17, in a location close and between the BMCF and BCF [Fig. 2.15a]. The Apex17 station is only 0.7 km to the northeast of CTD49, i.e. technically closer to the subtropical waters. However, during the three days between both casts the BCF moved significantly to the north [Fig. 2.8], in such a way that the Apex cast ended up entirely in subantarctic (relatively fresh and cold) waters. In the pair CTD47-Apex10 [Fig. 2.15b], although the time lapse and distance between both profiles is larger than in the preceding pair, the thermohaline variations are much smaller: both profiles display similar subantarctic θ-S properties, belonging to the inner MC [Fig. 2.9]. Finally, the pair in the outer field (Apex22-CTD61, Fig. 2.15c) belongs to a location in the border of SW-AC, separated by 1.4 km and only a few hours. Both profiles show the relatively fresh and cold characteristics of the subantarctic waters. As expected from the short-time interval between the casts, both have the same vertical structure and also share the existence of thermohaline intrusions; nevertheless, these intrusions present some significant differences, the principal one being the absolute value of the deep θ-S anomalies, which are indicative of their small horizontal extent.

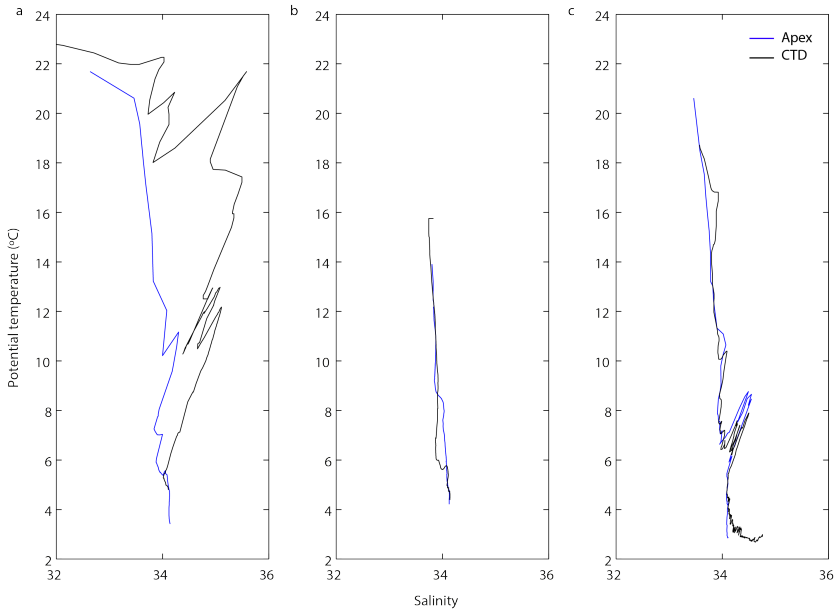

Fig. 2. 15: Comparison of potential temperature-salinity among the closest CTD (black) and APEX 9027 (blue) stations: (a) CTD49-Apex17, (b) CTD47-Apex10, and (c) CTD61-Apex22, corresponding to the three pairs in Table 2.2.

Garzoli and Garraffo (1989) have suggested that the thermohaline variability depends on the sampling position relative to the BCF. Latitudinal changes in the position of the BCF have been observed at annual and semiannual periods while zonal migrations have been detected at higher frequencies (3-5 months) (Ferrari et al., 2017). Superimposed on these low-frequency motions, shorter spatio-temporal changes can happen in weeks or even days (Legueckis and Gordon, 1982). The displacements and meanders of the BCF also affect the salinity structure of the BMC, especially near the 500-m isobath (Provost and Le Traon, 1993), as is the case for the pair CTD49-Apex17. This situation is even more complex during north-easterly winds, when river waters are exported over the frontal jet. On the other hand, the variability is maximum at the subsurface frontal layers, between 100 and 300 m, particularly in the northern side of the front, due to the presence of both mesoscale and submesoscale intrusions (Orúe-Echevarría et a., 2019b).

2.5 Conclusions

The dataset gathered during the TIC-MOC cruise provides a general hydrographic context of the Brazil-Malvinas Confluence (BMC) for late/early summer/fall 2015. During this time, the region is characterized by the convergence of the Malvinas (MC) and Brazil (BC) currents at approximately 39^{o}S, along the 1000 m isobath, and their posterior offshore diversion in the form of a high-velocity frontal jet. The southern position of the BMC over the shelf break responds to its inter-annual variability (Olson et al., 1988; Wainer et al., 2000; Goni and Wainer, 2001). The Subantarctic Front (SAF) only reached 40^{o}S, reflecting the exceptional southern position of the

front in 2014-2015 (Ferrari et al., 2017). The confluence of the two western boundary currents brought about numerous mesoscale features, the most notorious ones being an intense anticyclonic eddy at 41^{o}S-55^{o}W and a cyclonic ring at 41.5^{o}S-51.4^{o}W. This general surface overview is well captured by both the satellite images and the eddy-resolving Mercator reanalysis.

Overall, the southern margin of the BMC front is dominated by fresh, cold and nutrient-rich Malvinas waters, whereas the northern region is depicted by warmer, saltier and nutrient-poor subtropical waters advected within the BC. The frontal region is characterized by an abrupt transition in almost all sampled properties – potential temperature, salinity, dissolved oxygen, inorganic nutrients – and by the presence of intense eastward velocities. The BMC frontal system is approximately normal to the slope, with the less dense BC waters overriding heavier MC waters; at the front, the subantarctic waters are diverted offshore while simultaneously penetrate northward under the subtropical waters.

The CTD vertical sections and profiling floats have reveal the complex spatial structure of the frontal area, with thermohaline intrusions on both sides the front, being less common as the front flows eastward, where it is completely developed and has a sharper structure. These data also reveal the presence of important amounts of brackish shelf water on top the frontal area, which is related to the along-shelf wind regime. These surface waters reach maximum eastward velocities, up to 1.0 m s^{-1}, which are not in geostrophic balance.

Acknowledgments

We would like to thank captain, officers and crew of the R/V Hespérides and the scientific and technical teams for their support and indispensable help during the TIC-MOC cruise. We acknowledge support from the Spanish Government through grants CTM2011-28867 (TIC-MOC Project) and CTM2014-56987-P (VA-DE-RETRO Project) and through the funding of PhD scholarships for D.O.E. (FPU2013-02884), C.H. (CSIC JAE-Predoc program), S.R.G. (BES-2012-055970) and I.V.C. (BES- 2015-071314). In situ measurements of TIC-MOC cruise are available at Pelegrí et al. (2018). Satellite altimetry and GLORYS12V1 data are available at Copernicus Marine Environment Monitoring Service (CMEMS, http://marine.copernicus.eu/), and SST AMSR are produced by Remote Sensing Systems through the sponsoring of the NASA AMSR-E Science Team and the NASA Earth Science MEaSUREs Program (www.remss.com). Climatological fields are available at NOAA's National Centers for Environmental Information World Ocean Database 2013 (https://www.nodc.noaa.gov/OC5/WOD13/).

Supplementary materials

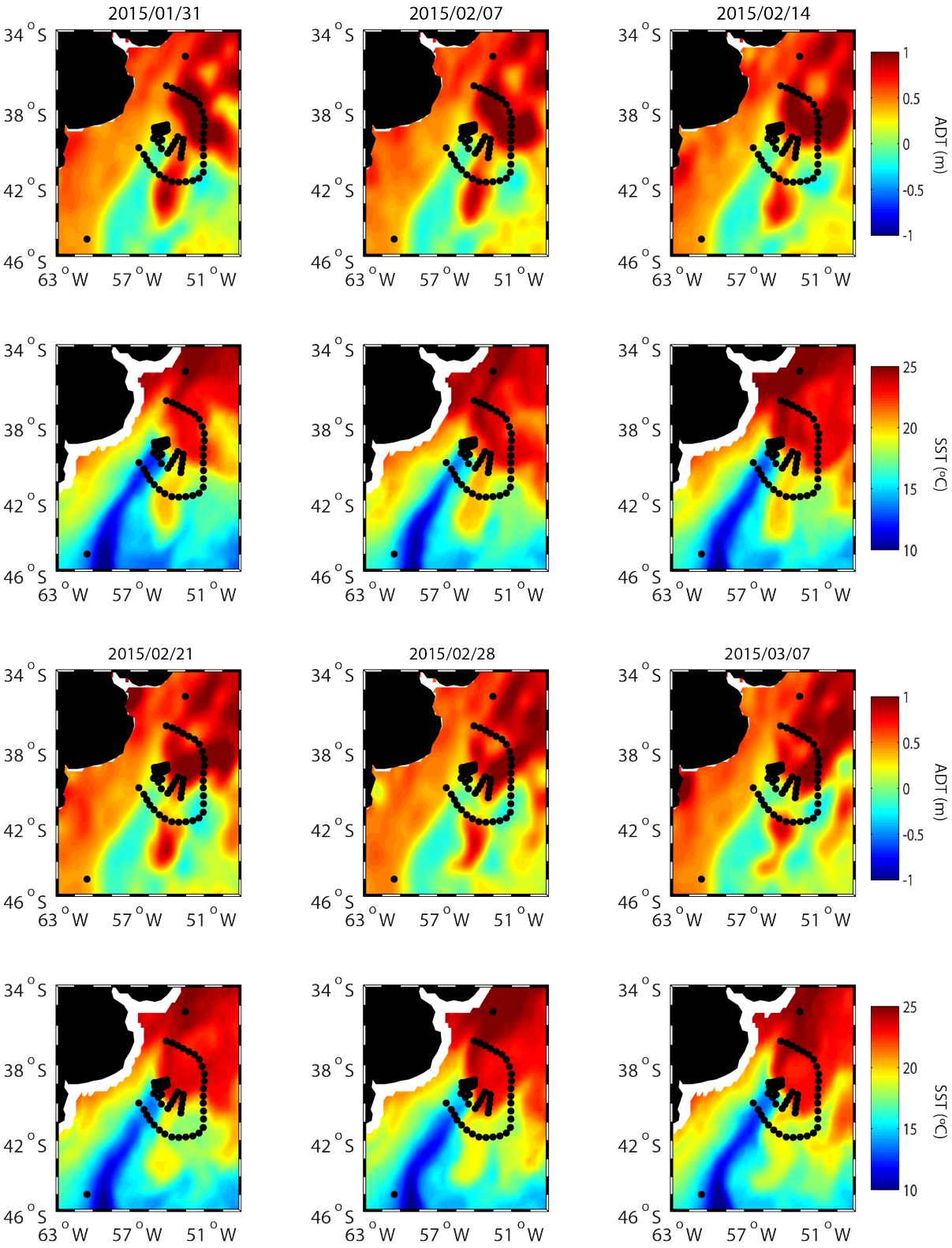

Fig. S.2. 1: Evolution of the ADT and SST fields from late January to early March 2015 in the BMC. Black dots indicate the position of the TIC-MOC hydrographic stations.

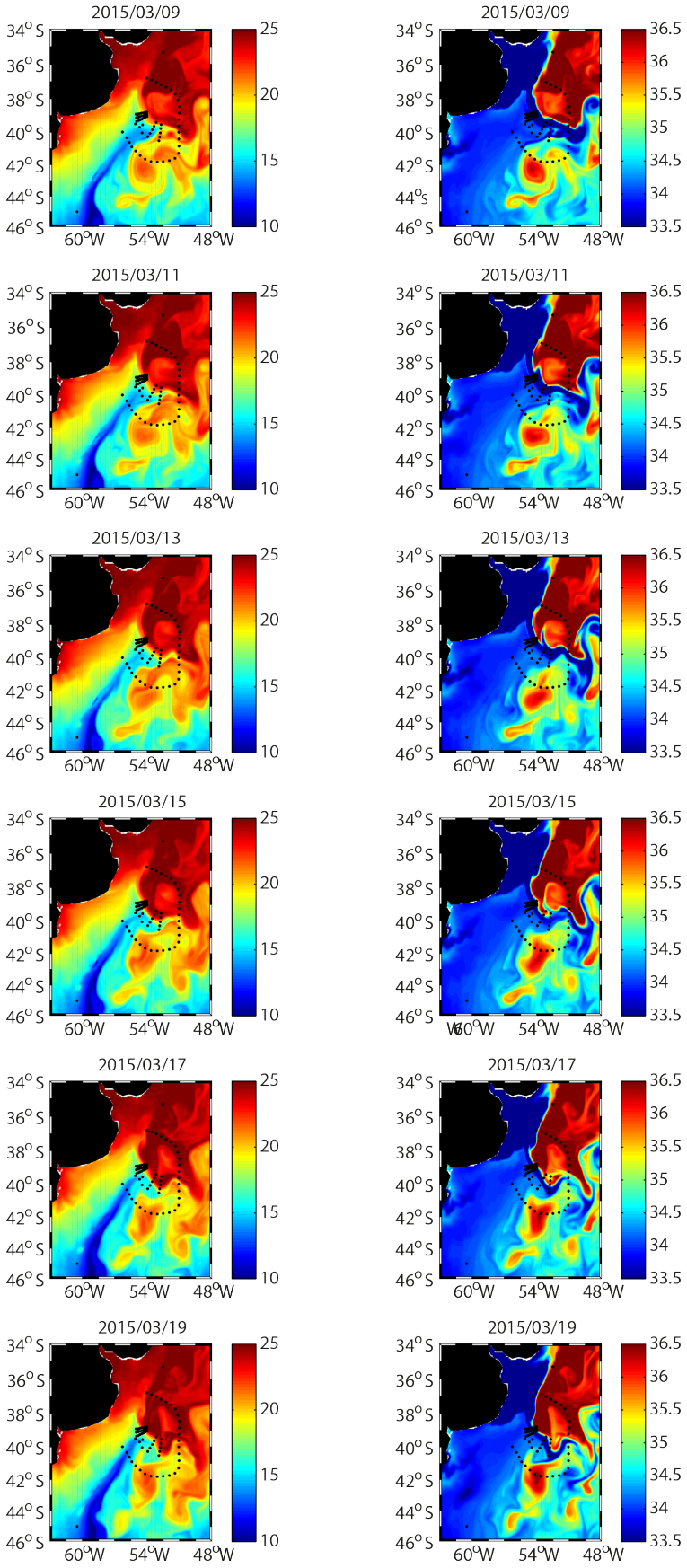

Fig. S.2. 2: Evolution of the SST and SSS fields during the TIC-MOC cruise as deduced from the reanalysis data. The black dots indicate the position of the TIC-MOC hydrographic stations.

Chapter 3

Inverse modelling the Brazil-Malvinas Confluence

Orúe-Echevarría, D., Pelegrí, J. L., Machín, F., Hernández-Guerra, A., and Emelianov, M.
Journal of Geophysical Research: Oceans, (2019), 124, 527-554

Abstract

The Brazil-Malvinas Confluence arises from the frontal encountering of the subtropical Brazil Current (BC) and subantarctic Malvinas Current (MC). It displays a complex regional circulation that is accompanied by mesoscale features and thermohaline intrusions. Here we combine altimetry and cruise data to describe the circulation pattern in the upper 2000 m at two spatial scales encircling the frontal system. The major regional features appear south of the Confluence latitude at 39-40^{o}S: (a) a relatively weak MC near (41^{o}S, 56^{o}W) (28.3 $\pm$ 1.4 Sv) followed by its cyclonic retroflection, (b) an intense subtropical anticyclone (59.3 $\pm$ 10.7 Sv) that replaces the BC overshoot, and (c) a very intense subantarctic inflow (78.9 $\pm$ 13.7 Sv) near 53^{o}W that is maintained through both an upstream (near 42^{o}S) earlier diversion of the MC and the cyclonic recirculation of the flow exiting east along the Confluence. North of the Confluence, the BC provides a net input of 30.8 $\pm$ 12.0 Sv (29.1 $\pm$ 8.3 Sv along the slope). The southern inflow splits nearly equal between barotropic and baroclinic contributions while the entire northern flow is essentially baroclinic. These northern and southern inputs add to an eastward along-front transport of 109.7 $\pm$ 15.1 Sv, with significant contribution of highly-oxygenated, relatively fresh Subantarctic Mode and Antarctic Intermediate Waters (58.7 $\pm$ 5.6 Sv). The regional circulation experiences substantial temporal variability, with southern waters flowing into the BMC through along-slope and interior pathways and partly recirculating within the subtropical South Atlantic gyre.

3.1 Introduction

An outstanding regional feature in the world ocean is the collision of the Brazil and Malvinas Currents (BC and MC), two major western boundary currents that carry waters of subtropical and subantarctic origin. The outcome of this encounter is a very intense thermohaline frontal system, the Brazil-Malvinas Confluence (BMC), with possibly the highest temperature horizonal gradients in the open ocean. The characteristics of the BMC, as for any frontal system, will depend on the relative effect of the advective and diffusive processes: the intensity of the impinging currents, as the element that brings together waters with contrasting characteristics, and the cross-frontal exchange, as the process that tends to dilute the differences in water properties.

Current descriptions of the BMC circulation pattern rely on remote sea surface temperature (SST) and altimetry data, hydrography and velocity data from shelf and slope moorings, and relatively low-resolution hydrographic data from regional cruises. The BMC mean position is about 38^{o}S, with a seasonal cycle of nearly 3^{o} along the continental shelf break, reaching its northernmost position during austral winter (Gordon and Greengrove, 1986; Goni and Wainer, 2001; Saraceno et al., 2004; Goni et al., 2011). The MC runs north along the Argentinean slope until the BMC, where it sharply turns south as the Malvinas Return Current (MRC) (Piola et al., 2013) before finally flowing east at about 45^{o}S (Peterson and Whitworth, 1989). The BC also follows close to the slope until the BMC, where it separates from the continent and continues at the eastern side of the MRC, drawing a loop known as the Brazil Current Overshoot (BCO) (Saraceno et al., 2004). Parts of the MRC and BCO continue eastward at about 40^{o}S as the South Atlantic Current (SAC) while other portions recirculate north to feed back the latitudinal flows into the BMC (Stramma and Peterson, 1990).

Several studies have analysed the mean intensity and variability of the MC and BC. Early estimates of the MC – assuming the current is in geostrophic balance – ranged between 5 and 15 Sv (1 Sv = 10^{6} m^{3} s^{-1} $\cong$ 10^{9} kg s^{-1}) (Gordon and Greengrove, 1986; Garzoli, 1993). However, these estimates did not consider a substantial barotropic contribution. Studies that combine hydrographic or altimetry data with direct current measurements have indeed reported higher transports, in the 35-60 Sv range (Peterson, 1992; Saunders and King, 1995; Vivier and Provost, 1999a; Spadone and Provost, 2009). Artana et al. (2018) combined 25 years of altimetry and mooring data to obtain a transport of 37.1 $\pm$ 6.6 Sv, with several instances of transports greater than 50 Sv. In contrast, most of the mean BC transport is baroclinic (Matano et al., 2010), so different geostrophic calculations have provided more consistent numbers. The BC volume transport generally increases with latitude, as a consequence of water recirculation within the subtropical gyre: 10 Sv at 24^{o}S (Stramma, 1989), 20-30 Sv at 32^{o}S (Zemba, 1991; Garzoli et al., 2013; Schmid, 2014) and 20-40 Sv at 38^{o}S, close to the BMC (Gordon and Greengorve, 1986;

Garzoli and Garraffo, 1989; Garzoli, 1993; Maamaatuaiahutapu et al., 1998; Piola and Matano, 2001).

Contrasting with the above extensive descriptions of the MC and BC, there are fewer studies on why and how the BMC frontal system becomes unstable and, particularly, on how this instability leads to cross-frontal exchange. At the locus of the collision, the BMC generally appears as one single frontal system, commonly named BMC front; on the leeside of the encounter, however, there are two well-differentiated fronts: the Subantarctic Front (SAF), as the northernmost front associated to the Antarctic Circumpolar Current (Orsi et al., 1995; Artana et al., 2016), and the Brazil Current Front (BCF), which sets the southern limit of the BC (Peterson and Whitworth, 1989). The latitude and longitude of these fronts changes continuously in time, at scales that vary from weeks to years. Several recent studies have identified the existence of two opposite regimes in the BMC – named weak and strong Malvinas flow – which are expressed in terms of the intensity of the along-slope MC near 41^{o}S (Artana et al., 2018; Ferrari et al., 2017, Paniagua et al., 2018). During the weak Malvinas regime, the SAF does not reach 41^{o}S over the slope, the BCF overshoots as far as 44^{o}S and the eddy kinetic energy (calculated at time scales less than 20 days) increases; during the strong Malvinas regime, the SAF and BCF meet near 39^{o}S along the slope, the BCO breaks down as an isolated anticyclone, and the eddy kinetic energy decreases. Despite this useful idealization, the time series of sea-surface altimetry show that the actual state at any time is quite complex (Ferrari et al., 2017), some sort of combination of both longitudinal and latitudinal dipoles (and even tripoles) that results in a highly variable and difficult to interpret pattern of mesoscale and regional recirculations.

Our lack of understanding of the processes that control the patterns of regional circulation becomes even more evident when we attempt to describe those processes that lead to net exchange across the frontal system. These include the latitudinal motions of a myriad of mesoscale features of both signs (Legeckis and Gordon, 1982; Olson et al., 1988; Lentini et al., 2006; Saraceno and Provost, 2012; Mason et al., 2017), and the subduction and thermohaline intrusions of subantarctic and subtropical mode waters (Gordon, 1981; Provost et al., 1999; Sato and Polito, 2014). This is relevant both regionally and globally, as the outcome of the horizontal and vertical processes at the BMC is a substantial transformation of those water masses that will ultimately flow to the North Atlantic Ocean as the returning limb of the Meridional Overturning Circulation (MOC) (Garzoli and Matano, 2011).

The purpose of this study is to produce a detailed portrait of the frontal structure and associated surface and subsurface circulation patterns in a relatively small region encompassing the BMC [Fig 3.1], placing this snapshot in perspective with the frontal evolution at time scales of months. We aim at describing the specific state at the time of the cruise, not only identifying the associated circulation patterns but also exploring what their complexity tells us about the

frontal evolution and dominant processes. For this purpose, we combine high-resolution hydrographic and velocity data in the upper 2000 m, from a cruise carried out in March 2015, with velocity time series for the along-slope MC at about 41^{o}S (Ferrari et al., 2017; Saraceno et al., 2017; Paniagua et al., 2018) and remote-sensing altimetry and temperature data over the entire region. The baroclinic and barotropic water mass transports are calculated using inverse models at two different spatial scales: frontal area and confluence region. The frontal area focuses on the flow at the frontal system itself while the confluence region is used to describe the characteristics of the impinging BC and MC, as well as the MRC and BCO.

The structure of the article is as follows. The cruise and remote sensing data are introduced in Section 3.2, and the fundamentals and application of the inverse model are presented in Section 3.3. Section 3.4 shows the surface geostrophic velocity fields and the hydrographic properties along the frontal and confluence perimeters, and Section 3.5 presents the velocities and transports into or out of the frontal and confluence domains as deduced with the inverse model. In Section 3.6 we compare the velocity fields as sampled with the ship and calculated with the inverse model, provide our best estimate of the transports associated with the main flow patterns, and assess the water transformations at the frontal system. We conclude in Section 3.7 with some remarks about what we have learnt and what yet remains unknown regarding the mean flow structure in the BMC.

3.2 Data

3.2.1 TIC-MOC cruise

The TIC-MOC cruise was carried out onboard the R/V Hespérides between 8 and 22 March 2015 [Fig 3.1]. The positioning of the hydrographic stations relative to the BMC was done using near real-time remote sensing altimetry and temperature data (see next section), as well as one-week-window daily forecasts of sea-surface absolute dynamic topography (ADT) and temperature, salinity and velocity at 0, 92, 453 and 1062 m, as provided by the Mercator Ocean PSY4QV2R2 operational model, with 1/12^{o} resolution (https://www.mercator-ocean.fr/). A full description of the cruise methods and sampling is presented by Orúe-Echevarría et al. (2019) and the entire dataset is available at Pelegrí et al. (2018), a summary follows.

A total of 66 hydrographic stations were done in the BMC, with 19 stations bounding the inner part of the front (frontal area) and 28 stations delimiting a larger and more external domain (confluence region) [Fig. 3.1]. Conductivity-temperature-depth (CTD) data were obtained with a SeaBird 911 Plus multi-parametric probe, with duplicate salinity and temperature sensors in order to detect any possible drift, and dissolved oxygen (DO) was sampled with a SBE-43 sensor and calibrated through Winkler titration of a selected number of samples.

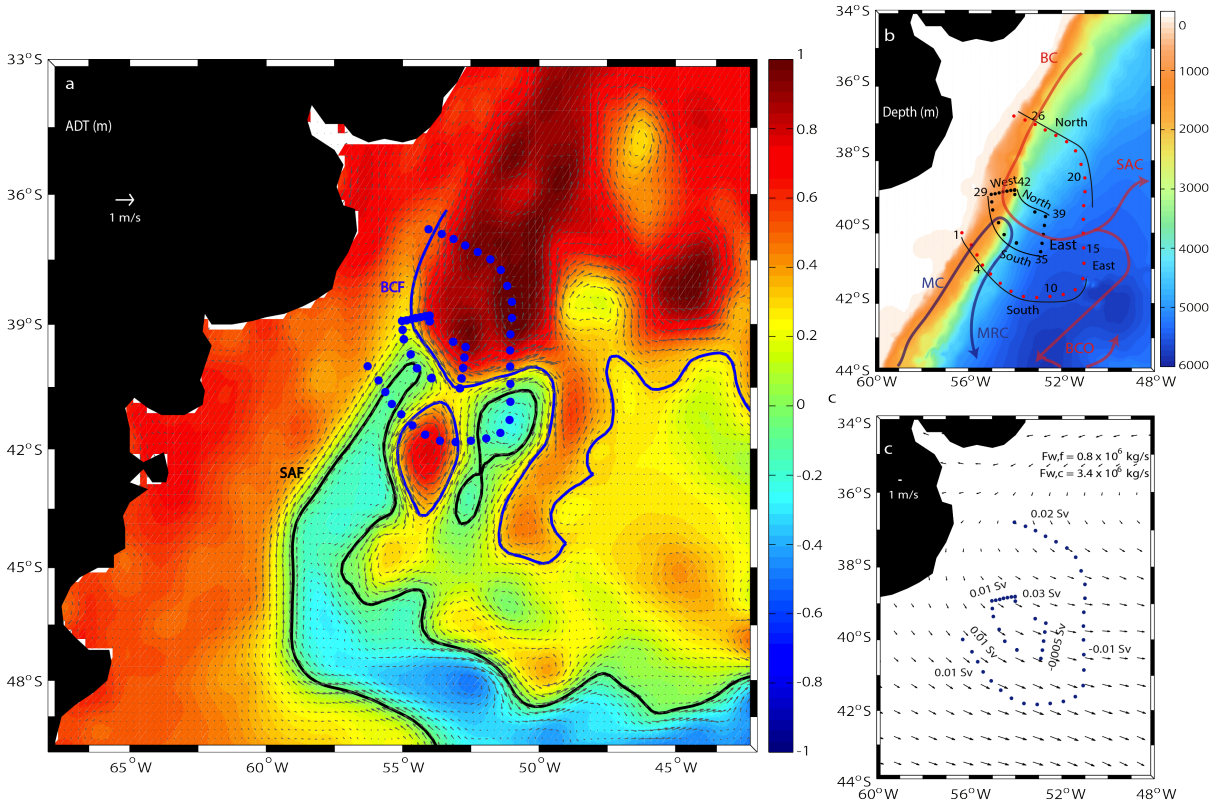

Fig. 3. 1: (a) Mean sea-surface ADT (m) in the south-western Atlantic Ocean for March 2015 and mean surface geostrophic velocities (black arrows) together with the location of the Brazil Current Front (BCF, blue line) and the Subantarctic Front (SAF, black line), ADT values for each of the fronts as in Ferrari et al. (2017). The positions of the hydrographic stations are shown as blue dots.b) Location of the hydrographic stations on top of the bathymetry (GEBCO 2008; color-coded, in m), distinguishing those stations used for the confluence (red dots, stations 1-28) and frontal (black dots, stations 29-47) models; the north, south, east and west positions of each perimeter are shown for reference. The predominant paths of the BC and MC, at the time of the cruise, are sketched.(c) Mean March 2015 sea-surface winds in the study area; the sea-surface Ekman transports (Sv) through each portion of the perimeter are indicated, with positive values denoting transfer out of the domain. The net freshwater fluxes for the frontal ($F_{w,f}$) and confluence ($F_{w,c}$) domains are shown in the upper right, with positive values denoting net transfer towards the ocean.

The frontal area is aligned with the frontal system, with a near-rectangular shape approximately 250 km x 100 km. The mean distance between stations is 30 km, although it varies from 15 km in the western section to 90 km between the two most-spaced northern stations; the frontal stations reached down to either the seafloor over the upper slope or 400 m in the open ocean. The confluence stations follow a nearly circular perimeter, with diameter about 500 km, closed to the west by the continental slope. These stations stretched down to the seafloor over the upper slope or a minimum depth of 2000 m in the open ocean, with the distance between each pair of stations close to 45 km everywhere. For all stations, conservative temperature (θ), absolute salinity (S) and neutral density (γ^n) are calculated with 2 dbar vertical resolution.

Horizontal velocity profiles were obtained at each hydrographic station through a lowered acoustic Doppler current profiler (LADCP). Due to the flooding of the upper-looking LADCP, in most stations the velocity was recorded using only the 300 kHz downward looking LADCP,

for 4-m vertical bins. Additionally, throughout the cruise, the vessel-mounted ADCP (VADCP) continuously sampled the horizontal currents between about 20 and 700 m, using 8-m depth bins.

3.2.2 Supplementary datasets

We use remote-sensing altimetry data in order to obtain surface velocities and locate the surface fronts. The daily ADT and corresponding surface geostrophic velocities come from the DUACS multi-satellite $1/4^{o}$ gridded delay-time product (Pujol et al., 2016), as provided by the Copernicus Marine Environment monitoring service (http://marine.copernicus.eu/). The mean March 2015 ADT field characterizes the surface flow at the time of the cruise and delimits the position of the SAF and BCF using the ADT definitions in Barré et al. (2011) and Ferrari et al. (2017) – contours of +0.30 m for the BCF and -0.05 m for the SAF. We also use Level-3 SST images from the Advanced Very High Resolution Radiometer (AVHRR) on National Oceanic and Atmospheric Administration (NOAA) satellites, with a spatial resolution of 4 km (https://data.nodc.noaa.go).

We obtain sea-surface wind stress and evaporation-precipitation (E-P) data (spatial resolution 0.75^{o} x 0.75^{o}) from the European Centre for Medium-Range Weather Forecasts, (https://www.ecmwf.int/). From the wind stress we calculate the Ekman transports T_{E} into or out of either the frontal or confluence domains; similarly, from the E-P values we compute the freshwater transports F_{w} for either dominion [Fig. 3.1c]. Additionally, the March 2015 monthly-mean freshwater discharge by La Plata River is estimated at 14,600 $\mathrm{m^3\ s^{-1}}$, as reported by the Argentinean hydrological service (Goniadzki et al., 2015).

We also consider Argo float trajectories from 2005 to 2018 provided by the Coriolis Global Data Acquisition Center of France (http://www.coriolis.eu.org/). These floats travel at 1000 m and, every 10 days, perform a CTD profile between 0 and 2000 m and transmit these data and position.

Finally, our analysis will benefit from recent reports of velocity time series during 2014-2015 at several cross-slope moorings near 41^{o}S, which sampled the along-slope MC precisely at the same location of our southwestern hydrographic stations (Ferrari et al., 2017; Paniagua et al., 2018). The mooring data is available at Saraceno et al. (2017).

3.3 Inverse model

3.3.1 Model formulation

Under the assumption of a conservative ocean in hydrostatic and geostrophic balance, inverse box models use direct hydrographic observations along the perimeter of an enclosed water vo-

lume in order to estimate the ocean circulation (Wunsch, 1978, 1996). Mass conservation is the minimum requirement, although conservation of other physical and biogeochemical properties is often invoked.

The closed volumes for the frontal and confluence models are shown in Figure 3.1. The frontal area reaches down to only 400 m and is completely locked by the hydrographic stations; the confluence domain reaches much deeper, down to 2000 m, but is closed to the west by the continental slope. The underlying assumption for the confluence model is that the flow over the slope runs approximately along isobaths, a coastal constrain that holds for poorly stratified flow in geostrophic balance (e.g. Lee et al., 2001); this is consistent with the nearshore orientation of the BCF and SAF, which run parallel to the shelf break while crossing the confluence perimeter. The only exception is the freshwater discharge from La Plata River, which is assumed to enter entirely through the north-western boundary of the confluence region.

We divide the water column in horizontal layers and impose mass and absolute salinity conservation, within uncertainties, for each layer and the entire water column. Between each pair of stations, the horizontal velocity normal to the hydrographic section is the linear addition of the barotropic or reference level velocity (b) and the baroclinic or relative contribution (u_r), the latter inferred from temperature and salinity data through the thermal wind equation:

$$u(s,z) = \frac{g}{\rho_0 f}\int_{z_r(s)}^{z} \frac{\partial \rho}{\partial s} dz + b(s) = u_r(s,z) + b(s) \tag{3.1}$$

where $(n, s, z$ are the coordinates – n pointing out from the domain, s along the perimeter in the counterclockwise direction and z in the vertical direction – with corresponding velocity components (u,v,w); z_r is the depth of the reference level, ρ is the water density (ρ_0 is a depth-mean density value), g is the gravity acceleration and f is the Coriolis parameter.

Additionally, we incorporate the mean March 2015 freshwater and Ekman transports to the uppermost layer, in contact with the atmosphere. Either quantity is calculated as a measured value plus a transport adjustment determined by the model, that is, $T_E = \widehat{T_E} + \delta T_E$ for the Ekman transport and $F_w = \widehat{F_w} + \delta F_w$ for the freshwater input. Part of the freshwater flux corresponds to precipitation minus evaporation, 34 x 10^{-4} Sv for the confluence region and 8 x 10^{-4} Sv for the frontal area; the contribution from La Plata River is 14.6 x 10^{-3} Sv, which adds entirely to either domain through the shelf break. Finally, the Ekman transports along the perimeter of the domain amount to 0.20 Sv and 0.045 Sv for the confluence and frontal domains, respectively.

The mass and property conservation equations for each layer take the following form:

$$\int\int_{A_v} \rho C(u_r + b)dsdz + A_h \left[\overline{K}\frac{\overline{\partial \rho C}}{\partial z} - \overline{w\rho}\,\overline{C}\right]\Bigg|_{bot}^{top} + \delta(C)F_w + CT_E = 0 \qquad (3.2)$$

where A_h and A_v respectively represent the horizontal and vertical areas enclosing an isoneutral, C is the property concentration per unit mass (C = 1 for mass), K and w respectively are the dianeutral diffusion coefficients and velocities, and $\delta(C)$ is a delta function equal to one when the property is mass and zero otherwise. The overbars in the second term represent mean values at the horizontal areas enclosing the isopycnal layers. The integral accounts for horizontal advection through the lateral limits of the domain, the second term quantifies vertical advection and diffusion (calculated at the upper and lower horizontal areas englobing the isopycnal layer, taken as zero at the sea surface and the bottom reference isoneutral) and the last two terms represent the freshwater and Ekman transport terms (entirely in the uppermost isopycnal layer, elsewhere being zero). Each isoneutral or depth level is limited laterally by either the perimeter of the domain or the continental slope, with the intersection of the isoneutrals and seafloor being determined from the World Ocean Database 2013 (https://www.nodc.noaa.gov/OC5/WOD13/). To improve the conditioning of the model, the salinity equation is set in terms of anomalies, defined as the difference between the actual value and the layer salinity average (McIntosh and Rintoul, 1997; Ganachaud, 2003a).

In the case of the frontal model, we define five layers using pressure levels (0-50, 50-100, 100-200, 200-300, 300-400 dbar), while in the confluence box we distinguish six neutral density layers, selected on the basis of previous studies (Ganachaud, 2003b; Jullion et al., 2010) [Table 3.1]. Although isoneutral layers appear as a more natural selection, this is unsuitable for the frontal area simply because the densest isoneutral in the subtropical side (about 26.8 kg m^{-3}) reaches very shallow in the subantarctic waters, only down to some 70 m. In contrast, the deepest isoneutral in the confluence region (27.81 kg m^{-3}) everywhere extends deeper than about 1400 m.

Table 3. 1: Water masses in the confluence model, indicating the corresponding neutral density boundaries and model layers (STMW: Subtropical Mode Water; SAMW: Subantarctic Mode Water; AAIW: Antarctic Intermediate Water; UCDW: Upper Circumpolar Deep Water)

Water mass	Neutral density (γ^n, kg m^{-3})	Layer
Surface water	Surface - 26.2	1
STMW	26.2 - 26.8	2
SAMW	26.8 - 27.2	30
AAIW	7.2 - 27.55	4
UCDW	27.55 - 27.81	5-6

The above partitioning results in six/seven domains for the frontal/confluence models (five/six layers plus the entire domain from the sea-surface to the deepest interface). Considering the number of domains and properties, the frontal/ confluence model consists of 12/14 equations (halved between mass and salt anomaly conservation). The 19/28 stations in the frontal/confluence model lead to 18/27 reference velocities, plus 4/5 dianeutral velocities and diffusion coefficients (one for each internal division of the domain) and the freshwater and Ekman transport adjustments. The system is solved using a Gauss-Markov estimator, a method that uses a priori variance information for each unknown [Table 3.2] in order to produce a minimum error-variance solution with uncertainty estimates (Wunsch, 1996).

3.3.2 Unknowns and uncertainties

The reference level for the thermal wind equation is often set at a boundary between two water masses of different origin, which are expected to flow in different directions, where the horizontal velocity is possibly small. However, the BC flows south from the surface down to some 2000 m (Peterson, 1992) and the MC displays a northward flow over the entire upper slope (Artana et al., 2018a). Therefore, we do not expect stable flow reversals within the vertical range of the frontal and confluence models, which burdens setting a proper reference level. Hence, we select the deepest possible reference-velocity level and allow for potentially high reference velocities: for the frontal model we choose 400 dbar, which is the deepest common level to all stations, while for the confluence model we select the deepest common isoneutral in the domain, 27.81 kg m^{-3}, at the base of layer 6 varying between about 1400 and 2000 m [Table 3.1]; note that the seafloor becomes the reference level in those slope areas where the water depth or isoneutral reference is not found. The possibility of high reference level velocities is fixed through a relatively large a-priori standard deviation, set at 0.3 m s^{-1} for both the frontal and confluence domains [Table 3.2].

Table 3. 2: A priori information on the reference-level velocity (b), vertical diffusion coefficient (K), vertical velocity (w), and freshwater (δF_w) and Ekman (δT_E) adjustment transports for both the confluence and frontal models)

Variable	Initial value	Standard deviation
b (m s^{-1})	0	0.3
K (m^2 s^{-1}	0	10^{-2}
w (m s^{-1})	0	10^{-5}
δF_w (Sv)	mean March 2015 value	50 % mean March 2015
δT_E (Sv)	mean March 2015 value	50 % mean March 2015

The initial dianeutral-velocity estimate at each interface layer is assumed to be zero. Since we are in a region with numerous intrusions and intense mixing, we expect high dianeutral veloci-

ties and diffusion coefficients, at least as large as what has been inferred by other authors in an analogous but more extense geographical domain (Jullion et al., 2010). Hence, we allow fairly high values for the a priori uncertainties of all these variables [Table 3.2]. Finally, the initial estimates for the Ekman and freshwater transports are set to the mean March 2015 values, and the corresponding a priori errors are taken as 50 of these mean values [Table 3.2].

3.3.3 Transport constraints

Several studies have emphasized the barotropic or barotropic-equivalent (considering a 1.5 reduced gravity model) character of the MC (Peterson, 1992; Vivier and Provost, 1999a,b; Piola et al., 2013). Spadone and Provost (2009) and Ferrari et al. (2017) have shown that the ADT-derived surface geostrophic velocities are in good agreement with near-surface measurements from moorings, confirming that the entire water column moves in approximate geostrophic balance. This result has been used in several studies to estimate MC transports in the top 1500 m of a section which approximately overlaps our first three stations (Vivier and Provost, 1999a; Spadone and Provost, 2009; Artana et al., 2018).

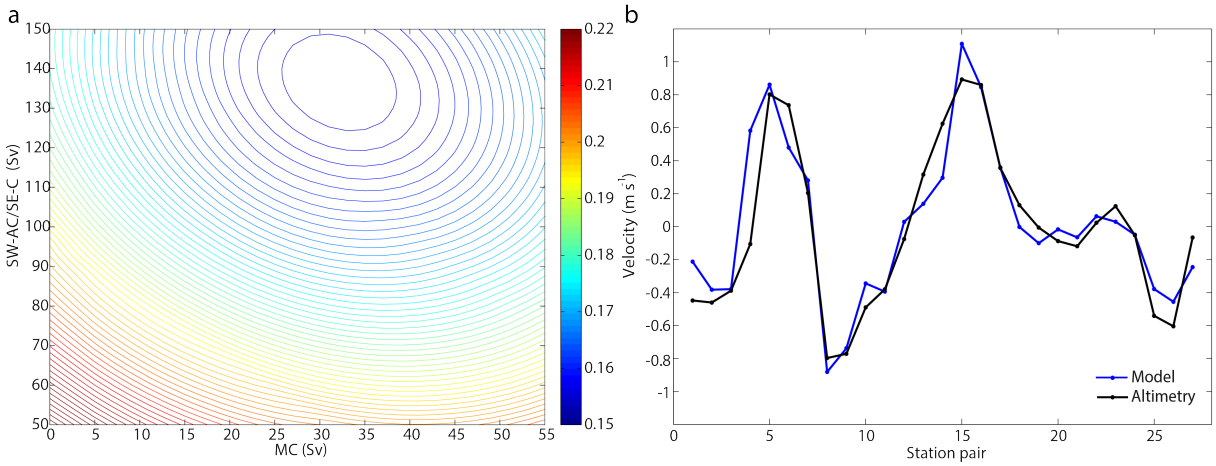

Fig. 3. 2: (a) Standard deviation between the inverse-model and altimetry-geostrophic velocities along the confluence perimeter as a function of northward transports in the along-slope MC (stations 1-4) and in the middle of the southern dipole (stations 8-12). (b) Sea-surface velocities from altimetry (black line) and the best-fit inverse model (blue line). The abscissa represents station pairs, so that j identifies the flow between stations j and j+1 in Figure 3.1; negative values represent flow into the confluence domain.

We have looked at the VADCP data along the confluence perimeter to further confirm the goodness of referencing to the altimetry-inferred velocities. A comparison of both velocity fields shows fairly good agreement (the standard deviation is 0.16 m s^{-1} in the top 700 m) [Fig. S3.1 and Table S3.1, Supplementary Materials]; Paniagua et al. (2018) obtained similar results when comparing in-situ mooring data with altimetry surface velocities across the MC during 2015. However, the ADCP data are much noisier than the altimetry-inferred velocities, reaching ma-

ximum values over the central portion of the eastern part; these peak values are associated with a filament of brackish waters stretching along the frontal zone, which is very likely not in geostrophic balance. Based on these results, we have decided to set the reference level velocities for the confluence model using the information that arises from the sea surface altimetry. Notice that the LADCP data will be used later, to assess the velocities obtained with the inverse model over the entire water column [Section 3.6.1].

Consequently, we constrain the southern flow into the BMC in such a way that the inverse model leads to surface velocities that best fit the altimetry-inferred surface field (at the time of each pair of hydrographic stations). Specifically, we set the integrated transports within those stations where the altimetry-inferred flow is northward – stations 1-4 for the along-slope MC and stations 8-12 in the middle of the southern anticyclonic-cyclonic dipole [Figs. 3.1 and 3.2] – which then translates into the γ^n=27.81 kg m^{-3} surface reference velocities. The minimum standard deviation corresponds almost exactly to an along-slope MC of 30 Sv and a northward transport of 135 Sv associated to the southern dipole [Fig. 3.2a].

Finally, with the help of the March 2015 mean ADT field [Fig. 3.3], we link the inflow to the frontal area (recall it reaches down to only 400 m) with the water entering the confluence region through the top 400 m. The transports through the upper 400 m of the confluence perimeter are calculated with the velocity fields from the inverse model. We then assume that the ADT contours coincide with the depth-integrated streamlines, i.e. the surface connections remain equal at depth (Vivier and Provost, 1999a), and use selected ADT values to connect the flow through the confluence and frontal perimeters. The contours selected are the SAF (0.05 m) and the 0.25-m for the MC inflow, and the BCF (0.30 m), 0.57-m and 0.90-m contours for the BC inflow [Fig S3.2 and Table S3.2, Supplementary Materials]. In all cases we allow an a priori uncertainty of 1 Sv.

3.4 Hydrographic description

3.4.1 Surface circulation

The mean March 2015 sea-surface ADT is characterized by the strangling of the northern portion of the MC, with a significant zonal turn near 42^{o}S, and the double meandering of the BCF, so that the original BCO breaks into a large anticyclonic warm eddy (SW-AC, centred at about 42.0^{o}S, 54.0^{o}W) and a warm ridge located further east (along about 49-50^{o}W); these two ADT highs englobe an elongated subantarctic cyclonic eddy (SE-C, centered at about 41.5^{o}S, 51.0^{o}W) [Figs. 3.1a and 3.3]. In the subtropical side of the frontal system, there is another anticyclonic eddy (NE-AC, centred at about 38.5^{o}S, 51.0^{o}W). It is worth emphasizing that all three eddy centers are crossed by those hydrographic stations comprising the confluence perimeter.

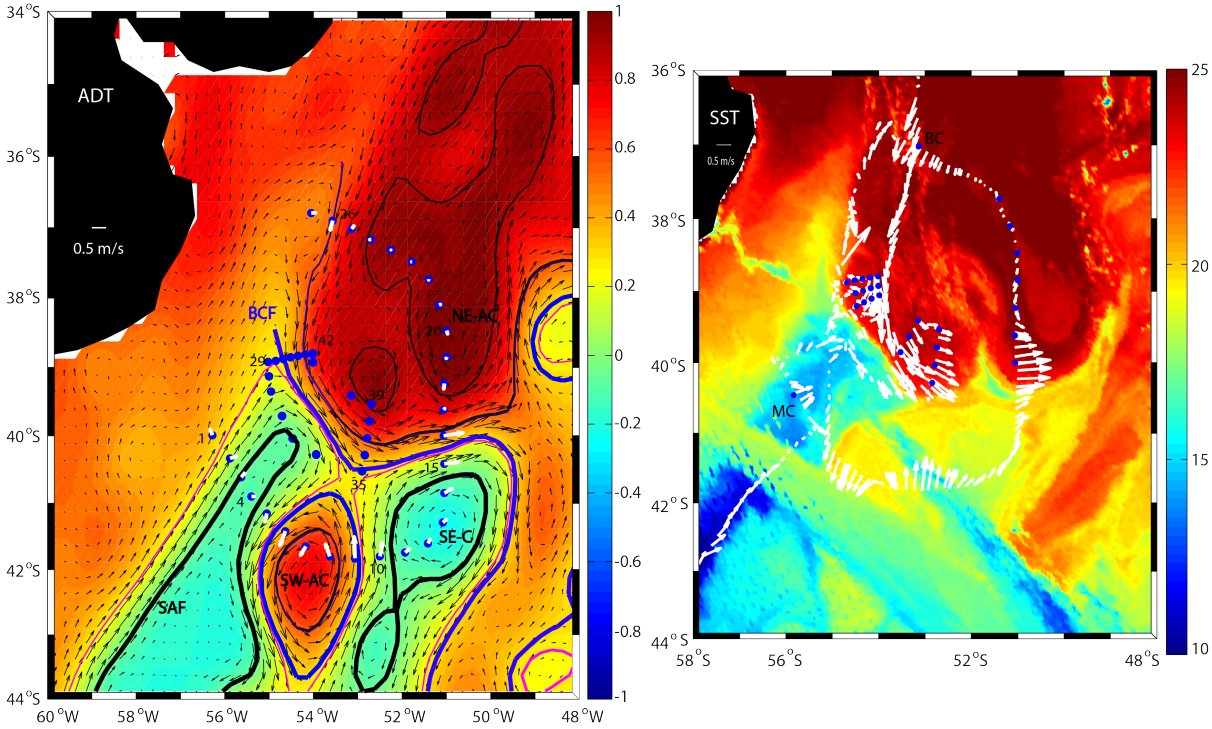

Fig. 3. 3: (Left) Mean sea-surface ADT (color-coded, in m) and surface velocities in the BMC for March 2015; the black arrows are the velocity vectors as inferred from altimetry and the white arrows denote the velocity vectors at each hydrographic station (blue dots) as obtained from the vessel's LADCP. The black and blue thick lines show the position of the SAF and BCF while the thin magenta, blue and black lines indicate the 0.25, 0.57 and 0.9 m ADT contours, respectively. The southwest anticyclone (SW-AC), southeast cyclone (SE-C) and northeast anticyclone (NE-AC) are identified. (Right) SST image for 17 March 2015, together with the 0-700 m depth-averaged VADCP velocity (white arrows) along the vessel's trajectory. The blue dots indicate the location of those stations used to analyse mixing fractions, and BC/MC indicate the positions of those stations used as reference BC/MC water types.

The two southern eddies (SW-AC and SE-C) behave as a non-isolated dipole, with a large fraction of water revolving around each eddy and another substantial fraction arriving into or departing from the mesoscale feature [Figs. 3.1a and 3.3]. Regarding the SW-AC, its western flank shows water input from the BCF and output towards the south while its eastern flank has water input from the south and output into the BCF. Analogously, the SE-C feeds partly from water arriving from the south along its western side and partly from water flowing east along the BCF; again, the surface flow associated to the SE-C does not close on itself, as some of it follows south along its eastern margin, away from this cyclone.

A sequence of ADT images prior to the cruise helps appreciate the temporal evolution of the mesoscale features and associated pathways [Fig. 3.4]. By the end of January, the SAF appeared as a wide wedge of low ADT values and the MRC-BCO were well defined, corresponding to a characteristic condition of intense MC transport at 41^{o}S (Artana et al., 2018). In contrast, during the second half of February the MRC-BCO flow was disconnected from the frontal system, forming a very large anticyclone. In early March, this large anticyclone broke into two anticyclone structures and the eastern ADT trough became more intense, setting up the dipole that

characterizes the weak MC condition at that latitude (Artana et al., 2018).

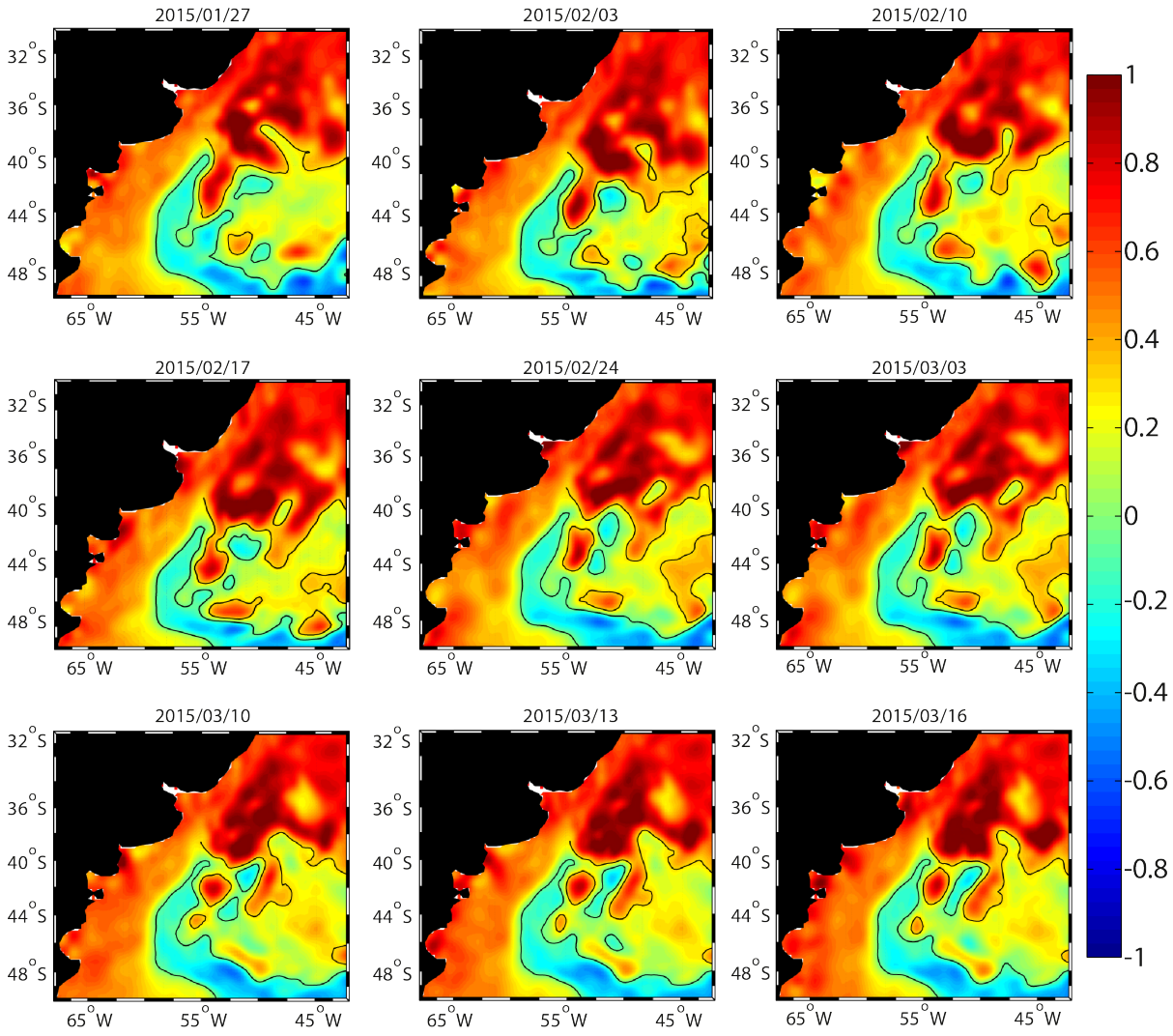

Fig. 3. 4: Sea-surface ADT maps (m), weekly from 27 January till 10 March and every three days from 10 March to 16 March, together with the position of the SAF and BCF (black lines).

Considering that the MRC cyclonic (and BCO anticyclonic) recirculation extends far south, around an ADT ridge that stretches all the way to about (46^{o}S, 50^{o}W) [Fig. 3.1a], the northward flow along the western margin of the SE-C should belong to a much earlier extension of the MRC-BCO southward flow. Indeed, a surface flow of 0.4 m s^{-1} would transit a 1000 km south-north pathway around this anticyclonic high in about one month. The likely evolution is that of an intense MC and MRC-BCO until mid-February, with high northward and southward flows at least between 45^{o}S and 41^{o}S. In late February, the along-slope MC weakened at higher latitudes as an eastern diversion appeared near 45^{o}S that connected with the intense interior northward flow near 53^{o}W (through the middle of the dipole); we will come back to these ideas in Section 3.6.2.

3.4.2 Water masses and vertical sections

Six water masses appear in the upper 2000 m of the BMC (Maamaatuaiahutapu et al., 1992) [Fig. 3.5]. In the surface layers of several stations we find low salinity and warm waters with a substantial contribution from La Plata River. In the thermocline and intermediate layers we identify four water masses [Table 3.1]: salty and warm Subtropical Mode Water (STMW, S = 36-37 g kg^{-1}, θ = 15-23°C, γ^n = 26.2-26.8 kg m^{-3}, z ≅ 50-300 m), fresh Subantarctic Mode Water (SAMW, S ≅ 34.4 g kg^{-1}, θ = 5-8°C, γ^n = 26.8-27.2 kg m^{-3}, z ≅ 100-650 m), fresh and cold Antarctic Intermediate Water (AAIW, S ≅ 34.3 g kg^{-1}, θ ≅ 3°C, γ^n ≅ 27.2-27.55 kg m^{-3}, z ≅ 800-1500 m), and low-oxygen Upper Circumpolar Deep Water (UCDW, S ≅ 34.7 g kg^{-1}, θ ≅ 2.8°C, γ^n ≅ 27.55- 27.92 kg m^{-3}). Below 1800 m, but only in station 4 and within the SE-C, we find North Atlantic Deep Water (NADW, S >34.8 g kg^{-1}, θ = 2.0-3.5°C, γ^n>27.92 kg m^{-3}).

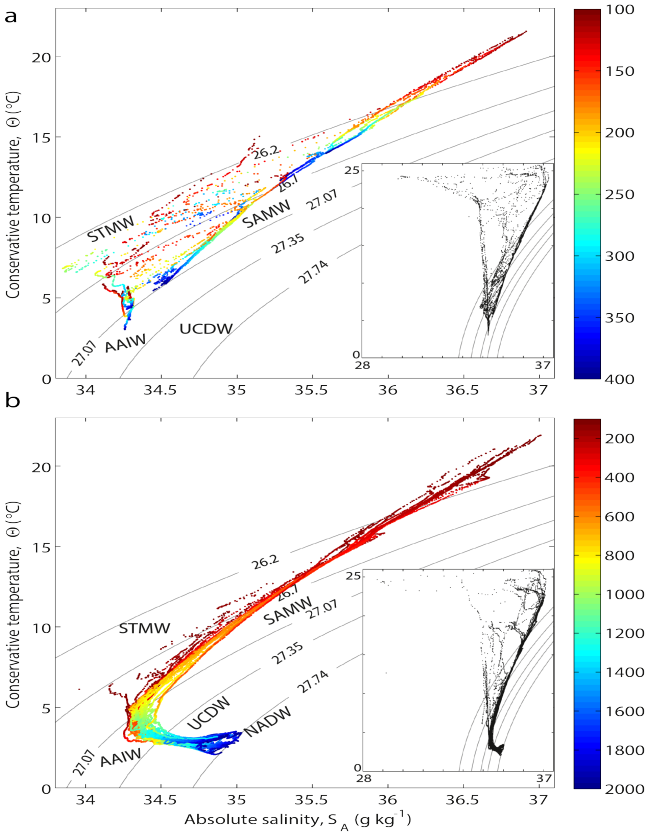

Fig. 3. 5: Conservative temperature – absolute salinity diagrams for the frontal and confluence domains: (a) the frontal diagram includes data from 100 to 400 m while (b) the confluence diagram uses all data between 100 and 2000 m (the inner panels include data in the top 100 m). The plots are colour-coded with depth (m), with the grey lines showing the isopycnals (kg m^{-3}) that approximately delimit the water-mass layers used in the confluence model.

Asides the surface waters, in the entire domain there are subantarctic mode and intermediate waters plus UCDW, with an abrupt transition from subantarctic (fresher, colder and denser) to subtropical (warmer, saltier and lighter) waters across the BMC. This transition is clear in the distribution of temperature and salinity along vertical sections following the perimeters of the frontal and confluence domains [Fig. 3.6; recall that the 400-m deep frontal perimeter closes on itself while the 2000-m deep confluence perimeter remains open along the shelf break]. Considering this distribution of water masses, we may safely say our inverse-model transports

encompass all surface, mode and intermediate waters plus most of the UCDW.

In the frontal area [Figs. 3.6a,b], the southern rim is dominated by subantarctic waters, the northern edge by subtropical waters, and the eastern and western sides display a remarkably steep frontal structure (the slope of the 26.8 kg m^{-3} isoneutral is about 10^{-2}). The entire area presents a very shallow (everywhere less than 10 m) warm and relatively fresh layer (temperatures over 15°C and salinities less than 34 g kg^{-1}), caused by the runoff from La Plata River. Additionally, the upper waters of the subantarctic side reflect summer warming, that is, temperatures over 7.5°C down to about 50 m, and the frontal system displays thermohaline intrusions of cold subantarctic waters at different levels, particularly intense near the slope.

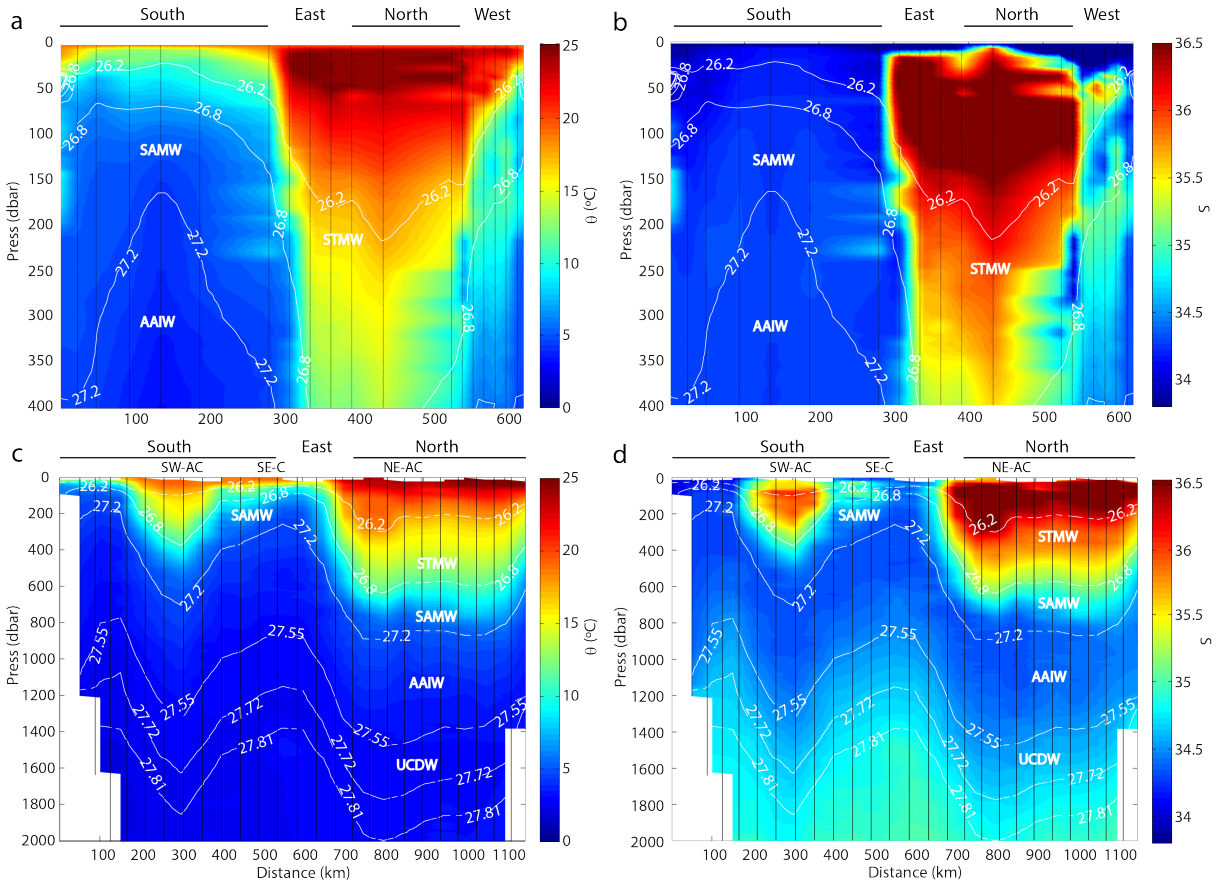

Fig. 3. 6: (a, c) Vertical sections of conservative temperature θ (°C), and (b, d) absolute salinity S (g kg^{-1}), for the (a, b) frontal and (c, d) confluence models. The white lines represent the isoneutral water-mass boundaries used in the confluence inverse model and the black dots indicate the data points, and the water masses are labelled according to the boundary definitions in Table 3.1. The southern, eastern and northern edges follow those sectors shown in Figure 3.1b, and the approximate extent of the mesoscale eddies is indicated.

The temperature and salinity distributions along the perimeter of the confluence region delimit the vertical extensions of the STMW, down to 26.8 kg m^{-3} or about 600 m. The subantarctic waters along the southern edge of the confluence domain are crossed by the large SW-AC

(diameter about 200 km), which is almost entirely formed by STMW; the 26.8 kg m^{-3} isoneutral in this eddy is somewhat shallower, about 400 m, which is the same depth reached by this isoneutral in the frontal area. The MC (stations 1-4) is mostly occupied by AAIW and UCDW (from about 200 to 1700 m), showing (θ, S) values similar to those characterizing weak MC conditions (Paniagua et al., 2018). The eastern cyclone (SE-C), of subantarctic origin, appears relatively isolated during the cruise but the time sequence of ADT images [Fig. 3.4] shows that it belongs to an earlier northward return of the MRC; its long transit over the region is reflected by a relatively deep, warm and fresh surface layer.

The vertical section along the confluence perimeter also shows that all deep isoneutrals follow the same shape as the 26.8 kg m^{-3} isoneutral, that is, replicating the base of the STMW down to at least 2000 m. This is consistent with the idea that these subantarctic waters have a relatively small baroclinic contribution. This is true even in the north-western end of the perimeter, where the modal and intermediate waters shallow towards the slope, suggesting the existence of a southward along-slope flow at these deep levels.

3.4.3 Baroclinic transports

We may calculate the geostrophic transports in and out the frontal and confluence domains without use of the inverse model, that is, maintaining null reference velocities and vertical exchange. The net transport imbalances into either domain will indicate the size of the transports that need to be accommodated by the inverse model.

We use the BCF in order to partition either perimeter into two segments (south and north of the BCF) where the water flow is of southern and northern origin. For each segment and layer, we separately add up all water transports in and out of the domain (recall positive values represent flow divergence; Fig. 3.7); the transports entering each segment will provide our first estimate of the baroclinic transports by the MC and BC in the upper 2000 m of the water column.

In the frontal model, the depth-integrated inflow (outflow) is -2.5 Sv (6.3 Sv) for the southern segment and -5.4 Sv (1.7 Sv) for the northern segment, for net imbalances of 3.8 Sv and -3.7 Sv, respectively. In the confluence model, the depth-integrated inflow (outflow) is -49.1 Sv (71.4 Sv) for the southern segment (most of it in the AAIW stratum) and -45.6 Sv (38.4 Sv) for the northern segment (dominated by the surface and STMW strata), for net imbalances of 22.2 Sv and -7.2 Sv, respectively. The total imbalance for the entire frontal area is very small, only 0.2 Sv, while for the confluence region it is 15.0 Sv (10.6 Sv in the SAMW and AAIW layers). The large input-output differences through the southern and northern segments of the frontal and confluence perimeters are difficult to justify. Further, the imbalance for the confluence model doubles the water inflow associated to the along-slope MC. Both discrepancies plenty justify the use of the inverse model.

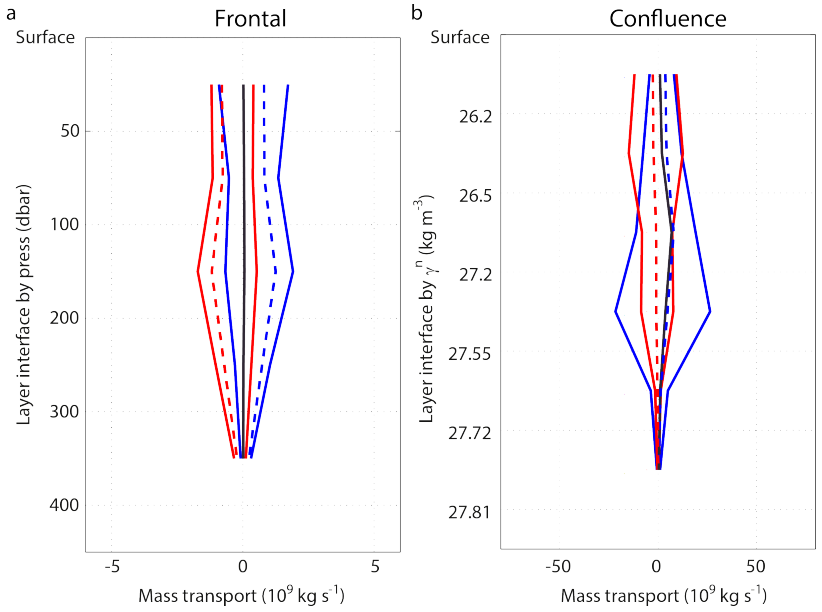

Fig. 3. 7: Baroclinic mass transports in the (a) frontal and (b) confluence models. The transports are calculated independently for the southern (blue) and northern (red) segments, which are separated by the BCF. Further, all flow into and out of the box is computed separately, with negative (positive) values indicating the flow entering (leaving) the domain; the dashed lines (blue for the southern segment and red for the northern segment) represent the differences between the flow leaving and entering each domain. The black line represents the net transport for the entire box.

3.5 Model results

We now turn to the results of the inverse model for both the confluence and frontal domains. In either case we present the velocities normal to the perimeter [Fig. 3.8] as well as the transports into or out of the domain and the transports accumulated along the perimeter [per layer and total, Figs. 3.9 and 3.10].

3.5.1 Confluence model

Water enters the confluence region via both the MC in the southwestern edge and the BC in the northern side, and output occurs at the southern and southeastern margins [Fig. 3.8c]. The pattern of water inflow and outflow in the southern side actually reflects the existence of the along-slope MC, the recirculations associated with the SW-AC and SE-C dipole, and the southern sources and sinks for this dipole [Fig. 3.3]. The reference velocities at 27.81 kg m^{-3} are fairly large in all stations south of the BCF (up to about 0.4 m s^{-1} in stations 8 to 11), with negative values (water input) in those places where northward transport is imposed (stations 1-4 and 8-12) [Section 3.3.3] and positive values elsewhere, confirming the barotropic character of the MC and associate recirculations. In contrast, the reference level velocities are small for all stations north of the BCF, indicating that most of the transport associated with the BC is baroclinic in the upper 2000 m [Fig. 3.8d].

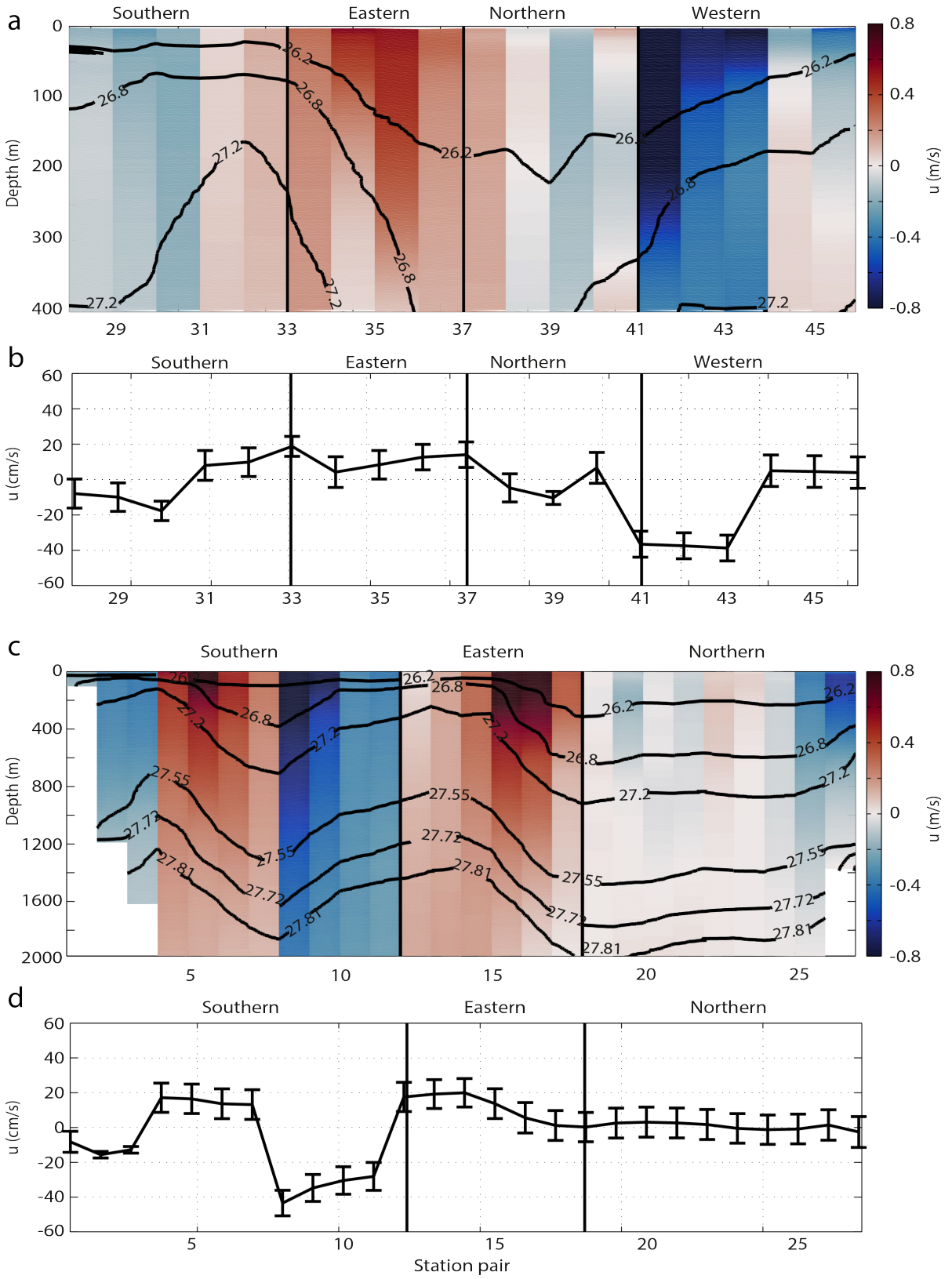

Fig. 3. 8: Vertical distribution of the inverse-model velocity through the along-perimeter section for the (a) frontal and (c) confluence models. Reference-level velocities along the perimeter for the (b) frontal (at 400 m) and (d) confluence (at the 27.81 kg m^{-3} isoneutral) models. Negative/positive (blue/red) values denote inflow/outflow velocities. The southern, eastern, northern and western edges (the latter only for the frontal area) follow those sectors shown in Figure 3.1b, and the abscissa represents stations pairs, as in Figure 3.2.

The vertical velocities range between 10^{-7} and 10^{-6} m s^{-1}, leading to relatively minor vertical mass transports between adjacent layers [Fig. S3.3, Supplementary materials]. The largest vertical transport takes place from the SAMW to the AAIW layers, accounting for 1.2 $\pm$ 1.5 Sv; however, because of the large a priori uncertainties, it is not significant. The vertical diffusion coefficients, which cause no water transport but do contribute to the salt balance, are on the order of 10^{-5} m^2 s^{-1}, neither significant [Fig. S3.3, Supplementary materials].

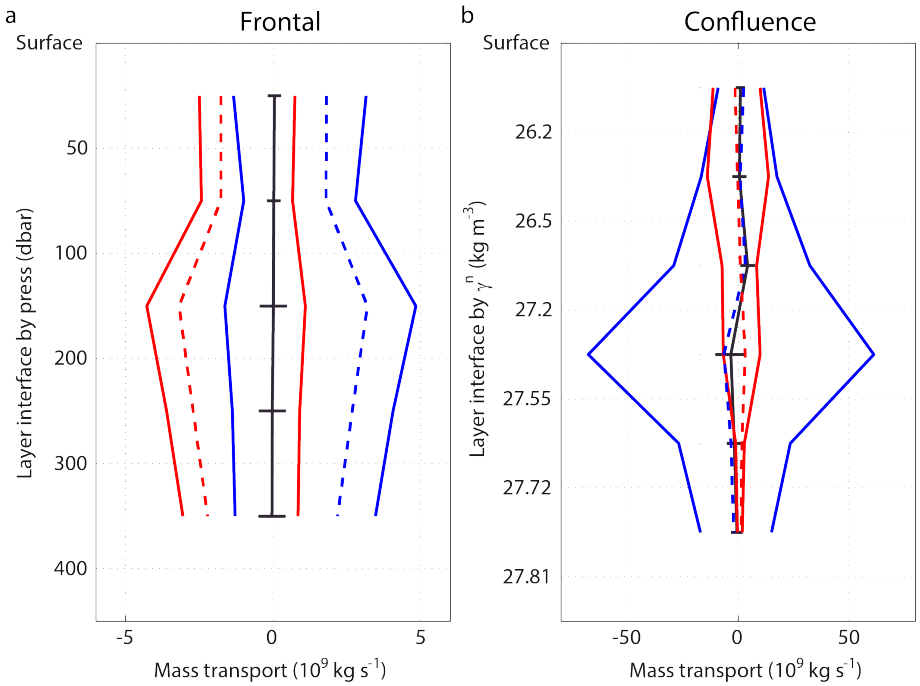

Fig. 3. 9: Mass transports in the (a) frontal and (b) confluence models as deduced from the inverse model (notation as in Figure 3.7).

We can use the BCF to distinguish between the transports associated to the MC and BC for each segment and layer [Fig. 3.9b]. The mass conservation condition is fulfilled for every layer, the transport uncertainties are larger than the residuals, though barely in the SAMW and AAIW layers. The total imbalance for the confluence region is -0.01 Sv. The very large southern transports in the AAIW, and to a lesser degree in the SAMW and UDCW layers, are a reflection of the recirculations associated with the two eddies south of the BCF. The net transports (inflow minus outflow) are relatively small for each segment and layer, always less than 2 Sv except in the southern segment for the AAIW, where there is a net inflow of 6.5 $\pm$ 2.0 Sv. In the northern segment, the largest transports occur in the top two layers (surface and STMW), although the largest imbalance is for AAIW, with a net loss of 3.1 $\pm$ 2.8 Sv.

These results are complemented with the cumulative transports per layer, starting at the southwestern corner [Fig. 3.10b; recall that there are no stations along the shelf break]. The MC contributes with 28.3 $\pm$ 1.4 Sv along the slope and there are as much as 87.6 $\pm$ 10.6 Sv flowing south along the western margin of the SW-AC. Assuming that the flows are connected and in

steady state, the difference between these two values tells us the maximum water transport that recirculates within the SW-AC, 59.3 $\pm$ 10.7 Sv; note that this is a maximum value because some water may continue further south, away from the anticyclone. Further east, along the eastern (western) side of SW-AC (SE-C), there is a northward transport of 138.2 $\pm$ 1.0 Sv. Subtracting the maximum water recirculating within the SW-AC, this gives an additional inflow of at least 78.9 $\pm$ 13.7 Sv, possibly even more. The major contribution to water transport in this southern segment corresponds to AAIW, accounting for about 40 % of the total transport at each location.

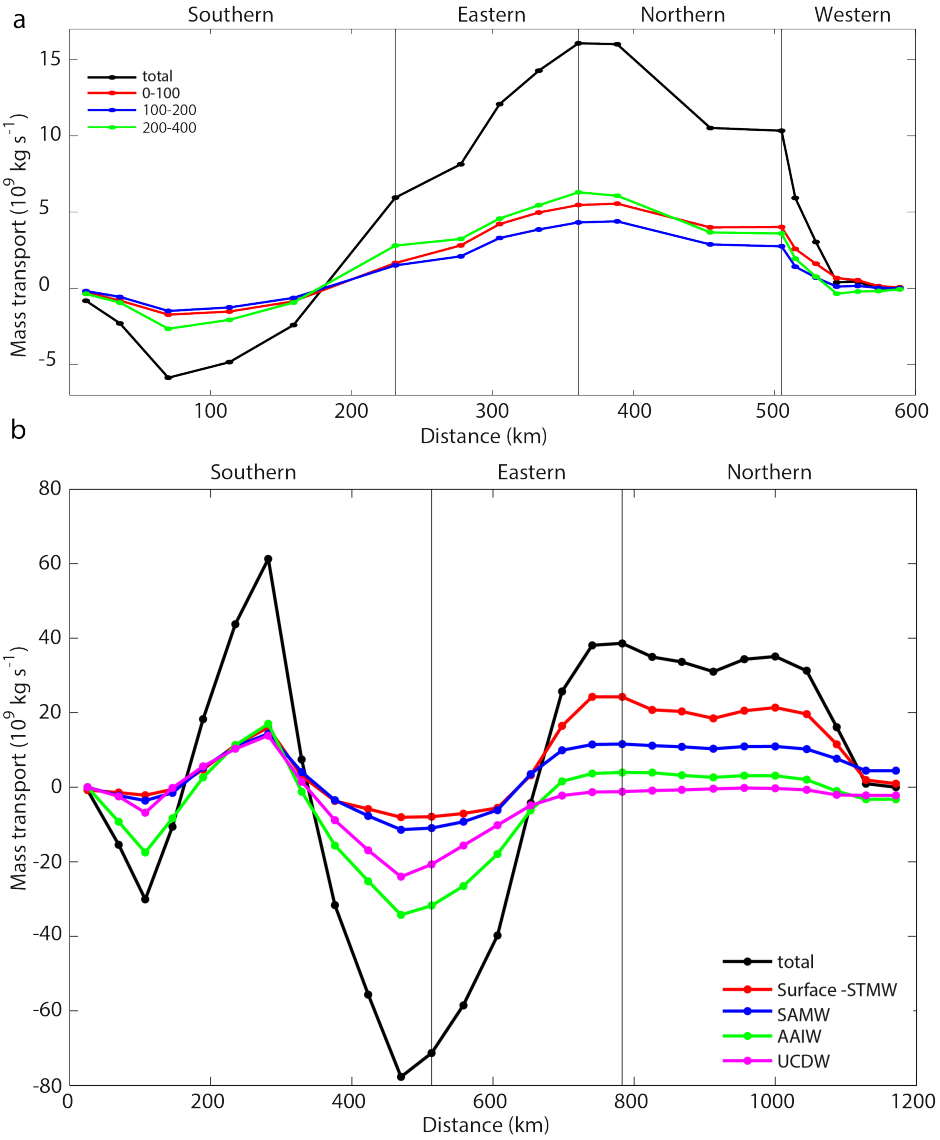

Fig. 3. 10: Accumulated mass transports, per layer and total, for the (a) frontal and (b) confluence models. The transports for the several frontal and confluence layers are color-coded with negative values indicating transports into the box. The southern, eastern and northern edges follow those sectors shown in Figure 3.1b.

North of the BCF, there is a total inflow of 35.9 $\pm$ 6.2 Sv; however, because of a local cyclonic recirculation (5.1 Sv), the net inflow accounts for only 30.8 $\pm$ 12.0 Sv, with an along-slope input

of 29.1 ± 8.3 Sv [Fig. 3.10b]. This net transport is split, roughly in equal parts, among subtropical (STMW) and subantarctic (SAMW and AAIW) waters. The southern (78.9 Sv) and northern (30.8 Sv) net inflows are eventually drained out of the confluence region through the eastern border, with a total of 109.7 ± 15.1 Sv. Part of this eastward flow will continue northward as the BC offshore recirculation, another will form the SAC and continue eastward and another one flows southward and feeds the SE-C as will be discussed in section 3.6.2.

3.5.2 Frontal model

Water enters the frontal area via the MC in the western half of the southern margin and via the BC in the western and, to a lesser degree, northern borders; the outflow takes place mostly through the eastern half and, to a lesser degree, through the eastern portion of the southern and northern sides [Fig. 3.8a]. The reference velocities are fairly large in stations 28-32, influenced by the MC, and stations 41-44, forced by the BC; they also reach large values in some of the southeastern and eastern stations, where intense outflow takes place.

The inverse model also shows that the vertical velocities are of order 10^{-7} m s^{-1}, leading to non-significant net vertical mass transports between adjacent layers [Fig. S3.3, Supplementary materials]. The vertical diffusion coefficients are on the order of 10^{-4} m^2 s^{-1}, again not significantly different from zero (not shown).

We again use the BCF to quantify the transports associated to the MC and the BC segments, in and out per segment and layer [Fig. 3.9a]. The main exchanges with the confluence region occur in the top 200 m. Mass output is higher than input along the southern flank while the opposite occurs in the northern flank. The net imbalance for the entire frontal area is of only -0.05 Sv.

The relatively intense recirculation pattern in the shallow frontal area arises after we constrain the flow through the perimeter of the confluence region to follow the ADT-streamlines into the frontal boundary [Section 3.3.3]. Without this constraint the southern and northern inputs into the frontal area were 2.0 and -5.4 Sv, respectively [Fig. 3.7]. After constraining the flow with the help of the mean March ADT, these transports increase largely, with a southern input of 6.6 ± 1.5 Sv and a northern contribution of 15.9 ± 0.8 Sv [Fig. 3.9].

The cumulative transports provide a complementary view of the exchange of water within the frontal area [Fig. 3.10a]. Beginning at its southwestern corner, after an input of 5.9 ± 1 Sv through the southern border, there is an outflow of 21.9 ± 1.7 Sv in the southern and eastern borders. This difference is accounted by inflow through the northern (5.7 ± 1.5 Sv) and western (10.4 ± 0.9 Sv) sides. About half of the input/output occurs in the top 100 m and the other half is split roughly equal in the 100-200 and 200-400 m levels.

3.6 Discussion

3.6.1 Comparison of inverse model and ADCP fields

One natural alternative to the inverse model would be the ADCP data. However, these measurements may incorporate large errors in areas of weak acoustic backscattering, such as in the deep ocean, or high instrumental tilt (heading, pitch and roll), as in the presence of strong currents (e.g. King et al., 2001; Ott, 2002; Polzin et al., 2002; Thurnherr et al., 2017). Nevertheless, since the inverse model solution has been possible with no need of in-situ velocity measurements, it is appropriate to compare the inferred velocity fields with both the LADCP and VADCP values (the latter in the top 700 m).

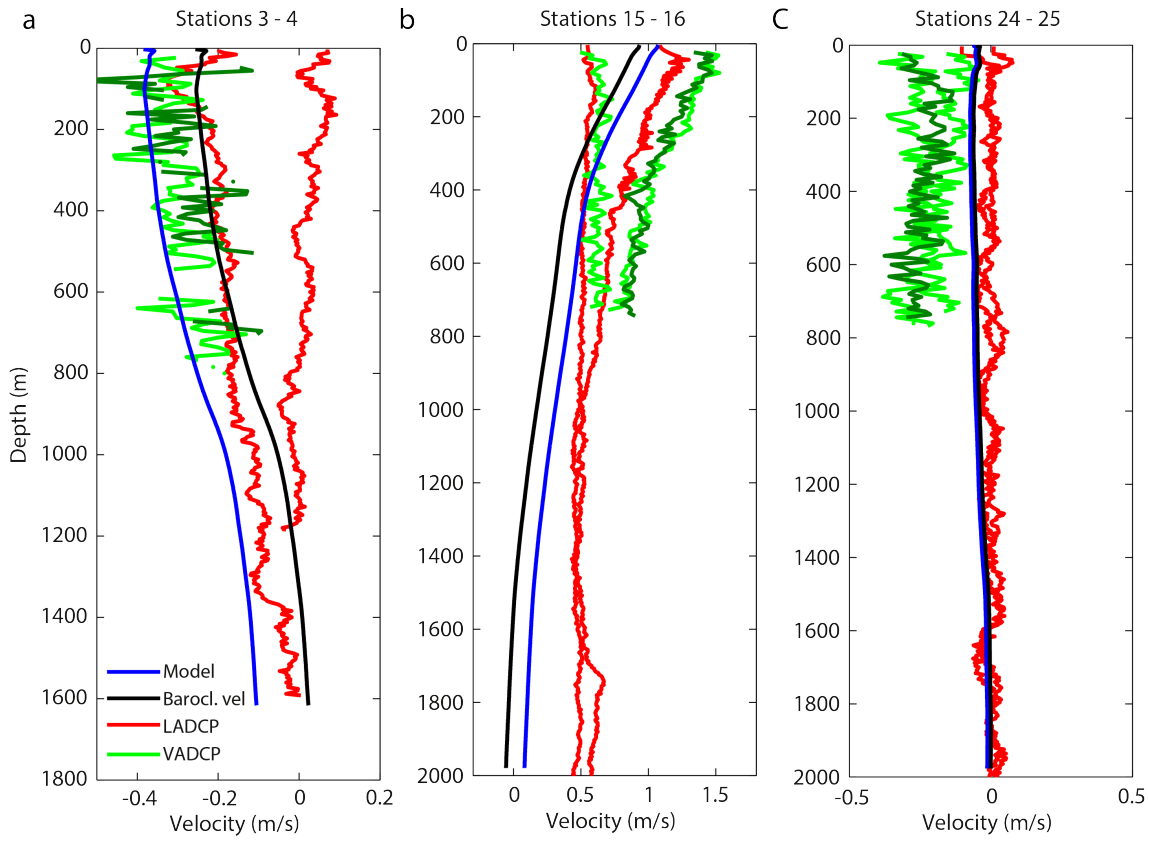

Fig. 3. 11: Velocity samples from three station pairs: baroclinic contribution referenced to the 27.81 kg m^{-3} isoneutral (black) and inverse model (blue) velocities at the mid-point between both stations; normal-to-section velocities with the LADCP at both stations (red) and with the VADCP at both stations and the central point (green, darker green for the midpoint profile).

For the model-measurement comparison, we must keep in mind that inverse-model velocities are calculated at the mid-points between hydrographic stations, the LADCP velocities are at the stations and the VADCP provides near-continuous values along the ship track. In Figure 3.11 we compare the velocities for selected stations in the southwestern (3-4), eastern (15-16) and northwestern (24-25) edges of the confluence model. In each case we have up to seven velocity profiles: the baroclinic contribution (determined through the thermal wind equation with zero

reference velocity) and the inverse model prediction at the midpoint between stations, LADCP data at the two adjacent stations and the VADCP data computed both at the stations and at the midpoint (for the comparison we always use the component of the LADCP and VADCP velocities normal to the section).

The results in Figure 3.11 illustrate the type of discrepancies among the several datasets and the model, showing the potential limitations if we were to use only the ADCP measurements. The VADCP velocities are always the noisiest. Most remarkable, we find several instances where the velocities are substantially different when sampled at one same location with different instruments (e.g. stations 24-25) or when sampled at adjacent locations with one same instrument (e.g. VADCP in stations 15-16 or LADCP in stations 3-4).

Using the normal-to-section LADCP velocity component, we may construct velocity sections that are suitable for direct comparison with the inverse model velocities [left panels in Figs. 3.12a,c]. The LADCP velocities reproduce the same patterns as deduced with the inverse model but with generally higher speeds, particularly in the eastern section. The velocity difference between the LADCP and the model is rather intermittent, with a standard deviation of 0.1 m s^{-1}, although the velocity difference in the eastern section can locally be as large as 0.4 m s^{-1} [right panels in Figs. 3.12a,c].

The LADCP velocity near the reference level [Fig. 3.12b, d] is calculated as the average velocity in the 360 to 400 m range along the frontal perimeter and within 200 m from γ^n = 27.81 kg m^{-3} along the confluence limit. Despite the LADCP and model velocities display similar spatial trends, there are large differences in the western and eastern transects of the frontal model [Fig. 3.12b] and in the eastern transect of the confluence model [Fig. 3.12d], leading to a substantial standard deviation (0.25 m s^{-1}).

The velocity differences between the model and the LADCP, throughout the entire water column and particularly at the reference level, peak in zones of high surface velocities, where the rosette-CTD-LADCP system experienced substantial tilt and the ship drifted large distances during the cast, degrading the quality of processed LADCP velocities. This is the case in the eastern sections of both the frontal (stations 35-36) and confluence (stations 15-16) perimeters, where the frontal area was accompanied by a swift filament of brackish waters (depths less than 30 m). Hence, it seems plausible that these high local LADCP bottom velocities are defective, pointing at the need of using the inverse model.

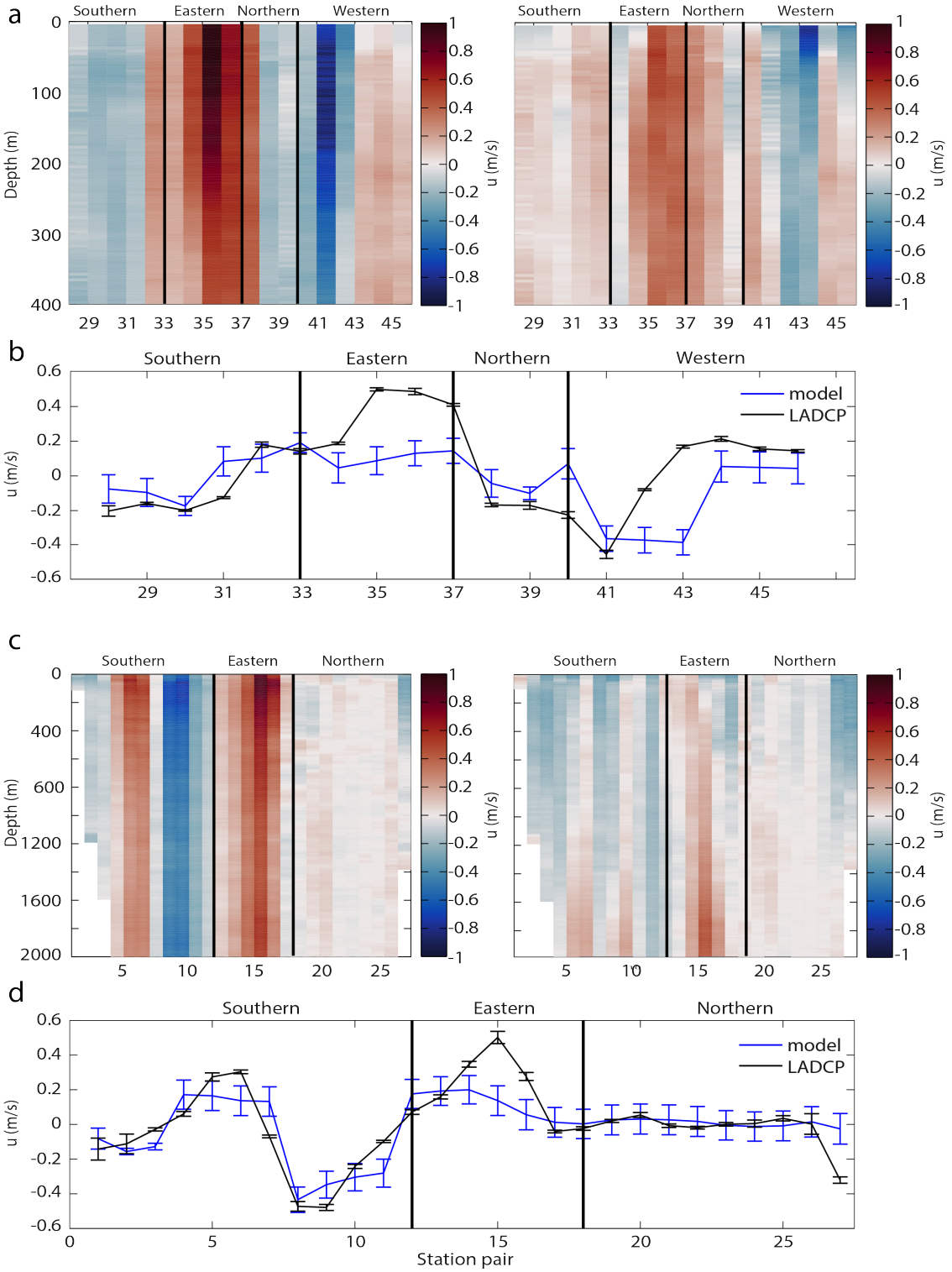

Fig. 3. 12: Normal-to-section velocities along the (a, b) frontal and (c, d) confluence perimeters; the southern, eastern, northern and western edges (the latter only for the frontal area) follow those sectors shown in Figure 3.1b, and the abscissa represents station pairs, as in Figure 3.2. (a, c). The left panels show the vertical distribution of the LADCP velocity and the right panels show the difference between the LADCP and model velocities; the negative/positive values denote inflow/outflow velocities. (b, d) Pseudo reference-level velocities (black line) are calculated along the perimeters as explained in the text and compared with the model solution (blue line).

Differences between the model and ADCP velocities may also result from the limited spatio-temporal resolution of the altimetry data (e.g. Pascual et al., 2013) when constraining the flow or simply because the velocity field may have high non-geostrophic local contributions; for example, both effects may add up in the relatively narrow surface brackish filament that flows along the BCF, causing the altimetry-inferred speeds to be much weaker than the VADCP values [Fig. S3.1, Supplementary materials]. However, notice that the error in transport over a restricted number of stations associated with a swift but shallow (<50 m) and narrow (<50 km) filament out of geostrophic balance would be relatively small (a velocity error of 0.4 m s^{-1} would cause a transport error less than 1 Sv), much less than the transport error for the entire water column due to a flawed bottom velocity of only 0.1 m s^{-1} (for a water column of 1400 m this would represent 28 Sv).

3.6.2 Baroclinic, barotropic and total transports

Our results for the upper 2000 m of the water column show very different situations north and south of the BCF. North of the BCF we find the BC, a highly baroclinic current with weak velocities at γ^n= 27.81 kg m^{-3}. Further, as the BC approaches the BMC, it experiences feeble interior-ocean recirculations, that is, there are no cyclonic eddies north of the BCF and the anticyclonic eddies are of moderate strength. In contrast, south of the BCF we find much higher reference velocities at 27.81 kg m^{-3}, reaching 0.4 m s^{-1} in the northward flow at the middle of the southern dipole, confirming a very substantial barotropic contribution. Additionally, the flow in this southern region displays intense mesoscalar structures, that is, there are several cyclonic and anticyclonic features south of the BCF: the cyclone formed by the MC and MRC, an anticyclone that replaces the BCO, and an interior-ocean cyclone.

Table 3. 3: Model barotropic, baroclinic and total contributions (in Sv), relative to γ^n= 27.81 kg m^{-3}, for the major pathways reaching the confluence region (negative/positive values refer to inflow/outflow); the transports for SW-AC and SE-C are maximum and minimum values, respectively

	Baroclinic	Barotropic	Total
MC	-13.3	-15.0	28.3
SW-AC	30.2	29.1	59.3
SE-C	-2.7	-76.2	-78.9
SAC	50.8	58.9	109.7
BC	-29.0	-0.1	-29.1

Figure 3.13 shows the local transports (between each station pair) associated with each water mass in the confluence model. These transports, which delineate the contributions by the boundary currents as well as the interior recirculations, are drawn on top of the surface geostrophic velocity field. In this figure we have also included the barotropic and baroclinic contributions

down to γ^n= 27.81 kg m^{-3} for the major pathways crossing the BMC: the along-slope MC and MRC, the SW-AC, the interior northward flow through the middle of the SW-AC and SE-C dipole, the outflow along the BCF, and the along-slope inflow and interior recirculations of the BC. These numbers illustrate the contrast between a MC with substantial barotropic transports and a BC that is essentially baroclinic, and further emphasize the northward inflow near 53^{o}W and the eastward outflow along the BCF [Table 3.3].

The along-slope BC transport (29.1 $\pm$ 8.3 Sv) agrees, within uncertainties, with previous estimates ranging between 20 and 44 Sv (Zemba, 1991; Peterson, 1992; Maamaatuaiahutapu et al., 1998; Garzoli et al., 2013). Most of the BC transport is baroclinic: 29.0 Sv in the upper 2000 m as opposed to only 0.1 Sv associated with the γ^n= 27.81 kg m^{-3} reference velocity. This very small barotropic contribution is consistent with the weak southward transport (2 Sv) obtained by Goni et al. (1996).

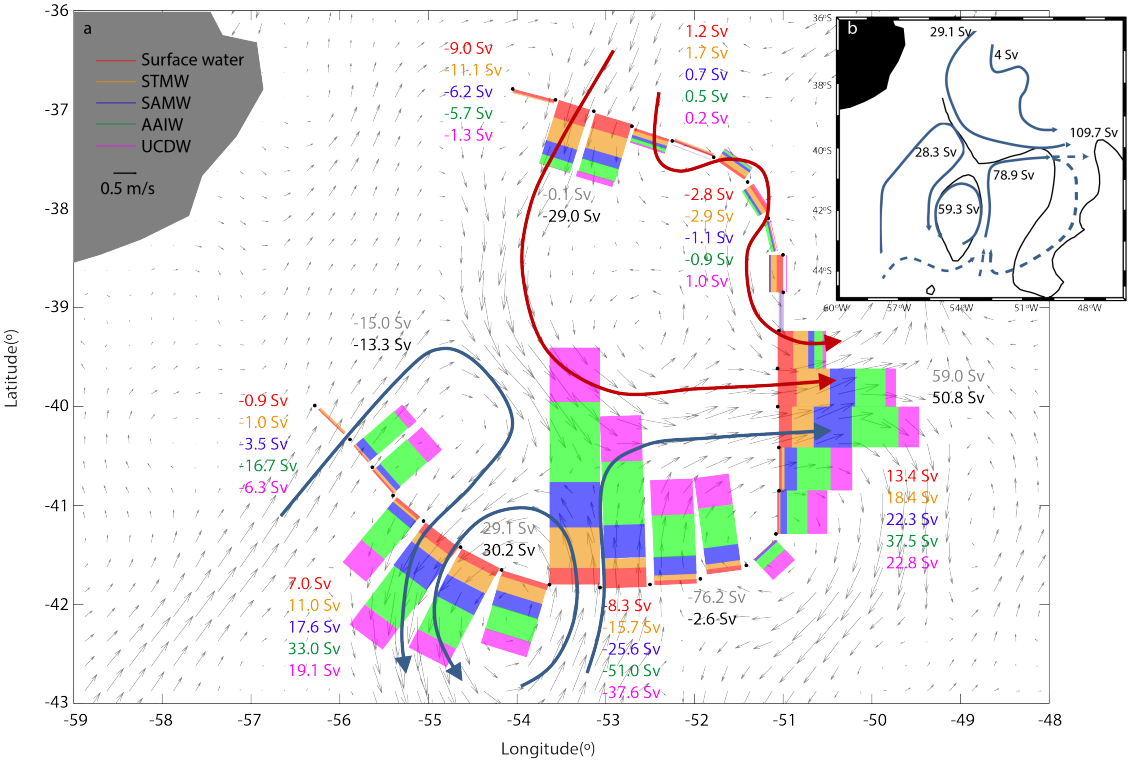

Fig. 3. 13: (a) Transports per water mass and for each station pair as inferred from the inverse model. The colour bars illustrate the partitioning of the transports among different water masses (surface, red; STMW, orange; SAMW, blue; AAIW, green; UCDW, magenta) and the coloured numbers refer to the depth-integrated transports between those stations where the transport changes sign. The lines depict the major currents and the associated numbers indicate the barotropic (grey digits) and baroclinic (black digits) contributions. The vectors (grey arrows) represent the surface geostrophic velocities as inferred from the altimetry. (b) Scheme of the main currents (solid lines) and associate transports, together with the proposed MC interior pathways (dashed lines); the BCF is shown as a black line.

The transport of the along-slope MC is -28.3 $\pm$ 1.4 Sv, below earlier estimates for this current, of the order of 35-60 Sv (Saunders and King, 1995; Vivier and Provost, 1999a; Spadone and

Provost, 2009), but not so far from the potential variability calculated by Artana et al. (2018) from the combined analysis of 25 years of altimetry and mooring data at 41^{o}S, 37.1 $\pm$ 6.6 Sv. The baroclinic contribution relative to γ^{n}= 27.81 kg m^{-3} (-13.3 Sv) is on the order of previous estimates when assuming a level of no motion at 1400 m (Gordon and Greengrove, 1986; Garzoli, 1993), although much less than the 23 Sv estimated by Vivier and Provost (1999b) using this same reference level. The barotropic and baroclinic contributions are fairly equal, 53 % and 47 %, in agreement with Vivier and Provost (1999b). Therefore, the constraints imposed onto the three southwestern stations of the confluence perimeter [Section 3.3.3] reproduce correctly the important barotropic inflow in the MC.

According to the time series reported by Artana et al. (2018), the MC at 41^{o}S was unusually weak between December 2014 and August 2015, with near-average transports between mid-January and the end of April 2015 (35-37 Sv) and much weaker between May and August. From the analysis of velocity, salinity and temperature variations during 2015 from mooring data along this same 41^{o}S line, Ferrari et al. (2017) and Paniagua et al. (2018) classified the January-April period as strong; however, considering Artana et al.'s (2018) results, this strength is relative to the very weak MC conditions that took place between May and August 2015. Close inspection of Paniagua et al.'s (2018) velocity time series further shows that the along-slope flow experienced a substantial decrease during the first 10 days of March 2015, which caused a short reversal of the along-slope-flow orthogonal function.

The mean ADT pattern in March 2015 [Figs. 3.1a and 3.3] indeed resembles the characteristic ADT distribution at times of minimum MC near the BMC (Artana et al., 2018): the SAF is at a southern position, the BCO has split into an anticyclonic eddy, and the MRC at 46^{o}S is connected with the interior-ocean cyclonic structure. The dipole formed by the SW-AC and the interior SE-C appears as a remarkable feature at the time of the cruise. The northward flow between both eddies is particularly strong as it accounts for the recirculation within the SW-AC (59.3 Sv) and an additional very intense inflow (78.9 Sv). This strong interior northward flow near 53^{o}W (hereafter to be referred as interior northward flow) cannot be solely explained in terms of a time-delay in the arrival of an earlier along-slope MC, simply because the January-February transport did not exceed 37 Sv (Artana et al., 2018).

We may explore if the existence of the interior northward flow can be sustained via meridional pathways from more southern latitudes. A preliminary analysis of along-slope Argo trajectories between 45^{o}S and 50^{o}S sustains the possibility of this interior pathway. We find that a substantial fraction of these floats, roughly one-third of all floats, divert from the slope much before reaching the BMC. Figure 3.14 shows 10 float trajectories that display such behaviour, with half of them diverting cyclonically near 42^{o}S and the other half following a meridional pathway near 46^{o}S. It seems likely that these pathways may become reinforced at times of weak along-slope MC conditions at 41^{o}S. Under these circumstances, we could envision that the entire

along-slope MC could be diverted at a southern latitude and continue as an interior northward current into the BMC near 53°W. However, based on the analysis of ADT along-slope data, Artana et al. (2016) have shown that this southern transport will not differ substantially from the values at 41°S. Hence, we may anticipate that the southern contribution will occasionally reach at least 44 Sv (mean plus SD transport at 41°S). This value, although relatively large, remains much less than our estimate of a minimum interior transport of 78.9 Sv into the BMC so we must turn to alternative water sources.

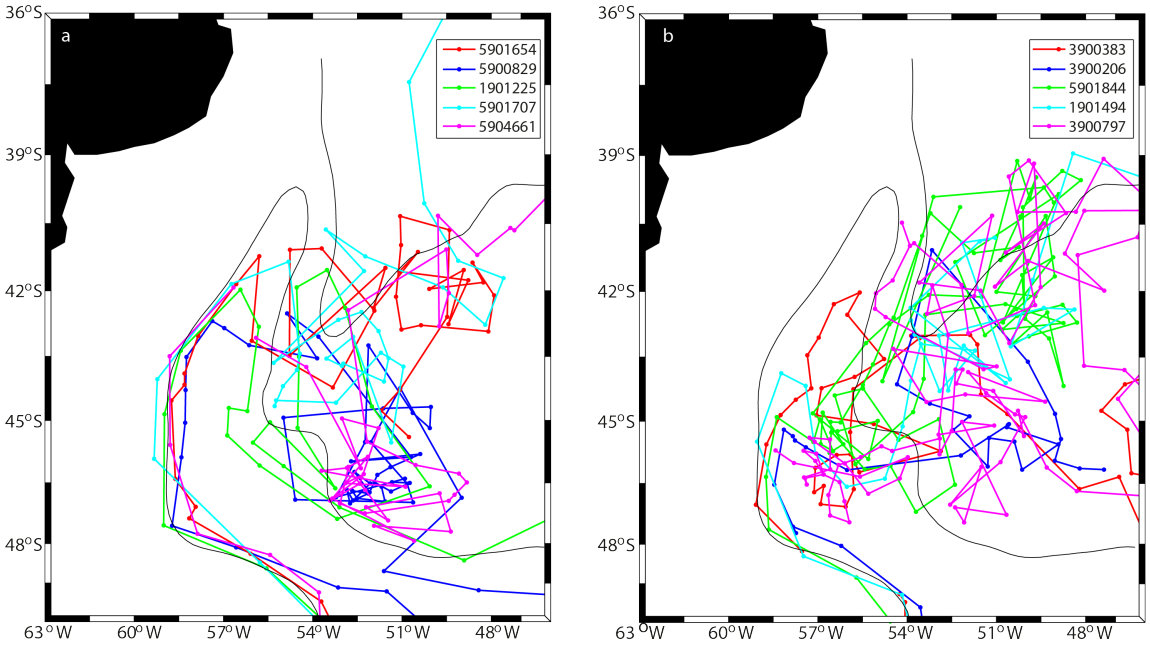

Fig. 3. 14: Selected trajectories of Argo floats (parking depth at 1000 m) that departed the along-slope MC (a) near 42°S and (b) south of 44°S. The dots indicate the location of the float as it surfaced approximately every 10 days.

The origin of the intense interior northward flow may be connected to the outflow transport associated with the BCF. Considering only the upper 400 m, this along-front jet intensifies largely from the frontal to the confluence perimeters through the incorporation of the subantarctic waters drawn by the cyclonic SE-C. As a consequence, there is an intense along-front eastward transport cross the confluence perimeter: down to γ^n= 27.81 kg m^{-3} this amounts to 109.7 $\pm$ 15.1 Sv, with about half (50.8 Sv) in baroclinic balance and the other half (58.9 Sv) associated with the flow at the reference isoneutral.

Our estimate for the along-front transport through the confluence perimeter is quite large, about twice the value of the SAC as obtained by other authors (Maamaatuaiahutapu et al., 1998; Jullion et al., 2010). The mean March 2015 ADT distribution indeed suggests that, after overtaking the perimeter of the confluence region, only a fraction of the flow will continue east as the true SAC, with most of it recirculating south to close the SE-C. We may use Jullion et

al.'s (2010) transport estimates along the BCF at 35^{o}W, 44 $\pm$ 14 Sv, in order to assess the size of this eastern recirculation. Their minimum transport condition (mean minus one standard deviation, i.e. 30 Sv) would imply that the entire eastward flow along the BCF at 35^{o}W was composed by waters of subtropical origin (recall our estimate for the BC is 29.1 $\pm$ 8.3 Sv). This situation (110 Sv flowing east at 51^{o}W with 30 Sv of subtropical origin) apparently leaves 80 Sv for recirculating south between 51^{o}W and 35^{o}W. However, we further notice that only about half the total along-front transport exiting the confluence perimeter is in barotropic transport (58.9 Sv) while most of the interior northward transport is barotropic (76.2 Sv out of 78.9 Sv). In the absence of any clear baroclinic-barotropic flow-conversion process, this sets an upper recirculation limit of about 61.6 Sv (the barotropic 58.9 Sv of the SAC plus the baroclinic 2.7 Sv of the SE-C).

Ferrari et al.'s (2017) analysis of the modes of spatial variability in the BMC helps identify the dominant contributions to the observed flow at the time of the cruise. These authors carried out an empirical orthogonal function (EOF) analysis of 24 years of ADT data in the BMC and found that the first mode (explaining 24 % of the variance) was associated to the northward penetration of the MC while the second mode (17 % of the variance) was associated to the development of a near-zonal pattern of anomalies changing sign every couple of degrees. The temporal evolution of the ADT field previous and during our cruise supports the view of such a zonal pattern along 40-42^{o}S, between about 47^{o}W and 57^{o}W, corresponding to a situation of maximum positive EOF-2 values. This condition could coincide with a period of maximum positive EOF-1 values – what Ferrari et al. (2017) identify as a strong Malvinas regime – hence leading to a short weakening of the along-slope MC (Paniagua et al., 2018) and the reinforcement of all interior recirculations, including the cyclone and anticyclone southeastern features responsible for the 78.9 Sv northward recirculation.

It is worth pointing at a possible connection between the reinforcement of the southeastern interior recirculation with the formation of anticyclonic features on the outer edge of the Zapiola Gyre (Saraceno and Provost, 2012). According to these authors, the anticyclones form on time scales on the order of a few months, that is, with intermittency comparable to the periodicity that holds most of the EOF-2 energy (Ferrari et al., 2017). Hence, the interaction of this anticyclone with the eastward along-BCF flow may be the initial factor leading to the creation of a zonal pattern of alternating ADT anomalies; confirmation of this hypothesis, however, lays beyond the objective of our study.

The above considerations endorse the idea that the observed interior northward transport (at least 78.9 Sv) is related to both the offshore diversion of the along-slope MC and the recirculation of the along-front flow exiting the BMC. The relative contributions are uncertain but our analyses suggest that most of it comes from the barotropic recirculation of the along-front

flow (up to about 61.6 Sv) although a non-negligible fraction (at least 17-18 Sv) comes from the MC itself, hence endorsing the idea of the existence of an interior MC branch. This branch would develop during the weak Malvinas regime (Ferrari et al., 2017), being associated with the upstream diversion of the along-slope MC and the intensification of near-barotropic interior mesoscale features, hence being neither a permanent nor a transient feature.

3.6.3 Transformation and incorporation of subantarctic waters to the subtropical gyre

The BMC has been reported to be a key site for the incorporation of intermediate waters of southern origin (SAMW and AAIW) into the subtropical South Atlantic Ocean (Gordon, 1981; Sloyan and Rintoul, 2001). These waters subduct at the SAF and BCF to become intermediate waters, which follow north into the Atlantic Ocean in order to balance the southward flow of NADW (Sloyan and Rintoul, 2001; Garzoli and Matano, 2011).

The inverse model shows that most waters of southern origin reaching the BMC (96.8 Sv out of 166.5 Sv) belong to the intermediate strata, composed by AAIW and SAMW. Considering the waters of southern and northern origin as being separated by the BCF, we find that these intermediate waters are the ones that have the largest transport imbalances [Table 3.4]. Indeed, the deepest layers of the Confluence model experience a net gain (there is a net inflow of 11.9 Sv of AAIW and UCDW in the southern segment and a net outflow of 6.5 Sv in the northern segment) while the SAMW experiences a net loss in both segments (3.2 Sv through the south and 1.0 Sv through the north); further, the surface and subtropical waters show a net loss (net inflow of 1.8 Sv of surface and STMW through the northern segment and net outflow of 3.3 Sv through the southern segment). All together, these results reveal 5-6 Sv of net upward diapycnal transfer in the frontal system, from the intermediate to the mode and central waters.

Table 3. 4: Mass transports south and north of the BCF (in Sv, positive out of the box) in the confluence model

	South BCF			North BCF		
Water mass	In	Out	Net	In	Out	Net
Surface	-9.0	11.5	2.5 ±0,4	-11.4	9.9	-1.5 ±1,8
STMW	-16.7	17.5	0.8 ±1,3	-14.0	13.7	-0.3 ±2,3
SAMW	-29.1	32.3	3.2 ±1,4	-7.3	8.3	1.0 ±2,3
AAIW	-67.7	61.2	-6.5 ±2,0	-6.7	9.9	3.2 ±2,8
UCDW	-43.9	38.5	-5.4 ±1,3	-1.3	4.6	3.3 ±2,6
Total	-166.5	161.1	-5.4 ±6,2	-40.6	46.2	5.4 ±6,2

The results in Table 3.4 show that most of the SAMW and AAIW transported east along the BCF are of subantarctic origin (relatively cold, fresh and highly oxygenated) but also indicate that about 20 % of these water masses come from the BC, after having traveled through the

subtropical gyre [Fig. 3.13] (Garzoli and Gordon, 1996; Boebel et al., 1999; Garzoli and Matano, 2001). Valla et al. (2018) have recently argued that this recirculation of SAMW and AAIW is meridionally elongated, with the northward flow occurring only 400-600 km from the slope. Indeed, along the confluence perimeter, the isoneutral strata holding the SAMW and AAIW (26.8-27.55 kg m^{-3}) present waters relatively fresh and with high DO values in the southern segment that contrast with saltier and much less oxygenated waters incorporated through the north [Figs. 3.6d and 3.15].

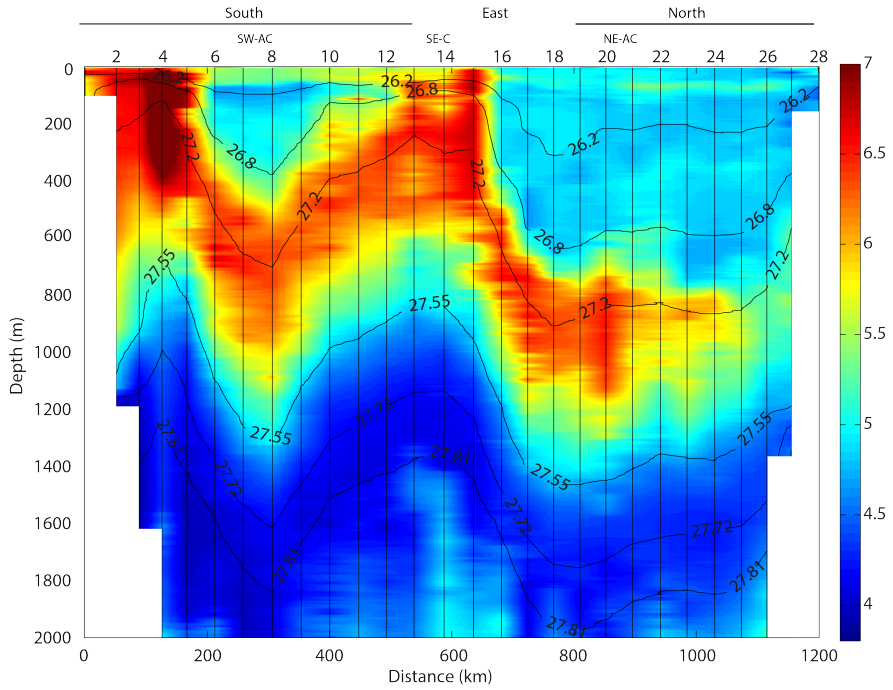

Fig. 3. 15: Vertical section of DO (ml l^{-1}) along the rim of the confluence model. The black lines represent the isoneutral water-mass boundaries used in the inverse model and the vertical black lines indicate the data points. The southern, eastern and northern edges follow those sectors shown in Figure 3.1b, and the approximate extent of the mesoscale eddies is indicated.

The θ, S and DO distributions point at the existence of substantial variability in the frontal region but the details are not clear. Hence, we turn to property-property diagrams to further investigate the mixing of southern and northern waters in the frontal region [Fig. 3.16]. We consider four different groups of stations: station 3 to characterize the upstream MC, station 26 to typify the upstream BC, a third group of 20 stations within the frontal area, and a fourth group of seven stations along the confluence perimeter (stations 16 to 22); all stations (except number 3) are located north of the BCF in order to investigate the intrusions of subantarctic waters [Fig. 3.3b].

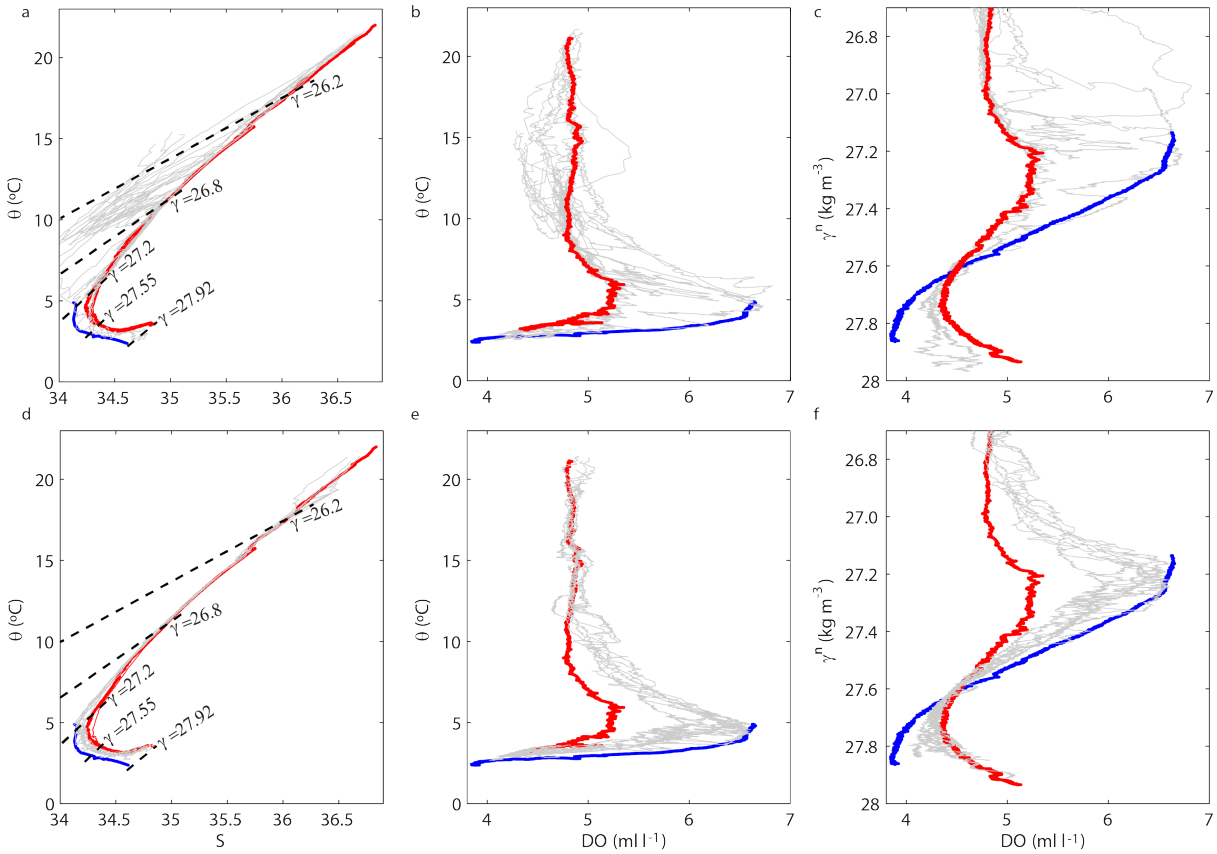

Fig. 3. 16: (a, d) θ - S diagrams, (b, e) θ – DO diagrams and (c, f) DO as a function of γ^n. In all panels the blue and red lines characterize the MC (station 3) and BC (station 26), respectively. In the upper panels the grey lines represent all stations within the frontal area and north of the BCF; in the lower panels the grey lines correspond to stations in the eastern sector of the confluence perimeter and north of the BCF (stations 16 to 22). The black dashed lines in (a, d) represent the γ^n contours used to define the different water masses.

Possibly the most evident aspect in the property-property diagrams is the practical absence of the STMW strata in the southern stations. North of the BCF, this water mass is less oxygenated in the upper slope (stations 27 and 28, not shown) and within the frontal stations; in contrast, the middle-slope BC station (26) and all stations along the confluence perimeter show STMW with relatively high DO values. This is consistent with the view that old STMW enters de BMC through the boundary current and follows along the BCF, where it mixes with younger water and becomes oxygenated, before continuing both eastwards and northwards (Valla et al., 2018).

Considering the intermediate waters (SAMW and AAIW), all slope southern and northern stations (here illustrated by stations 3 and 26) have similar vertical distributions of θ, S and DO [Fig. 3.16]. In contrast, within the frontal stations there is high variability between adjacent stations and depths, due to substantial horizontal interleaving. Similarly to what happened with the STMW, the variability in these deep strata is largely gone by the time these waters reach the confluence perimeter.

We may investigate what processes are behind this smoothing out of properties by considering the case of along-isopycnal mixing between two end members. Specifically, we select stations 3 and 26 to respectively characterize the MC and BC conditions and, for each neutral density level, we obtain the corresponding temperature, salinity and DO end-water values. The temperature, salinity and DO values of a water parcel at any neutral-density level of a frontal station are then expressed as the linear combination of the two end-water types. For steady-state conditions and conservative water properties, along-isopycnal mixing should lead to the same mixing fraction for all water properties, so that any observed difference may be attributed to diapycnal mixing.

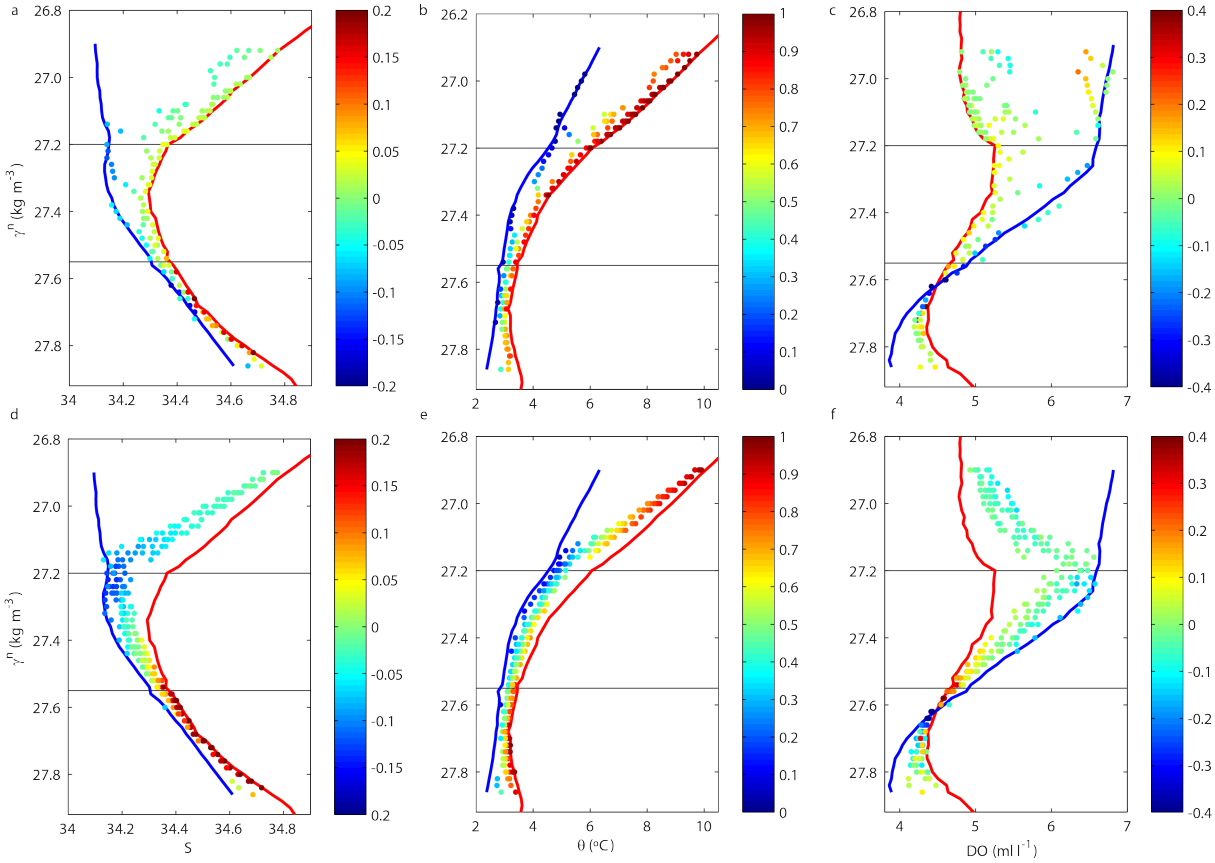

Fig. 3. 17: (a, d) S, (b, e) θ and (c, f) and DO as a function of γ^n, at intervals of 0.02 kg m^{-3}. In all panels the blue and red lines characterize the MC (station 3) and BC (station 26), respectively, and the horizontal lines delimit the different water masses. In the upper panels, the dots represent data from stations north of the BCF within the frontal area; in the lower panels, the dots correspond to stations in the eastern sector of the confluence perimeter and north of the BCF (stations 16 to 22). (b, e) The color-coded values indicate the mixing fraction, with zero indicating pure MC water (dark blue) and one denoting pure BC water (dark red); (a, d) difference between the S and θ mixing fractions, and (c, f) difference between the DO and S mixing fractions (notice the change in colour code).

The results of the above procedure are shown in Figure 3.17, with the θ, S and DO profiles plotted as a function of γ^n. In the conservative-temperature versus neutral-density profile we

show the fraction of the BC water type that contributes to the observed value (the complement to one represents the fraction of the MC water type); notice that the contribution of the BC and MC water types to the observed temperature is inversely proportional to the along-isopycnal difference between the observed temperature and the BC and MC temperatures, respectively. If we repeat the procedure for the salinity and DO profiles we would obtain water fractions that, for entirely along-isopycnal mixing, should not change (given the smallness of the frontal and confluence domains, we may reasonably assume DO as conservative). However, we observe that the S and θ mixing fractions differ by up to 20 %, and the DO and θ mixing fractions differ by as much as 40 %. We interpret these differences as the consequence of diapycnal mixing between water masses that bear different ratios among water properties. For example, over the entire SAMW stratum DO is approximately constant but both θ and S change linearly with depth, so that vertical mixing brings larger property anomalies for θ and S than for DO.

3.7 Concluding remarks

The Brazil-Malvinas Confluence (BMC) is a very intense frontal system that results from the encountering of two major western boundary currents: the northward Malvinas Current (MC), which carries subantarctic waters, and the southward Brazil Current (BC), which carries a mixture of subantarctic and subtropical waters. At the BMC, the surface manifestation of this frontal system is the Brazil Current Front (BCF), set at the absolute dynamic topography (ADT) contour of 0.30 m (Ferrari et al., 2017).

The MC is possibly the strongest equatorward boundary current in the entire global ocean, with intense surface and subsurface currents. As the MC encounters the BC along the continental slope, it undergoes a sharp 180^{o} turn and the entire frontal system follows south, in what is known as the MC retroflection (MRC) and BC overshoot (BCO). The characteristics of this convoluted turn and its leeward structure at 41^{o}S has been the subject of several recent studies (Ferrari et al., 2017; Artana et al., 2018; Paniagua et al., 2018; Valla et al., 2018). These studies show that the BMC has substantial temporal variability, between times of an intense impinging MC and a powerful MRC-BCO return flow, and times when the MC weakens, characterized by the MRC-BCO breaking into an isolated anticyclone and a cyclone forming further east.

Our study of this intense frontal system refers to the March 2015 conditions, as observed with cruise data (8-22 March) encircling the BMC at two different spatial scales. These data are analysed with an inverse model, helped by both altimetry data and velocity time series over the slope near 41^{o}S, in order to assess the patterns of circulation associated with the boundary and frontal currents, their barotropic and baroclinic contributions, and the intensity of the cross-frontal exchange in the upper 2000 m. The model reference level is set at γ^{n} = 27.81 kg m^{-3} (found between 1400 and 2000 m) for the outer (confluence) region and at z = 400 m for the inner (frontal)

area, and altimetry data are used to connect both domains.

The March 2015 BC depicts a fairly classic picture: its along-slope transport down to γ^n = 27.81 kg m^{-3} (29.1 $\pm$ 8.3 Sv) lies in the middle of the reported range of variation, largely baroclinic (29.0 Sv). Most of the flow belongs to the surface and Subtropical Mode Waters (18.0 $\pm$ 2.0 Sv), although there is a quite significant southward flow of subantarctic waters (10.2 $\pm$ 2.8 Sv). These southward-flowing subantarctic waters are much depleted in oxygen, indicating that they have followed a long subtropical pathway before returning to the northern edge of the BMC.

The situation for the MC and the eastward jet associated with the BCF, however, differs greatly from the classic description. The ADT reveals conditions that characterize a weak along-slope MC at 41^{o}S: the northward loop is strangulated and the MRC-BCO system has evolved into an anticyclone, and an elongated cyclone is formed further east. Surprisingly, this corresponds to a period (January-April) that Ferrari et al., (2017) and Paniagua et al. (2018) identify as a strong Malvinas regime. Close inspection of Paniagua's time series, however, shows that the along-slope MC at 41^{o}S weakened substantially during the first 10 days of March, precisely before our cruise. Our inverse model indeed shows a weak along-slope MC near the collision latitude (39.5^{o}S) at the beginning of the cruise and, in contrast, finds a remarkably intense northward interior flow, located between the eastern anticyclone and cyclone (near 53^{o}W). Down to γ^n = 27.81 kg m^{-3}, the along-slope MC transports 28.3 $\pm$ 1.4 Sv, the anticyclone recirculates up to 59.3 $\pm$ 10.7 Sv, and the interior flow accounts for at least 78.9 $\pm$ 13.7 Sv.

We have carefully explored the origin of the intense interior northward flow. The temporal evolution of the sea-surface ADT and the trajectories of Argo floats suggest that there is an eastward diversion of the along-slope upstream MC at latitudes 42^{o}S or greater, potentially favoring the interior branch. Periods of weak along-slope MC transport probably come together with the intensification of the interior currents, as the convoluted MC and MRC strangle, and the slope flow is deviated at either 42^{o}S or 46^{o}S. During this weak-MC periods, it seems possible that the upstream (beyond 46^{o}S) along-slope MC flow finds an alternative interior pathway to reach the BCF. However, the interior northward current is also sustained by the cyclonic recirculation of the water outflow along the BCF. Indeed, we observe a very intense (109.7 $\pm$ 15.1 Sv) South Atlantic Current (SAC) exiting the convergence zone along the BCF and the ADT field and barotropic-baroclinic decomposition suggest that a major fraction of this outflow recirculates cyclonically to feed the interior flow. Grossly speaking, we estimate that the offshore diversion of no less than 17-18 Sv from the upstream along-slope MC and the cyclonic recirculation of some 60 Sv of along-front outflow add together to produce the observed interior northward transport; further, we anticipate that similar situations may occur during the occurrence of a weak-Malvinas regime, hence leading to the notion of an intermittent interior MC.

The inverse model provides other pieces of useful information. The first one is a large barotropic contribution in the MC and SAC for water layers lighter than γ^n = 27.81 kg m^{-3}, by barotropic meaning the contribution associated with the velocities at that reference level. Over half of the SAC transport responds to the reference velocities (58.9 Sv) and the rest to the baroclinic velocities (50.8 Sv). Regarding the along-slope MC at 41^{o}S, 13.3 Sv are baroclinic and 15.0 Sv are barotropic; for the interior northward flow, nearly the entire flow is barotropic (76.2 out of 78.9 Sv). Further, about 70 % of this southern inflow corresponds to Subantarctic Mode and Intermediate Waters (SAMW and AAIW, respectively).

Another relevant piece of information is the net exchange of subantarctic and subtropical waters through the BMC, along some 500 km of the frontal system. The water balance per stratum reveals about 5-6 Sv of net upward diapycnal transfer in the confluence region, with intermediate AAIW and SAMW being transferred to the shallower layers. In particular, we find a substantial net inflow (11.9 Sv) of AAIW and Upper Circumpolar Deep Waters (UCDW) south of the BCF. Assuming along-isopycnal mixing, we calculate the mixing fractions for different water properties, which reveal large differences depending on water property: up to 20 % between temperature and salinity and 40 % between temperature and dissolved oxygen. Both evidences – the transport imbalances per layer on both sides of the BCF and the differences in mixing fraction from one property to another – point at substantial cross-frontal and diapycnal water exchange in the BMC.

The BMC, at the crossroads of subantarctic and subtropical waters, is a regional process with global implications. We are urged to improve our understanding of its different modes of functioning, characterized by extraordinary temporal and spatial variability (e.g. Ferrari et al., 2017; Artana et al., 2018; Paniagua et al., 2018; Valla et al., 2018). Our results show that the regional pattern of circulation evolves on time scales on the order of weeks and emphasizes the idea that any description of the BMC cannot be understood without monitoring the time history of the upstream along-slope (BC and MC) and interior (Zapiola gyre) conditions. The time series of satellite ADT and mooring velocity indeed expose the existence of many possible combinations, resembling a baroque musical improvisation with an unpredictable outcome. Additionally, there are short and fast submesoscale processes that produce noticeable water mass transformations in the frontal system, causing an even more capricious evolution. The challenge is to decipher the spatial and temporal predominant rhythms but also the way they preferentially connect to create a perpetually changing melody.

Acknowledgments

We are very grateful to the crew, technicians and scientists in the R/V Hespérides for their work during TIC-MOC cruise. We are also indebted to Fabrice Hernandez and the entire MyO-

cean team at Mercator Ocean for providing the one-week-window daily forecasts during the TIC-MOC cruise. We are also thankful to Silvia Garzoli and another two anonymous reviewers for their constructive and useful comments and suggestions. This research has been supported by the Spanish Government through projects TIC-MOC (CTM2011-28867) and VA-DE-RETRO (CTM2014-56987-P), and by RIS-3, PO Feder Canarias through project BOUNDARY (ProID2017010083). Dorleta Orúe-Echevarría has been funded through a FPU contract (ref. FPU2013-02884). In situ CTD and ADCP data are available at Pelegrí et al. (2018). Satellite altimetry data are available at Copernicus Marine Environment monitoring service (CMEMS, http://marine.copernicus.eu/) and SST data at NOAA AVHRR Pathfinder version 5.3 (https://data.nodc.noaa.go). Data for the determination of climatological isoneutral surfaces is available at NOAA's National Centers for Environmental Information World Ocean Database 2013 (https://www.nodc.noaa.gov/OC5/WOD13/). Argo data were collected and made freely available by the International Argo Program and the national programs that contribute to it (http://www.argo.ucsd.edu, http://argo.jcommops.org). The Argo Program is part of the Global Ocean Observing System, http://doi.org/10.17882/42182.

Supplementary material

Table S.3. 1: Comparison (rmsd) between the VADCP at different depths (0 to 700 m, 24 m, 200 m and 600 m) and altimetry derived surface geostrophic current, for the zonal (u) and meridional (v) components and the modulus of the velocity (V) in the confluence model, stations 1 to 4 (MC) and stations 8 to 12 (SW-AC-SEC).

	Confluence model				MC				SW-AC/SE-C			
Depth	0-800	24	200	600	0-800	24	200	600	0-800	24	200	600
rmsd u	0.16	0.25	0.19	0.19	0.13	0.11	0.13	0.14	0.12	0.20	0.14	0.12
rmsd v	0.17	0.20	0.19	0.22	0.32	0.26	0.35	0.31	0.24	0.34	0.30	0.21
rmsd V	0.16	0.22	0.18	0.20	0.16	0.19	0.18	0.19	0.19	0.30	0.26	0.16

Table S.3. 2: Transport (in Sv) constraints through selected portions of the frontal perimeter, imposed following the inverse-model calculations between selected ADT contours through the confluence perimeter. The SAF and BCF correspond to ADT contours of 0.05 and 0.3 m, respectively.

	SAF - 0.25	BCF - 0.57	0.57 - 0.90
Confluence stations	1-3	26-28	
Frontal stations	29-33	43-46	39-43
Transport	5.7	9.7	5.4

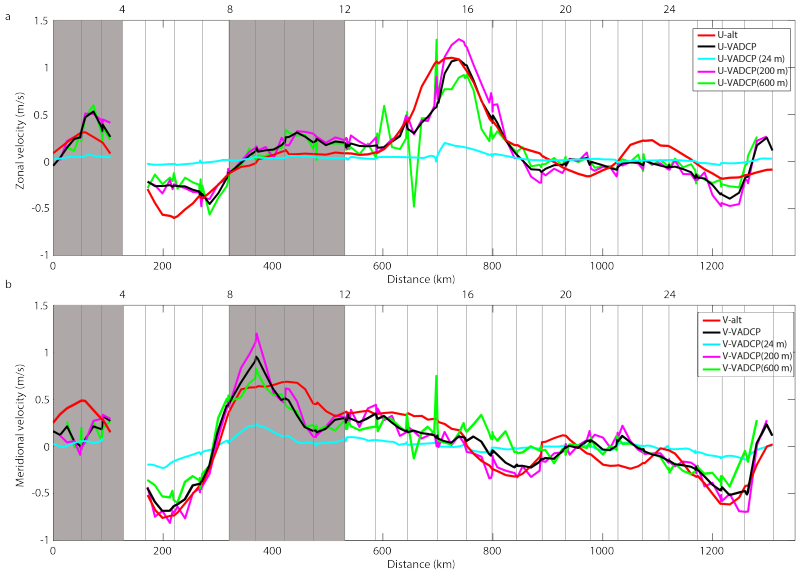

Fig. S.3. 1: Zonal (a) and meridional (b) velocity components retrieved from the satellite altimetry (red) and from the VADCP (at 200 m in magenta, at 600 m in green and the mean value from 24 to 800 m in black). The grey shaded area corresponds to the stations where the confluence model transport is constrained.

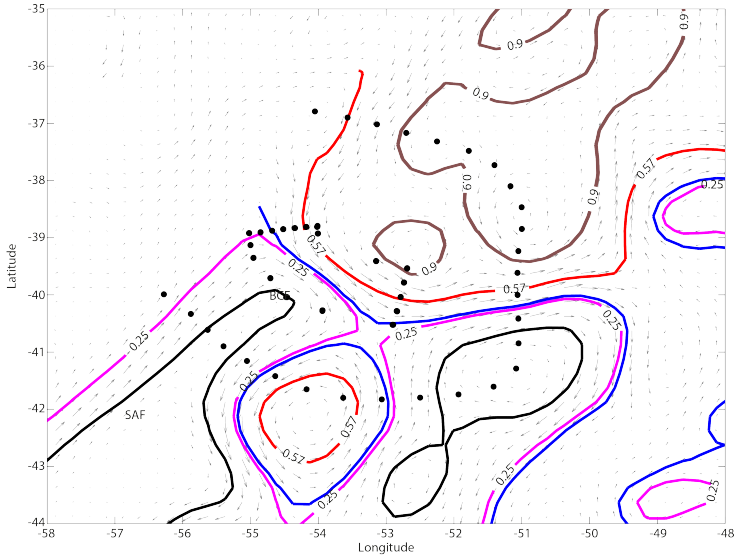

Fig. S.3. 2: Mean sea-surface ADT contours (magenta: 0.25 m; red: 0.57 m; brown: 0.9 m) together with the SAF (black) and BCF (blue). The hydrographic stations are shown as black dots.

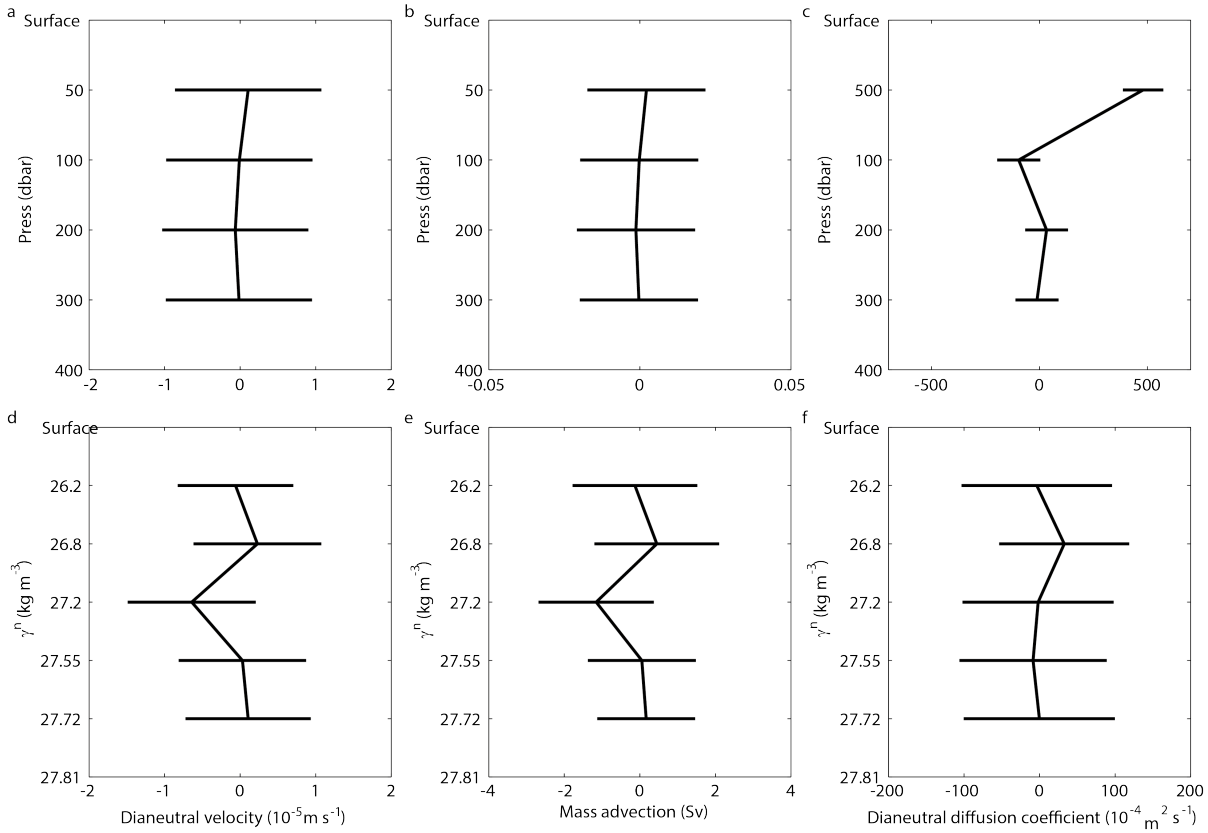

Fig. S.3. 3: (a, d) Dianeutral velocity, (b, e) dianeutral mass advection and (c, f) dianeutral diffusion coefficients for the (a, b, c) frontal and (d, e, f) confluence models. Positive values indicate upward fluxes.

Chapter 4

Temperature spatio-temporal correlation scales in the Brazil-Malvinas Confluence from high-resolution in-situ and remote sensing data

Orúe-Echevarría, D., Castellanos,P., Sans, J., Emelianov, M., Vallès-Casanova, I., and Pelegrí, J.L.
GRL, Accepted

Abstract

Ocean frontal systems may act both as barriers and mixers between different water masses, the latter thanks to very energetic structures with relatively short temporal and spatial scales. Here, we explore the high-frequency temperature variability in the Brazil-Malvinas Confluence through the joint analysis of novel high-resolution SeaSoar measurements and sea surface temperature imagery. Surface spatio-temporal correlation scales range between 1.5 and 6 days and between 20 and 50 km, with the shortest scales along the shelf-break path of the Brazil Current and over the Confluence and the longest ones along the Malvinas Current. The spatial scales display minima along the front, at the surface because of the presence of brackish shelf waters and at the subsurface due to both meso and submesoscale thermohaline intrusions. The smallest cross-frontal vertical correlations, in the 5-10 m range, are associated with submesoscale processes. Overall, temperature variability is enhanced at depth in the frontal system.

4.1 Introduction

Frontal regions are characterized by multiple-scale turbulence (Fu et al., 2007; Lumpkin and Johnson, 2013). In the Southwest Atlantic Ocean, the dominant frontal system is the Brazil Malvinas Confluence (BMC), generated at the encounter of the Brazil (BC) and Malvinas (MC) Currents [Fig. 4.1]. The meandering and retroflection of these currents leads to an intricate multi-scale and highly-energetic region, filled with meso and submesoscale structures such as eddies, rings, filaments and intrusions (Legeckis and Gordon, 1982; Bianchi et al., 1993; Provost et al., 1999; Lentini et al., 2002; 2006). Therefore, this region is thought to be characterized by short temporal and spatial scales of variability (Barré et al., 2006).

The MC (subantarctic) and BC (subtropical) waters present intense contrasts in sea surface height (SSH), primary production and sea surface temperature (SST). These sharp gradients have allowed assessing the spatial and temporal variability of the surface BMC using satellite imagery (Goni and Wainer, 2001; Garcia et al., 2008; Saraceno et al., 2004; 2005; Gonzalez-Silveira et al., 2006; Goni et al., 2011; Machado et al., 2013). In particular, high SST horizontal gradients, of the order of 0.1 ^{o}C km^{-1}, are found in the main frontal systems: the shelf-break Brazil region, the BMC front, the Subantarctic Front (SAF) and the Brazil Current Front (BCF) (Saraceno et al., 2004). Less pronounced SST gradients also show up at the meso and submesoscale structures formed downstream of the BMC (Barré et al., 2006).

Regarding surface temporal variability, most studies have focused on the semi-annual and interannual scales, characterized by the migration of the latitude where the BC diverts from the shelf (Olson et al., 1988; Goni and Wainer, 2001; Goni et al., 2011). Synoptic variability has been associated with the regional and mesoscale structures, particularly with the position of the MC, the BC and the BC overshoot (BCO) (Legeckis and Gordon, 1982; Goni and Wainer, 2001). Garzoli and Garraffo (1989) and Ferrari et al. (2017) found that the BCO moves zonally with time scales of 90-150 days and Provost and LeTraon (1993) have observed that the dominant mesoscale features have temporal and spatial scales of 75-150 days and 100-500 km. Higher frequency surface variations are also expected in the BMC, as for example SST consecutive images show changes up to $\pm$ 4 ^{o}C d^{-1} (Barré et al., 2006). One potential source are the changing winds, which can flush shelf water over much of the frontal area, bringing potential temperature and salinity (θ, S) changes in only a few days (Guerrero et al., 2014; Combes and Matano, 2018). Other studies on thermohaline changes in the Patagonian shelf-break front have found 1- to 5-day correlation times for temperature in the upper 100 m, which have been associated with synoptic atmospheric storms (Garzoli and Simionato, 1990; Valla et al., 2015; Carranza et al., 2017).

Contrary to sea-surface studies, the subsurface variability of θ and S in the BMC remains barely explored. Paniagua et al. (2018) have reported θ/S changes of 0.3 ^{o}C/0.18 in three days at

a slope mooring in the path of the MC (near 41^{o}S and 1000 m depth). This high-frequency variability has been ascribed to either the intense mesoscale activity of the region, with eddies translating at velocities between 1 and 10 km d^{-1} (Pilo et al., 2015; Mason et al., 2017) or to the east-west and north-south BMC migrations at speeds up to 10 km d^{-1} (Legeckis and Gordon, 1982; Garzoli and Bianchi, 1987). Subsurface rapid changes may also be caused by thermohaline intrusions with lifetimes of 5-13 days (Bianchi et al., 1993; 2002) or baroclinic frontal instabilities oscillating with periods of 3-5 days (Garzoli and Simionato, 1990).

Subsurface structures may be largely decoupled from the surface fields due to the development of the seasonal thermocline (Provost et al., 1996; Saraceno et al., 2004) and the presence of localized thermohaline frontal intrusions (Orúe-Echevarría et al., 2019). However, their existence does influence the conditions at the sea surface, especially affecting the water elevation and velocity (Maamaatuaiahutapu et al., 1999). Hence, a proper knowledge of these subsurface scales is necessary not only to quantify the water transfer cross the frontal system, of major relevance in the large-scale redistribution of properties, but also to improve the design of operational models.

4.2 Data and methods

The RETRO-BMC cruise was conducted on board R/V Hespérides between 8 and 28 April 2017 in the BMC frontal region (Pelegrí et al., 2019). Here, we analyse data from 12 cross-frontal high-resolution transects aimed at finding the short temporal and spatial scales in the frontal region. These transects were done within five days, between 40.6^{o}S-56.7^{o}W and 39^{o}S-53.6^{o}W, as part of two surveys carried out with a winged and towed undulating platform (SeaSoar), which included temperature, salinity and pressure sensors (Annex 4.1, Supporting Information).

Each of the two SeaSoar surveys consisted of 6 near-parallel transects, ranging from 55 to 90 km, with all tracks separated by 18 km (except tracks I and II of SeaSoar1, which were 27 km apart) and covering an area of approximately 135 km zonally and 100 km meridionally [Fig. 4.1]. The individual transects were oriented cross the frontal region, following tracks either 25^{o} or 205^{o} from the true north. The first survey (SeaSoar1, 17-18 April) covered 620 km and was completed within 46 hours; the second survey (SeaSoar2, 19-21 April) started 40 hours after completion of SeaSoar1 and extended over 751 km in 52 hours.

The temperature and salinity data were gathered as a function of pressure for all cross-frontal tracks as well as in the five short transects between them. These raw data were linearly binned to 1-dbar vertical intervals, every 5 km along the SeaSoar tracks following the methodology in Sans (2018). Finally, the potential temperature (θ) field was calculated and interpolated horizontally onto a regular 0.05^{o} x 0.05^{o} grid; hereafter, whenever mentioning temperature, we will always implicitly refer to the potential values.

Both surveys were carried out from west to east, in the same direction of the mean flow over the frontal region, as an attempt to minimize aliasing effects. Considering the distance between the first and last cross-frontal transect (90-100 km) and the time of the survey (40-50 hours) it turns out that the vessel moved along the front with a mean speed of 0.5-0.7 m s^{-1}, similar to the characteristic along-front sea-surface velocities [Fig. 4.1 and Fig. S4.3, Supporting Information) (Orúe-Echevarría et al., 2019). Further confidence on the results comes from the fact that, during each survey, the frontal displacements were relatively small as compared with the extension of the cross-frontal tracks; the only large displacement occurred between 20 and 21 April 2017, in the western portion of the survey area, when the ship had already reached the eastern part of the domain (Fig. S4.4, Supporting Information).

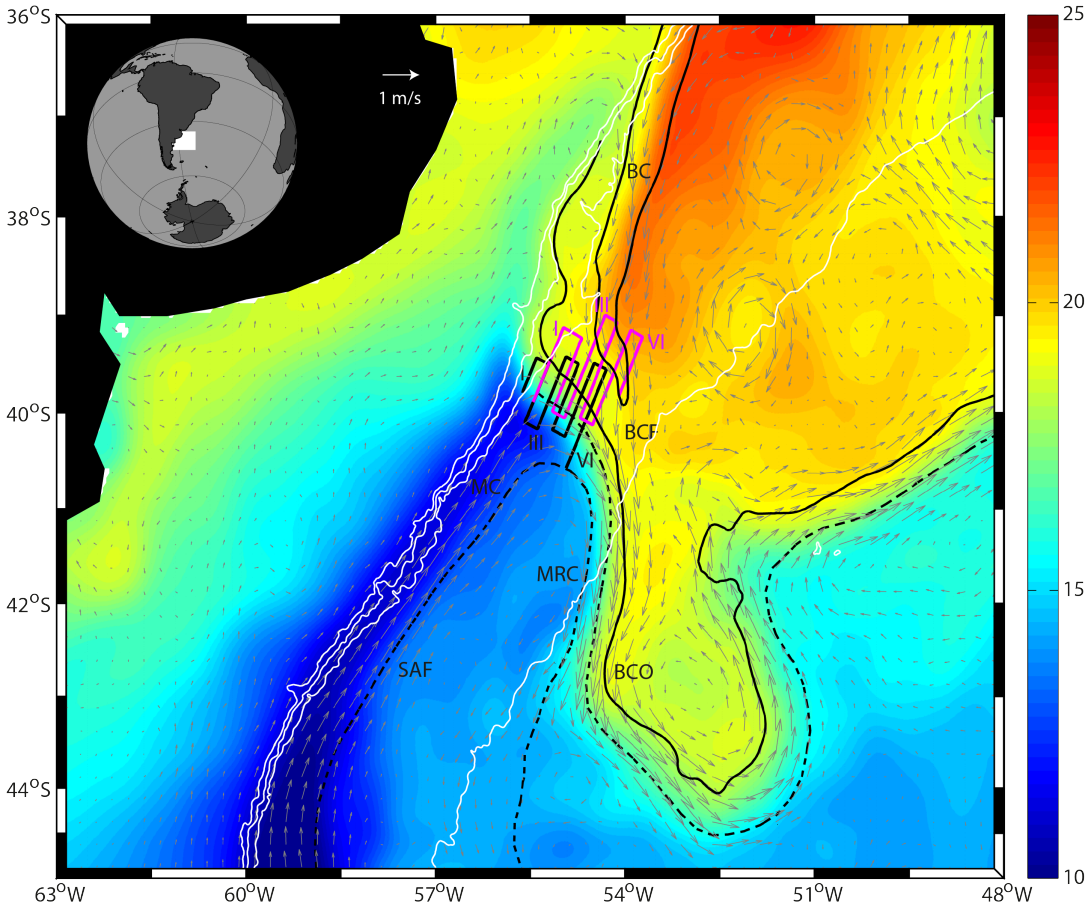

Fig. 4. 1: Mean SST (°C) in the southwest Atlantic Ocean for 17-21 April 2017 as deduced from the OSTIA data. The location of the SeaSoar1/SeaSoar2 survey tracks are shown by black/magenta lines, with Roman numbers indicating the cross-frontal transects for each survey. Grey vectors correspond to mean surface velocities from gridded altimetry for these days. Dashed black lines indicate the mean position of the Subantarctic Front (SAF, ADT=-0.05 m) and Brazil Current Front (BCF, ADT=0.3 m) as defined by Ferrari et al. (2017). Solid black lines indicate the position of the BCF based on SST gradients following the methodology in Saraceno et al. (2004). White lines correspond to the 200, 500, 1000 and 5000 m isobaths (GEBCO, 2008). The main streams are labelled: Brazil Current (BC), Malvinas Current (MC), Malvinas Return Current (MRC) and Brazil Current Overshoot (BCO).

In addition to hydrographic data, we also use satellite SST and SSH data for April 2017. Both datasets are provided by the Copernicus Marine and Environment Monitoring Service (CMEMS)

(http://marine.copernicus.eu). The multi-scale optimal interpolation scheme in the SST product allows studying the frontal variability at temporal/horizontal scales larger than about 1day/10 km (Donlon et al., 2012; Reynolds et al., 2013) while the SSH can only resolve temporal/horizontal scales longer than 20 days/40 km (Pujol et al., 2016).

The autocorrelation decreases with time and distance, over scales that depend both on external forcing and local dynamics (Sumata et al., 2018). A correlation scale can be defined as to characterize the prevailing temporal and spatial scales, with short scales identifying areas of high-frequency changes. Throughout this study we fit the autocorrelation to a Gaussian function and define the correlations in terms of *e*-folding scales (Molinari and Festa, 2000) (Annex 4.2, Supporting Information). Using SST satellite data, we can determine the sea-surface temporal and horizontal correlation scales. Similarly, the SeaSoar data allow estimating the horizontal correlation scales in the survey area and the vertical correlation scales along the cross-frontal sections. In contrast, the two SeaSoar provide temperature differences in about three days but do not allow calculating the temporal subsurface time correlation. The signal-to-noise ratio (SNR) in the autocorrelation functions is inferred from the fraction of explained variability (Sprintall and Meyers, 1991; Hosoda and Kawamura, 2004) (Annex 4.2, Supporting Information).

4.3 Results

4.3.1 High-resolution three-dimensional view of the frontal system

The SST and surface geostrophic velocity fields show the MC flowing northward along the 500-1000 isobaths and reaching 40^{o}S with θ <10 ^{o}C and S <34.5, where it encounters warmer and saltier subtropical waters [Fig. 4.1]. These velocity fields, together with the salinity and temperature sections [Fig. 4.2 and Figs. S4.5 and S4.6, Supporting Information] also reveal the BC crossing the north-eastern end of the study area, and show relatively colder shelf waters covering most of the northern and western sections. Surface salinity values confirm the presence of widespread low-salinity shelf waters over the study area [Figs. S4.5 and S4.7, Supporting Information]. East of 55^{o}W, the BC follows south as a well-developed elongated BCO that reaches as far as 44^{o}S and 51^{o}W.

Figure 4.1 also shows the intricate confluence of the SAF and BCF in the BMC region, i.e. the collision of the two boundary currents that leads to a single yet complex BMC frontal system. The three-dimensional θ and S fields [Fig. 4.2 and Fig. S4.5-S4.8, Supporting Information] illustrates this complexity, with one main transition from subantarctic to subtropical waters at the isotherm/isohaline of 12 ^{o}C/34.7 and a second transition at the isotherm/isohaline of 17 ^{o}C/35.3. Interestingly, the classical definition of the BCF (in terms of ADT=0.3 m) coincides with the first transition and the entire region between the first and second transition is the one that displays most of the interleaving. North of the second transition, which is observed on

the northeastern end of the survey region (crossed by tracks III-VI of SeaSoar2), the subtropical waters remain fairly unperturbed.

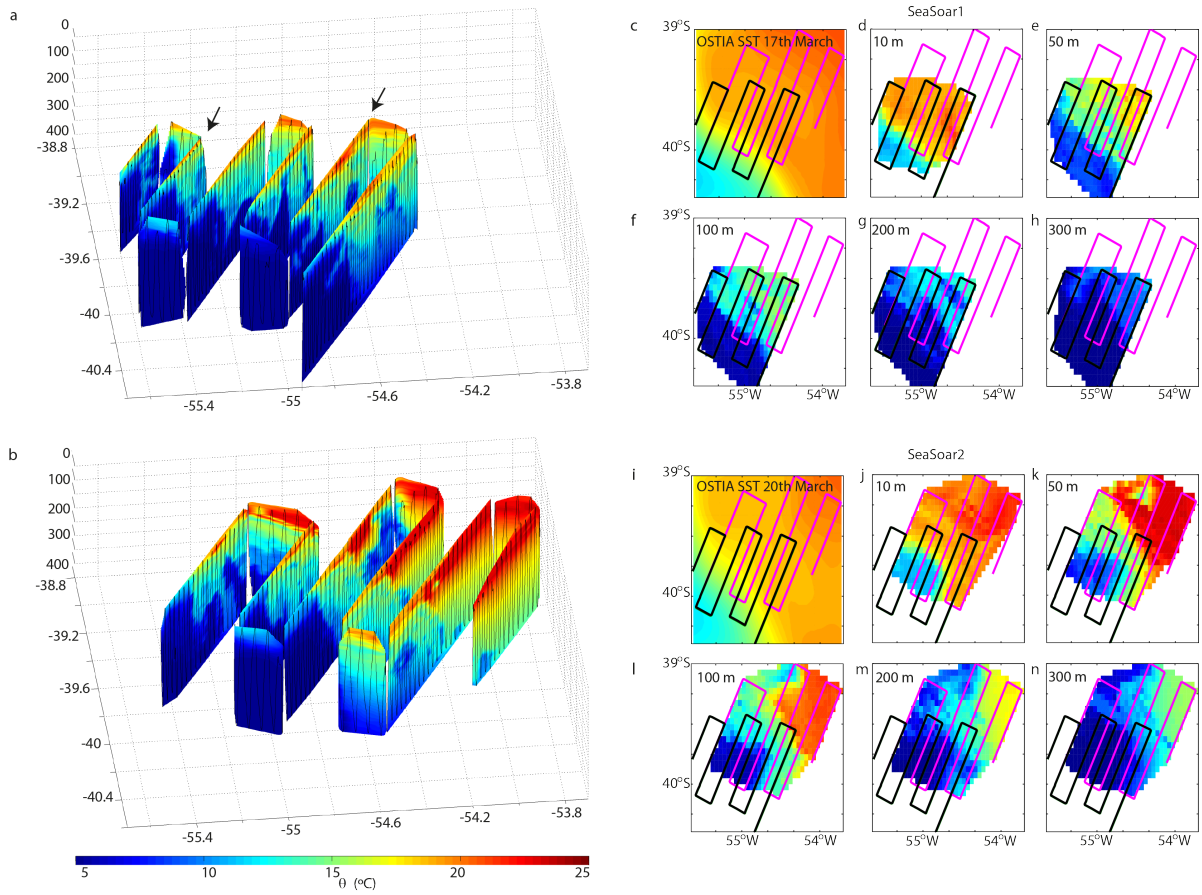

Fig. 4. 2: Three-dimensional temperature view during (a) SeaSoar1 and (b) Seasoar2. The black vertical lines indicate the central point of the SeaSoar diving cycle. The black arrows show vertical sections II and V of SeaSoar1, used to illustrate the vertical correlation scales in Figure 4.4. OSTIA SST for the (c) 17 and (i) 20 April 2017. Horizontal temperature fields at 10, 50, 100, 200 and 300 m for (d-h) SeaSoar1 and (j-n) SeaSoar2. The location of the SeaSoar1/SeaSoar2 tracks is shown by black/magenta lines. (Additional horizontal temperature and salinity fields are shown in Figs. S4.7 and S4.8, Supporting Information.)

The frontal system is also characterized by substantial thermohaline intrusions. In the western stations (I-III in SeaSoar1 and I-II in Seasoar2), the subantarctic side remains fairly immaculate but the subtropical side displays mesoscale features. There are at least two tongues or wedges of subantarctic waters intruding into the subtropical region – a central one during SeaSoar1 and a western one during SeaSoar2 – some 10-30 km wide and stretching by as much as 100 km [Figs. 4.2d-h and 4.2j-n, Figs. S4.7 and S4.8, Supporting Information]. These subsurface tongues are smaller than the surface ones and have no surface expression in the SST and ADT images [Fig. 4.1 and Fig. S4.3, Supporting Information]. In contrast, the eastern sections (IV-VI in SeaSoar1 and III-VI in SeaSoar2) reveal opposite-sign submesoscale intrusions, i.e. warm/cold in the subantarctic/subtropical sides of the front. All mesoscale and submesoscale intrusions are found between the 26.5 and 27.0 isopycnals, displaying temperature gradients sharper than at

the sea-surface (0.3-0.8 ^{o}C km^{-1}) [Figs. S4.5 and S4.6, Supporting Information].

4.3.2 Temporal correlation scales

For the entire Southwest Atlantic Ocean, the OSTIA SST temporal correlation scales range between 1.5 and 6 days [Fig. 4.3a]. The shortest scales (1.5-3.5 days) are associated with the shelf-break in subtropical waters, the BMC front and the BCO, i.e. to frontal regions with intense currents and high mesoscale activity, characterized by elevated eddy kinetic energy and rapid migrations of the frontal structures [Fig. S4.4, Supporting Information] (Legeckis and Gordon, 1982; Garzoli and Simionato, 1990; Saraceno and Provost, 2012). In other areas, including the MC and MRC, fewer mesoscale structures develop (Artana et al., 2016), leading to less variability, longer temporal correlation scales (5-6 days) and higher SNR [Fig. S4.9a, Supporting Information].

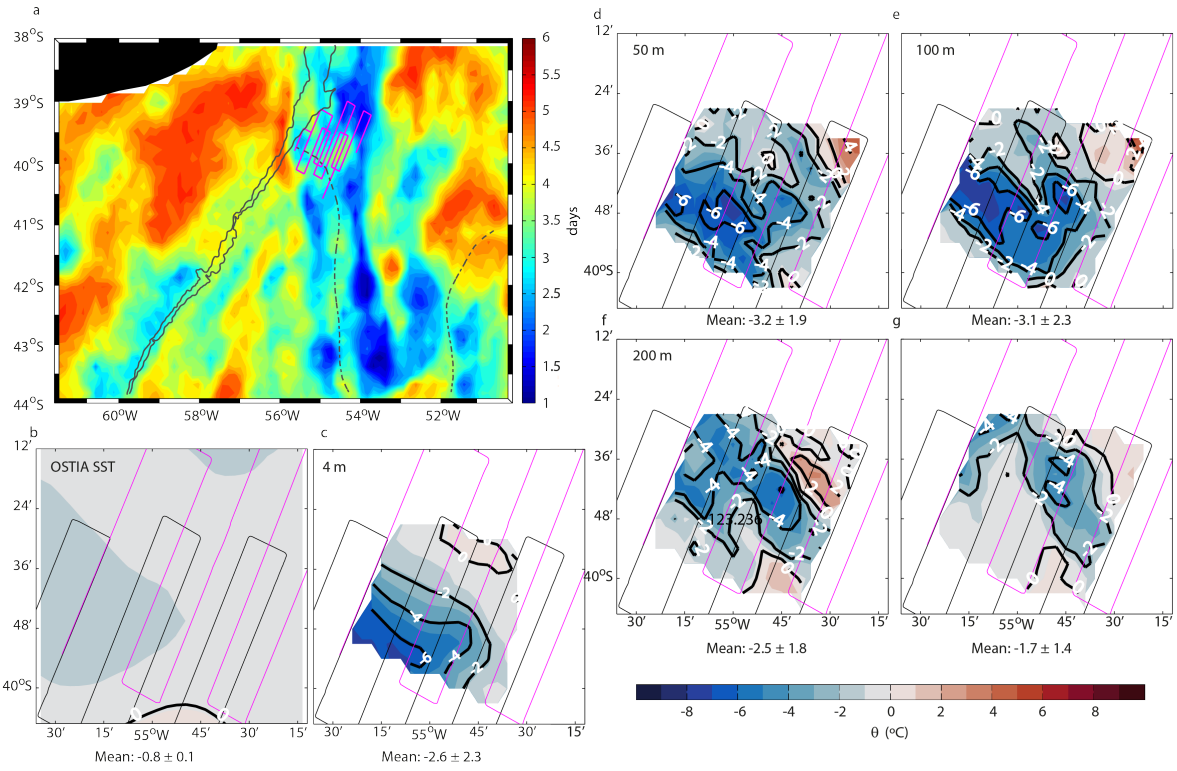

Fig. 4. 3: (a) OSTIA SST temporal correlation scale (days); the black solid lines correspond to the 500 and 1000 m isobaths while the black dashed line indicates the mean position of the BCF for April 2017. (b) OSTIA SST difference between the 20 and 17 April 2017. Temperature differences between SeaSoar2 and SeaSoar1 at (c) 10, (d) 50, (e) 100, (f) 200 and (g) 300 m. Negative values denote cooling; in each panel, the mean standard deviation temperature differences are indicated. The black/magenta lines show the SeaSoar1/SeaSoar2 tracks.

During April 2017 and in the limited region enclosing the SeaSoar survey area, the OSTIA SST temporal correlation scales range between 2 and 4.5 days, with a mean monthly value of 3.0 $\pm$ 0.2 days (see the sampling window in Fig. 4.3b). Over the SeaSoar survey tracks, the OSTIA

SST differences between 17 and 20 April (precisely 3 days) range between -1.9 ^{o}C and 2.1 ^{o}C, with the greatest cooling over the western sections and slight warming south of the SeaSoar tracks. We may also use the entire April data to generate, at each grid point, time series of SST differences for 3-day intervals (not shown); when averaged over the SeaSoar survey area the mean standard deviation is 1.1 ^{o}C and the mean maximum-absolute-difference is 2.6 ^{o}C.

The sea-surface OSTIA and 4-m SeaSoar temperature differences indicate cooling over the frontal region, though the SeaSoar data shows greater temperature differences [Figs. 4.3b,c]; these discrepancies possibly reflect some level of near-surface homogenization due to a shallow summer mixed layer (Provost et al., 1996) and the spreading of brackish shelf waters over the frontal region, but may also respond to an increased uncertainty caused by high cloud-coverage in April 2017 (around 65 %). The subsurface temperatures also display a generalized cooling between 17 and 20 April, with peak absolute values between 50 and 150 m [Figs. 4.3d-f]. At 300 m, the peak absolute differences are smaller (yet reaching values similar to 10 m) and remain restricted to the central region, associated with the intrusion of subantarctic waters [Fig. 4.3g].

The different character of the surface and subsurface fields in the frontal SeaSoar survey area is remarkable. The characteristic 3-day SST variability (mean 1.1 ^{o}C and maximum 2.6 ^{o}C from OSTIA for April, and mean 2.2 ^{o}C and maximum about 5 ^{o}C from the 10-m SeaSoar data between 17 and 20 April) is substantially less than the mean values in the 50-150 m depth interval (mean 2.8 ^{o}C and maximum about 7 ^{o}C from the SeaSoar data between 17 and 20 April).

4.3.3 Vertical correlation scales

We examine the vertical correlation scales through both individual and ensemble SeaSoar cross-frontal sections. In every individual section, the distribution of the vertical correlation scales is patchy, with values ranging between 10 and 25 m [Fig. S4.10, Supporting Information]. Low values are related to large vertical changes in temperature, either associated with the seasonal thermocline, with the edge of frontal structures or with intrusions of distinct water masses.

An inspection of all sections suggests that some differences are associated with the distance (and hence time) from the initial encounter of the MC and BC. In Figure 4.4a,b we illustrate the results for two sections: one in the western boundary of the survey area, close to the encounter point of the BC and MC (section II of SeaSoar1), and the other in the eastern margin (section V of SeaSoar1). The small correlation lengths (8-12 m) correspond roughly to those bands of high background vertical stratification; the SNR is large over the entire domain, generally above 3 and reaching 7 in the unperturbed well-stratified subtropical waters [see Fig. S4.9b, Supporting Information, for section II of SeaSoar1]. In the western section, the subantarctic side of the frontal system displays relatively high correlation values, indicative of the absence of intrusions,

while the subtropical side shows some large features, about 50-80 m thick and 60 km long [Fig. 4.4a]. In the eastern section, we still find some large features in the subtropical side but there are also small intrusions on both sides of the frontal system, some 10-50 m thick and 10-20 km long [Fig. 4.4b].

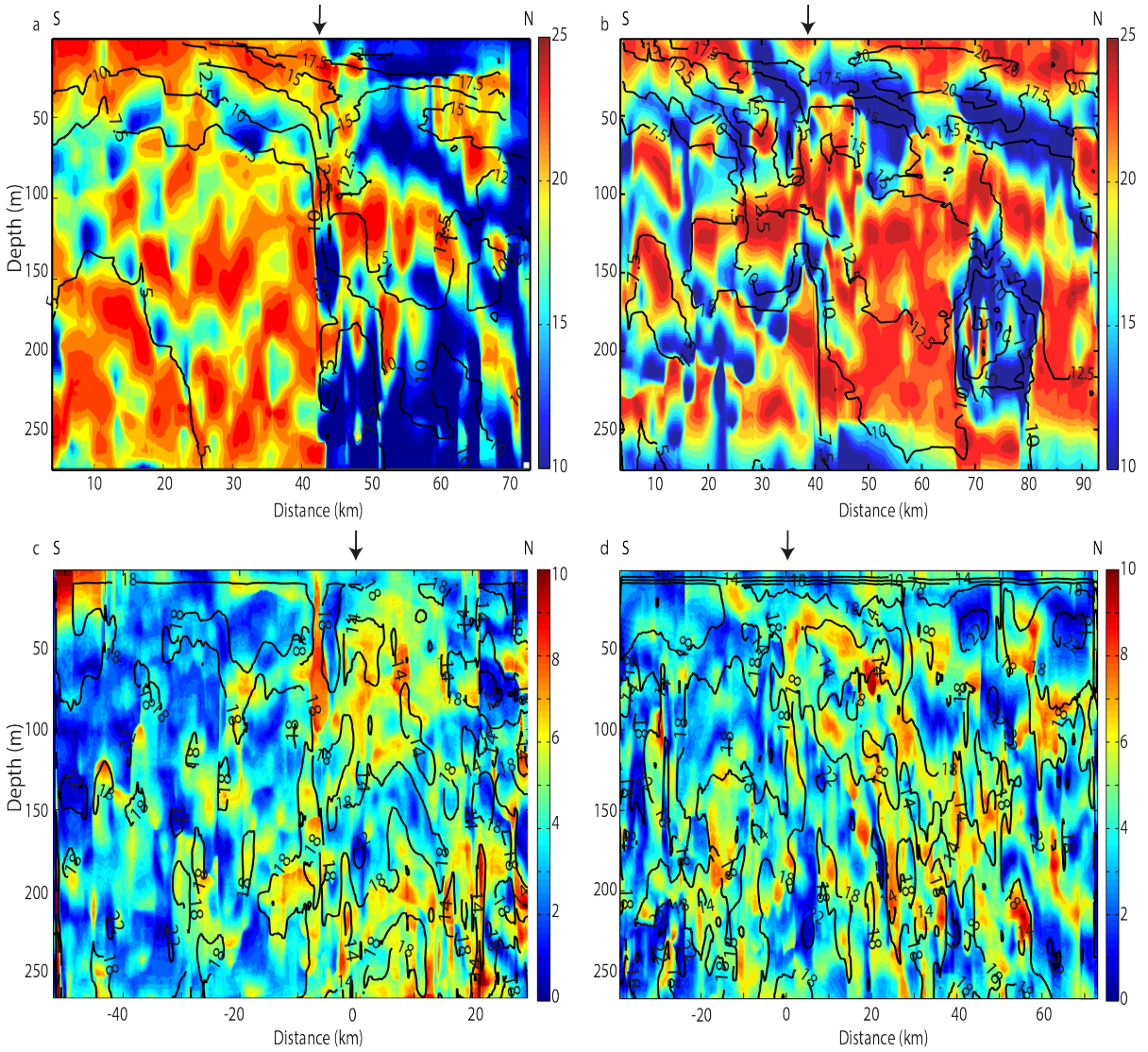

Fig. 4. 4: Vertical correlation scales (m) for (a) section II and (b) section V of SeaSoar1; black contours represent isothermals (ºC). Mean (black contours) and standard deviation (coloured) of the vertical correlation scales (m) for the (c) western and (d) eastern stations. The black arrows show the position of the front.

In order to best identify the longitudinal differences, we divide the sections into western (sections I-III in SeaSoar1 and I-II in Seasoar2), close to the shelf-break confluence point, and eastern (all other seven sections), where the two colliding currents have been in close contact for a longer time. The division is set about 55 km offshore from the 500-m isobath, which we consider as the shelf-break emergence of the confluence (see the bathymetry and location of the BCF in Figure 4.1); considering along-front mean velocities of 0.5-1 m s^{-1} (Orúe-Echevarría et al., 2019),

this represents that the water masses reaching the eastern sections have been in contact for at least an additional 15-30 hours. Following this separation, we produce ensemble sections with the origin referenced to the location of the BCF, defined as the point where the 10 ^{o}C isotherm crosses 200 m (Garzoli and Bianchi, 1987). In this way, there are five western and seven eastern realizations (one of the eastern sections did not cross the BCF) that can be combined to compute the mean and standard deviation of the vertical correlation at each cross-frontal coordinate and depth.

In Figures 4.4c,d we show the mean (obtained using a 10-m low-pass vertical filter) and standard deviation of the vertical correlation scales; only the portion of the vertical section with three or more realizations is shown. The two ensemble sections have fairly similar mean values (14-18 m). The main difference appears in the standard deviations: the western section shows a clear contrast across the front, between small values in the subantarctic side versus high values in the subtropical side; contrarily, the eastern section shows little difference between both sides of the front, with substantially greater intermittency. These results are consistent with the view of the frontal system as the locus of subsurface mesoscale incursions at any position (in section 4.3.1 we pointed at the existence of cold-fresh subsurface tongues of subantarctic waters penetrating northwards in the western and central tracks) and submesoscale thermohaline intrusions developing in the central and eastern sections. The submesoscale intrusions appear to be enhanced after the two water masses have been in contact for a sufficiently long time, of the order of one inertial period or 19 hours in our survey area (Shcherbina et al., 2010), either because of high salt-fingering activity in the BMC (Bianchi et al., 2002).

4.3.4 Horizontal correlation scales

We first examine the sea-surface horizontal correlation lengths for the extended BMC region during April 2017, as deduced using the OSTIA SST fields [Figs. 4.5a,b]. The maximum correlations (major-axes of the correlation ellipses) follow the pathway of the western boundary currents and its interior retroflections, ranging between about 35 and 55 km. Over the shelf and in the eastern portion of the domain, these values decrease, ranging between 20 and 30 km. The situation reverses for the minimum correlation lengths (minor axes), with the largest values occurring over the platform and the smallest ones taking place along the path of the major currents. Both results indicate that the boundary currents are largely asymmetric, with the longest correlation lengths well aligned with the current, while the shelf and other interior regions of high kinetic energy are dominated by shorter scales and more symmetric features [Fig. S4.11, Supporting Information]. The SNR is fairly low, always less than 1.5, slightly less than the mean values found by Hosoda and Kawamura (2004) using microwave SST images [Fig. S4.9, Supporting Information]; the largest SNR values occur over the platform and along the pathway of the MC.

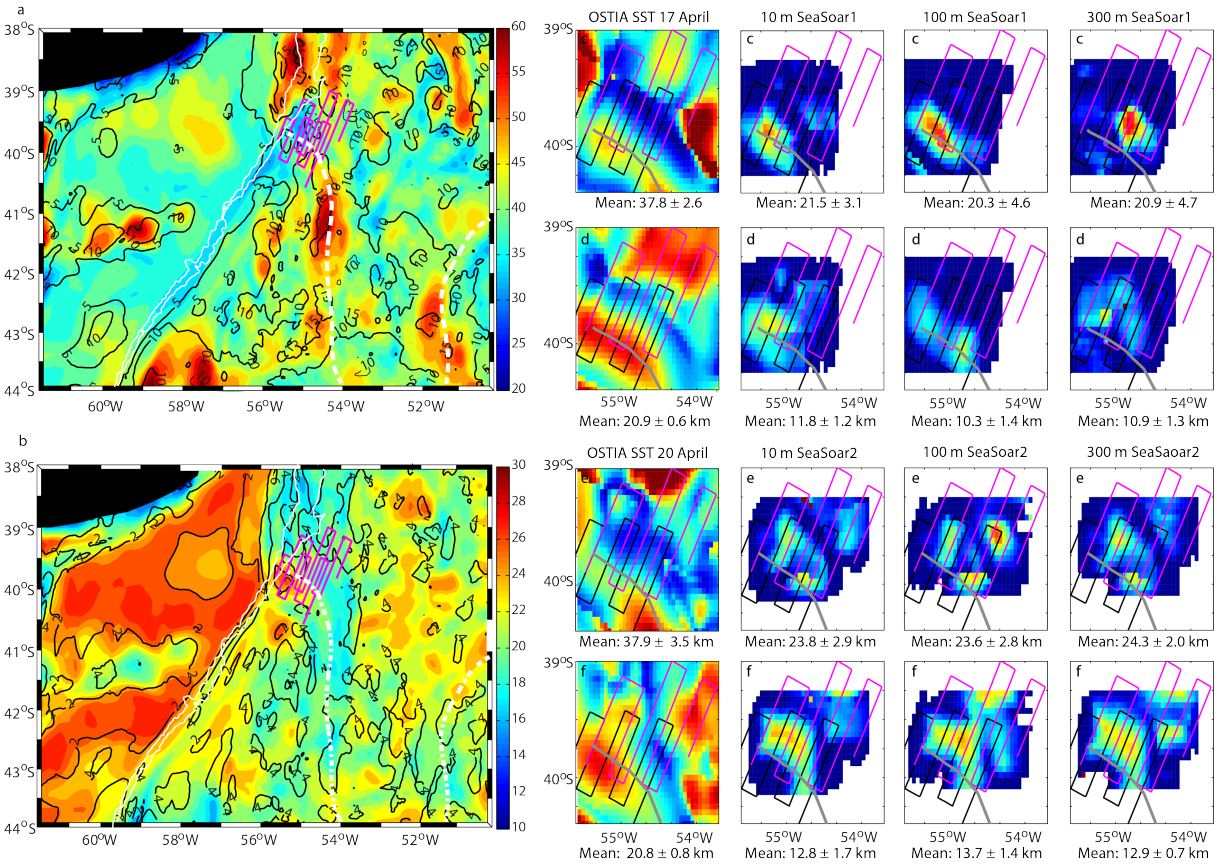

Fig. 4. 5: (a) Major- and (b) minor-axis lengths of the correlation ellipses, calculated using the April 2017 OSTIA SST data (colour-coded). The colours indicate the mean values and the black contours the standard deviation. Correlation-ellipse values: major-axis lengths for (c) the OSTIA SST on 17 April and SeaSoar1 and (e) the OSTIA SST on 20 April and SeaSoar2, color-coded as in (a); minor-axis lengths for (d) the OSTIA SST on 17 April and SeaSoar1 and (f) the OSTIA SST on 20 April and SeaSoar2, colour-coded as in (b); the SeaSoar data is at 10, 100 and 300 m, as indicated. The black/magenta lines show the SeaSoar1/SeaSoar2 tracks, the white solid lines correspond to the 500 and 1000 m isobaths, and the white dashed line indicates the mean position of the BCF for April 2017. The grey line shows the position of the BCF for the 17th April (c, d) and 21st April (e, f) 2017.

Over the SeaSoar survey area, the situation differs substantially at the surface and subsurface [Figs. 4.5c-f and Figs. S4.11c, S4.12 and S4.13, Supporting Information]. The OSTIA SST field displays a band of minimum major- and minor-axis correlation lengths along the frontal system (less than 25/15 km for the major/minor axes), surrounded by values that are at least twice as large. In contrast, the subsurface SeaSoar data is noisy but shows fairly large values south of the front (40-50 km for the major axis), in the subantarctic water domain, and much smaller values along and north of the front (20-30 km for the major axis); nevertheless, the correlations in the southern domain decrease as we move away from the slope, consistent with the idea of thermohaline intrusions developing when the two water masses remain in contact for long enough [section 4.3.3]. Remarkably, the band of minimum surface values is included in the southern portion of subsurface maximum values, sustaining the idea that this narrow surface band responds to brackish and relatively cold platform waters stretching along the southern

sector of the front (Orúe-Echevarría et al., 2019). This is confirmed by the surface salinity values [Fig. S4.5 and S4.7, Supporting Information].

4.4 Conclusions

We have combined high-resolution remote-sensing surface and SeaSoar-survey subsurface temperature data to explore the structure of the BMC, a very dynamic and intricate open-ocean frontal system. The spatial resolution of both data sets is about 5 km, although the spatial coverage of the subsurface data is much smaller. The temporal resolution of the surface remote-sensing data is 1 day while for the subsurface data we only have two (3-day apart) realizations.

At the sea-surface, the large areal coverage of the SST data allows separating the shelf and deep-ocean regions. Over the shelf, the temporal correlations are relatively large (5 days) yet the spatial correlations are moderate (40 km) except in the northern shelf (50-55 km). These results reflect that, except for the northern margin off La Plata River, the entire shelf is characterized by weak currents. Off the shelf, the results display three major regions: (1) the MC and its retroflection, characterized by long temporal (4-5 days) and spatial (40-60 km) correlations, as expected for an intense and coherent current with relatively few mesoscale features; (2) the BC and its overshoot, represented by short temporal (1.5-3.5 days) but long spatial (40-60 km) correlations, as foreseen for an intense but more intermittent current, with substantial mesoscale variability; (3) the interior ocean away from the boundary currents, depicted by relatively long temporal (5-6 days) and short spatial (25-45 km) correlations, reflecting smaller and less energetic structures.

The SeaSoar data permits having a closer look at the frontal region. The surface waters display both low temporal (1.5-4 days) and spatial (20-30 km) correlations, with an outstanding narrow band of minimum spatial correlation values, which we ascribe to brackish filaments stretching from the shelf along the front. At the subsurface, the front is characterized by relatively long/short spatial correlations in its southern/northern sides (40-50 km versus 20-30 km), although the southern correlation distances decrease as we move away from the slope. These values are consistent with the idea of two colliding water masses, with small mesoscale intrusions of subantarctic water at the collision and the downstream development of both-sign submesoscale thermohaline intrusions. Further comparison of the surface and subsurface patterns shows that subantarctic waters are located right below the brackish filament.

The vertical correlation scales reflect the seasonal thermocline, the frontal structure and the presence of intrusions. The values range between 10 and 25 m, with the longest distances occurring in the subantarctic waters close to the shelf. The observed subsurface distributions are again consistent with the presence of mesoscale tongues of subantarctic waters close to the

slope, penetrating north through the front, and submesoscale thermohaline intrusions further offshore.

Our results point at the frontal system as the locus of high-frequency small-scale processes, leading to the down-gradient transfer of properties. These subsurface processes, which are smaller and faster at the subsurface (down to at least about 200 m) than at the sea-surface, are hardly represented in operational models. An improved representation of the intrusion dynamics in frontal systems is needed if we wish to properly typify those subsurface processes that bear global implications.

Acknowledgments

We are very grateful to the crew of R/V Hespérides and the scientific and technical teams for their vital help during the RETRO-BMC cruise. We are also thankful to our two anonymous reviewers for their constructive and useful comments and suggestions. We acknowledge funding from the Spanish Government through projects VA-DE-RETRO (CTM2014-56987-P) and SAGA (RTI2018-100844-B-C33). D.O.E was funded through an FPU contract and I.V.C. through and FPI contract. In situ SeaSoar data are available for download at Pelegrí et al. (2019). Satellite SST and altimetry data are available at Copernicus Marine Environment monitoring service (CMEMS; http:// marine.copernicus.eu/).

Supporting Information

Annex 4.1: Data

The position of the Confluence front was initially estimated from daily SST and SSH images together with one-week forecasts of θ, S and horizontal velocity down to 1000 m, as provided by the MERCATOR Ocean PSY4V3R1 operational model ($1/12^{o}$ resolution) (http://marine.copernicus.eu). The precise position was eventually obtained with along-track in-situ measurements of near-surface θ, S and velocity as well as with hydrographic stations. The hydrographic measurements were gathered with a SeaBird 911 conductivity-temperature-depth (CTD) instrument mounted on the SeaSoar, with redundant temperature and conductivity sensors and additional dissolved oxygen, fluorescence and turbidity probes. The SeaSoar collected data in a sawtooth pattern between the sea-surface and a maximum depth of 400, with a horizontal spacing of 4 km between apogees and a typical tow speed of 8.5 knots. The entire dataset is available at Pelegrí et al. (2019).

SST data, with spatial and temporal resolutions of 0.05^{o} x 0.05^{o} and 1 day, correspond to the Operational Sea Surface Temperature and Sea Ice Analysis (OSTIA) product, which combines in-situ data with infrared and microwave satellite data.

Satellite altimetry data are from the multi-satellite delayed time DUACS gridded products (Pujol et al., 2016). These products include absolute dynamic topography (ADT) and surface geostrophic velocity at daily sampling and spatial resolution of $1/4^{o}$ on a Mercator regular grid. The altimetry data helps position the SAF and BCF, providing the dynamic context of the region at the time of the cruise. Due to its spatio-temporal coverage, however, it cannot resolve the variability at periods shorter than 20 days and spatial scales less than 40 km (Pujol et al., 2016).

The temperature gradients are sharp (up to 0.2 ^{o}C km^{-1}) at the BMC surface front and less intense along the BCO path ($\cong$ 0.08 ^{o}C km^{-1}). The sampling area is north of the SAF and is entirely crossed by the BCF; a second thermal front ($\cong$ 0.03 ^{o}C km^{-1}) is found in the northern limit of SeaSoar1, separating the shelf waters stretching on top the BMC front from the northern subtropical BC waters [Figs. 4.1 and 4.2]. During both surveys, the westernmost sections sampled the near-shore emergence of the confluence point, marked by the MC retroflection and the BC diversion from the shelf-break.

The comparison of the two surveys reveals a very dynamic region, with substantial θ temporal changes [Fig. 4.2]. In particular, the ADT and SST fields illustrate that during the three days between the two surveys (17 and 20 April) the BCF moved north some 20 km (this expansion of subantarctic waters is confirmed by a temperature decrease in the southern portion of the three western sections) and the BCO shifted westwards [Fig. S4.4]. Further, the subsurface structures evolved rapidly, as for example, the cold-water intrusions in the northern extreme of SeaSoar1 were not sampled three days later.

Annex 4.2: Methods

For the OSTIA SST, we calculate the temporal autocorrelation function for each grid point (i,j) of our extended BMC domain [Fig. 4.1] as follows:

$$ACF_t(i,j,n) = \frac{\sum_{r=1+n}^{N+n}\left(SST(i,j,r) - \overline{SST(i,j)}\right)\left(SST(i,j,r-n) - \overline{SST(i,j)}\right)}{\sum_{r=1}^{N}\left(SST(i,j,r) - \overline{SST(i,j)}\right)^2} \quad \text{(S.4.1)}$$

where the data are available at daily time steps Δt and $\tau = n\Delta$t is the time lag. SST can vary at many different temporal scales, with the largest variations often at seasonal scales. However, since we focus on processes taking place at time scales of the order of a few days, the selection of $N\Delta$t = 20 days (with r= 1 corresponding to 1 April 2017) turns out to be adequate; the results are essentially insensitive to small changes in N. At each grid point, we fit ACF_t to a Gaussian function and define the temporal scale as an e-folding time (Molinari and Festa, 2000), the temporal separation where the autocorrelation decays to e^{-1} [Fig. S4.1].

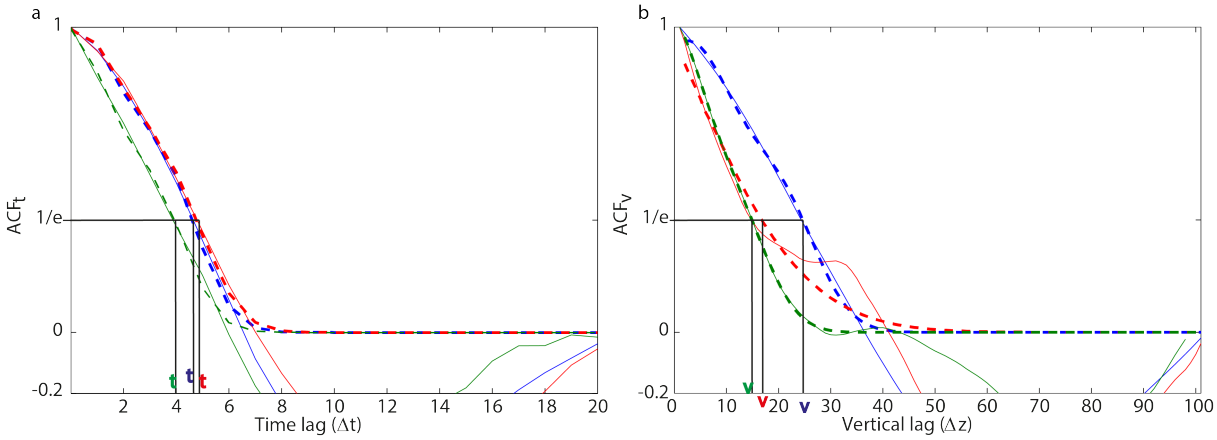

Fig. S.4. 1: Examples illustrating the procedure used to calculate the autocorrelation function: (a) the temporal autocorrelation ACF_t in three grid points of our domain during April 2017 and (b) the vertical autocorrelation ACF_v at 1 m in three grid elements along section II of Seasoar1. The solid lines show the calculated autocorrelations and the dashed lines represent the best-fit Gaussian functions; the corresponding e-folding times/distances are also shown.

Similarly, for each SeaSoar potential temperature vertical profile, we calculate the vertical autocorrelation function at each cross-frontal grid element l and depth level k as follows:

$$ACF_v(l,k,m) = \frac{\sum_{r=k+m}^{M+m+k-1}\left(\theta(l,k,r)-\overline{\theta(l,k)}\right)\left(\theta(l,k,r-m)-\overline{\theta(l,k)}\right)}{\sum_{r=k}^{k+M}\left(\theta(l,k,r)-\overline{\theta(l,k)}\right)^2} \tag{S.4.2}$$

where the data are available at vertical intervals of Δz =1 m and the vertical lag is $\lambda = m\Delta z$. The calculation is carried out from z=1 m down to z=267 m, at each level over a depth interval of $M\Delta z$ = 100 m. The selection of M =100 turns out to be adequate to encompass the range of vertical correlation scales that characterize the frontal structures.; small increases in M cause little differences except that there are no results in a more extended lower portion of the water column. A Gaussian function is adjusted to the autocorrelation function at each frontal position and depth, and the e-folding distance is selected to be the depth scale [Fig. S4.1].

For both the OSTIA SST and SeaSoar (potential) temperatures at any depth level, we can calculate the horizontal autocorrelation function at each grid point (i,j). For the OSTIA SST this can be done for any single day while for the SeaSoar we have only two realizations. For either case, we use a 0.5^o x 0.5^o window that moves both zonally and meridionally over the entire frontal region, with an overlapping of 90 % between adjacent windows. Prior to calculating the autocorrelation, a least-square planar trend is applied to each sub-image in order to eliminate those scales longer than the window. The autocorrelation function is determined relative to any (vector) position $\mathbf{x}$ through a two-dimensional fast Fourier transform, normalized to the zero-lag value. From this autocorrelation function, the principal correlation scales are determined by adjusting an ellipse (r) to the e-folding correlation coordinates $\mathbf{x_l} = (x_l, y_l)$

$$r(\mathbf{x},\mathbf{x_l}) = a_1x_l^2 + a_2y_l^2 + a_3x_ly_l + a_4x_l + a_5y_l + a_6 \tag{S.4.3}$$

where the coefficients $a_i = a_i(\mathbf{x})$ $(i = 1, 2, ... 6)$ are obtained using a least-mean square method [Fig. S4.2]. From the orientation of the ellipse, we can identify both the size and direction of the longest (major axis) and shortest (minor axis) correlation scales.

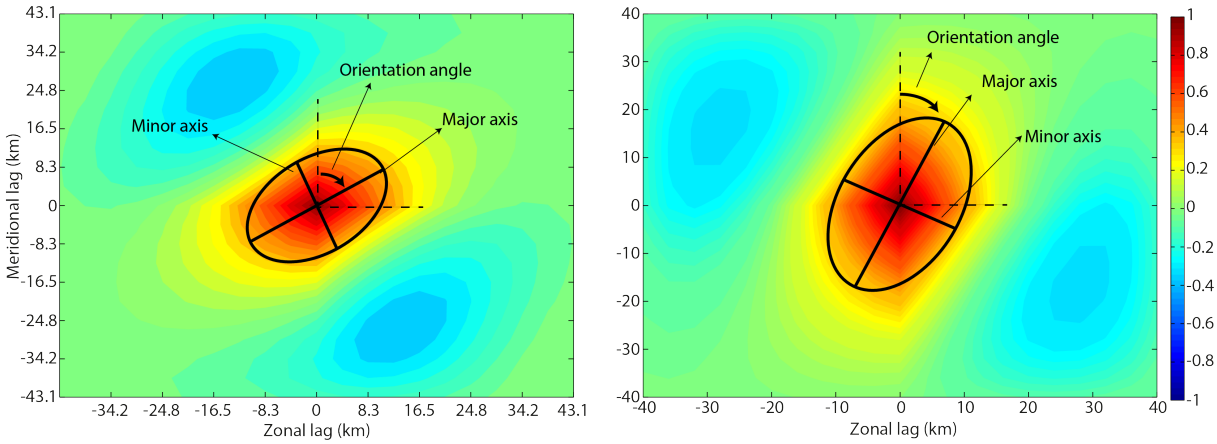

Fig. S.4. 2: Two examples of the horizontal autocorrelation function (color-coded) and the ellipse fitted to the *e*-folding correlation coordinates (black contour). The major and minor axes, and the orientation angle, defined clockwise from the true north, are shown.

Considering the temporal and spatial resolution of our datasets, we cannot resolve scales shorter than 1 day for OSTIA and smaller than 1 m in the vertical for the SeaSoar, and shorter than about 5 km in the horizontal for both datasets. For the temporal and vertical autocorrelation functions, the signal-to-noise ratio (SNR) is estimated from the explained variability at the shortest discriminated scale, with values less than one meaning that most of the fluctuations are not resolved (Sprintall and Meyers, 1991)

$$SNR_{t,v} \equiv \sqrt{\frac{ACF_{t,v}(1)}{1 - ACF_{t,v}(1)}} \tag{S.4.4}$$

where $ACF_{t,v}(1)$ is the value of the autocorrelation function in the first adjacent bin. For the horizontal spatial scales, the SNR is determined as (Hosoda and Kawamura, 2004)

$$SNR_h \equiv \sqrt{exp(-a_6)/[1 - exp(-a_6)]} \tag{S.4.5}$$

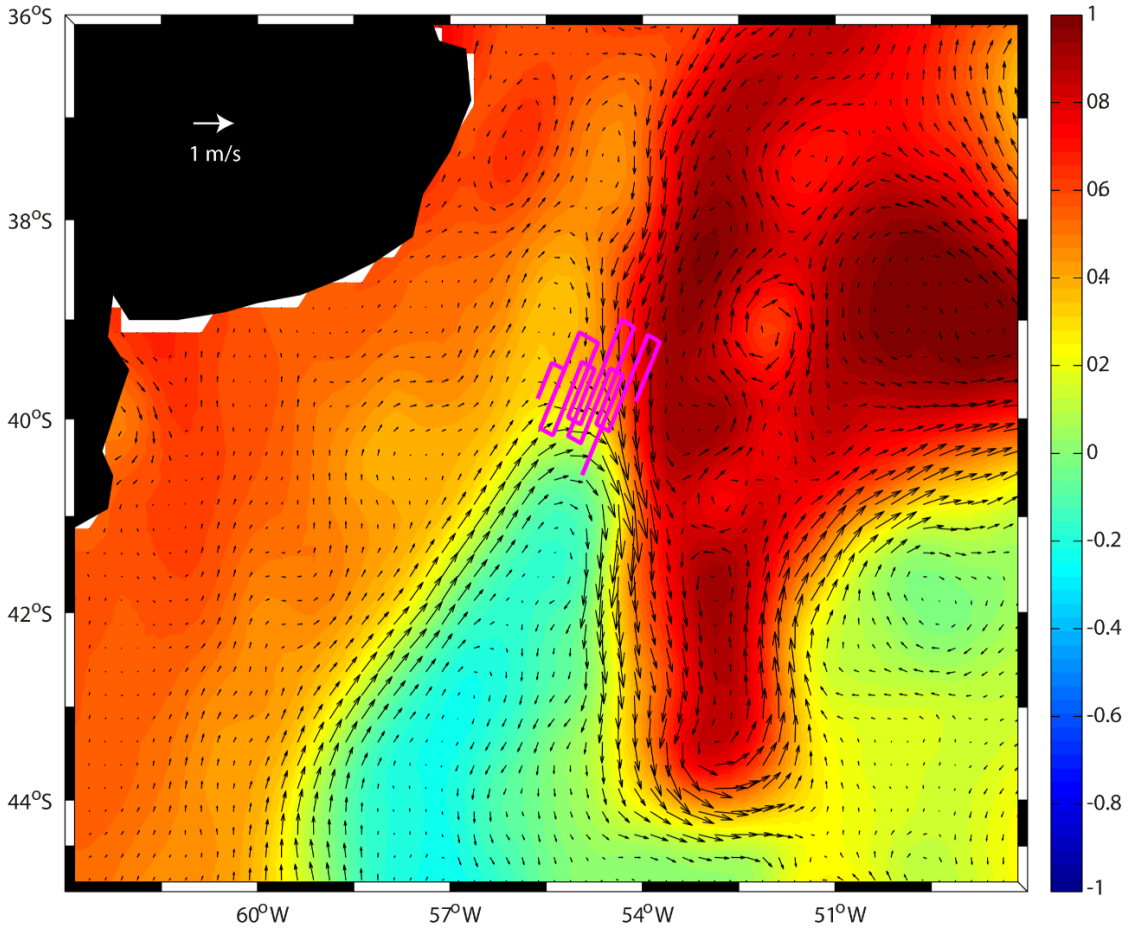

Fig. S.4. 3: Mean ADT (m) for April 2017 (color-coded). The black arrows show the associated mean surface geostrophic velocity. The magenta lines indicate the path of the SeaSoar surveys.

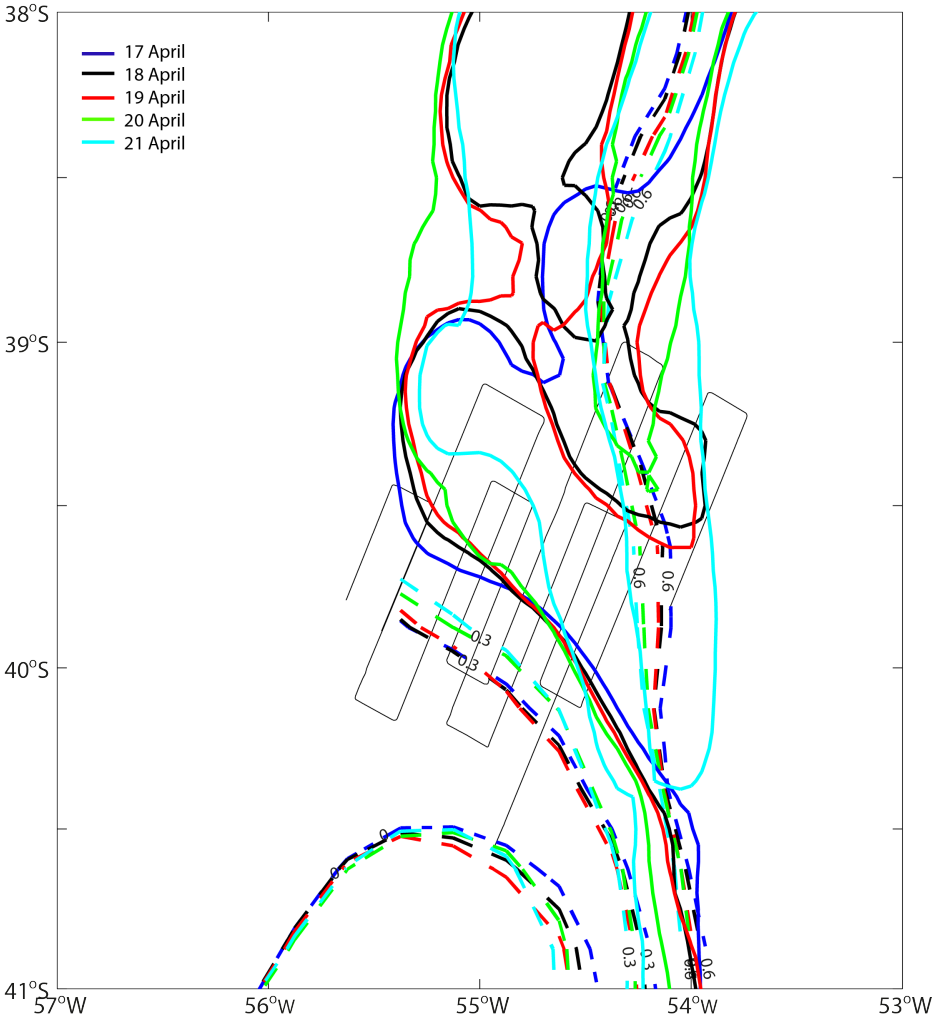

Fig. S.4. 4: Frontal positions as derived from the ADT and SST-gradients during 17-21 April 2017, color-coded per day. The dashed lines show the position of the Subantarctic Front (ADT=0 m) and Brazil Current Front (ADT=0.3 m) defined as in Ferrari et al. (2017); the 0.6-m ADT contour is also shown as dashed lines. The continuous lines indicate the position of the BMC based on SST-gradients, following the methodology in Saraceno et al. (2004). The black thin lines show the SeaSoar tracks.

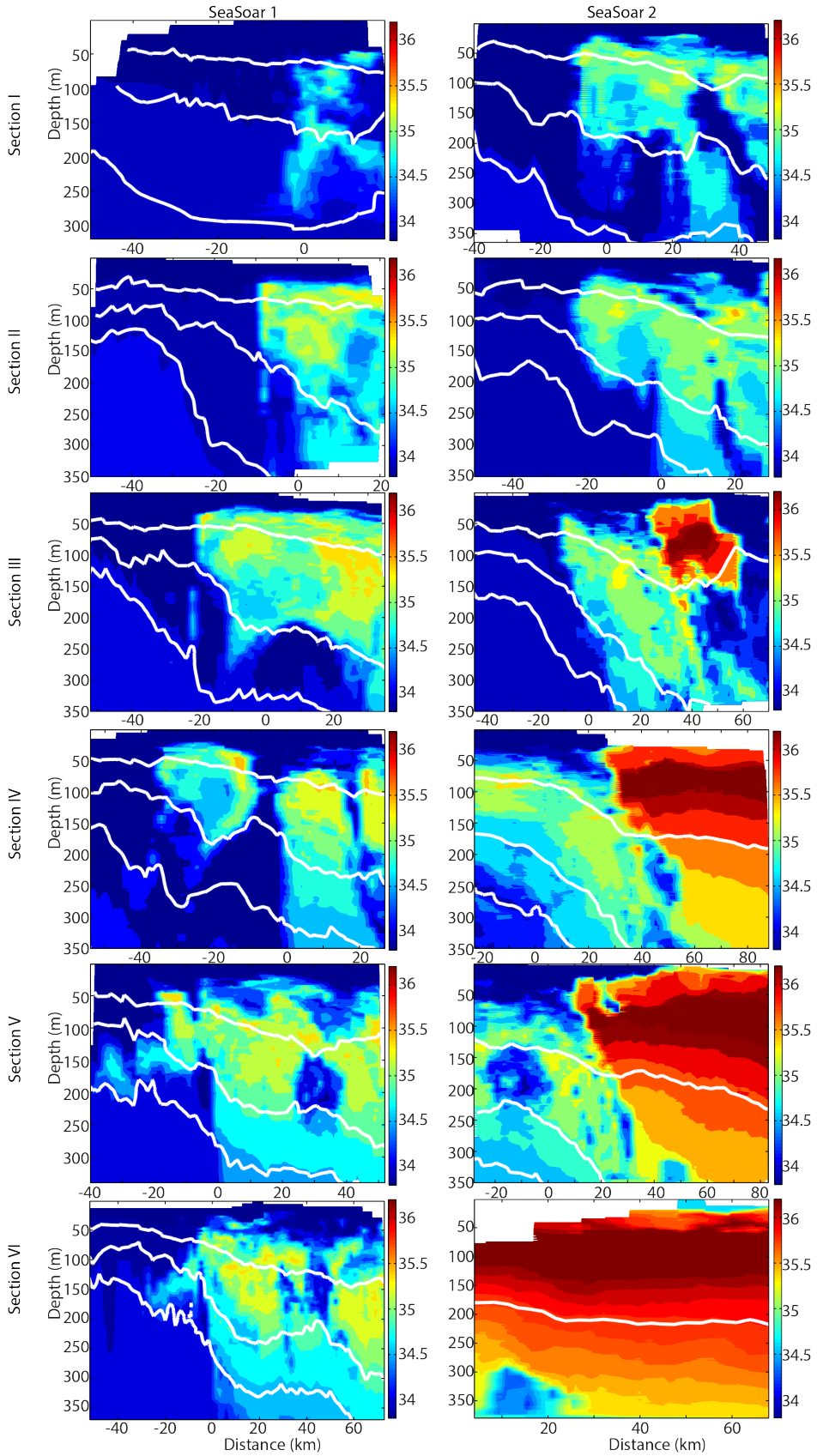

Fig. S.4. 5: Vertical sections of salinity along sections I to VI (from top to bottom, as labelled), during SeaSoar1 (left) and SeaSoar2 (right). The white contours in each panel (displayed from top to bottom) correspond to the 26.2, 26.8 and 27.0 isoneutral surfaces.

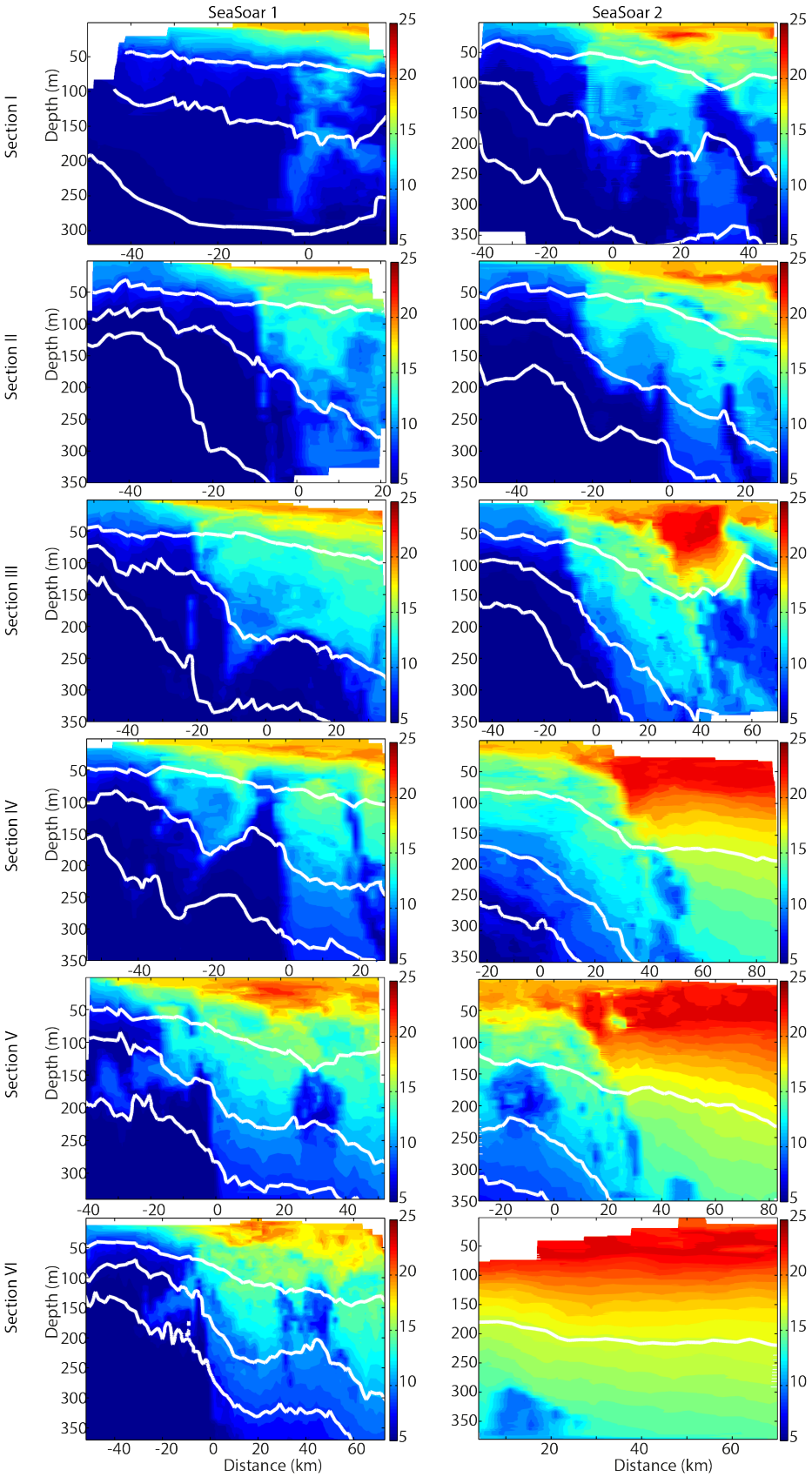

Fig. S.4. 6: Vertical sections of potential temperature (°C) along sections I to VI (from top to bottom, as labelled), during SeaSoar1 (left) and SeaSoar2 (right). The white contours in each panel (displayed from top to bottom) correspond to the 26.2, 26.8 and 27.0 isoneutral surfaces.

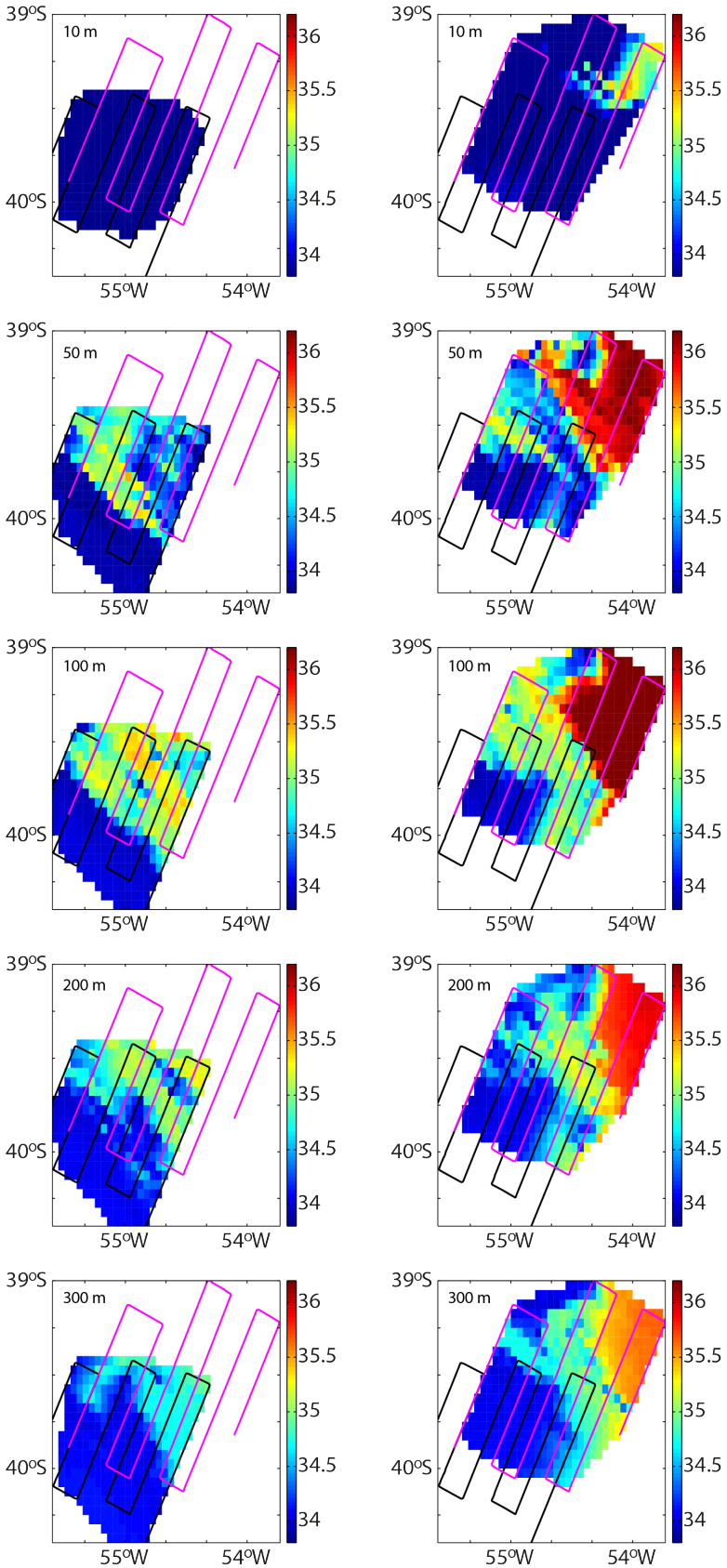

Fig. S.4. 7: Horizontal salinity fields at 10, 50, 100, 200 and 300 m for (left) SeaSoar1 and (right) SeaSoar2. The location of the SeaSoar1/SeaSoar2 tracks is shown by black/magenta lines.

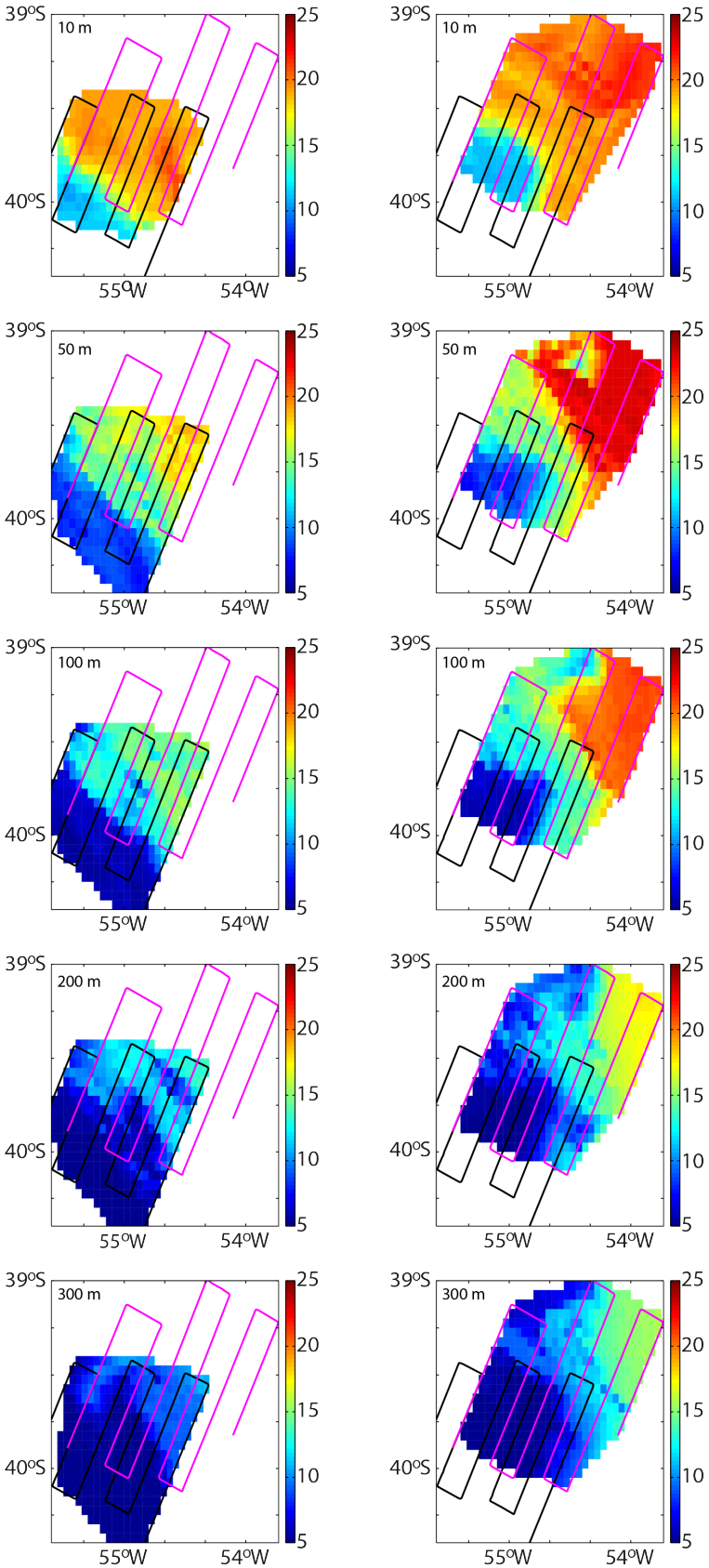

Fig. S.4. 8: Horizontal potential temperature (°C) fields at 10, 50, 100, 200 and 300 m for (left) SeaSoar1 and (right) SeaSoar2. The location of the SeaSoar1/SeaSoar2 tracks is shown by black/magenta lines.

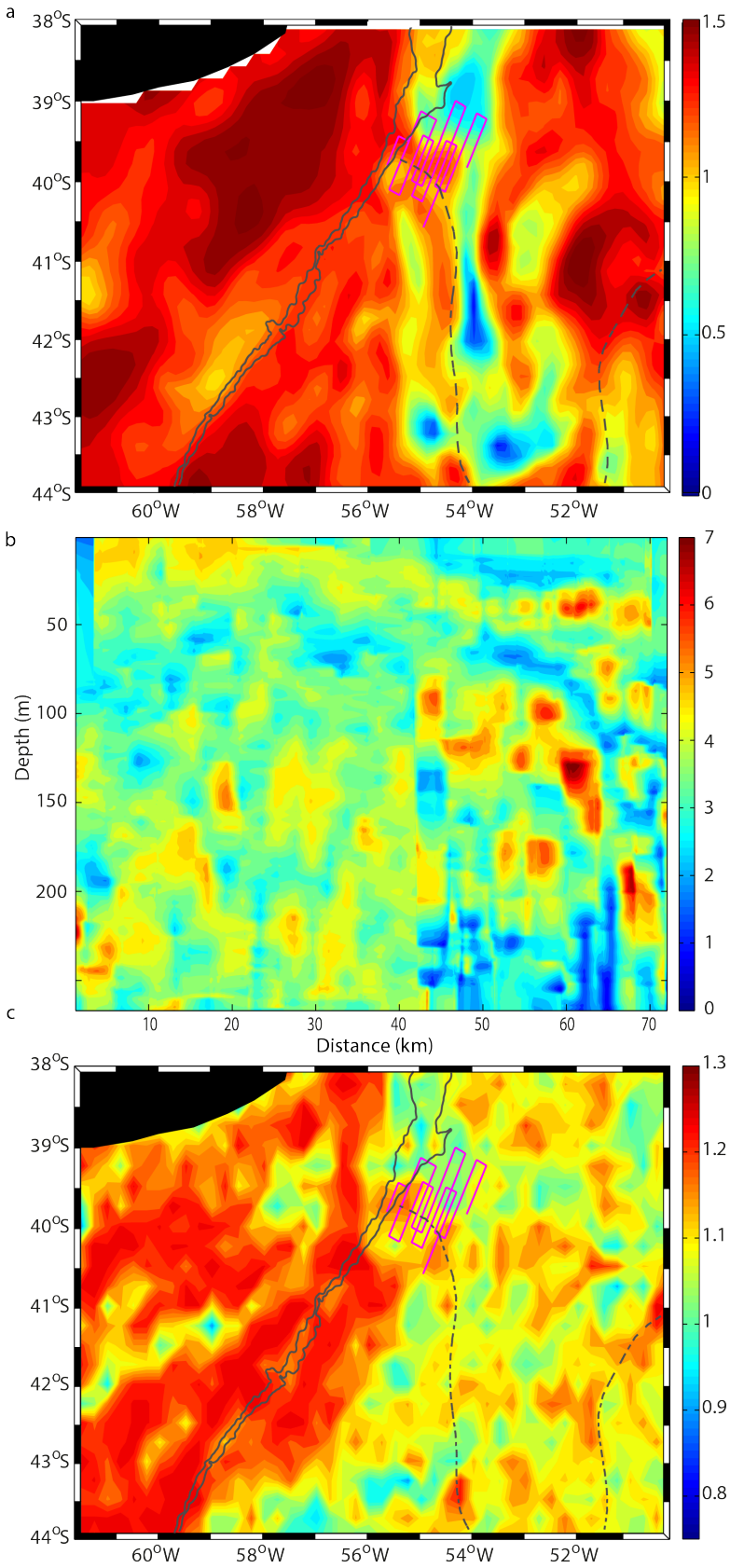

Fig. S.4. 9: Samples of SNR for (a) temporal scales (April 2017), (b) vertical scales (Section II in SeaSoar1), and (c) OSTIA SST spatial scales (April 2017). In panels (a, c) the magenta lines show the SeaSoar tracks, the black solid lines correspond to the 500 and 1000 m isobaths and the black dashed line indicates the mean position of the BCF for April 2017.

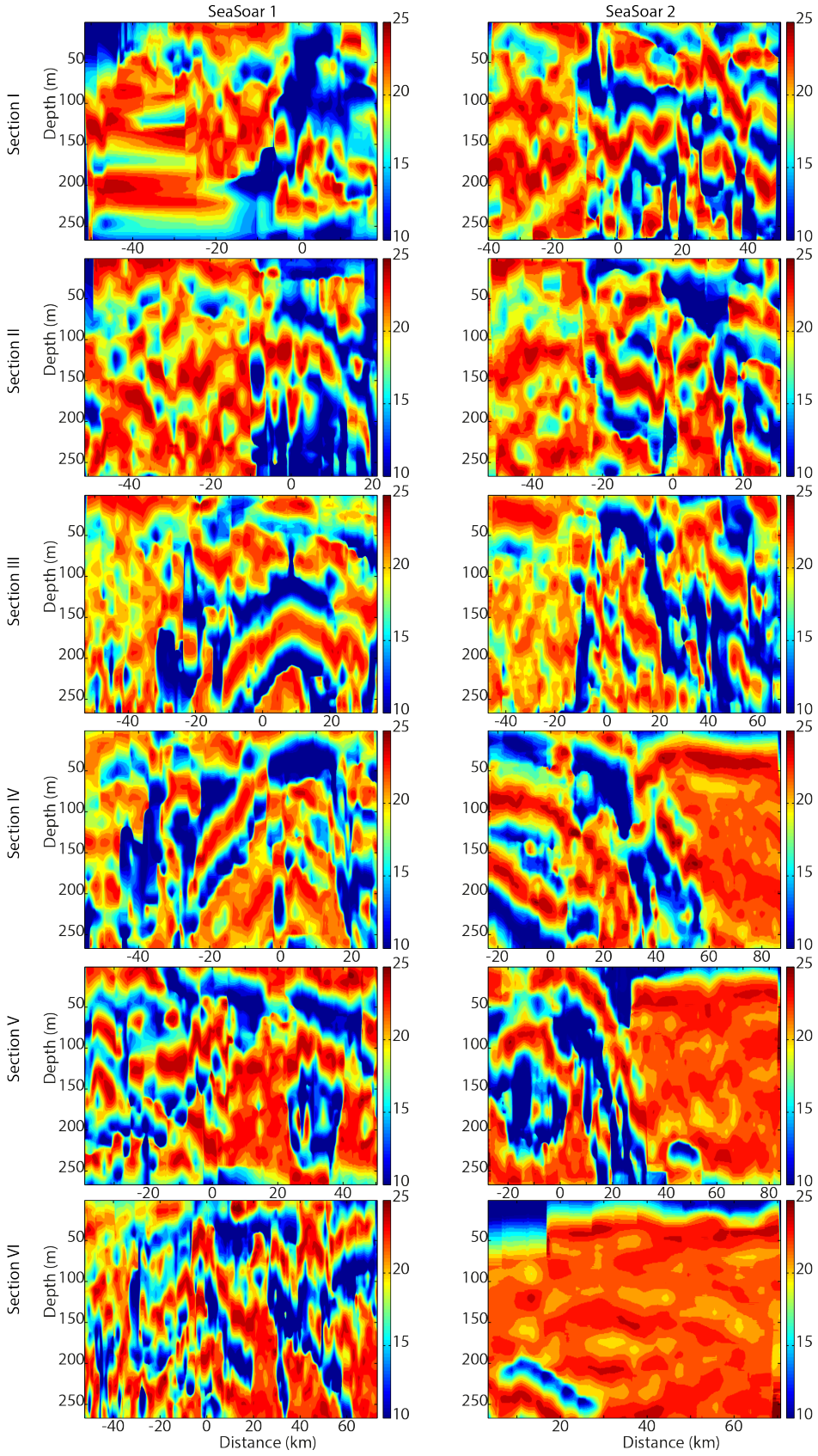

Fig. S.4. 10: Vertical correlation scales along sections I to V1 (from top to bottom, as labelled) during (left) SeaSoar1 and (right) SeaSoar2. The distance shows the relative position with respect to the BCF, except for section VI of SeaSoar2 whose origin is set at the southern end.

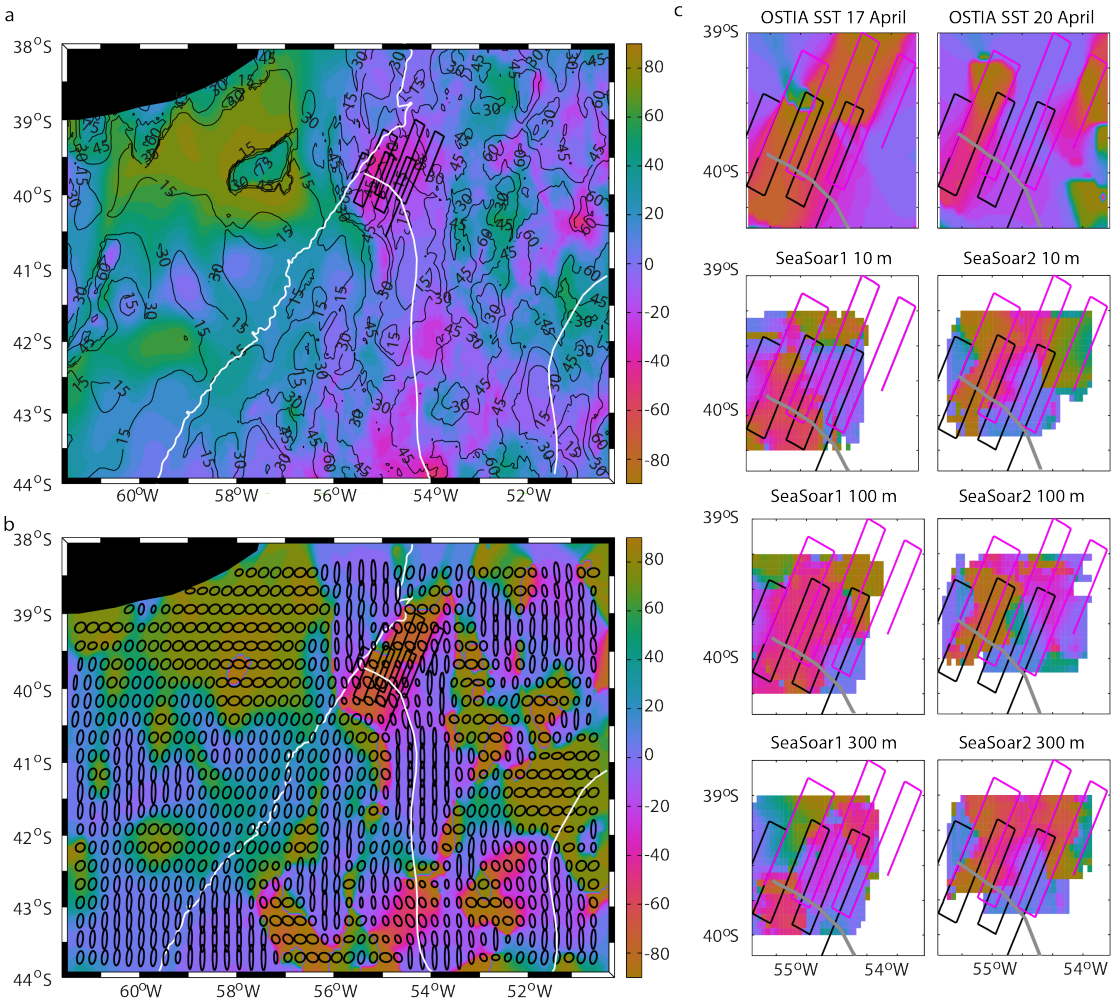

Fig. S.4. 11: (a) Mean values (color-coded) and standard deviations (contours) of the correlation-ellipses orientation during April 2017; the angle is defined clockwise from the true north. (b) Orientation angle and elliptical contours ($1/e$ correlation length) for 17 April 2017. The white lines correspond to the 1000 m isobath and the mean BCF position for April 2017. (c) Orientation angle as determined from OSTIA SST for 17 and 20 April 2017 (top row panels) and SeaSoar1 and SeaSoar2 at 10, 100 and 300 m (panels in rows 2-4). The grey line shows the position of the BCF for the 17th April (left figures) and 21st April (right figures) 2017.

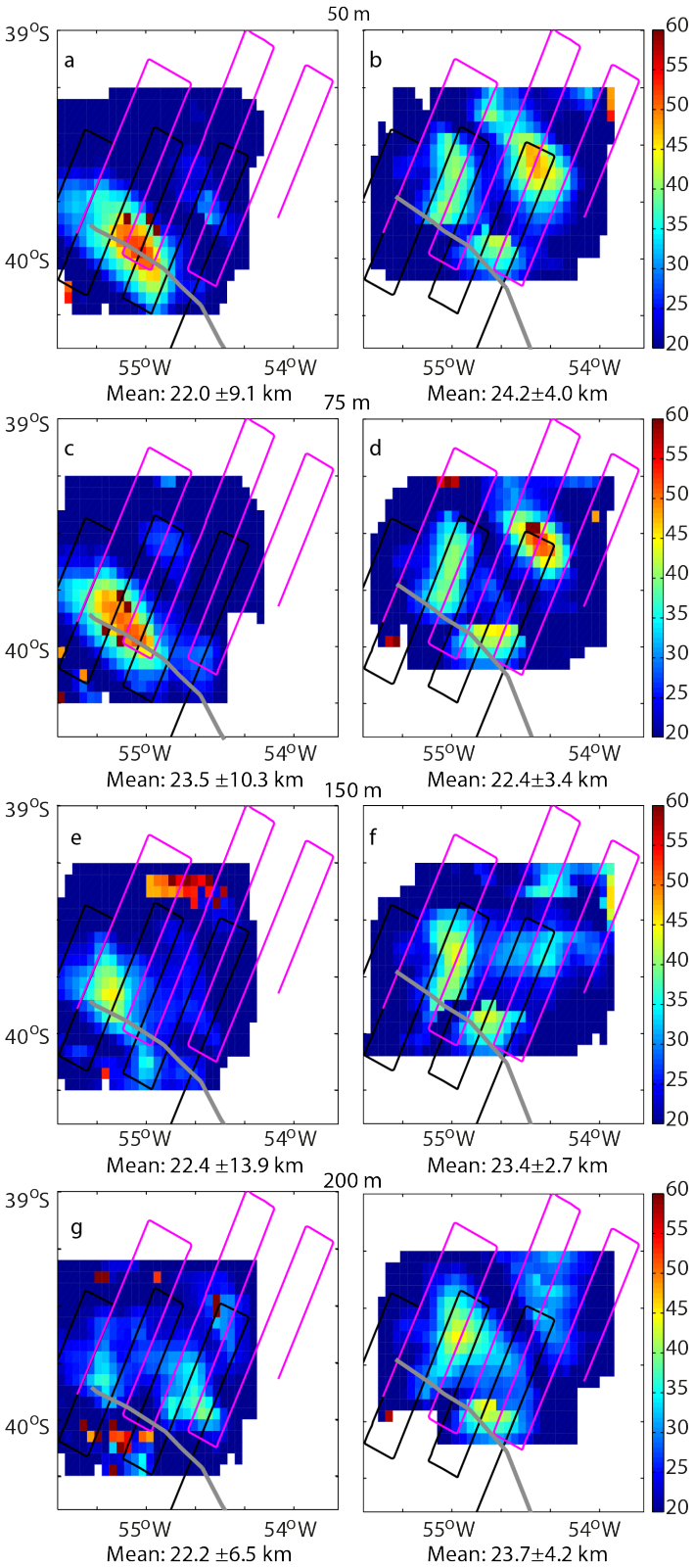

Fig. S.4. 12: Major-axis of the correlation ellipses (km) at (a, b) 50, (c, d) 75, (e, f) 150 and (g, h) 200 m for (left panels) SeaSoar 1 and (right panels) SeaSoar 2. The grey line shows the position of the BCF for the 17th April (left figures) and 21st April (right figures) 2017.

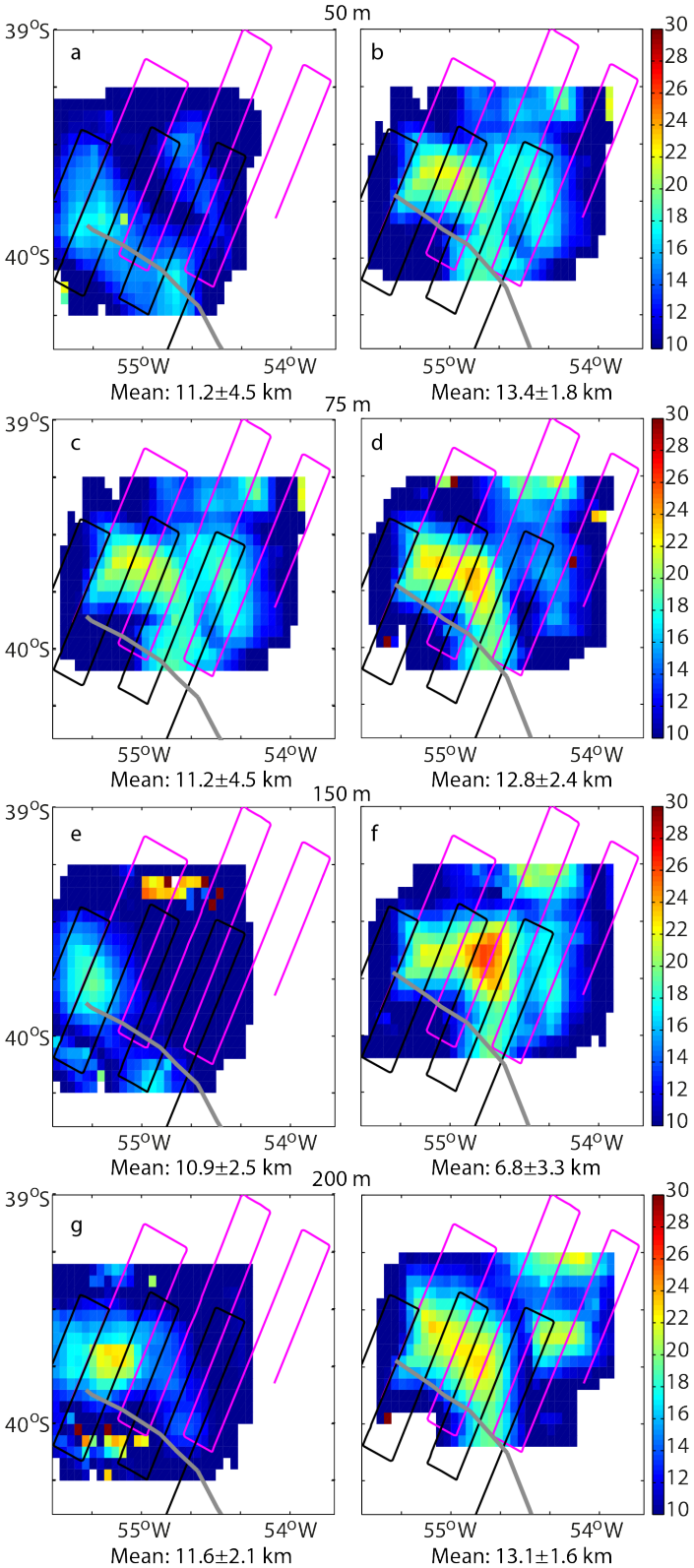

Fig. S.4. 13: Minor-axis of the correlation ellipses (km) at (a, b) 50, (c, d) 75, (e, f) 150 and (g, h) 200 m for (left panels) SeaSoar1 and (right panels) SeaSoar2. The grey line shows the position of the BCF for the 17th April (left figures) and 21st April (right figures) 2017.

Chapter 5

Mixing in the Brazil-Malvinas Confluence

Orúe-Echevarría, D., Naveira Garabato, A.C., Polzin, K.L., and Pelegrí, J.L.

[In preparation]

Abstract

The temperature-salinity distribution in the ocean is the outcome of energy inflow at many different scales and its transfer towards smaller scales and eventual dissipation at molecular scales. Here, we use microstructure data collected along the South Atlantic Subtropical Front in order to assess the role of dianeutral mixing by small-scale turbulent diffusive fluxes and isoneutral mixing induced by mesoscale eddy stirring in setting the temperature-salinity relationship in the Argentine basin. Enhanced dianeutral diffusivity values are found in the upper 500 downstream the Brazil Current Overshoot region and at depth near each side of the basin, associated with the continental margin on the west and the abrupt topography of the mid-Atlantic ridge on the eastern limit. Isoneutral eddy diffusivity is high below 500 m, mostly exceeding 10^3 m^2 s^{-1}, and intensifies below 800 m in the centre of the basin. Finally, the isoneutral diffusivity is combined with climatological potential vorticity data in a flux-gradient parameterization in order to estimate the along isoneutral eddy-induced meridional volume flux across the Subtropical Front. Most intense eddy-induced advection occurs in the upper 600 m. The basin integrated eddy overturning streamfunction contributes to the subduction of about 2.5 Sv of Subtropical Mode Water and Antarctic Intermediate Water into the subtropical thermocline and the poleward transport of around 1 Sv in the Upper Circumpolar Deep Water layer.

5.1 Introduction

Turbulent mixing plays a major role in the distribution of oceanic tracers such as heat, salt, nutrients or dissolved oxygen (Dong et al., 2014; Dufour et al., 2015), in the water mass formation (Cerovečki et al., 2013; Groeskamp et al., 2017) and in the meridional overturning circulation (MOC) (Munk and Wunsch, 1998; Marshall and Speer, 2012; Naveira Garabato et al., 2016). These mixing processes are the direct consequence of different physical phenomena, including small-scale dianeutral mixing and isoneutral stirring induced by mesoscale eddies.

Small-scale turbulent dianeutral fluxes are the major process leading to vertical smoothening of water properties. Dianeutral mixing is quantified in terms of a turbulent dianeutral diffusivity which presents high spatial variability, ranging between $O\,(10^{-7})$ and $O\,(10^{-3})$ $m^2\ s^{-1}$ (Kunze et al., 2006; Whalen et al., 2012; Waterhouse et al., 2014). Intense diffusivities are found in the upper 1000 m, related to wind-generated near-inertial waves (Whalen et al., 2012; Waterhouse et al., 2014). At higher depths, high values are associated with breaking internal waves at regions with strong near-bottom flows, rough topography and abrupt ridges or continental margins (Polzin et al., 1997; Ledwell et al., 2000; Nash et al., 2004; Walter et al., 2005; Naveira Garabato et al., 2013; Waterhouse et al., 2014).

Mesoscale eddies mix ocean properties along isoneutral surfaces, stirring background tracers such as heat, salt or dissolved gases. Below the Ekman layer, this mechanism is responsible for most of the poleward transport of these tracers across the Antarctic Circumpolar Current (ACC) fronts, which act as barriers for the meridional fluxes (Dufour et al., 2015). Besides diffusive fluxes, eddies induce southward advective volume transports across frontal systems. At the ACC, this eddy-advection settles an overturning cell where deep waters upwell poleward and balance the equatorward subduction of intermediate waters along isonetrual surfaces (Marshall and Radko, 2003; Marshall and Speer, 2012; Mazloff et al., 2013). In addition, at Subtropical Fronts (STF), these mesoscale eddy fluxes strengthen the subduction of newly ventilated mode water into the main thermocline (Marshall, 1997; Henning and Vallis, 2004; Xu et al., 2016).

Eddy-induced transports are usually parameterized as a down-gradient eddy property flux (e.g. Treguier et al., 1997), which depends on the mixing capacity of mesoscale eddies, characterized in terms of an isoneutral diffusivity (Abernathey et al., 2010). This diffusivity varies with longitude, latitude and depth between $O\,(10^{1})$ and $O\,(10^{4})$ $m^2\ s^{-1}$ (Abernathey and Marshall, 2013; Bates et al., 2014 Cole et al., 2015; Roach et al., 2018), and becomes intensified in regions of strong zonal currents and elevated eddy kinetic energy, such as in the equatorial current system, the ACC and the western boundary current extensions (Abernathey and Marshall, 2013; Klocker and Abernathey, 2013; Cole et al., 2015; Roach et al., 2018). At these locations, maximum diffusivity values are found at the steering level, that is, where the propagation speed

of eddies approaches that of the mean flow, but are reduced at the surface where both velocities differ (Abernathey et al., 2010; Ferrari and Nikurashin, 2010; Naveira Garabato et al., 2011; Bates et al., 2014; Tulloch et al., 2014).

Regional and global surface and subsurface isoneutral diffusivity estimates highlight the elevated values at the Argentine basin, particularly over the Confluence of the two western boundary currents, the Brazil and Malvinas Currents (BM and MC), and around the Zapiola Drift (Abernathey and Marshall, 2013; Cole et al., 2015; Roach et al., 2018). The BMC is a particularly relevant region in the Atlantic Meridional Overturning Circulation (AMOC). It holds intense water mass transformations that arise from the high property contrast between the subantarctic and subtropical waters south and north the STF, respectively (Garzoli and Matano, 2011; Valla et al., 2018; Orúe-Echevarría et al., 2019). Besides, important meridional transferences take place across the front (Bianchi et al., 1993; Campos et al., 1995; Schouten and Matano, 2006; Jullion et al., 2010) as well as the formation and subduction of Subtropical Mode Water (Campos et al., 1999; Porovost et al., 1999; Sato et al., 2014).

Mesoscale eddy fluxes and small-scale turbulent mixing have a leading role in these processes. On one hand, diapycnal diffusivities estimated with direct microstructure data reveal mean values of order 10^{-5} m^2 s^{-1} (Waterhouse et al., 2014). These diapycnal fluxes contribute to the intense water mass modifications in the region, such as the transformation of deep waters (Upper Circumpolar Deep Water, UCDW, and North Atlantic Deep Water, NADW) into intermediate Subantarctic Mode Water (SAMW) and Antarctic Intermediate Water (AAIW), and the transformation of these masses through heat and salt fluxes from the overriding Subtropical Mode Water (STMW) (Piola et al., 2000; Sloyan and Rintoul, 2001). This, for example, results in AAIW over the mid-Atlantic ridge (MAR) that is warmer and saltier than over the BMC (Sloyan and Rintoul, 2000). On the other hand, isoneutral diffusivity determined from Argo floats are overall high, between $O(10^2$ m^2 $s^{-1})$ and $O(10^4$ m^2 $s^{-1})$ (Cole et al., 2015; Chapman et al., 2017; Roach et al., 2018). This suggests the prominent role of the BMC in the poleward transference of properties, also suggested by the eddy heat fluxes estimated from numerical models (Schouten and Matano, 2006) or sea surface height anomalies (Foppert et al.; 2017). Furthermore, numerical models indicate that eddy-induced mass advection may have a relevant contribution to the along isoneutral subduction of mode and intermediate waters into the subtropical gyre (Schouten and Matano, 2006; Tanaka and Hasumi, 2008).

Here, based on in-situ microstructure and hydrographic data as well as climatological information, we assess the relative roles of dianuetral and isonetrual diffusivities setting the mean potential temperature - salinity (θ-S) relationship in the Argentine basin as well as the eddy-induced transports across the STF. The study is organized as follows. The theory of how turbulent fluxes establish the mean temperature-salinity relationship and contribute to the meridional volume fluxes is discussed in section 5.2. The dataset and analysis methodology are

described in section 5.3. Section 5.4 presents the synoptic conditions and estimates the mixing coefficients and finally we provide the main conclusions in section 5.5.

5.2 Methodology

5.2.1 The temperature-salinity relationship

The θ-S relationship is the result of thermohaline variability induced by fluctuations acting at different scales, from the large-scale general circulation to intermediate and dissipative scales. This variability can be assessed through the potential temperature variance $\left(\overline{\theta'^2}\right)$ equation, obtained from the heat equation following a "Reynolds decomposition" of the temperature $\theta = \bar{\theta} + \theta'$ and velocities $\mathbf{u} = \bar{\mathbf{u}} + \mathbf{u}'$,

$$\frac{\partial \overline{\theta'^2}}{\partial t} + \nabla \cdot (\overline{\mathbf{u}}\overline{\theta'^2} + \overline{\mathbf{u}'\theta'^2} - \kappa \nabla \overline{\theta'^2}) + 2\overline{\mathbf{u}'\theta'} \cdot \nabla \bar{\theta} = -2\kappa \overline{\nabla\theta' \cdot \nabla\theta'} \tag{5.1}$$

where $\mathbf{u}$ is the three-dimensional velocity vector and κ the heat molecular diffusivity, overbars denote temporal mean and primes the deviations from that mean. This equation states that the generation and transport of potential temperature fluctuations (left-hand side) is balanced by its dissipation by molecular motions (right-hand side). Assuming that fluctuations are statistically stationary and homogeneous (Ferrari and Polzin, 2005), the first four terms vanish, and the equations simplify to

$$\overline{\mathbf{u}'\theta'} \cdot \nabla \bar{\theta} = -\kappa \overline{\nabla\theta' \cdot \nabla\theta'} \equiv -\frac{1}{2}\chi \tag{5.2}$$

where χ is the rate of dissipation of temperature variance, which can be measured with fast-response thermistor probes. Equation 5.2 is the Osborn-Cox relation (Osborn and Cox, 1972) which equals the generation of variance by eddies stirring the background gradient (left-hand side) with its removal by molecular mixing (right-hand side).

In order to assess the interactions between the large, intermediate and small-scale flows in setting the large scale θ-S distribution, we consider the triple decomposition of variables into large-scale motions, mesoscale fluctuations and microscale turbulence (Joyce, 1977; Davis, 1994; Garret, 2001; Ferrari and Polzin, 2005); in a way, this is as decomposing the fluctuations into intermediate (mesoscale and internal waves) and microscale (turbulence supporting unstable overturns and direct molecular dissipation) scales: $\theta' = \theta_e + \theta_t$ and $\mathbf{u}' = \mathbf{u}_e + \mathbf{u}_t$ (Ferrari and Polzin, 2005; Naveira Garabato et al., 2016). The previous equation becomes

$$\langle \mathbf{u}_t \theta_t' \rangle \cdot \nabla_\perp \overline{\theta} + \langle \mathbf{u}_e \theta_e' \rangle \cdot \nabla_\parallel \overline{\theta} = -K_t |\nabla_\perp \overline{\theta}|^2 - K_e |\nabla_\parallel \overline{\theta}|^2 = -\frac{1}{2}\langle \chi \rangle \tag{5.3}$$

where K_t and K_e respectively are the dianeutral and isoneutral diffusivities, and $\nabla_\perp$ and $\nabla_\parallel$ indicate gradient operators across and along neutral density surfaces, respectively. Equation 5.3 states that the variance of potential temperature is produced by both small scale turbulence (taken as a dianeutral or vertical turbulent flux acting on the vertical mean temperature gradient, $\langle \mathbf{u}_t \theta_t' \rangle \cdot \nabla_\perp \overline{\theta} = -K_t |\nabla_\perp \overline{\theta}|^2$), and by mesoscale eddies (taken as a lateral isoneutral eddy flux acting onto horizontal gradients of the large-scale $\langle \mathbf{u}_e \theta_e' \rangle \cdot \nabla_\parallel \overline{\theta} = -K_e |\nabla_\parallel \overline{\theta}|^2$), and that both together equal molecular mixing. The balance between the generation of temperature variance by mesoscale eddy stirring and its dissipation by molecular mixing is not expected to meet locally. Therefore, the balance in Equation 5.3 might only be fulfilled when integrated over large horizontal scales of persistent thermohaline variability (Naveira Garabato et al., 2016).

The dianeutral diffusivity, K_t, can be determined from the turbulent kinetic energy dissipation rate (ϵ), estimated from microstructure measurements, through a mixing efficiency coefficient (Γ),

$$K_t = \frac{\Gamma \epsilon}{N^2} \tag{5.4}$$

where N^2 is the squared buoyancy frequency $\left(N^2 = -\frac{g}{\rho_0}\frac{\partial \rho}{\partial z}\right)$ and Γ is taken to be 0.2 (Osborn, 1980). Replacing in Equation 5.3 it is possible to estimate the isoneutral diffusivity (K_e), which characterizes the rate of eddy stirring,

$$K_e = \frac{\chi/2 - \Gamma \epsilon / N^2 |\nabla_\perp \overline{\theta}|^2}{|\nabla_\parallel \overline{\theta}|^2} \tag{5.5}$$

Equation 5.5 does not specifically include the effect of double-diffusive instabilities in the dianeutral production of temperature variance. Instead, the variance generated by these processes will be included in the isoneutral production, resulting in larger K_e values (Merrifield et al., 2016). This effect could be significant in the BMC region, particularly in the top 600 m and the upper NADW layer, where double diffusivity is a possible mechanism for vertical mixing (You, 1999, 2002; Bianchi et al., 2002).

5.2.2 Eddy induced overturning

Mesoscale eddies, besides inducing the poleward flux of tracers, contribute to the overturning circulation of the Southern Ocean, through southward mass advection. In addition, eddy advection helps strengthen the subduction of intermediate and mode waters at STFs (Speer et al., 2000; Henning and Vallis, 2004; Xu et al., 2016). The eddy-induced meridional transports have been related to the downgradient transport of potential vorticity (PV, $q = \frac{(\zeta+f)}{\rho_0}\frac{\partial \rho}{\partial z}$) (Marshall et al., 1993; Speer et al., 2000; Karsten and Marshall, 2002). PV is defined as $q \equiv (f+\zeta)/h \cong f/h$, where $h = \rho_0 \frac{\partial z}{\partial \gamma}$ is the thickness of the isoneutral layer, z is the vertical coordinate, ρ_0 is a constant reference density, and ζ is the vertical component of the relative vorticity.

Assuming that eddies mix PV along isoneutral surfaces (Green, 1970; Rhines and Young, 1982), the mean geostrophic eddy meridional flux of PV $\left(\overline{\mathbf{u}'q'}\right)$ is determined as an isoneutral downgradient diffusion of PV (Treguier et al., 1997),

$$\overline{\mathbf{u}'q'} \approx -K_e \partial_{\|} q \tag{5.6}$$

where $\partial_{\|}\overline{q}$ is the along-isoneutral meridional PV gradient; this equation simply assumes that PV will diffuse as any other tracer (Plumb and Mahlman, 1987; Smith and Marshall, 2009; Bates et al., 2014).

From the along-isoneutral eddy PV flux, using the equation for the residual meridional velocity in a transformed Eulerian-mean formulation (Ferreira et al., 2005, Abernathey et al., 2010), the eddy induced advective velocity ($\mathbf{u}^*$) is defined as the ageostrophic part balanced by the PV flux,

$$\mathbf{u}^* = \frac{\partial \psi^*}{\partial z} \equiv \frac{1}{f}\overline{\mathbf{u}'q'} \tag{5.7}$$

where ψ^* is the eddy-induced streamfunction and f the Coriolis parameter. From this velocity we can estimate the meridional eddy volume

$$\overline{h'\mathbf{u}^*} = \overline{h} L \frac{k_e}{f} \partial_{\|} q \tag{5.8}$$

where $\overline{h}$ is the isoneutral surface thickness and L a characteristic length scale (Argentine basin length). The eddy induced meridional volume flux will thus vary spatially with K_e and the large-scale isoneutral PV gradient.

5.3 Data

The hydrographic, velocity and microstructure data were gathered during the GEOTRACES 40S zonal section across the South Atlantic, on board the RRS James Cook during January 2012, as part of the GEOTRACES program (http://www.geotraces.org/). We use data from 9/10 CTD/microstructure stations in the western part of this section, along 40°S between about 20°W and 47°W and from this last location normal into the slope [Fig. 5.1]. The bottom topography changes along the section, with the first two stations over the Argentine slope, stations 3 to 6 over the smooth topography of the Argentine basin and stations 7 to 9 over a rough topography associated with the MAR [Fig. 5.1a].

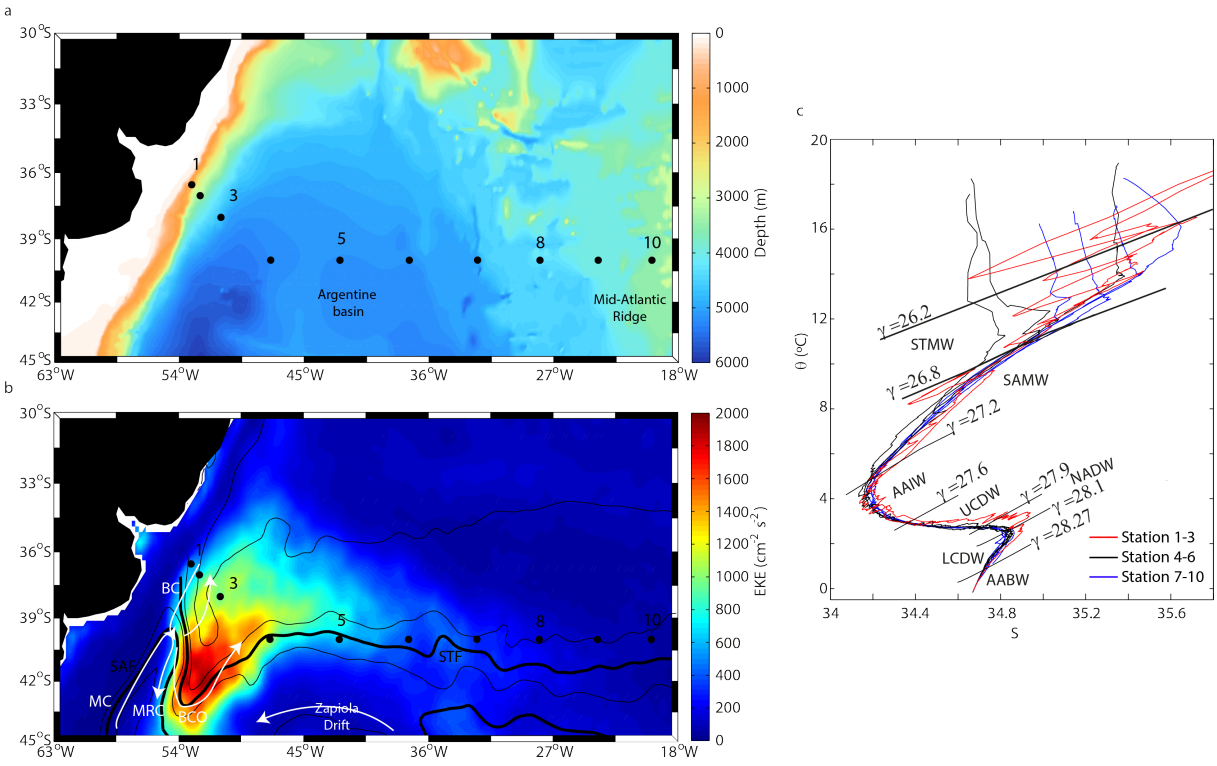

Fig. 5. 1: Southwest Atlantic. (a) Bottom topography (GEBCO, 2008). (b) Mean EKE for 24 years (1993-2016) as determined from the DUACS gridded absolute dynamic topography (ADT) product (Pujol et al., 2016). Black contours are ADT contours at intervals of 0.2 m. Thicker contours indicate the mean location of the Subantarctic Front (SAF) and Subtropical Front (STF), determined using ADT values of -5 and +30 cm. Representative pathways of the Brazil Current (BC), Malvinas Current (MC), Malvinas Return Current (MRC), Brazil Current Overshoot (BCO) and Zapiola Drift are indicated in white. The locations of the GEOTRACES 40S microstructure stations analysed in this study are indicated by black dots. (c) θ-S diagram along the zonal section. Black lines indicate density levels delimiting the different water masses, STMW (Subtropical Mode Water), SAMW (Subantarctic Mode Water), AAIW (Antarctic Intermediate Water), UCDW (Upper Circumpolar Deep Water), NADW (North Atlantic Deep Water (NADW), LCDW (Lower Circumpolar Deep Water), AABW (Antarctic Bottom Water).

The section roughly follows the STF, a boundary between relatively warm-salty subtropical and cold-fresh subantarctic waters. Stations 1 to 3 occupy slightly northern positions, being over the BC core. Stations 6 to 10 are north of the front while stations 4 and 5 are on the southern

flank, presenting slightly fresher and colder subantarctic origin waters [Fig. 5.1c]. The western stations (2 to 4) are on a very energetic region, where eddy kinetic energy (EKE) values exceed 1000 cm^2 s^{-2}, associated to eddies detached from meanders of the BC (Lentini et al., 2006; Saraceno and Provost, 2012) [Fig. 5.1b].

Conductivity-temperature-depth (CTD) data were obtained with a SeaBird 911 plus multiparametric probe, processed at a vertical resolution of 2 dbar. Horizontal velocity profiles were measured at each CTD cast with a downward-looking 300 kHz RDI Workhorse lowered acoustic Doppler current profiler (LADCP) fitted to the CTD frame, providing velocity measurements in 10-m bins from the surface to the seafloor. LADCP data were processed using the velocity inverse method (Visbeck, 2002).

Microstructure profiles were collected with a free-falling Vertical Microstructure Profiler 5500 (VMP), from the UKORS instrument pool. This equipment allows resolving the velocity and temperature microstructure, necessary to estimate ϵ and χ were estimated. The VMP consisted of two airfoil shear probes, two fast response thermistors and a dual needle conductivity cell capable of resolving scales from one meter to several millimetres. It also included a high-resolution SeaBird 3–4 CTD. The frequency of microstructure and CTD data sampling was 512 Hz and 32 Hz respectively. Variance of the vertical gradient in velocity and temperature were gridded at 0.5 dbar using 1-second bin lengths. Microstructure cast locations were recorded as the midpoint between the instrument deployment and recovery position.

The ϵ and χ measurements are bin-averaged at neutral density (γ^n) intervals of 0.08 kg m^{-3}. This bin size represents a compromise between the vertical resolution and a sufficient number of data at each interval so as to be statistically robust. N^2 is determined from the CTD data and averaged over the same neutral-density bins.

The large-scale mean potential temperature $\overline{\theta}$ is determined in two steps, following the methodology in Naveira Garabato et al. (2011). We first bin-average the CTD potential temperature over the same γ^n intervals as the microstructure variables and then fit a cubic spline to each isoneutral level. The dianeutral gradients are determined using centered differences in the neutral density space, except for those bins adjacent to bins with no data where we use forward or background differencing. In the case of isoneutral gradients, we looked for cross frontal property gradients.

We estimate along-isoneutral PV gradients from climatological data. We use the World Ocean Atlas 2013 (WOA-13, http://www.nodc.noaa.gov/OC5/woa13/) (Locarnini et al., 2013; Zweng et al., 2013), which provides temperature and salinity fields at standard depths and $1/4^o$ resolution, from which we determine the climatological γ^n. We bin-average the climatological PV and meridional PV gradients ($\partial_{||}\overline{q}$) at the same γ^n intervals as the microstructure data and

determine the layer thickness $\overline{h}$ as the difference in depth of the isoneutral surfaces. Finally, we interpolate these variables onto the position of the microstructure stations.

5.4 Results

5.4.1 Hydrographic and microstructure properties

The θ-S distribution along 40^{o}S shows large thermohaline fluctuations at almost all density classes [Fig. 5.1c]. Below the mixed layer, the largest isoneutral variability is found between 500 and 1100 m (27.1<γ^{n}<27.4 kg m^{-3}) and in the NADW layer (27.9<γ^{n}<28.1 kg m^{-3}). This may suggest important along isoneutral temperature variance production at these density levels. On the other hand, the AABW layer shows a tighter θ-S relation, where we may expect a dominant role of dianeutral mixing.

The maximum horizontal and vertical $\bar{\theta}$ gradients are found above the 27.2 kg m^{-3} isoneutral [Fig. 5.2]. At these levels there is substantial variability in the horizontal $\bar{\theta}$ gradients, responding to reversals in the isoneutral slopes associated with mesoscale features. The most intense gradients mark the transition between the warm waters in the core of the BC (stations 1-2) and the relatively cold waters in the BC offshore recirculation (BC overshoot or BCO) (stations 3-4), and from warm waters north of the STF (stations 6-7) to cold waters in stations further south (stations 4-5), in all cases associated with the shoaling of isoneutral surfaces. In contrast, all variables ($\bar{\theta}$, $\partial_{\perp}\bar{\theta}$, $\partial_{||}\bar{\theta}$ and N^2) are relatively homogeneous in denser layers. Maximum velocities occur in the western stations, especially over the BC, where velocities keep high down to about 600 m. Station 7, located over the western limit of the MAR, presents relatively high velocities at all depths.

Microstructure estimates of turbulent dissipation ϵ and dissipation of temperature variance χ [Fig. 5.3] show elevated values in the upper 500 m (near or above 10^{-9} W kg^{-1} and 10^{-7} ^{o}C s^{-1}, respectively), and decrease between one and two orders of magnitude below the 27.2 kg m^{-3} isoneutral. The most intense ϵ values are found in the upper 400 m of the station downstream the BCO (station 4), where mean turbulent dissipation value is 5.4 x 10^{-9} W kg^{-1}. At denser levels, the stations over a more complex bathymetry (stations 1, 2 and 7) show enhanced ϵ values. Regarding dissipation of temperature variance, values in the western stations (1 to 5) are higher than in the eastern stations (6 to 10) at almost all density classes, with mean values of 1.8 x 10^{-7} ^{o}C s^{-1} and 1.3 x 10^{-7} ^{o}C s^{-1}, respectively. Particularly intense χ values take place in the upper 400 m of station 3, where it reaches up to two orders of magnitude more than in the remaining stations.

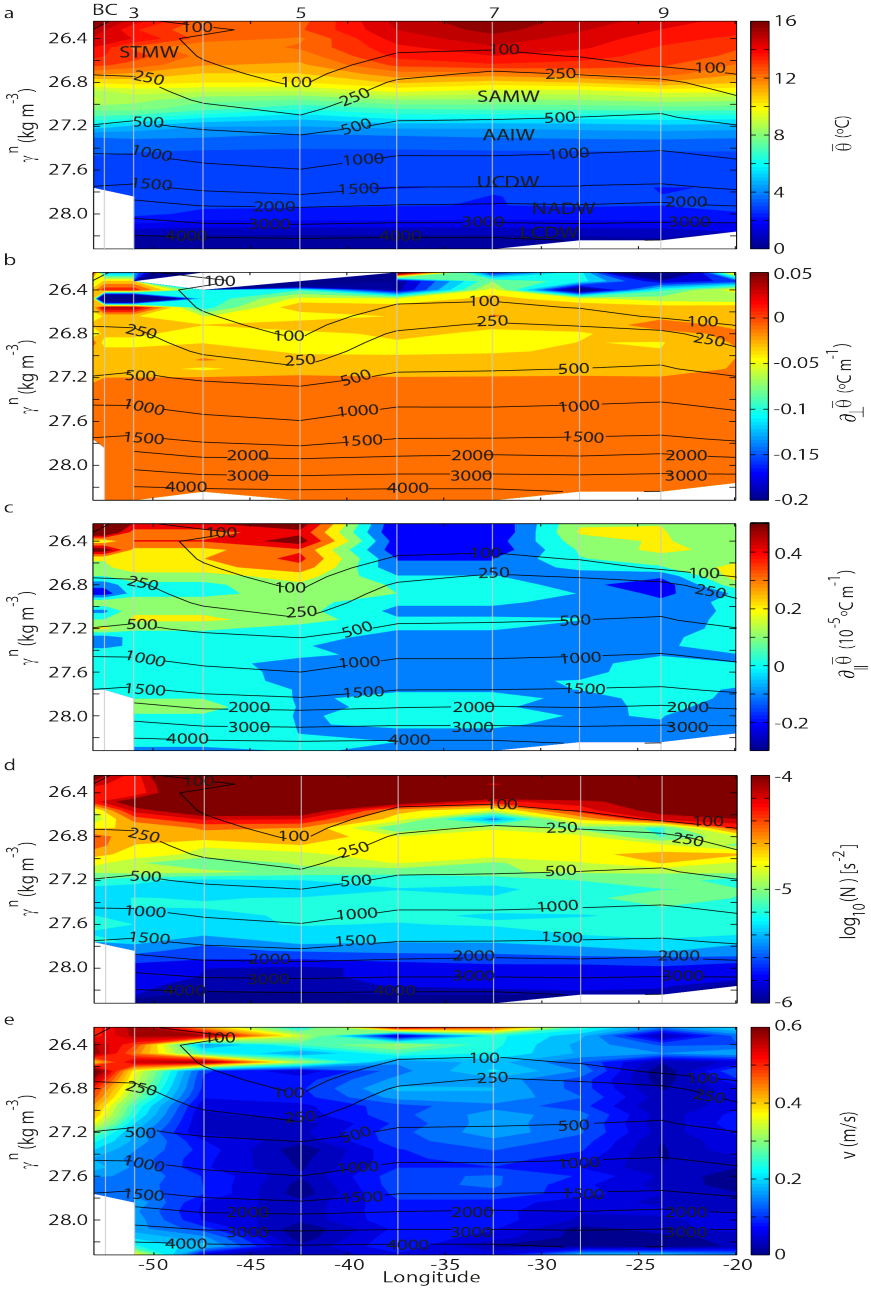

Fig. 5. 2: Zonal section of (a) mean potential temperature $\bar{\theta}$, (b) vertical potential temperature gradient $\partial_\perp \bar{\theta}$, (c) horizontal potential temperature gradient $\partial_\parallel \bar{\theta}$, (d) buoyancy frequency N^2, and (d) LADCP absolute velocity v, along each isoneutral surface. Black contours show pressure contours. vertical lines indicate the position of the microstructure stations.

The distribution of both variables is very similar, with a general increase, both at depth and especially in the upper ocean, at the BMC (west of station 4). The general qualitative enhancement of χ over ϵ suggests isoneutral stirring might be the principal process counterbalancing the dissipation of temperature variance across the basin, whereas the qualitative decline of χ between 1100-2500 m in the stations over the MAR may indicate the important implication of dianeutral mixing at this location.

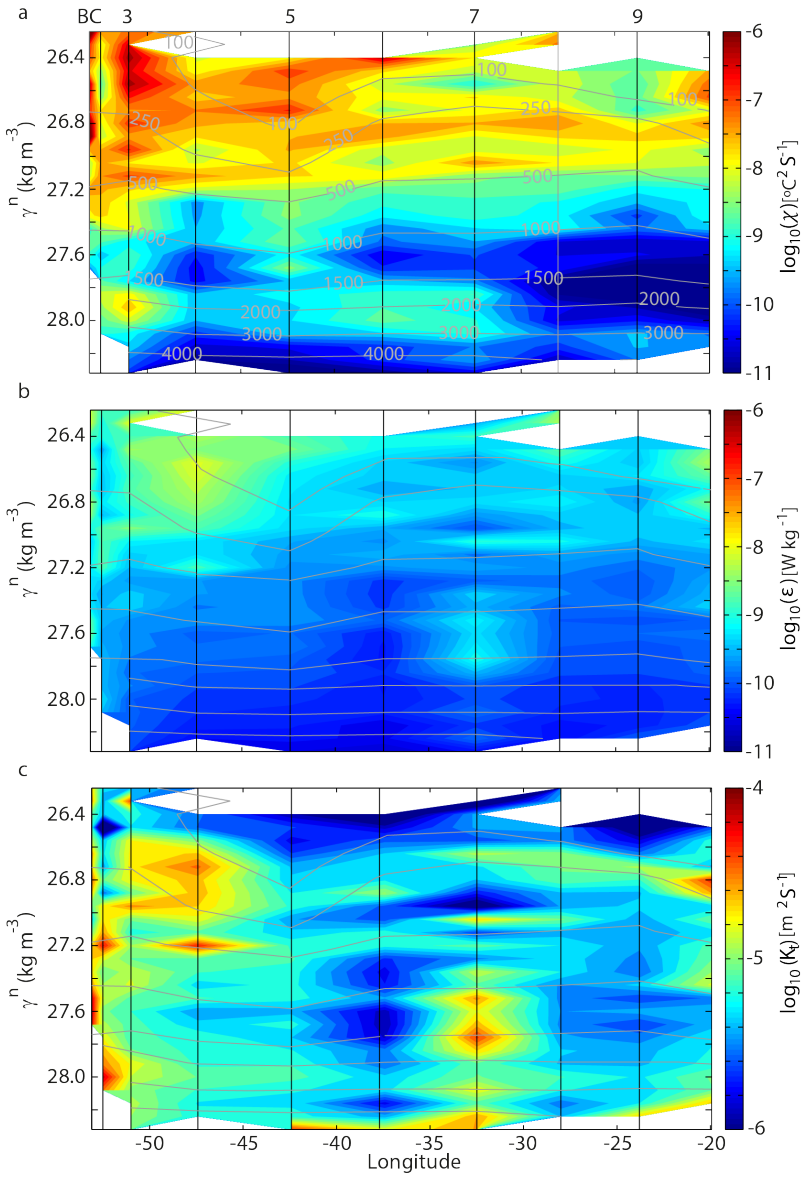

Fig. 5. 3: Vertical zonal section of the log distributions of (a) rate of dissipation of temperature variance χ, (b) turbulent kinetic energy dissipation rate ϵ, and (c) dianeutral diffusivity K_t. Gray contours show pressure contours. Black vertical lines indicate the position of microstructure stations.

5.4.2 Dianeutral and isoneutral stirring

The mean K_t across the basin is 1.2 x 10^{-2} m^2 s^{-1}, with values varying by as much as two orders of magnitude in the vertical along the section [Fig. 5.3c]. Below 100 m, the western four stations present values higher than stations to the east, with mean values of 2.0 x 10^{-5} m^2 s^{-1} and 0.8 x 10^{-5} m^2 s^{-1} respectively. Especially remarkable are the large values (>2.0 x 10^{-2} m^2 s^{-1}) in the 26.6-27.24 kg m^{-3} density range of stations 3 and 4, where K_t is between half and one order of magnitude larger than in the rest of the section. Below 500 m, enhanced K_t values are found in stations over rough topography or near the shelf-break (stations 1, 2 and 7), being particularly high in the AAIW-UCDW layers of station 7 (peak values of 2.4 x 10^{-5} m^2 s^{-1}).

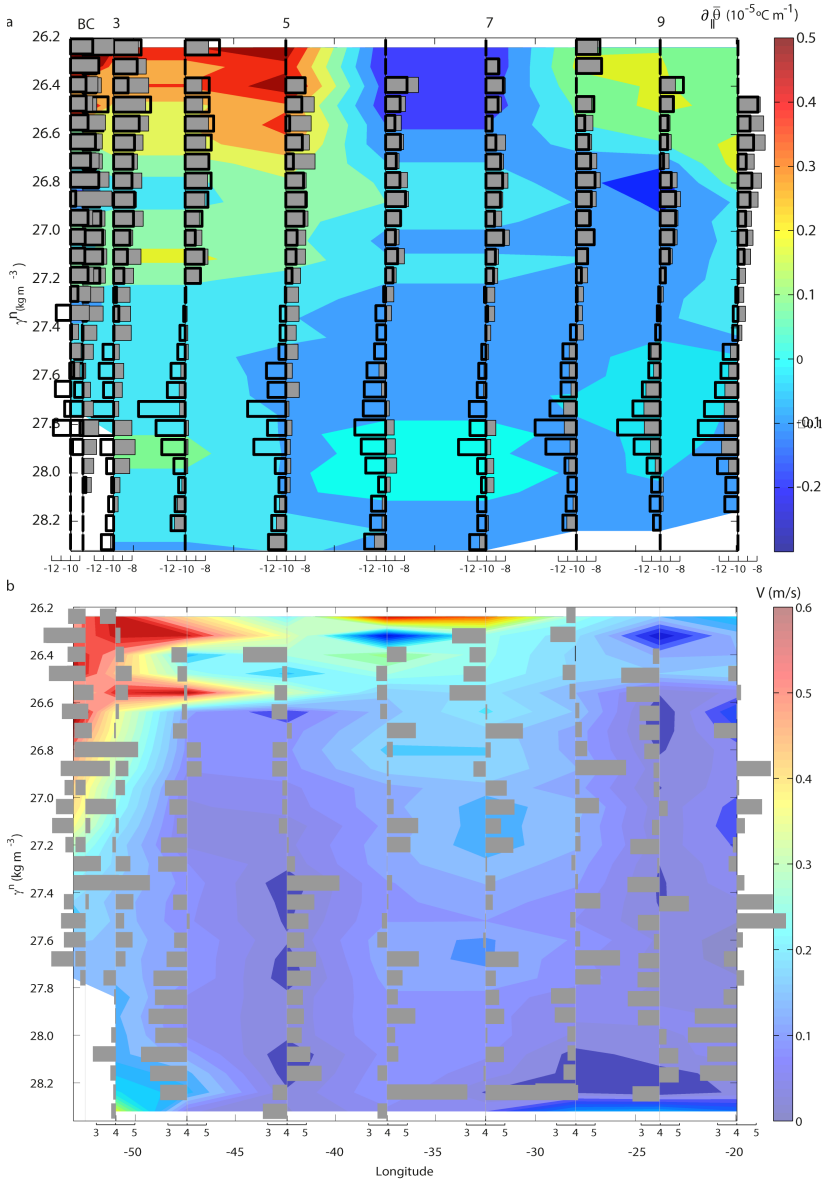

Fig. 5. 4: (a) Rate of dissipation of temperature variance $\chi/2$ (gray bars) and rate of dianeutral production of temperature variance $K_t \left|\nabla_\perp \bar{\theta}\right|^2$ (thicker contour bars) with along isoneutral potential temperature gradient $\partial_{\|}\bar{\theta}$ (color-coded). (b) Isoneutral diffusivity K_e (gray bars) with LADCP speed (color-coded).

For density layers lighter than 27.3 kg m^{-3}, most stations show an approximate balance between the dianeutral production of temperature variance ($K_t \left|\nabla_\perp \bar{\theta}\right|^2$) and its dissipation ($\chi/2$) [Fig. 5.4a]. On the contrary, deeper layers show low dianeutral variance production, suggesting a relatively large isoneutral production. Large temperature variance deficits, that is dianeutral production less than dissipation, are found in the 27.8 - 28.1 kg m^{-3} density range and vary between one and three orders of magnitude. The low $\nabla_\perp \bar{\theta}$ values in these layers may lead to an underestimation of dianeutral temperature variance production. Yet, it corresponds to NADW, where thermohaline variability is high [Fig. 5.1c] and therefore large isoneutral diffusivities are expected.

Since ϵ and χ show qualitative differences east (stations 6-10) and west (stations 1-5) of the BC-BCO, we expect a different balance between temperature variance production and dissipation in each flank of the section [Fig. 5.5]. In the upper 500 m, both variables show a fair balance between production and dissipation. On the other hand, for density classes 27.2-27.8 kg m^{-3}, there are large differences, with imbalances about one order of magnitude larger in the western than in the eastern stations. Finally, the densest layers show an imbalance of around one order at magnitude both sides of the section.

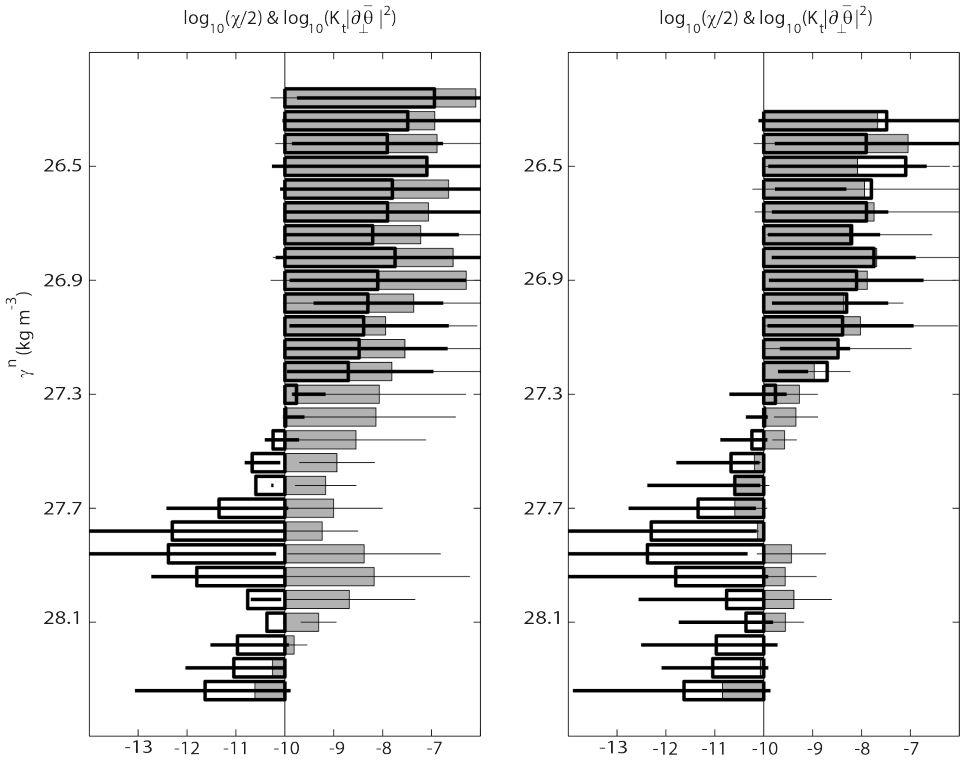

Fig. 5. 5: Mean profiles of the rate of dissipation of temperature variance $\chi/2$ (gray bars) and $K_t \left|\nabla_\perp \bar{\theta}\right|^2$ (thicker contour bars) distinguishing between (a) western stations (1, 2, 3, 5) and (b) eastern stations (6, 7, 8, 9, 10).

Along isoneutral diffusivity (K_e) varies by as much as two orders of magnitude but is usually above 10^3 m^2 s^{-1} [Fig. 5.4b]. In most stations, isoneutral diffusivity increases below 200 m (γ^n<26.8 kg m^{-3}), once the intense horizontal gradients and velocities of the upper layers decrease [Fig. 5.2]. In the upper 200 m, the BC station is the only one that has K_e exceeding 10^4 m^2 s^{-1}. Below 500 m (>27.2 kg m^{-3}), K_e is generally enhanced, with peak values over the smooth topography of the Argentine basin (station 5 to 8). Below 1300 m, K_e decreases at both extremes of the section, where bottom topography is more complex and dianeutral diffusivity values are high. There are remarkable the low K_e diffusivity values found at all density classes in the station located downstream the BCO (station 4); indeed, in this station dianeutral production nearly balances the dissipation of temperature variance.

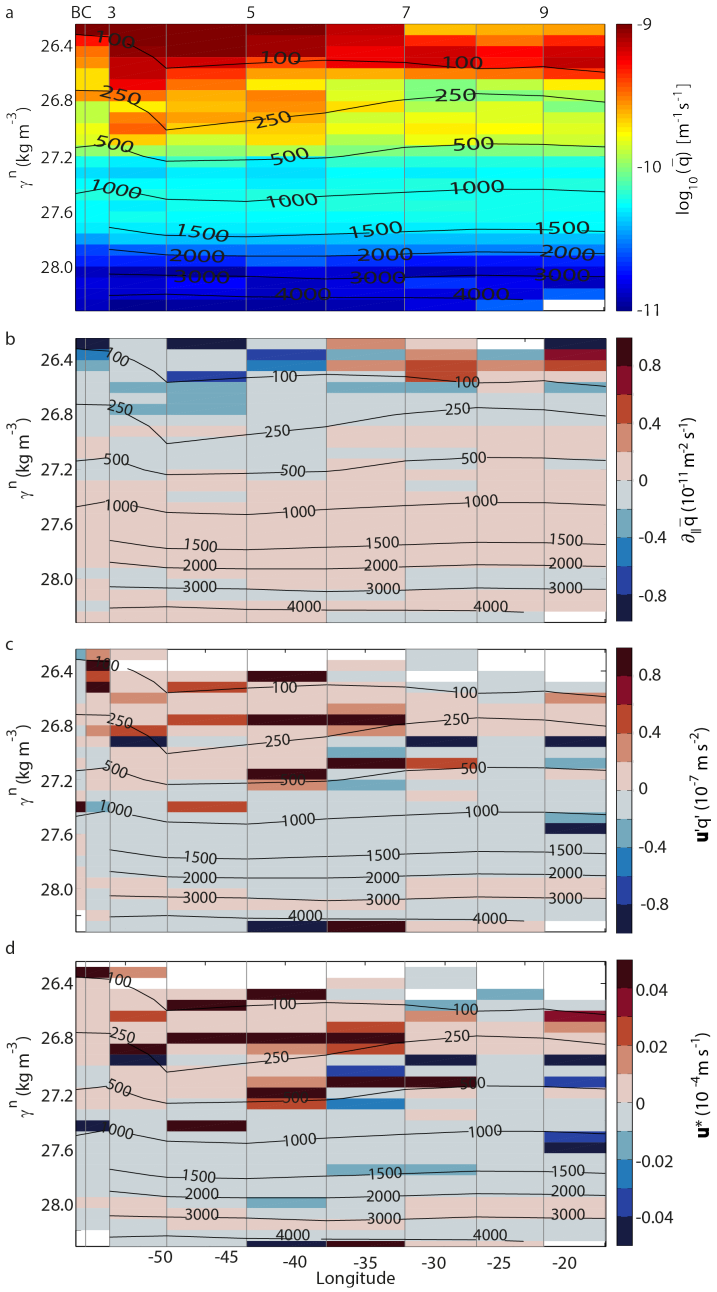

Fig. 5. 6: (a) Isoneutral potential vorticity expressed as $log_{10}(-\overline{q})$, (b) along isoneutral potential vorticity gradient $\partial_{\|}\overline{q}$, (c) eddy potential vorticity flux $\overline{\mathbf{u}'q'}$, and (d) eddy volume flux eddy induced advective velocity $\mathbf{u}^*$. Black contours show pressure levels (in dbar).

5.4.3 Eddy PV transport

The lowest $\overline{q}$ values, $O(10^{-9}\ m^{-1}\ s^{-1})$, are found in layers lighter than γ^n=27.2 kg m^{-3}, especially over the BC and downstream the BCO (stations 4-5), corresponding to mode waters near the BMC [Fig. 5.6a]: STMW formed over the BCO (Provost et al., 1999; Sato and Polito, 2014) and SAMW transported by the MC (Piola and Gordon, 1989). Below 600 m, the $\overline{q}$ differences along the section decrease.

The mean PV gradient is around 10^{-13} m^{-2} s^{-1} in the upper 400 m, intensifying in the western three stations [Fig. 5.6b], but decreases in layers denser than 27.3 kg m^{-3}, with values one or two orders of magnitude lower. The sign of the PV gradient indicates the sense of the flux: positive/negative $\partial_{||} q$ indicate poleward/equatorward eddy transports. The lighter layers (γ^n<26.6 kg m^{-3} or $z \leq 100$ m) present positive/negative values east/west of the MAR. The density range 26.6 <γ^n<27.3 kg m^{-3} shows negative $\partial_{||} \overline{q}$ values in most of the section, while positive values dominate for γ^n>27.3 kg m^{-3} or depths down to 1800 m. Finally, we find overall positive $\partial_{||} q$ values in the bottom layers.

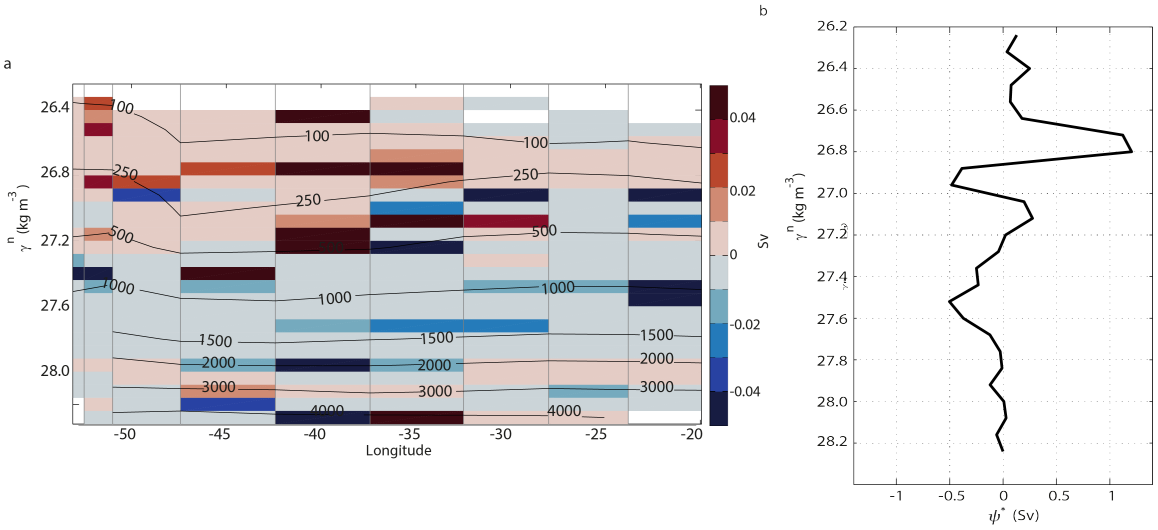

Fig. 5. 7: a) Eddy volume flux $\overline{h' \mathbf{u}^*}$. b) Section integrated eddy overturning streamfunction. Positive (negative) values indicate northward (southward) transports.

As expected from the spatial variability of both PV gradients and K_e, the $\overline{\mathbf{u}' q'}$ transports change along the section and with depth, with absolute values ranging between $O(10^{-12}$ m s$^{-2})$ and $O(10^{-7}$ m s$^{-2})$ [Fig. 5.6c]. The peak transports (4.2 x 10^{-8} m s^{-2}) are found in the upper 600 m. There are flow reversals at different density levels, mostly equatorward (positive values) in the upper 500 m and bottom waters and poleward (negative values) between 500 and 2500 m. The largest equatorward fluxes (2.5 x 10^{-8} m s^{-2}) take place in the uppermost 150 m of stations 3-4, where $\partial_{||} \overline{q}$ is more intense despite the low K_e values, and in stations 5-7 below 200 m, where both positive PV gradients and K_e increase. Below 800 m, the differences along the section are reduced, with a mean poleward PV flux of 4.3 x 10^{-9} m s^{-2}.

The eddy volume transport $\overline{h' \mathbf{u}^*}$ [Fig. 5.7a], determined from $\overline{\mathbf{u}' q'}$ and mean isoneutral layer thickness, presents peak values of 0.5 Sv, although mean values are of O (10^{-2} Sv). The largest equatorward eddy volume fluxes are determined by the large $\overline{\mathbf{u}' q'}$ in the top 250 m of station 2 and between 150 and 500 m of stations 5-7. Below 700 m, the eddy volume flux is poleward along the entire section, being more intense in the 27.4<γ^n <27.8 kg m^{-3} density classes.

Finally, we sum up the eddy-induced advection in a zonally integrated eddy overturning streamfunction [Fig. 5.7b]. This is generally negative, presenting a 1.2 Sv poleward transport in the $27.3<\gamma^n<27.9$ kg m^{-3} density classes. On the contrary, lighter layers show the equatorward subduction of around 0.5 Sv in the AAIW layer and a maximum of around 2 Sv in the STMW-SAMW layers.

5.5 Conclusions

We have examined the distribution of dianeutral and isoneutral diffusivity across the South Atlantic Subtropical Front (STF) in the Argentine basin. From the analysis of microstructure measurements in the framework of the triple decomposition of the temperature variance, which assumes that the heat variance generated by dianeutral small-scale stirring and by isoneutral mesoscale stirring is dissipated by molecular mixing. In addition, from this isoneutral diffusivity and the climatological potential vorticity gradients (PV), we determine the eddy induced meridional advective velocity and therefore the eddy-induced overturning streamfunction across the STF.

The turbulent dissipation of temperature variance (χ) increases in the western Argentine basin, with enhanced values downstream the main meanders of the Brazil Current (BC), the BC offshore recirculation and the BC overshoot (BCO). The mean dianeutral diffusivity is O (10^{-5}) m^2 s^{-1}, which is of the order of mean values reported by Whaterhouse et al. (2014) for this same dataset. However, in this study we have assessed the spatial distribution along the section, finding maximum values at depth over the rough topography of the mid-Atlantic ridge and the continental platform and between 200 and 800 m ($26.6<\gamma^n<27.3$ kg m^{-3}). These are particularly high downstream the BCO, about two orders of magnitude larger than the background values in the section. The associated mixing may contribute to the winter and mid-spring Subtropical Mode Water and Subantarctic Mode Water formation (Provost et al., 1999; Sato and Polito, 2014), as has been suggested for the formation of SAMW north of the Subantarctic Front in the South Pacific Ocean (Sloyan et al., 2010).

Isoneutral diffusivity by mesoscale eddies is overall above 10^3 m^2 s^{-1}. The density classes $26.4<\gamma^n<27.4$ kg m^{-3} present high values all along the section ($2.2 \times 10^3 - 3.8 \times 10^5$ m^2 s^{-1}), about one order of magnitude than shallower layers. Overall, the most intense diffusivity values are found downstream the BCO, over the smooth topography of the Argentine basin. Particularly high values are present in the $26.9<\gamma^n<27.2$ kg m^{-3} density classes and below 1300 m ($\gamma^n>27.76$ kg m^{-3}). The isonetrual diffusivities determined in this study are 1 to 2 orders of magnitude larger than estimates from Argo floats, with the greatest differences occurring in the centre of the basin at depths below 1500 m (Chapman et al., 2017; Cole et al., 2018). These large discrepancies may be related to either the different methodologies used in each case or to the

intense double diffusive activity in these deep layers.

Enhanced isoneutral diffusivity values in the upper 500 m are associated with the presence of intense potential vorticity (PV) gradients and drive the northward PV fluxes at these layers. Below, despite the low PV gradients, the strengthen of isoneutral mixing in the centre of the basin leads to the southward flux of UCDW. This flux results in the equatorward subduction of about 3 Sv of Subtropical Mode Water and lighter Antarctic Intermediate Water into the Subtropical gyre. Only few studies have quantified the eddy contribution to the mode water subduction across the STF of the South Atlantic. Our diffusivity estimates are comparable to previous estimates based on eddy-resolving models (Schouten and Matano, 2006; Tanaka and Hasumi, 2008), although the eddy-transport accounts for about only the 25 % of the total intermediate water subduction determined by Karstensen and Quadfasel (2002) with a water-age approach or by Jullion et al. (2010) from an inverse box model. Nevertheless, our measurements confirm that eddy stirring contribute substantially to the subduction of new STMW and AAIW into the subtropical thermocline. Further deep, the eddy transports induce a poleward flux of about 1 Sv in the $27.3 < \gamma^n < 27.9$ kg m^{-3} density classes, mainly occupied by Upper Circumpolar Deep Water.

Part IV | General conclusions and future perspective

Conclusions

The BMC is one of the most outstanding frontal systems in the world ocean. Despite the regional character of this system, it holds processes with implications in the whole South Atlantic circulation, becoming a key point in the returning path of the AMOC. The encounter of subantarctic and subtropical waters, together with the rich eddy field generated downstream the collision point, favours intense mixing processes and enhances the exchange of heat and salt across the STF, therefore driving strong water mass modifications. In addition, it holds the formation and northward subduction of mode water masses, hence contributing to the ventilation of the permanent thermocline.

Despite its remarkable importance, we still know little about the dynamics of the BMC. Its high spatial and temporal variability (e.g., Barré et al., 2006; Ferrari et al., 2017; Paniagua et al., 2018; Valla et al., 2018) contests the proper description of the main dynamic processes, from the regional circulation patterns to the fine-structure mixing, there still being numerous research gaps to fill. The conceptual and observational challenge is the study of very different processes that cover many spatial and temporal orders of magnitude and, very particularly, their interactions.

In this dissertation we have addressed this challenge through the revision of historical data, which includes recent studies of the MC at 41^{o}S (Ferrari et al., 2017; Artana et al., 2018; Paniagua et al., 2018), and the analyses of two novel high-resolution oceanographic cruises as well as remote sensing (SST and SSH), model and climatological data. These analyses have included a variety of techniques that encompass inverse regional-scale modelling, mesoscale diffusivity, submesoscale variability and energy dissipation at the microstructure.

Choke regions in the global heat transport

The ocean plays a crucial role in the Earth's global energy budget, being the Earth's primary heat reservoir and accounting for about half the tropical latitudinal heat transport (e.g. Palmer and McNeall, 2014; Von Schuckmann et al., 2016). Variations in ocean heat content and, very particularly, changes in the intensity and location of the latitudinal transports do play a fundamental role in global and regional climate variability.

In **Chapter 1** we have used a five-box model to explore what is the steady-state of the atmosphere-ocean latitudinal heat budget and how it changes at glacial-interglacial time-scales. Both the atmosphere and oceans are split into two latitudinal zones: a low-latitude zone (tropical- subtropical) where incoming solar radiation exceeds outgoing radiation and a high-latitude zone (subpolar-polar) with the opposite radiative balance. This model has allowed us to explore how the heat content and transport relate these to different processes such as changes in the global overturning circulation or the ice-albedo feedback at high latitudes.

We have found that the strength of the meridional heat exchange is primarily determined by the temperature gradient between the tropical-subtropical and subpolar-polar latitudes. High temperature gradients are found at key ocean regions – choke regions – that characterize the meeting site of the different radiative regimes. In these choke regions there are regional, mesoscale and small-scale processes that may either contribute to block or enhance meridional heat transfer. The two major choke points in the South Atlantic Ocean are the Agulhas retroflection and the BMC. Both regions connect the Atlantic basin with the other two major oceanic basins, Indian and Pacific Oceans, in what are known as the warm and cold routes of the MOC. The BMC, in particular, is a key western-boundary site connecting subtropical and subantarctic waters.

Circulation at the BMC

In **Chapter 2** we describe the hydrographic conditions found during an early fall cruise (TIC-MOC, March 2015) in the BMC and compare them with the conditions provided by both an eddy-resolving reanalysis product and climatological data. The description focuses in the contrasting properties of the two western boundary currents, in the mesoscale features surrounding the confluence front and in the cross-frontal structures. The most notorious features of the frontal system are the very intense frontal jet, where the surface velocity is higher than 1 m s^{-1}, and the cross-frontal thermohaline intrusions, which are reproduced neither in the reanalysis nor in the climatology.

We also assess the presence of large amounts or RdlP water on top the Confluence. Our results indicate that offshore transport of surface waters (RdlP and SASW) is related to the local wind forcing (intensity and directionality), the location of the maximum detrainment (position of the BMC) and the intensity of the two western boundary currents (Guerrero et al., 2014; Matano and Combes, 2014; Combes and Matano, 2018; Franco et al., 2018). The signature of these surface waters disappears at around 50^{o}W but they contribute to the freshening and cooling of the near-surface waters of subtropical origin, TW and STMW; these subtropical waters are transported eastwards by an intense jet that develops along the BCF, with a substantial ageostrophic contribution, and stretches for several hundred kilometres into the interior ocean. The frontal jet also transports coastal-origin nutrients, which will contribute to sustain the high productivity found at regional scales (Saraceno et al., 2005, Romero et al., 2006).

In **Chapter 3** we complete the regional and frontal description of the BMC during March 2015, through the development of two inverse models that allow calculating the main water-mass transports at two different scales, frontal and confluence. These models determine that the BC transport is in the range of reported mean values and point at a relative weak along-slope MC, which appears to correspond to the 'weak' MC mode at 41^{o}S (Ferrari et al., 2017). The models also help identify and quantify several regional features: the recirculation pathways of

both subtropical and subantarctic waters, the subduction of subantarctic waters at the frontal structure, and the high-latitude (42^{o}S or more) diversion of the MC and the development of intense mesoscale features between 40-42^{o}S during the weak MC mode [Fig. 3.1].

Water mass modifications and subduction at BMC

Fronts act both as *barriers* and *blenders* of contrasting properties (Bower et al., 1985). On one hand, the frontal system is highly stratified (hence statically very stable) and the usually intense currents run parallel to the front, hence strongly suggesting that fronts act as a barrier for tracer exchange. On the other hand, the front itself may be quite unstable, both laterally, as evidenced by the presence of multiple sub and mesoscale structures, and vertically, high vertical shear converts a statically stable into a dynamically unstable water column. These instability processes favour water-mass modifications and the meridional exchanges of heat and freshwater, among other properties, through vertical mixing and lateral surface and subsurface intrusions.

The results in **Chapters 2** and **Chapter 4** reveal the high variability of the frontal region. Thermohaline variability at the front can be triggered by changes in the intensity of the colliding currents, particularly the MC, and by high-frequency migrations of the BCF. Surface changes are also favoured by changes in the wind direction at characteristic scales of 2 to 5 days, which condition the presence or river waters on top of the frontal jets (**Chapter 2**). Notorious subsurface variability is the outcome of numerous thermohaline intrusions with dimensions of about 10-50 m thick and 10-20 km wide, evolving rapidly along the front (**Chapter 2**).

In **Chapters 2** and **Chapter 3** we also show the complex thermohaline and horizontal structure at the BCF as well as the rich eddy field. These features may favour the existence of dianeutral fluxes in the STMW-SAMW-AAIW layers and cross-frontal exchange of waters suggested at the end of **Chapter 3**. Additionally, in **Chapter 3** we assess the transformations experienced by waters of subtropical origin (TIC-MOC stations north of the BCF) before leaving the BMC and joining the returning path of the MOC.

In **Chapter 4** we use high-resolution data, from a second cruise at the BMC (RETRO-BMC, April 2017) and a daily SST product, to analyse the temperature temporal, vertical and spatial correlation scales. Near the continental slope, where the two boundary currents collide, the presence of mesoscale and submesoscale structures leads to high frontal variability, with a shortening of the correlation scales between 100 and 300 m. The vertical and spatial correlation scales are related in the subtropical side of the frontal system, largely as a consequence of mesoscale and submesoscale thermohaline intrusions. On the contrary, south of the BCF, the water masses are more homogeneous and submesoscale intrusions take longer to develop, in agreement with the lower variability found south of the BCF (**Chapter 2**). As the frontal system waters flow east, the thermohaline intrusions develop on both sides of the front and the

spatial scales decrease to similar levels as observed in the subtropical waters north of the front.

In **Chapter 5**, we complete the analysis of the mixing processes at the BMC and evaluate the dianeutral and isoneutral diffusive processes in the Argentine Basin along the STF. In agreement with the conclusions of **Chapter 3**, we find that the dianeutral diffusivity is enhanced in the upper 600 m of the water column, being particularly intense downstream the BCO. West of the BCO, over the shelf break, the dianeutral fluxes are intense below 200 m and down to the seafloor. These fluxes contribute to the transformations in the SAMW/AAIW layers observed in **Chapter 3** or the ones observed by Valla et al. (2018), whereby water masses get warmer and saltier. On the contrary, downstream the BCO, below 500 m and especially below 1300 m, the isoneutral mesoscale diffusivity dominates.

Finally, in **Chapter 5** we analyse the role of eddy-induced advection in the subduction of mode water into the local thermocline. Eddy-resolving models suggest that at regions with high eddy activity such as the BMC, the mesoscale eddy contribution to the subduction of mode waters can be of the same order of magnitude as the mean-flow subduction (e.g. Mashall, 1997). The results in **Chapter 5**, however, show that the along isoneutral subduction of the upper water masses (including STMW, SAMW and AAIW) is about 25 % of the total subduction. Nevertheless, these water masses contribute substantially to exchanges between the ACC and the subtropical gyre, thereby cooling, freshening and ventilating the thermocline layers of the South Atlantic Ocean.

Main conclusions

The above studies have extended our understanding on the dynamics in the BMC and their contribution to the transport of heat and other principal properties at different scales. The main general scientific contributions of this dissertation follow:

* The eddy-resolving GLORYS12V1 reanalysis product correctly reproduces the surface structure of the BMC during the TIC-MOC cruise whereas at depth it does not show the presence of thermohaline intrusions across the BMC front. Climatological products smooth the water properties so that the view of the highly variable BMC differs greatly from the cruise observations.

* The northeasterly prevailing winds during March 2015 favour the off-shelf detrainment of brackish river water, flowing eastward on top the frontal jet. The salinity anomaly on top the BMC correlates well with the high surface ageostrophic velocities.

* During March 2015, the inverse model at the Confluence scale leads to MC transports in agreement with mooring observations, 28.3 $\pm$ 1.4 Sv. Additionally, the inverse model predicts a southward 29.1 $\pm$ 8.3 Sv transport by the BC near 37^{o}S.

* During March 2015, between the eastern anticyclone and cyclone, we find a very intense subantarctic inflow into the Confluence, around double of the along-slope MC transport. This inflow is sustained through the cyclonic recirculation of flow exiting east along the Confluence and by an upstream earlier diversion of the MC. All transports add to cause an eastward along-front transport of 109.7 $\pm$ 15.1 Sv.

* In the northern edge of the BCF the flow is principally baroclinic. On the other hand, the MC inputs are split near equally between barotropic and baroclinic contributions while the interior subantarctic inflow is mainly barotropic.

* The inverse model reveals the existence of net upward dianeutral transference of AAIW and SAMW in the Confluence region. Moreover, the different mixing fractions for distinctive water properties point at the presence of cross-frontal and dianeutral exchanges.

* During April 2017, high-resolution SST images allow the identification of short temporal and spatial temperature correlation scales at the subtropical waters of the shelf-break BC and BMC. The MC and MRC present larger scales, probably caused by the presence of fewer mesoescalar structures. The BC and BCO presented short temporal scales, due to the significant mesoscale variability, but long spatial correlations, corresponding to their elongated structure.

* At the frontal region, the minimum correlation scales are associated with filaments stretching from the shelf. Overall, at the subsurface, the southern side of the front presents correlation scales that are larger than in the northern extreme. However, as the frontal jet flows eastward, the correlation scales at the south decrease due to the development of thermohaline intrusions on both sides of the front.

* The role of turbulent diffusive fluxes (dianeutral and isoneutral) in setting the temperature-salinity relationship in the Argentine Basin has been assessed. Dianeutral diffusivity is intensified at depth on both extremes of the basin, over the shelf-break and in the western side of the MAR. It is particularly intense is in the upper layers (26.6 $<\gamma^n<$27.3 kg m^{-3}) downstream the BCO. On the other hand, isoneutral diffusivity is enhanced at depths greater than 500 m.

* The isoneutral eddy-induced meridional volume flux across the STF is largest in the upper 600 m. It leads to the poleward subduction of SAMW and AAIW into the subtropical thermocline, in the 27.3 $<\gamma^n<$27.9 kg m^{-3} density classes.

Future research

One of the most relevant results in this thesis has been to elucidate the prominent role of mesoscale structures in the regional circulation and mixing processes at the BMC. In **Chapter 3**

we have examined the recirculations associated to the mesoscale features and their influence on the regional BMC circulation and in **Chapter 5** we have assessed the role of eddy diffusive (eddy stirring) and eddy advection in the Argentine basin. Nevertheless, we have not presented any results regarding the role of eddies in the trapping and transfer of properties across the STF and SAF. Lentini et al. (2006) estimated, from SST and altimetry data, that each BC anticyclonic ring can carry a heat anomaly of 0.045 PW cross the BCF. However, they did not consider the three-dimensional shape of the eddy or their evolution.

At any time, it is common to observe anticyclones south of the BCF and cyclones north of it (Lentini et al., 2006; Pilo et al., 2015). The formation of rings in this area is related to the large-scale retroflection of the BCO (da Silveira et al., 1999), which can occlude and shed a large anticyclonic eddy in a process forced by continental geography, bathymetry and wind patterns (e.g. Olson, 1991; Matano, 1993; De Boer et al., 2013); this process can also lead to the formation of additional anticyclonces/cyclonic eddies south/north of the BCF, as observed during TIC-MOC cruise (**Chapter 2** and **Chapter 3**). However, there are no statistics of the average number of cyclonic and anticyclonic eddies exchanged between the subtropical and subantarctic zones per year. Altimetry could be used to identify and track the number, and associated surface areas, of those eddies crossing the frontal system.

Once we have the number and areal extent of eddies, in order to quantify their property content, we still need to characterize their vertical extent and distribution of properties. Mesoscale eddies in the Argentine basin have been studied using high-resolution radiometer sea surface data, altimetry data (Lentini et al., 2002; 2006; Saraceno and Provost, 2012; Pilo et al., 2015), in-situ measurements from the Argo program (Dong et al., 2014; Zhang et al., 2014; Frenger et al., 2015) and the ARMOR-3D data set, which combines in-situ, SST and altimetry data (Mason et al., 2017). However, only a few of these studies have characterized the subregional vertical structure of these features, based on either the relatively scarce in-situ available measurements or a combination of Argo and auxiliary SST and altimetry data (Lentini et al., 2002; Mason et al., 2017). For example, anticyclonic eddies detaching from the BMC at origin are about 5^{o}C warmer and 1 psu saltier than the surrounding subantarctic waters (Lentini et al., 2002), although these property anomalies may change as eddies spread into different subregions.

The combination of these analyses – the characterization of the subregional properties of eddies and the number of anticyclones and cyclones crossing the BCF – could be used to assess the potential impact of mesoscale eddies in the cross-frontal transport of heat in the BMC. This is work currently in progress.

Throughout the thesis, the BMC frontal system has emerged as a source of questions and surprises that indeed deserve further attention, such as the temporal development of the subsurface thermohaline intrusions, the spatial extension and temporal intermittency of the brackish

shelf waters, and the ageostrophic horizontal and vertical motions. Of special interest has been to understand how the BMC evolves as a result of upstream (e.g. the offshore diversion of the MC) and downstream (the anticyclones in the outer ring of the Zapiola Gyre). The recent efforts in monitoring the MC (Ferrari et al., 2017; Artana et al., 2018; Paniagua et al.,2018) and the BC (Meinen et al., 2012; 2013; 2017; 2018; Valla et al., 2018; 2019) will be fundamental in this direction; these should be completed in the future with the surveying (remote sensing and Argo floats) of the Zapiola Gyre.

Part V ‖ References

Abernathey, R. P., and Marshall, J. (2013). Global surface eddy diffusivities derived from satellite altimetry. *Journal of Geophysical Research: Oceans*, 118(2), 901-916.

Abernathey, R., Marshall, J., Mazloff, M., and Shuckburgh, E. (2010). Enhancement of mesoscale eddy stirring at steering levels in the Southern Ocean. *Journal of Physical Oceanography*, 40, 170–184.

Acha, E. M., Mianzan, H. W., Guerrero, R. A., Favero, M., and Bava, J. (2004). Marine fronts at the continental shelves of austral South America: Physical and ecological processes. *Journal of Marine Systems*, 44(1), 83-105.

Alexeev, V. A., and Lindberg, K. (2004). A study of the effects of different parameterizations of the surface fluxes on stability of the climate system using a simple box model. *Russian Journal of Numerical Analysis and Mathematical Modelling*, 19, 361.

Álvarez, M., Brea, S., Mercier, H., and Álvarez-Salgado, X. A. (2014). Mineralization of biogenic materials in the water masses of the South Atlantic Ocean. I: Assessment and results of an optimum multiparameter analysis. *Progress in Oceanography*, 123, 1-23.

Annan, J. D., and Hargreaves, J. C. (2013). A new global reconstruction of temperature changes at the Last Glacial Maximum. *Climate of the Past*, 9(1), 367-376.

Artana, C., Ferrari, R., Koenig, Z., Saraceno, M., Piola, A.R., and Provost, C. (2016). Malvinas Current variability from Argo floats and satellite altimetry. *Journal of Geophysical Research: Oceans*, 121, 4854–4872.

Artana, C., Ferrari, R., Koenig, Z., Sennéchael, N., Saraceno, M., Piola, A. R., and Provost, C. (2018a). Malvinas Current volume transport at 41S: A 24 yearlong time series consistent with mooring data from 3 decades and satellite altimetry. *Journal of Geophysical Research: Oceans*, 123(1), 378-398.

Artana, C., Lellouche, J. M., Park, Y. H., Garric, G., Koenig, Z., Sennéchael, N., Ferrari, R., Piola, A.R., Saraceno, M., and Provost, C. (2018b). Fronts of the Malvinas Current System: Surface and subsurface expressions revealed by satellite altimetry, Argo floats, and Mercator operational model outputs. *Journal of Geophysical Research: Oceans*, 123, 5261-5285.

Artana C., Provost, C., Lellouche, J.M., Rio, M.H., Ferrari, R., and Sennéchael, N. (2019). The Malvinas Current at its Confluence with the Brazil Current: inferences from 25 years of satellite altimetry and Mercator Ocean reanalysis. *Journal of Geophysical Research: Occeans*,124.

Atlas, R., Hoffman, R. N., Ardizzone, J., Leidner, S. M., Jusem, J. C., Smith, D. K., and Gombos, D. (2011). A Cross-calibrated, Multiplatform Ocean Surface Wind Velocity Product for Meteorological and Oceanographic Applications. *Bulletin of the American Meteorological Society*, 92(2), 157-174.

Ballantyne, A. P., Lavine, M., Crowley, T. J., Liu, J., and Baker, P. B. (2005). Meta-analysis of tropical surface temperatures during the Last Glacial Maximum. *Geophysical Research Letters*, 32(5).

Barré, N., Provost, C., Renault, A., and Sennéchael, N. (2011). Fronts, meanders and eddies in Drake Passage during the ANT-XXIII/3 cruise in January-February 2006: A satellite perspective. *Deep Sea Research Part II: Topical Studies in Oceanography*, 58, 2533–2554.

Barré, N., Provost, C., and Saraceno, M. (2006). Spatial and temporal scales of the Brazil–Malvinas Current confluence documented by simultaneous MODIS Aqua 1.1-km resolution SST and color images. *Advances in Space Research*, 37(4), 770-786.

Bates, M., Tulloch, R., Marshall, J., and Ferrari, R. (2014). Rationalizing the spatial distribution of mesoscale eddy diffusivity in terms of mixing length theory. *Journal of Physical Oceanography*, 44, 1523–1540.

Berger, A. (1978). Long-Term Variations of Daily Insolation and Quaternary Climatic Changes. *Journal of the Atmospheric Sciences*, 35(12), 2362-2367.

Berger, A., and Loutre, M. F. (1991). Insolation values for the climate of the last 10 million years. *Quaternary Science Reviews*, 10(4), 297-317.

Bianchi, A. A., Giulivi, C.F., and Piola, A. R. (1993). Mixing in the Brazil-Malvinas confluence. *Deep Sea Research Part I: Oceanographic Research Papers*, 40(7), 1345-1358.

Bianchi, A. A., Pino, D. R., Perlender, H. G. I., Osiroff, A. P., Segura, V., Lutz, V., Clara, M. L., Balestrini, C. F., and Piola, A. R. (2009). Annual balance and seasonal variability of sea-air CO_2 fluxes in the Patagonia Sea: Their relationship with fronts and chlorophyll distribution. *Journal of Geophysical Research: Oceans*, 114, C03018.

Bianchi, A. A., Piola, A. R., and Collino, G. J. (2002). Evidence of double diffusion in the Brazil–Malvinas Confluence. *Deep Sea Research Part I: Oceanographic Research Papers*, 49(1), 41-52.

Birchfield, G. E. (1989). A coupled ocean-atmosphere climate model: temperature versus salinity effects on the thermohaline circulation. *Climate Dynamics*, 4(57).

Boebel, O., Schmid, C., and Zenk, W. (1999). Kinematic elements of Antarctic Intermediate Water in the western South Atlantic. *Deep-Sea Research Part II: Topical Studies in Oceanography*, 46 (1-2), 355-392.

Bower, A.S., Rossby, H.T., and Lillibridge, J.L. (1985). The Gulf Stream—Barrier or Blender?. *Journal of Physical Oceanography*, 15, 24–32.

Brandini, F. P., Boltovskoy, D., Piola, A., Kocmur, S., Röttgers, R., Cesar Abreu, P., and Mendes Lopes, R. (2000). Multiannual trends in fronts and distribution of nutrients and chlorophyll in the southwestern Atlantic (30–62°S). *Deep Sea Research Part I: Oceanographic Research Papers*, 47(6), 1015-1033.

Broecker, W. S. (1997). Thermohaline circulation, the Achilles heel of our climate system: Will man-made CO_2 upset the current balance? *Science*, 278(5343), 1582–1588.

Broecker, W. S. (2003). Does the trigger for abrupt climate change reside in the ocean or in the atmosphere? *Science*, 300(5625), 1519–1522.

Broecker, W. S., Peteet, D. M., and Rind, D. (1985). Does the ocean–atmosphere system have more than one stable mode of operation? *Nature*, 315(6014), 21-26.

Bryan, K., Manabe, S., and Pacanowski, R.C. (1975). A global ocean-atmosphere climate model. Part II. The oceanic circulation. *Journal of Physical Oceanography*, 5, 30-46.

Bryden, H. L., and Imawaki, S. (2001). Ocean heat transport, in Ocean Circulation and Climate, Int. Geophys. Ser., vol. 77, edited by by G. Siedler, J. Church, and J. Gould, pp. 455–474, Academic, San Diego, Calif.

Buckley, M. W., and Marshall, J. (2016). Observations, inferences, and mechanisms of the Atlantic Meridional Overturning Circulation: A review. *Review of Geophysics*, 54.

Budyko, M. I. (1969). The effect of solar radiation variations on the climate of the Earth. *Tellus*, 21(5), 611-619.

Bush, A. B. G., and Philander, S. G. H. (1999). The climate of the Last Glacial Maximum: Results from a coupled atmosphere-ocean general circulation model. *Journal of Geophysical Research: Atmospheres*, 104(D20), 24509-24525.

Campos, E., Busalacchi, A., Garzoli, S. L., Lutjeharms, J., Matano, R. P., Nobre, P., Olson, D., Piola, A. R, Tanajura, C. and Wainer, I. (1999). The South Atlantic and the Climate. OCEANOBS99: International Conference on the Ocean Observing System for Climate, 18 - 22 October 1999, Saint-Raphael, France.

Campos, E. J. D., Miller, J. L., Müller, T. J., and Peterson, R. G. (1995). Physical oceanography of the southwest Atlantic Ocean. *Oceanography*, 8(3), 87-91.

Carranza, M. M., Gille, S. T., Piola, A. R., Charo, M., and Romero, S. I. (2017). Wind modulation of upwelling at the shelf-break front off Patagonia: Observational evidence. *Journal of Geophysical Research: Oceans*, 122(3), 2401-2421.

Caspers, H. (1985), K. Grasshoff, M. Ehrhardt, K. Kremling (Editors): Methods of Seawater Analysis. Second, Revised and Extended Edition. With 108 figs, 26 tab., 419 pp. Weinheim/Deerfield Beach, Florida: Verlag Chemie 1983. ISBN 3–527-2599-8 (Weinheim) 0–89573-7 (Deerfield Beach). DM 140,00. Int. Revue ges. Hydrobiol. Hydrogr., 70, 302-303.

Cerovečki, I., Talley, L. D., Mazloff, M. R., and Maze, G. (2013). Subantarctic Mode Water Formation, Destruction, and Export in the Eddy-Permitting Southern Ocean State Estimate. *Journal of Physical Oceanography*, 43(7), 1485-1511.

Chapman, C., and Sallée, J.-B. (2017). Isopycnal Mixing Suppression by the Antarctic Circumpolar Current and the Southern Ocean Meridional Overturning Circulation. *Journal of Physical Oceanography*, 47(8), 2023-2045.

Chelton, D. B., Schlax, M. G., and Samelson, R. M. (2011b). Global observations of nonlinear mesoscale eddies. *Progress in Oceanography*, 91, 167–216.

Cole, S. T., Wortham, C., Kunze, E., and Owens, W. B. (2015). Eddy stirring and horizontal diffusivity from Argo float observations: Geographic and depth variability. *Geophysical Research Letters*, 42, 3989–3997.

Combes, V., and Matano, R. P. (2014). Trends in the Brazil/Malvinas Confluence region. *Geophysical Research Letters*, 41(24), 8971-8977.

Combes, V., and Matano, R. P. (2014). A two-way nested simulation of the oceanic circulation in the Southwestern Atlantic. *Journal of Geophysical Research: Oceans*, 119(2), 731-756.

Combes, V., and Matano, R. P. (2018). The Patagonian shelf circulation: Drivers and variability. *Progress in Oceanography*, 167, 24-43.

Confluence Group. (1990). Confluence 1988-1990: An intensive study of the Southwestern Atlantic. *Eos Trans. AGU*, 71(41), 1131-1134.

Cox, P.M., Betts, R.A., Jones, C.D., Spall, S.A., and Totterdell, I.J. (2000). Acceleration of global warming due to carbon-cycle feedbacks in a coupled climate model. *Nature*, 408, 184-187.

Czaja, A., and Marshall, J. (2006). The Partitioning of Poleward Heat Transport between the Atmosphere and Ocean. *Journal of Atmosphere Science*, 63, 1498–1511.

D'Asaro, E. A. (1985). The energy flux from the wind to near-inertial motions in the surface mixed layer. *Journal of Physical Oceanography*, 15, 1043–1059.

da Silveira, I.C., Flierl, G.R., and Brown, W.S. (1999). Dynamics of Separating Western Boundary Currents. *Journal of Physical Oceanography*, 29, 119–144.

Davis, R. E. (1994). Diapycnal Mixing in the Ocean: The Osborn–Cox Model. *Journal of Physical Oceanography*, 24(12), 2560-2576.

De Boer, A. M., Graham, R. M., Thomas, M. D., and Kohfeld, K. E. (2013). The control of the Southern Hemisphere Westerlies on the position of the Subtropical Front. *Journal of Geophysical Research: Oceans*, 118, 5669–5675.

Dogliotti, A. I., Lutz, V. A., and Segura, V. (2014). Estimation of primary production in the southern Argentine continental shelf and shelf-break regions using field and remote sensing data. *Remote Sensing of Environment*, 140, 497-508.

Dong, C., McWilliams, J. C., Liu, Y., and Chen, D. (2014). Global heat and salt transports by eddy movement. *Nature Communications*, 5, 3294.

Donlon, C. J., Martin, M., Stark, J., Roberts-Jones. J., Fiedler, E. and Wimmer, W. (2012). The Operational Sea Surface Temperature and Sea Ice Analysis (OSTIA) system. *Remote Sensing of Environment*, 116, 140-158.

Donners, J., Drijfhout, S.S., and Hazeleger, W. (2005). Water Mass Transformation and Subduction in the South Atlantic. *Journal of Physical Oceanography*, 35, 1841–1860.

Donohoe, A., and Battisti, D. S. (2011). Atmospheric and Surface Contributions to Planetary Albedo. *Journal of Climate*, 24(16), 4402-4418.

Dufour, C.O., Griffies, S.M., de Souza, G.F., Frenger, I., Morrison, A.K., Palter, J.B., Sarmiento, J.L., Galbraith, E.D., Dunne, J.P., Anderson, W.G., and Slater, R.D. (2015). Role of Mesoscale Eddies in Cross-Frontal Transport of Heat and Biogeochemical Tracers in the Southern Ocean. *Journal of Physical Oceanography*, 45, 3057–3081.

Environmental Protection Agency. (2003). Guidelines establishing test procedures for the analysis of pollutants. Appendix B: Definition and procedure for the determination of the Method Detection Limit.

Ferrari, R., Artana, C., Saraceno, M., Piola, A.R., and Provost, C. (2017). Satellite Altimetry and Current-Meter Velocities in the Malvinas Current at 41S: Comparisons and Modes of Variations. *Journal of Geophysical Research: Oceans*, 122, 9572–9590.

Ferrari, R., and Ferreira, D. (2011). What processes drive the ocean heat transport? *Ocean Modelling*, 38(3–4), 171–186.

Ferrari, R., Jansen, M. F., Adkins, J. F., Burke, A., Stewart, A. L., and Thompson, A. F. (2014). Antarctic sea ice control on ocean circulation in present and glacial climates. *Proceedings of the National Academy of Sciences*, 111(24), 8753-8758.

Ferreira, D., J. Marshall, and Heimbach, P. (2005). Estimating Eddy Stresses by Fitting Dynamics to Observations Using a Residual-Mean Ocean Circulation Model and Its Adjoint. *Journal of Physical Oceanography*, 35, 1891–1910.

Ferrari, R., and Nikurashin, M. (2010). Suppression of eddy diffusivity across jets in the Southern Ocean. *Journal of Physical Oceanography*, 40, 1501–1519.

Ferrari, R., and Polzin, K. L. (2005). Finescale Structure of the T–S Relation in the Eastern North Atlantic. *Journal of Physical Oceanography*, 35(8), 1437-1454.

Ferrari, R., Provost, C., Park, Y.-H., Sennéchael, N., Koenig, Z., Sekma, H., Garric, G., and Bourdallé-Badie, R. (2014). Heat fluxes across the Antarctic Circumpolar Current in Drake Passage: Mean flow and eddy contributions. *Journal of Geophysical Research: Oceans*, 119, 6381-6402.

Fetter, A. F. H., and Matano, R. P. (2008). On the origins of the variability of the Malvinas Current in a global, eddy-permitting numerical simulation. *Journal of Geophysical Research: Oceans*, 113(C11).

Firing, E. (1995). Processing ADCP data with the CODAS software system version 3.1, Joint Institute for Marine and Atmospheric Research, University of Hawaii National Oceanographic Data Center., Bremerhaven, PANGAEA.

Flato, G., Marotzke, J., Abiodun, B., Braconnot, P., Chou, S.C., Collins, W., Cox, P., Driouech, F., Emori, S., Eyring, V., Forest, C., Gleckler, P., Guilyardi, E., Jakob, C., Kattsov, V., Reason, C., and Rummukainen, M. (2013). Evaluation of Climate Models. In: Climate Change 2013: The Physical Science Basis. Contribution of Working Group I to the Fifth Assess-ment Report of the Intergovernmental Panel on Climate Change [Stocker, T.F., D. Qin, G.-K. Plattner, M. Tignor, S.K. Allen, J. Boschung, A. Nauels, Y. Xia, V. Bex and P.M. Midgley (eds.)]. Cambridge University Press, Cambridge, United Kingdom and New York, NY, USA.

Flierl, G. G. R. (1981). Particle motions in large-amplitude wave fields. *Geophysical and Astrophysical Fluid Dynamics*, 18(1–2), 39–74.

Foppert, A., Donohue, K. A., Watts, D. Randolph, and Tracey, K. L. (2017). Eddy heat flux across the Antarctic Circumpolar Current estimated from sea surface height standard deviation. *Journal of Geophysical Research: Oceans*, 122, 6947–6964.

Franco, B. C., Palma, E. D., Combes, V., Acha, E. M., and Saraceno, M. (2018). Modeling the offshore export of Subantarctic Shelf Waters from the Patagonian shelf. *Journal of Geophysical Research: Oceans*, 123, 4491-4502.

Frenger, I., Münnich, M., Gruber, N., and Knutti, R. (2015). Southern Ocean eddy phenomenology. *Journal of Geophysical Research: Oceans*, 120, 7413–7449.

Fu, L.-L. (2007). Interaction of Mesoscale Variability with Large-Scale Waves in the Argentine Basin. *Journal of Physical Oceanography*, 37(3), 787-793.

Ganachaud, A. (2003a). Error Budget of Inverse Box Models: The North Atlantic. *Journal of Atmospheric and Oceanic Technology*, 20(11), 1641-1655.

Ganachaud, A. (2003b). Large-scale mass transports, water mass formation, and diffusivities estimated from World Ocean Circulation Experiment (WOCE) hydrographic data. *Journal of Geophysical Research: Oceans*, 108(C7), 2156-2202.

Ganachaud, A., and Wunsch, C. (2003). Large-scale ocean heat and freshwater transports during the World Ocean Circulation Experiment. *Journal of Climate*, 16(4), 696–705.

Ganopolski, A., and Rahmstorf, S. (2001). Rapid changes of glacial climate simulated in a coupled climate model. *Nature*, 409(6817), 153-158.

Garcia, C.A.E., Sarma, Y.V.B., Mata, M.M., and Garcia, V.T.M. (2004). Chlorophyll variability and eddies in the Brazil–Malvinas Confluence region. *Deep Sea Research Part I: Oceanographic Research Papers*, 51, 159–172.

García, N. O., and Vargas, W. M. (1996). The spatial variability of runoff and precipitation in the Rio de la Plata basin. *Hydrological Sciences Journal*, 41:3, 279-299.

Garcia-Ladona, E., Salvador, J., Fernandez, P., Pelegrí, J.L., Elósegui, P., Sánchez, O., Jiménez, J.A., Pérez, F., Ballabrera, J., Isern-Fontanet, J., Salat., J., and Font, J. (2016). Thirty years of research and development of Lagrangian buoys at the Institute of Marine Sciences. *Scientia Marina*, 80S1, 141-158.

García-Olivares, A., and Herrero, C. (2012). Fitting the last pleistocene $\delta^{18}O$ and CO_2 time-series with simple box models. *Scientia Marina*, 76S1, 209–218.

García-Olivares, A., and Herrero, C. (2013). Simulation of glacial-interglacial cycles by simple relaxation models: Consistency with observational results. *Climate Dynamics*, 41, 1307–1331.

Garrett, C. (2001). Stirring and mixing: What are the rate controlling processes?. From Stirring to Mixing in a Stratified Ocean: Proc. 12th 'Aha Hulikoa' Hawaiian Winter Workshop, Honolulu, HI, University of Hawaii at Mānoa, 1–8.

Garzoli, S. L. (1993). Geostrophic velocity and transport variability in the Brazil-Malvinas Confluence. *Deep Sea Research Part I: Oceanographic Research Papers*, 40, 1379-1403.

Garzoli, S. L., Baringer, M.O., Dong, S., Perez, R.C., and Yao, Q. (2013). South Atlantic meridional fluxes. *Deep Sea Research Part I: Oceanographic Research Papers*, 71(C), 21-32.

Garzoli, S. L., and Bianchi, A. (1987). Time-space variability of the local dynamics of the Malvinas-Brazil confluence as revealed by inverted echo sounders. *Journal of Geophysical Research: Oceans*, 92(C2), 1914-1922.

Garzoli, S. L., and Garraffo, Z. (1989). Transports, frontal motions and eddies at the Brazil-Malvinas currents confluence. *Deep Sea Research Part A: Oceanographic Research Papers*, 36, 681-703.

Garzoli, S. L., and Gordon, A.L. (1996). Origins and variability of the Benguela Current. *Journal of Geophysical Research: Oceans*, 101(C1), 897-906.

Garzoli, S. L., and Matano, R. (2011). The South Atlantic and the Atlantic Meridional Overturning Circulation. *Deep Sea Research Part II: Topical Studies in Oceanography*, 58, 1837-1847.

Garzoli, S.L., and Simionato, C. (1990). Baroclinic instabilities and forced oscillations in the Brazil/Malvinas confluence front. *Deep Sea Research Part A: Oceanographic Research Papers*, 37(6), 1053-1074.

Gaube, P., McGillicuddy, D. J., Chelton, D. B., Behrenfeld, M. J., and Strutton, P. G. (2014). Regional variations in the influence of mesoscale eddies on near-surface chlorophyll. *Journal of Geophysical Research: Oceans*, 119(12), 8195-8220.

Gent, P.R., and Mcwilliams, J.C. (1990). Isopycnal Mixing in Ocean Circulation Models. *Journal of Physical Oceanography*, 20, 150–155.

Gildor, H., and Tziperman, E. (2003). Sea-ice switches and abrupt climate change. *Philosophical Transactions of the Royal Society of London. Series A: Mathematical, Physical and Engineering Sciences*, 361(1810), 1935-1944.

Gill, A. E. (1982). Atmosphere-Ocean Dynamics. 30, 1-662.

Goddard Institute for Space Studies/Earth Sciences Division/Science and Exploration Directorate/Goddard Space Flight Center/NASA, and Physical Oceanography Department/Woods Hole Oceanographic Institution. 2006. Objectively Analyzed Air-Sea Fluxes (OAFlux) For Global Oceans. Research Data Archive at the National Center for Atmospheric Research, Computational and Information Systems Laboratory.

Goni, G. J., Bringas, F., and DiNezio, P.N. (2011). Observed low frequency variability of the Brazil Current front. *Journal of Geophysical Research: Oceans*, 116(C10).

Goni, G., Kamholz, S., Garzoli, S., and Olson, D. (1996). Dynamics of the Brazil-Malvinas Confluence based on inverted echo sounders and altimetry. *Journal of Geophysical Research: Oceans*, 101(C7), 16273-16289.

Goni, G. J., and Wainer, I. (2001). Investigation of the Brazil Current front variability from altimeter data. *Journal of Geophysical Research: Oceans*, 106(C12), 31117-31128.

Goniadzki, D., Borús, J., Almeira, G., Diaz, L., Núñez, V., and Contreras, G. (2015). Posibles escenarios hidrológicos en la Cuenca del Plata durante el periodo abril-mayo-junio 2015. Instituto Nacional del Agua.

Gonzalez-Silvera, A., Santamaria-del-Angel, E., and Millán-Núñez, R. (2006). Spatial and temporal variability of the Brazil-Malvinas Confluence and the La Plata Plume as seen by SeaWiFS and AVHRR imagery. *Journal of Geophysical Research: Oceans*, 111, C06010.

Gordon, A. L. (1981). South Atlantic thermocline ventilation. *Deep Sea Research Part A: Oceanographic Research Papers*, 28, 1239-1264.

Gordon, A. L. (1986). Interocean exchange of thermocline water. *Journal of Geophysical Research: oceans*, 91(C4), 5037–5046.

Gordon, A. L. (1989). Brazil-Malvinas Confluence–1984. *Deep Sea Research Part A: Oceanographic Research Papers*, 36(3), 359-384.

Gordon, A. L., and Greengrove, C.L. (1986). Geostrophic circulation of the Brazil-Falkland confluence. *Deep Sea Research Part A: Oceanographic Research Papers*, 33, 573-585.

Gordon, A. L., Weiss, R. F., Smethie, W. M., and Warner, M. J. (1992). Thermocline and intermediate water communication between the south Atlantic and Indian oceans. *Journal of Geophysical Research: oceans*, 97(C5), 7223–7240.

Green, J. S. A. (1970). Transfer properties of the large-scale eddies and the general circulation of the atmosphere. *Quarterly Journal of the Royal Meteorological Society*, 96(408), 157-185.

Gregg, M.C. (1999). Uncertainties and Limitations in Measuring ϵ and χ_t. *Journal of Atmospheric and Oceanic Technology*, 16, 1483–1490.

Groeskamp, S., Sloyan, B. M., Zika, J. D., and McDougall, T. J. (2017). Mixing Inferred from an Ocean Climatology and Surface Fluxes. *Journal of Physical Oceanography*, 47(3), 667-687.

Guerrero, R. A., and Piola, A. R. (1987). Masas de agua en la plataforma continental, El mar Argentino y sus Recursos Pesqueros, 1E. E. Boschi, 107–118, Inst. Nac. de Invest. y Desarrollo Pesquero, Mar del Plata, Argentina, 1997.

Guerrero, R. A., Piola, A. R., Fenco, H., Matano, R. P., Combes, V., Chao, Y., James, C., Palma, E. D., Saraceno, M., and Strub, P. T. (2014). The salinity signature of the cross-shelf exchanges in the Southwestern Atlantic Ocean: Satellite observations. *Journal of Geophysical Research: Oceans*, 119(11), 7794-7810.

Hanawa, K., and Talley, L.D. (2001). Mode Waters. Ocean circulation and climate: observing and modelling the global ocean. (Siedler G, Church J, Gould WJ, Eds.).:373-386., San Diego, Calif. London: Academic.

Haney, R. L. (1971). Surface Thermal Boundary Condition for Ocean Circulation Models. *Journal of Physical Oceanography*, 1(4), 241-248.

Hansen, J., Ruedy, R., Sato, M., and Lo, K.(2010). Global surface temperature change. *Review of Geophysics*, 48, RG4004.

Hays, J. D., Imbrie, J., Shackleton, N. J. (1976). Variations in the Earth's Orbit: Pacemaker of the Ice Ages. *Science*, 194(4270), 1121.

Held, I. M. and Suarez, M. J. (1974). Simple albedo feedback models of the icecaps. *Tellus*, 26: 613-629.

Henning, C. C., and Vallis, G. K. (2004). The Effects of Mesoscale Eddies on the Main Subtropical Thermocline. *Journal of Physical Oceanography*, 34(11), 2428-2443.

Herbert, T. D., Peterson, L. C., Lawrence, K. T., and Liu, Z. (2010). Tropical Ocean Temperatures Over the Past 3.5 Million Years. *Science*, 328(5985), 1530.

Hoffert, M. I., Callegari, A. J., and Hsieh, C.-T. (1980). The role of deep sea heat storage in the secular response to climatic forcing. *Journal of Geophysical Research: Oceans*, 85(C11), 6667-6679.

Hogg, A. M. (2008). Glacial cycles and carbon dioxide: A conceptual model. *Geophysical Research Letters*, 35(1).

Holloway, M. D., Sime, L. C., Singarayer, J. S., Tindall, J. C., Bunch, P., and Valdes, P. J. (2016). Antarctic last interglacial isotope peak in response to sea ice retreat not ice-sheet collapse. *Nature Communications*, 7, 12293.

Hosoda, K., and Kawamura, H. (2004). Global space-time statistics of sea surface temperature estimated from AMSR-E data. *Geophysical Research Letters*, 31(17).

Imbrie, J., Berger, A., Boyle, E. A., Clemens, S. C., Duffy, A., Howard, W. R.,Kukla, G., Kutzbach, J., Martinson, D.G., McIntyre, A., Mix, A.C., Molfino, B., Morley, J.J., Peterson, L.C., Pisias, N.G., Prell, W.L., Raymo, M.E., Shckleton, N.J., and Toggweiler, J. R. (1993). On the structure and origin of major glaciation cycles 2. The 100,000-year cycle. *Paleoceanography*, 8(6), 699-735.

Jayne, S.R., and Marotzke, J. (2002). The Oceanic Eddy Heat Transport. *Journal of Physical Oceanography*, 32, 332-3345.

Johnson, G. C., and Bryden, H. L. (1989). On the size of the Antarctic Circumpolar Current. *Deep-Sea Research*, 36, 39–53.

Joyce, T. M. (1977). A Note on the Lateral Mixing of Water Masses. *Journal of Physical Oceanography*, 7(4), 626-629.

Jullion, L., Heywood, K.J., Naveira Garabato, A.C., and Stevens, D.P. (2010). Circulation and Water Mass Modification in the Brazil–Malvinas Confluence. *Journal of Physical Oceanography*, 40(5), 845-864.

Kahl, L. C., Bianchi, A. A., Osiroff, A. P., Pino, D. R., and Piola, A. R. (2017). Distribution of sea-air CO_2 fluxes in the Patagonian sea: seasonal, biological and thermal effects. *Continental Shelf Research*, 143, 18-28.

Kageyama, M., Merkel, U., Otto-Bliesner, B., Prange, M., Abe-Ouchi, A., Lohmann, G., Ohgaito, R., Roche, D.M., Singarayer, J., Swingedouw, D., and Zhang, X. (2013). Climatic impacts of fresh water hosing under Last Glacial Maximum conditions: a multi-model study. *Climate of the Past*, 9(2), 935-953.

Karsten, R., Jones, H., and Marshall, J. (2002). The Role of Eddy Transfer in Setting the Stratification and Transport of a Circumpolar Current. *Journal of Physical Oceanography*, 32(1), 39-54.

Karstensen, J., and Quadfasel, D. (2002). Formation of Southern Hemisphere Thermocline Waters: Water Mass Conversion and Subduction. *Journal of Physical Oceanography*, 32, 3020–3038.

Kiehl, J. T., and Trenberth, K. E. (1997). Earth's Annual Global Mean Energy Budget. *Bulletin of the American Meteorological Society*, 78(2), 197-208.

King, B. A., Firing, E., and Joyce, T.M. (2001). Shipboard observations during WOCE. In G. Siedler, J. Church, and J. Gould (Eds.), Ocean Circulation and Climate: Observing and Modelling the Global Ocean (pp. 99-122). Academic Press.

Kuhlbrodt, T., Griesel, A., Montoya, M., Levermann, A., Hofmann, M., and Rahmstorf, S. (2007). On the driving processes of the Atlantic meridional overturning circulation. *Reviews of Geophysics*, 45.

Kunze, E., Firing, E., Hummon, J. M., Chereskin, T. K., and Thurnherr, A. M. (2006). Global Abyssal Mixing Inferred from Lowered ADCP Shear and CTD Strain Profiles. *Journal of Physical Oceanography*, 36(8), 1553-1576.

Ledwell, J. R., Montgomery, E. T., Polzin, K. L., St. Laurent, L. C., Schmitt, R. W., and Toole, J. M. (2000). Evidence for enhanced mixing over rough topography in the abyssal ocean. *Nature*, 403, 179–182.

Lee, S.K., Pelegrí, J.L., and Kroll, J. (2001). Slope Control in Western Boundary Currents. *Journal of Physical Oceanography*, 31(11), 3349-3360.

Legeais, J.-F., Ollitrault, M., and Arhan, M. (2013). Lagrangian observations in the intermediate western boundary current of the South Atlantic. *Deep Sea Research Part II*, 85, 109–126.

Legeckis, R., and Gordon, A. L. (1982). Satellite observations of the Brazil and Falkland currents— 1975, 1976 and 1978. *Deep Sea Research Part A: Oceanographic Research Papers*, 29(3), 375-401.

Lentini, C. A. D., Goni, G. J., and Olson, D. B. (2006). Investigation of Brazil Current rings in the confluence region. *Journal of Geophysical Research: Oceans*, 111 (C6).

Lentini, C. A. D., Olson, D. B. and Podestá, G. P. (2002). Statistics of Brazil Current rings observed from AVHRR: 1993 to 1998. *Geophysical Research Letters*, 29(16), 58-51-58-54.

Locarnini, R. A., Mishonov, A. V., Antonov, J. I., Boye, T. P., Garcia, H. E., Baranova, O. K., and Seidov, D. (2013). World Ocean Atlas 2013, Volume 1: Temperature. S. Levitus, Ed., A. Mishonov Technical Ed.; NOAA Atlas NESDIS 73, 40 pp.

Loeb, N. G., Wielicki, B. A., Doelling, D. R., Smith, G. L., Keyes, D. F., Kato, S., Manalo-Smith, M., and Wong, T. (2009). Toward Optimal Closure of the Earth's Top-of-Atmosphere Radiation Budget. *Journal of Climate*, 22(3), 748-766.

London, J., New York, U., Department of, M., Oceanography. (1957). A study of the atmospheric heat balance. New York: New York University.

Lumpkin, R., and Garzoli, S. L. (2011). Interannual to decadal changes in the western South Atlantic's surface circulation. *Journal of Geophysical Research*, 116, C01014.

Lumpkin, R., and Johnson, G. C. (2013). Global ocean surface velocities from drifters: Mean, variance, El Niño–Southern Oscillation response, and seasonal cycle. *Journal of Geophysical Research: Oceans*, 118(6), 2992-3006.

Maamaatuaiahutapu, K., Garçon, V. C., Provost, C., Boulahdid, M., and Bianchi, A. A. (1994). Spring and winter water mass composition in the Brazil-Malvinas Confluence. *Journal of Marine Research*, 52(3), 397-426.

Maamaatuaiahutapu, K., Garçon, V., Provost, C., Boulahdid, M., and Osiroff, A.P. (1992). Brazil-Malvinas Confluence: Water mass composition. *Journal of Geophysical Research: Oceans*, 97(C6), 9493-9505.

Maamaatuaiahutapu, K., Garçon, V., Provost, C., and Mercier, H. (1998). Transports of the Brazil and Malvinas Currents at their Confluence. *Journal of Marine Research*, 56(2), 417-438.

Maamaatuaiahutapu, K., Provost, C., Andrié, C., and Vigan, X. (1999). Origin and ages of mode waters in the Brazil-Malvinas Confluence region during austral winter 1994. *Journal of Geophysical Research: Oceans*, 104(C9), 21051-21061.

Machado, I., Barreiro, M., and Calliari, D. (2013). Variability of chlorophyll-a in the Southwestern Atlantic from satellite images: Seasonal cycle and ENSO influences. *Continental Shelf Research*, 53, 102-109.

MacKinnon, J. A., St. Laurent, L. C., and Naveira Garabato, A. C. (2013). Dianeutral transport processes in the ocean interior. Ocean Circulation and Climate a 21st Century Perspective, G. Siedler et al., Eds., Academic Press, 159–183.

Manabe, S., and Bryan, K. (1969). Climate calculations with a combined ocean-atmosphere model. *Journal of Climate*, 26, 786-789.

Manabe, S., Bryan, K. and Spelman, M.J. (1975). A global ocean-atmosphere climate model. Part I. The atmospheric circulation. *Journal of Physical Oceanography*, 5, 3-29.

Manabe, S., and Stouffer, R. J. (1988). Two Stable Equilibria of a Coupled Ocean-Atmosphere Model. *Journal of Climate*, 1(9), 841-866.

Marshall, D. (1997). Subduction of water masses in an eddying ocean. *Journal of Marine Research*, 55(2), 201–222.

Marshall, J., Olbers, D., Ross, H., and Wolf-Gladrow, D. (1993). Potential Vorticity Constraints on the Dynamics and Hydrography of the Southern Ocean. *Journal of Physical Oceanography*, 23(3), 465-487.

Marshall, J., and Radko, T. (2003). Residual-mean solutions for the Antarctic Circumpolar Current and its associated overturning circulation. *Journal of Physical Oceanography*, 33(11), 2341–2354.

Marshall, J., and Speer, K. (2012). Closure of the meridional overturning circulation through Southern Ocean upwelling. *Nature Geosciences*, 5(3), 171–180.

Mason, E., Pascual, A., Gaube, P., Ruiz, S., Pelegrí, J.L., and Delepoulle, A. (2017). Subregional characterization of mesoscale eddies across the Brazil-Malvinas Confluence. *Journal of Geophysical Research: Oceans*, 122(4), 3329-3357.

Matano, R. P. (1993). On the separation of the Brazil Current from the coast. *Journal of Physical Oceanography*, 23, 79–90.

Matano, R. P., Combes, V., Piola, A. R., Guerrero, R., Palma, E. D., Ted Strub, P., James, C., Fenco, H., Chao, Y., and Saraceno, M. (2014). The salinity signature of the cross-shelf exchanges in the Southwestern Atlantic Ocean: Numerical simulations. *Journal of Geophysical Research: Oceans*, 119(11), 7949-7968.

Matano, R. P., Palma, E.D., and Piola, A.R. (2010). The influence of the Brazil and Malvinas Currents on the Southwestern Atlantic Shelf circulation. *Ocean Science Discussions*, 7, 837-871.

Mazloff, M. R., Ferrari, R., and Schneider, T. (2013). The Force Balance of the Southern Ocean Meridional Overturning Circulation. *Journal of Physical Oceanography*, 43(6), 1193-1208.

McCartney, M. S. (1977). Subantarctic mode water. A voyage of Discovery. *Deep-Sea Research*, 24, 103-119.

McCartney, M. S. (1982). The subtropical recirculation of Mode Waters. *Journal of Marine Research*, 40, 427–464.

McIntosh, P. C., and Rintoul, S.R. (1997). Do Box Inverse Models Work? *Journal of Physical Oceanography*, 27(2), 291-308.

Meinen, C. S., Garzoli, S. L., Perez, R. C., Campos, E., Piola, A. R., Chidichimo, M. P., Shenfy, D., and Sato, O. T. (2017). Characteristics and causes of Deep Western Boundary Current transport variability at 34.5ºS during 2009–2014. *Ocean Science*, 13(1), 175-194.

Meinen, C. S., Piola, A. R., Perez, R. C., and Garzoli, S. L. (2012). Deep Western Boundary Current transport variability in the South Atlantic: preliminary results from a pilot array at 34.5º S. *Ocean Science*, 8(6), 1041-1054.

Meinen, C. S., Speich, S., Perez, R. C., Dong, S., Piola, A. R., Garzoli, S. L., Baringer, M.O., Gladyshev, S., and Campos, E. J. D. (2013). Temporal variability of the meridional overturning circulation at 34.5ºS: Results from two pilot boundary arrays in the South Atlantic. *Journal of Geophysical Research: Oceans*, 118(12), 6461-6478.

Meinen, C. S., Speich, S., Piola, A. R., Ansorge, I., Campos, E., Kersalé, M., Terre, T., Chidichimo, M.P., Lamont, T., Sato, O.T., Perez, R.C., Valla, D., van den Berg, M., Le Hénaff, M., Dong, S., and Garzoli, S. L. (2018). Meridional Overturning Circulation Transport Variability at 34.5ºS During 2009–2017: Baroclinic and barotropic flows and the dueling Influence of the boundaries. *Geophysical Research Letters*, 45(9), 4180-4188.

Memery, L., Arhan, M., Alvarez-Salgado, X. A., Messias, M-J., Mercier, H., Castro, C. G., and Rios, A. F. (2000). The water masses along the western boundary of the south and equatorial Atlantic. *Progress in Oceanography*, 47, 69–98.

Merrifield, S. T., Laurent, L. S., Owens, B., Thurnherr, A. M., and Toole, J. M. (2016). Enhanced Diapycnal Diffusivity in Intrusive Regions of the Drake Passage. *Journal of Physical Oceanography*, 46(4), 1309-1321.

Molinari, R. L., and Festa, J. F. (2000). Effect of subjective choices on the objective analysis of sea surface temperature data in the tropical Atlantic and Pacific oceans. *Oceanologica Acta*, 23(1), 3-14.

Möller, O. O., Piola, A. R., Freitas, A. C., and Campos, E. J. D. (2008). The effects of river discharge and seasonal winds on the shelf off southeastern South America. *Continental Shelf Research*, 28(13), 1607-1624.

Morrison, A. K., Frölicher, T. L., and Sarmiento, J. L. (2015). Upwelling in the Southern Ocean. *Physics Today*, 68(1), 27-32.

Munk, W., 1966. Abyssal Recipes. D*eep Sea Research and Oceanographic Abstracts*, 13, 707–730.

Munk, W., and Wunsch, C. (1998). Abyssal recipes II: Energetics of tidal and wind mixing. *Deep Sea Research Part I*, 45, 1977–2010.

Nash, J.D., Kunze, E., Toole, J.M., and Schmitt, R.W. (2004). Internal Tide Reflection and Turbulent Mixing on the Continental Slope. *Journal of Physical Oceanography*, 34, 1117–1134.

Naveira Garabato, A. C., Ferrari, R., and Polzin, K. L. (2011). Eddy stirring in the Southern Ocean. *Journal of Geophysical Research: Oceans*, 116, C09019.

Naveira Garabato, A.C., Nurser, A.J., Scott, R.B., and Goff, J.A. (2013). The Impact of Small-Scale Topography on the Dynamical Balance of the Ocean. *Journal of Physical Oceanography*, 43, 647–668.

Naveira Garabato, A.C., Polzin, K.L., Ferrari, R., Zika, J.D., and Forryan, A. (2016). A Microscale View of Mixing and Overturning across the Antarctic Circumpolar Current. *Journal of Physical Oceanography*, 46, 233–254.

Naveira Garabato, A. C., Williams, A. P., and Bacon, S. (2014). The three-dimensional overturning circulation of the Southern Ocean during the WOCE era. *Progress in Oceanography*, 120, 41–78.

Nikurashin, M., and Ferrari, R. (2010). Radiation and dissipation of internal waves generated by geostrophic motions impinging on small-scale topography: Theory. *Journal of Physical Oceanography*, 40, 1055–1074.

Nikurashin, M. and Vallis, G. (2011). A Theory of Deep Stratification and Overturning Circulation in the Ocean. *Journal of Physical Oceanography*, 41, 485–502.

Nishikawa, S., Tsujino, H., Sakamoto, K., and Nakano, H. (2010). Effects of Mesoscale Eddies on Subduction and Distribution of Subtropical Mode Water in an Eddy-Resolving OGCM of the Western North Pacific. *Journal of Physical Oceanography*, 40, 1748–1765.

Oakey (1982). Determination of the rate of dissipation of turbulent energy from simultaneous temperature and velocity shear microstructure measurements. *Journal of Physical Oceanography*, 12, 256–271.

Olson, D. B. (1991). Rings in the ocean. *Annual Review Earth Planet Science*, 19, 283–311.

Olson, D. B., Podestá, G. P., Evans, R. H., and Brown, O. B. (1988). Temporal variations in the separation of Brazil and Malvinas Currents. *Deep Sea Research Part A: Oceanographic Research Papers*, 35(12), 1971-1990.

Orsi, A. H., Whitworth, T., and Nowlin, W.D. (1995). On the meridional extent and fronts of the Antarctic Circumpolar Current. *Deep Sea Research Part I: Oceanographic Research Papers*, 42, 641-673.

Orúe-Echevarría, D., Pelegrí, J. L., Alonso-González, I. J., Benítez-Barrios, V. M., De La Fuente, P., Emelianov, M., Gasser, M., Herrero, C., Isern-Fontanet, J., Peña-Izquierdo, J., Ramírez-Garrido, S., Rosell-Fieschi, M., Salvador, J., Saraceno, M., Valla, D., and Vidal, M. (2019). Dataset on the TIC-MOC cruise onboard the R/V Hespérides, March 2015, Brazil-Malvinas Confluence. *Data in Brief*, 22, 185-194.

Orúe-Echevarría, D., Pelegrí, J. L., Machín, F., Hernández-Guerra, A., and Emelianov, M. (2019). Inverse Modeling the Brazil-Malvinas Confluence. *Journal of Geophysical Research: Oceans*, 124(1), 527-554.

Osborn, T.R. (1980). Estimates of the local rate of vertical diffusion from dissipation measurements. *Journal of Physical Oceanography*, 10, 83–89.

Osborn, T. R., and Cox, C. S. (1972). Oceanic fine structure. *Geophysical Fluid Dynamics*, 3(1), 321-345.

Ott, M. W. (2002). An Improvement in the Calculation of ADCP Velocities. *Journal of Atmospheric and Oceanic Technology*, 19(10), 1738-1741.

Paillard, D. (1998). The timing of Pleistocene glaciations from a simple multiple-state climate model. *Nature*, 391, 378–381.

Paillard, D. (2001). Glacial cycles: Toward a new paradigm. *Reviews of Geophysics*, 39(3), 325-346.

Paillard, D., Ghil, M., and Le Treut, H. (1993). Dissolved organic matter and the glacial-interglacial pCO_2 problem. G*lobal Biogeochemical Cycles*, 7(4), 901–914.

Paillard, D., and Parrenin, F. (2004). The Antarctic ice sheet and the triggering of deglaciations. *Earth and Planetary Science Letters*, 227, 263–271.

Palma, E. D., Matano, R. P., and Piola, A. R. (2004). A numerical study of the Southwestern Atlantic Shelf circulation: Barotropic response to tidal and wind forcing. *Journal of Geophysical Research: Oceans*, 109(C8).

Palma, E. D., Matano, R. P., and Piola, A. R. (2008). A numerical study of the Southwestern Atlantic Shelf circulation: Stratified ocean response to local and offshore forcing. *Journal of Geophysical Research: Oceans*, 113(C11).

Palmer, M.D., and McNeall, D.J. (2014). Internal variability of Earth's energy budget simulated by CMIP5 climate models. *Environmental Research Letters*, 9, 034016.

Palter, J. B., Sarmiento, J. L., Gnanadesikan, A., Simeon, J., and Slater, R. D. (2010). Fueling export production: nutrient return pathways from the deep ocean and their dependence on the Meridional Overturning Circulation. *Biogeosciences*, 7(11), 3549-3568.

Paniagua, G. F., Saraceno, M., Piola, A. R., Guerrero, R., Provost, C., Ferrari, R., Lago, L. S., and Artana, C. (2018). Malvinas Current at 40-41S: First Assessment of Temperature and Salinity Temporal Variability. *Journal of Geophysical Research: Oceans*, 123,5323-5340.

Pascual, A., Bouffard, J., Ruiz, S., Buongiorno Nardelli, B., Vidal-Vijande, E., Escudier, R., Sayol, J.M., and Orfila, A. (2013). Recent improvements in mesoscale characterization of the western Mediterranean Sea: synergy between satellite altimetry and other observational approaches. *Scientia Marina*, 77, 19-36.

Peacock, S., Lane, E., and Restrepo, J. M. (2006). A possible sequence of events for the generalized glacial-interglacial cycle. *Global Biogeochemical Cycles*, 20, GB2010.

Peixoto, J., and Oort, A. H. (1996). The Climatology of Relative Humidity in the Atmosphere. *Journal of Climate*, 9(12), 3443-3463.

Pelegrí, J. L., De La Fuente, P., Olivella, R., and García-Olivares, A. (2013). Global constraints on net primary production and inorganic carbon supply during glacial and interglacial cycles. *Paleoceanography*, 28, 713–725.

Pelegrí, J.L., Orúe-Echevarría, D., Alonso-González, I.J., Benítez-Barrios, V.M., De La Fuente, P., Emelianov, M., Gasser, M., Herrero, C., Peña-Izquierdo, J., Ramírez-Garrido, S., Rosell-Fieschi, M, Isern-Fontanet, J., Salvador, J., Saraceno, M., Valla, D., and Vidal, M. (2018). Data for the March 2015 TIC-MOC cruise, R/V Hespérides, Brazil-Malvinas Confluence. Mendeley Data, v2.

Peterson, R. G. (1992). The boundary currents in the western Argentine Basin. *Deep Sea Research Part A. Oceanographic Research Papers*, 39, 623-644.

Peterson, L.C., Haug, G.H., Hughen, K.A., and Röhl, U. (2000). Rapid changes in the hydrologic cycle of the tropical Atlantic during the last glacial. *Science*, 290(5498), 1947-1951.

Peterson, R. G., and Whitworth, T. (1989). The subantarctic and polar fronts in relation to deep water masses through the southwestern Atlantic. *Journal of Geophysical Research: Oceans*, 94(C8), 10817-10838.

Petit, J. R., Jouzel, J., Raynaud, D., Barkov, N. I., Barnola, J. M., Basile, I., Bender, M., Chappellaz, J., Davis, M., Delaygue, G., Delmotte, M., Kotlyakov, V.M., Legrand, M., Lipenkov, V.Y., Lorius, C., Pépin, C., Ritz, E., Saltzman, E., and Stievenard, M. (1999). Climate and atmospheric history of the past 420,000 years from the Vostok ice core, Antarctica. *Nature*, 399, 429.

Pilo, G. S., Mata, M. M., and Azevedo, J. L. L. (2015). Eddy surface properties and propagation at Southern Hemisphere western boundary current systems. *Ocean Science*, 11(4), 629-641.

Piola, A. R., Campos, E. J. D., Möller, O. O., Charo, M., and Martinez, C. (2000). Subtropical Shelf Front off eastern South America. *Journal of Geophysical Research: Oceans*, 105(C3), 6565-6578.

Piola, A. R., Franco, B.C., Palma, E.D., and Saraceno, M. (2013). Multiple jets in the Malvinas Current. *Journal of Geophysical Research: Oceans*, 118(4), 2107-2117.

Piola, A. R., and Gordon, A. L. (1989). Intermediate Waters in the Southwest South-Atlantic. *Deep Sea Research: Part I*, 36(1), 1–16.

Piola, A. R., Martínez Avellaneda, N., Guerrero, R. A., Jardón, F. P., Palma, E. D., and Romero, S. I. (2010). Malvinas-slope water intrusions on the northern Patagonia continental shelf. *Ocean Science*, 6(1), 345-359.

Piola, A., and Matano, R. (2001). The South Atlantic Western Boundary Currents Brazil/Falkland (Malvinas) Currents. In Steel, J.M. Thorpe, S.A. and Turekin, K.K. (Eds.), Encyclopedia of Ocean Sciences (pp. 340-349). Academic Press, Waltham, MA.

Piola, A. R., Matano, R. P., Palma, E. D., Möller, O. O., and Campos, E. J. D. (2005). The influence of the Plata River discharge on the western South Atlantic shelf. *Geophysical Research Letters*, 32(1).

Piola, A. R., Möller, O. O., Guerrero, R. A., and Campos, E. J. D. (2008). Variability of the subtropical shelf front off eastern South America: Winter 2003 and summer 2004. *Continental Shelf Research*, 28(13), 1639-1648.

Plumb, R. A., and Mahlman, J. D. (1987). The Zonally Averaged Transport Characteristics of the GFDL General Circulation/Transport Model. *Journal of the Atmospheric Sciences*, 44(2), 298-327.

Polzin, K., Kunze, E., Hummon, J., and Firing, E. (2002). The finescale response of lowered ADCP velocity profiles. *Journal of Atmospheric and Oceanic Technology*,19(2),205-224.

Polzin, K. L., Toole, J. M., Ledwell, J. R., and Schmitt, R. (1997). Spatial variability of turbulent mixing in the abyssal ocean. *Science*, 276, 93–96.

Provost, C., Escoffier, C., Maamaatuaiahutapu, K., Kartavtseff, A., and Garçon, V. (1999). Subtropical mode waters in the South Atlantic Ocean. *Journal of Geophysical Research: Oceans*, 104(C9), 21033-21049.

Provost, C., Garçon, V., and Falcon, L.M. (1996). Hydrographic conditions in the surface layers over the slope-open ocean transition area near the Brazil-Malvinas confluence during austral summer 1990. *Continental Shelf Research*, 16, 215-235.

Provost, C., and Le Traon, P.-Y. (1993). Spatial and temporal scales in altimetric variability in the Brazil-Malvinas current confluence region: Dominance of the semiannual period and large spatial scales. *Journal of Geophysical Research: Oceans*, 98(C10), 18037-18051.

Pujol, M.-I., Faugère, Y., Taburet, G., Dupuy, S., Pelloquin, C., Ablain, M., and Picot, N. (2016). DUACS DT2014: the new multi-mission altimeter data set reprocessed over 20 years. *Ocean Science*, 12, 1067-1090.

Qu, T., Xie, S.-P., Mitsudera, H., and Ishida, A. (2002). Subduction of the North Pacic Mode Water in a global high-resolution GCM. *Journal of Physical Oceanography*, 32, 746–763.

Rahmstorf, S. (2002). Ocean circulation and climate during the past 120,000 years. *Nature*, 419(6903), 207–214.

Ramanathan, V., Cess, R. D., Harrison, E. F., Minnis, P., Barkstrom, B. R., Ahmad, E., and Hartmann, D. (1989). Cloud-Radiative Forcing and Climate: Results from the Earth Radiation Budget Experiment. *Science*, 243(4887), 57.

Ramaswamy, V., Boucher, O., Haigh, J., Hauglustaine, D., Haywood, J., Myhre, G., Nakajima, T., Shi, G., and Solomon, S. (2001). Radiative forcing of climate change. In Climate Change 2001: The Scientific Basis, edited by J. T. Houghton, et al., pp. 350-406, Cambridge Univ. Press, New York.

Redi, M. H. (1982). Oceanic isopycnal mixing by coordinate rotation. *Journal of Physical Oceanography*, 12, 1154–1158.

Reid, J.L. (1989). On the total geostrophic circulation of the South Atlantic Ocean: Flow patterns, tracers, and transports. *Progress in Oceanography*, 23, 149–244.

Reid, J.L., Nowlin, W.D., and Patzert, W.C. (1977). On the Characteristics and Circulation of the Southwestern Atlantic Ocean. *Journal of Physical Oceanography*, 7, 62–91.

Reynolds, R. W., Chelton, D. B., Roberts-Jones, J., Martin, M. J., Menemenlis, D.,and Merchant, C. J. (2013). Objective Determination of Feature Resolution in Two Sea Surface Temperature Analyses. *Journal of Climate*, 26(8), 2514-2533.

Rhines, P. B., and Young, W. R. (2006). Homogenization of potential vorticity in planetary gyres. *Journal of Fluid Mechanics*, 122, 347-367.

Rintoul, S. R. (1991). South Atlantic interbasin exchange. *Journal of Geophysical Research*, 96(C2), 2675–2692.

Rintoul, S.R. (2018). The global influence of localized dynamics in the Southern Ocean. *Nature*, 558:7709, 209-218.

Roach, C. J., Balwada, D., and Speer, K. (2018). Global observations of horizontal mixing from Argo float and surface drifter trajectories. *Journal of Geophysical Research: Oceans*, 123, 4560–4575.

Roca, J.M., and Pelegrí, J.L. (2019). Analysis of the planetary thermal distribution with a simple three-zone maximum-flux model. Submitted to the Int. J. Heat Mass Transfer.

Roden, G. I. (1986) Thermohaline fronts and baroclinic flow in the Argentine Basin during the austral spring of 1984. *Journal of Geophysical Research*, 91, 5075-5093.

Rodrigues, R. R., Wimbush, M., Watts, D. R., Rothstein, L. M., and Ollitrault, M. (2010). South Atlantic mass transports obtained from subsurface float and hydrographic data. *Journal of Marine Research*, 68(6), 819-850.

Roget, E., Lozovatsky, I., Sanchez, X., and Figueroa, M. (2006). Microstructure measurements in natural waters: Methodology and applications. *Progress in Oceanography*, 70, 126-148.

Romanova, V., Lohmann, G., and Grosfeld, K. (2006). Effect of land albedo, CO_2, orography, and oceanic heat transport on extreme climates. *Climate of the Past*, 2.

Romero, S. I., Piola, A. R., Charo, M., and Garcia, C. A. E. (2006), Chlorophyll-a variability off Patagonia based on SeaWiFS data. *Journal of Geophysical Research: oceans*, 111, C0502.

Rossow, W. B., and Dueñas, E. N. (2004). The International Satellite Cloud Climatology Project (ISCCP) Web Site.

Ruddick, B., Anis, A., and Thompson, K. (2000). Maximum Likelihood Spectral Fitting: The Batchelor Spectrum. *Journal of Atmospheric and Oceanic Technology*, 17, 1541–1555.

Sans, J. (2018). Metodología de reconstrucción de estructuras frontales. (Master's thesis, Universitat Oberta de Catalunya).

Saraceno, M., Guerrero, R., Piola, A.R., Provost, C., Perault, F., Ferrari, R., Paniagua, G.F., Lago, L., and Artana, C. (2018). Malvinas Current 2014-2015: Mooring velocities. SEANOE.

Saraceno, M., and Provost, C. (2012). On eddy polarity distribution in the southwestern Atlantic. *Deep Sea Research Part I*, 69, 62-69.

Saraceno, M., Provost, C., and Piola, A. R. (2005). On the relationship between satellite-retrieved surface temperature fronts and chlorophyll a in the western South Atlantic. *Journal of Geophysical Research: Oceans*, 110(C11).

Saraceno, M., Provost, C., Piola, A.R., Bava, J., and Gagliardini, A. (2004). Brazil Malvinas Frontal System as seen from 9 years of advanced very high resolution radiometer data. *Journal of Geophysical Research: Oceans*, 109, C05027.

Sarmiento, J. L., and Toggweiler, J. R. (1984). A new model for the role of the oceans in determining atmospheric pCO_2. *Nature*, 308(5960), 621–624.

Sato, O. T., and Polito, P.S. (2014). Observation of South Atlantic subtropical mode waters with Argo profiling float data. *Journal of Geophysical Research: Oceans*, 119(5), 2860-2881.

Saunders, P. M., and King, B.A. (1995). Bottom Currents Derived from a Shipborne ADCP on WOCE Cruise A11 in the South Atlantic. *Journal of Physical Oceanography*, 25(3), 329-347.

Schmid, C. (2014). Mean vertical and horizontal structure of the subtropical circulation in the South Atlantic from three-dimensional observed velocity fields. *Deep Sea Research Part I: Oceanographic Research Papers*, 91(C), 50-71.

Schmid, C.and Garzoli, S.L. (2009). New observations of the spreading and variability of the Antarctic Intermediate Water in the Atlantic. *Journal of Marine Research*, 67 (6), 815–843.

Schmid, C., Siedler, G., and Zenk, W. (2000). Dynamics of Intermediate Water Circulation in the Subtropical South Atlantic. *Journal of Physical Oceanography*, 30(12), 3191-3211.

Schneider, S. H. (1972). Cloudiness as a Global Climatic Feedback Mechanism: The Effects on the Radiation Balance and Surface Temperature of Variations in Cloudiness. *Journal of the Atmospheric Sciences*, 29(8), 1413-1422.

Schouten, M. W., and Matano, R. P. (2006). Formation and pathways of intermediate water in the Parallel Ocean Circulation Model's Southern Ocean. *Journal of Geophysical Research: Oceans*, 111(C6).

Sellers, W. D. (1969). A Global Climatic Model Based on the Energy Balance of the Earth-Atmosphere System. *Journal of Applied Meteorology*, 8(3), 392-400.

Shcherbina, A.Y., Gregg, M.C., Alford, M.H., and Harcourt, R.R. (2010). Three-Dimensional Structure and Temporal Evolution of Submesoscale Thermohaline Intrusions in the North Pacific Subtropical Frontal Zone. *Journal of Physical Oceanography*, 40, 1669–1689.

Siegenthaler, U., Stocker, T. F., Monnin, E., Lüthi, D., Schwander, J., Stauffer, B., Raynaud, D., Barnola, J.M., Fischer, H., Masson-Delmotte, V., and Jouzel, J. (2005). Stable Carbon Cycle-Climate Relationship During the Late Pleistocene. *Science*, 310(5752), 1313.

Siegenthaler U, and Wenk, Th. (1984). Rapid atmospheric CO2 variations and ocean circulation. *Nature*, 308, 624–626.

Sigman, D. M., Hain, M. P., and Haug, G. H. (2010). The polar ocean and glacial cycles in atmospheric CO_2 concentration. *Nature*, 466(7302), 47–55.

Skinner, L.C. (2009). Glacial–interglacial atmospheric CO_2 change: a possible standing volume effect on deep-ocean carbon sequestration. *Climate of the Past*, 5, 1259-1296.

Sloyan, B. M., and Rintoul, S. R. (2000). Estimates of Area-Averaged Diapycnal Fluxes from Basin-Scale Budgets. *Journal of Physical Oceanography*, 30(9), 2320-2341.

Sloyan, B. M., and Rintoul, S.R. (2001). Circulation, Renewal, and Modification of Antarctic Mode and Intermediate Water. *Journal of Physical Oceanography*, 31(4), 1005-1030.

Sloyan, B.M., Talley, L.D., Chereskin, T.K., Fine, R., and Holte, J. (2010). Antarctic Intermediate Water and Subantarctic Mode Water Formation in the Southeast Pacific: The Role of Turbulent Mixing. *Journal of Physical Oceanography*, 40, 1558–1574.

Smith, K. S., and Marshall, J. (2009). Evidence for Enhanced Eddy Mixing at Middepth in the Southern Ocean. *Journal of Physical Oceanography*, 39(1), 50-69.

Spadone, A., and Provost, C. (2009). Variations in the Malvinas Current volume transport since October 1992. *Journal of Geophysical Research: Oceans*, 114(C2).

Speer, K., Rintoul, S. R., and Sloyan, B. (2000). The Diabatic Deacon Cell. *Journal of Physical Oceanography*, 30(12), 3212-3222.

Sprintall, J., and Meyers, G. (1991). An optimal XBT sampling network for the eastern Pacific Ocean. *Journal of Geophysical Research: Oceans*, 96(C6), 10539-10552.

Stephens, G. L., Li, J., Wild, M., Clayson, C. A., Loeb, N., Kato, S., L'Ecuyer, T., Stackhouse, P.W., Lbsock, M., and Andrews, T. (2012). An update on Earth's energy balance in light of the latest global observations. *Nature Geoscience*, 5, 691.

Stott, L., Poulsen, C., Lund, D., and Thunell, R. (2002). Super ENSO and global climate oscillations at millenial time scales. *Science*, 297(5579), 222-226.

Stramma, L. (1989). The Brazil current transport south of 23S. *Deep Sea Research Part A. Oceanographic Research Papers*, 36(4), 639-646.

Stramma, L., and England, M. (1999). On the water masses and mean circulation of the South Atlantic Ocean. *Journal of Geophysical Research*, 104(C9), 20863–20883.

Stramma, L., and Peterson, R.G. (1990). The South Atlantic Current. *Journal of Physical Oceanography*, 20(6), 846-859.

Strub, P. T., James, C., Combes, V., Matano, R. P., Piola, A. R., Palma, E. D., Saraceno, M., Guerrero, R.A., Fenco, H., and Ruiz-Etcheverry, L. A. (2015). Altimeter-derived seasonal circulation on the southwest Atlantic shelf: 27º–43ºS. *Journal of Geophysical Research: Oceans*, 120(5), 3391-3418.

Sumata, H., Kauker, F., Karcher, M., Rabe, B., Timmermans, M. L., Behrendt, A., Gerdes, R., Schauer, U., Shimada, K., Cho, K. H., and Kikuchi, T. (2018). Decorrelation scales for Arctic Ocean hydrography – Part I: Amerasian Basin. *Ocean Science*, 14(1), 161-185.

Talley, L. D. (1996). Antarctic Intermediate Water in the South Atlantic. The South Atlantic: Present and Past Circulation, G. G. Wefer, W. H. Berger, and D. Webb, Eds., Springer-Verlag, 219–238.

Talley, L.D. (2003). Shallow, Intermediate, and Deep Overturning Components of the Global Heat Budget. *Journal of Physical Oceanography*, 33, 530-560.

Talley, L.D. (2013). Closure of the global overturning circulation through the Indian, Pacific and Southern Oceans: schematics and transports. *Oceanography*, 26(1), 80-97.

Talley, L. D., Pickard, G. L., Emery, W. J., and Swift, J. H. (2011). Descriptive Physical Oceanography: An Introduction (Sixth Edition), Elsevier, Boston, 560 pp.

Tanaka, Y., and Hasumi, H. (2008). Injection of Antarctic Intermediate Water into the Atlantic subtropical gyre in an eddy resolving ocean model. *Geophysical Research Letters*, 35(11).

Thurnherr, A. M., Goszczko, I., and Bahr, F. (2017). Improving LADCP velocity with external heading, pitch, and roll. *Journal of Atmospheric and Oceanic Technology*, 34(8), 1713-1721.

Toggweiler, J. R. (1999). Variation of atmospheric CO_2 by ventilation of the ocean's deepest water. *Paleoceanography*, 14(5), 571–588.

Toggweiler, J. R., and Samuels, B. (1995). Effect of Drake Passage on the global thermohaline circulation. *Deep Sea Research Part I*, 42, 477–500.

Treguier, A. M., Held, I. M., and Larichev, V. D. (1997). Parameterization of Quasigeostrophic Eddies in Primitive Equation Ocean Models. *Journal of Physical Oceanography*, 27(4), 567-580.

Trenberth, K.E. and Caron, J.M. (2001). Estimates of Meridional Atmosphere and Ocean Heat Transports. *Journal of Climate*, 14, 3433–3443.

Trenberth, K.E., and Stepaniak, D.P. (2003). Seamless Poleward Atmospheric Energy Transports and Implications for the Hadley Circulation. *Journal of Climate*, 16, 3706–3722.

Tsuchiya, M., Talley, L. D., and McCartney, M. S. (1994). Water-mass distributions in the western South Atlantic; A section from South Georgia Island (54S) northward across the equator. *Journal of Marine Research*, 52(1), 55-81.

Tulloch, R., Ferrari, R., Jahn, O., Klocker, A., LaCasce, J., Ledwell, J. R., and Watson, A. (2014). Direct Estimate of Lateral Eddy Diffusivity Upstream of Drake Passage. *Journal of Physical Oceanography*, 44(10), 2593-2616.

Valla, D., and Piola, A. R. (2015). Evidence of upwelling events at the northern Patagonian shelf break. *Journal of Geophysical Research: Oceans*, 120(11), 7635-7656.

Valla, D., Piola, A. R., Meinen, C. S., and Campos, E. (2018). Strong mixing and recirculation in the northwestern Argentine Basin. *Journal of Geophysical Research: Oceans*, 123, 4624-4648.

Valla, D., Piola, A. R., Meinen, C. S., and Campos, E. (2019). Abyssal transport variations in the southwest South Atlantic: First insights from a long-term observation array at 34.5S. *Geophysical Research Letters*, 46, 6699–6705.

Vigan, X., Provost, C., Bleck, R., and Courtier, P. (2000). Sea surface velocities from sea surface temperature image sequences: 1. Method and validation using primitive equation model output. *Journal of Geophysical Research: Oceans*, 105(C8), 19499-19514.

Visbeck, M. (2002). Deep velocity profiling using lowered acoustic doppler current profilers: Bottom track and inverse solutions. *Journal of Atmospheric and Oceanic Technology*, 19, 794–807.

Visbeck, M. (2007). Power of pull. *Nature*, 447(7143), 383.

Vivier, F., and Provost, C. (1999a). Direct velocity measurements in the Malvinas Current. *Journal of Geophysical Research: Oceans*, 104(C9), 21083-21103.

Vivier, F., and Provost, C. (1999b). Volume transport of the Malvinas Current: Can the flow be monitored by TOPEX/POSEIDON? *Journal of Geophysical Research: Oceans*, 104(C9), 21105-21122.

von Schuckmann, K., Palmer, M.D., Trenberth, K.E., Cazenave, A., Chambers, D., Champollion, N., Hansen, J., Josey, S.A., Loeb, N., Mathieu, P.-P, Meyssignac, B., and Wild, M. (2016). An imperative to monitor Earth's energy imbalance. *Nature Climate Change*, 6,138–144.

Wainer, I., Gent , P., and Goni, G. (2000). Annual cycle of the Brazil-Malvinas confluence region in the National Center for Atmospheric Research Climate System Model. *Journal of Geophysical Research: Oceans*, 105(C11), 26167-26177.

Walter, M., Mertens, C., and Rhein, M. (2005). Mixing estimates from a large-scale hydrographic survey in the North Atlantic. *Geophysical Research Letters*, 32, L13605.

Warren, S. G., Hahn, C. H., London, J., Chervin, R. M., and Jenne, R. L. (1988). Global distribution of Total Cloud Cover and Cloud Type Amounts over the Ocean. NCAR Technical Note NCAR/TN-317+STR, 212.

Waterhouse, A.F., MacKinnon, J.A., Nash, J.D., Alford, M.H., Kunze, E., Simmons, H.L., Polzin, K.L., St. Laurent, L.C., Sun, O.M., Pinkel, R., Talley, L.D., Whalen, C.B., Huussen, T.N., Carter, G.S., Fer, I., Waterman, S., Naveira Garabato, A.C., Sanford, T.B., and Lee. C.M. (2014). Global patterns of diapycnal mixing from measurements of the turbulent dissipation rate. *Journal of Physical Oceanography*, 44, 1854–1872.

Waterman, S., Naveira Garabato, A. C., and Polzin, K. L. (2013). Internal waves and turbulence in the Antarctic Circumpolar Current. *Journal of Physical Oceanography*, 43, 259–282.

Watson, A.J., Vallis, G.K., and Nikurashin, M. (2015). Southern Ocean buoyancy forcing of ocean ventilation and glacial atmospheric CO2. *Nature Geoscience*, 8, (11), 861-864.

Watts, D.R., Tracey, K.L., Donohue, K.A., and Chereskin, T.K. (2016). Estimates of Eddy Heat Flux Crossing the Antarctic Circumpolar Current from Observations in Drake Passage. *Journal of Physical Oceanography*, 46, 2103–2122.

Wetherald, R. T., and Manabe, S. (1980). Cloud Cover and Climate Sensitivity. *Journal of the Atmospheric Sciences*, 37(7), 1485-1510.

Whalen, C. B., Talley, L. D., and MacKinnon, J. A. (2012). Spatial and temporal variability of global ocean mixing inferred from Argo proles. *Geophysical Research Letters*, 39, L18612.

Wienders, N., Arhan, M., and Mercier, H. (2000). Circulation at the western boundary of the south and equatorial Atlantic: Exchanges with the ocean interior. *Journal of Marine Research*, 58, 1007–1039.

Winkler, L.W. (1888). The determination of dissolved oxygen. Ber. Dtsch. Chem. Ges., 21, 2843–2846.

Worthington, L. V. (1976). On the North Atlantic circulation, Johns Hopkins Oceanographic Studies, 6, John Hopkins University Press, Baltimore, Md., 110 pp.

Wunsch, C. (1978). The North Atlantic general circulation west of 50^{o}W determined by inverse methods. *Reviews of Geophysics*, 16(4), 583-620.

Wunsch, C. (1996). The Ocean Inverse Circulation Inverse Problem. Cambridge University Press, 442 pp.

Wunsch, C. (1999). Where do ocean eddy heat fluxes matter? *Journal of Geophysical Research*, 104(C6), 13235–13249.

Wunsch, C. (2005). The Total Meridional Heat Flux and Its Oceanic and Atmospheric Partition. *Journal of Climate*, 18, 4374–4380.

Wunsch, C., and Ferrari, R. (2004). Vertical mixing, energy, and the general circulation off the oceans. *Annual Review of Fluid Mechanics*, 36(1), 281–314.

Xu, L., Li, P., Xie, S.-P., Liu, Q., Liu, C., and Gao, W. (2016). Observing mesoscale eddy effects on mode-water subduction and transport in the North Pacific. *Nature Communications*, 7, 10505.

You, Y. (1999). Dianeutral mixing, transformation and transport of Antarctic Intermediate Water in the South Atlantic Ocean. *Deep Sea Research Part II: Topical Studies in Oceanography*, 46(1), 393-435.

You, Y. (2002). A global ocean climatological atlas of the Turner angle: implications for double-diffusion and water-mass structure. *Deep Sea Research Part I: Oceanographic Research Papers*, 49(11), 2075-2093.

You, Y. (2002). Quantitative estimate of Antarctic Intermediate Water contributions from the Drake Passage and the southwest Indian Ocean to the South Atlantic. *Journal of Geophysical Research: Oceans*, 107(C4), 6-1-6-20.

Zemba, J. C. (1991). The structure and transport of the Brazil Current between 27º and 36º south. Ph.D. thesis, Massachusetts Institute of Technology / Woods Hole Oceanographic Institution, 160 pp.

Zhang, Z., Zhong, Y., Tian, J., Yang, Q., and Zhao, W. (2014). Estimation of eddy heat transport in the global ocean from Argo data. *Acta Oceanologica Sinica*, 33, 42.

Zweng, M. M., Reagan, J. R., Antonov, J. I., Locarnini, R. A., Mishonov, A. V., Boyer, T. P., and Biddle, M. M. (2013). World Ocean Atlas 2013, Volume 2: Salinity. S. Levitus, Ed., A. Mishonov Technical Ed.; NOAA Atlas NESDIS 74, 39 pp.